Background–Source separation in astronomical images with Bayesian Probability Theory

Fabrizia Guglielmetti

München 2010

Background–Source separation in astronomical images with Bayesian Probability Theory

Fabrizia Guglielmetti

Dissertation der Fakultät für Physik
der *Ludwig–Maximilians–Universität* München
für den Grad des
Doctor rerum naturalium

vorgelegt von
Fabrizia Guglielmetti
aus Rivarolo Canavese (Torino) - Italien

München, November 2010

Erstgutachter: Prof. Dr. Hans Böhringer
Zweitgutachter: Prof. Dr. Dr.h.c. Volker Dose
Tag der mündlichen Prüfung: 1. Februar 2011

Contents

List of Figures

List of Tables

Acronyms

In the following is a list of acronyms frequently appearing in the thesis:

2dFGRS	two–degree-field Galaxy Redshift Survey (Colless *et al.*, 2001)
ACIS	Advanced CCD Imaging Spectrometer
ACS	Advanced Camera for Surveys
AGN	active galactic nucleus
BPT	Bayesian Probability Theory
BSC	*ROSAT* Bright Source Catalogue (Voges *et al.*, 1999)
BSS	Background–Source Separation
CCD	charge–coupled device
cdf	cumulative distribution function
CDF–S	*Chandra* Deep Field South
CDF–S 1Ms	*Chandra* Deep Field South survey (Giacconi *et al.*, 2002*b*)
CDF–S 2Ms	*Chandra* Deep Field South survey (Luo *et al.*, 2008)
CDF–S 500ks	*Chandra* Deep Field South 500ks test fields 1-4
c_{f}	conversion factor of $(4.6 \pm 0.1) \times 10^{-12}$ erg cm^{-2} (Rosati *et al.*, 2002*a*)
CIAO	*Chandra* Interactive Analysis of Observations software package
CXO	*Chandra X*–ray Observatory (Weisskopf *et al.*, 2000)
DSS	Digitized Sky Survey (Lasker *et al.*, 2008)
E–CDF–S	Extended *Chandra* Deep Field South (Lehmer *et al.*, 2005)
fov	field–of–view
FSC	*ROSAT* Faint Source Catalogue (Voges *et al.*, 2000)
FWHM	Full–Width at Half Maximum
GCA	Growth Curve Analysis (Böhringer *et al.*, 2000)
GOODS	Great Observatories Origins Deep Survey (Dickinson *et al.*, 2003)
HRI	High Resolution Imager
IDA	integrated data analysis
LSS	large–scale structure
MAP	maximum a posteriori
MaxEnt	maximum entropy (principle)
MCMC	Markov–Chain Monte Carlo
ML	Maximum Likelihood
MPD	marginal Poisson distribution
NORAS	Northern ROSAT All–Sky Galaxy Cluster Survey (Böhringer *et al.*, 2000)

PD	Poisson distribution
pdf	probability density function
POSS	Palomar Observatory Sky Survey
PSF	point–spread function
PSPC	Position–Sensitive Proportional Counter
QSO	quasistellar object
RASS	*ROSAT* All–Sky Survey
RBF	radial basis function
RDCS	ROSAT Deep Cluster Survey (Rosati *et al.*, 1998)
REFLEX	ROSAT–ESO Flux Limited X–ray Galaxy Cluster Survey (Böhringer *et al.*, 2004)
SASS	Standard Analysis Software System
SDSS	Sloan Digital Sky Survey (Abazajian, 2009)
SPM	source probability map
SNR	supernova remnant
TPS	thin–plate spline
VTP	Voronoi Tessellation and Percolation (Ebeling and Wiedenmann, 1993)
WGACAT	(*ROSAT*) White, Giommi, Angelini Catalogue (White *et al.*, 1994)
WFI	Wide Field Imager
WHIM	warm–hot intergalactic medium
WT	Wavelet Transform
XLF	X–ray luminosity function
XMM-COSMOS	XMM–*Newton* Cosmological Evolution Survey (Hasinger *et al.*, 2007)
XMM-LSS	XMM–*Newton* Large Scale Structure survey (Pierre *et al.*, 2004)

Abstract

In this work a new method for the detection of faint, both point–like and extended, astronomical objects based on the integrated treatment of source and background signals is described. This technique is applied to public data obtained by imaging methods of high–energy observational astronomy in the X–ray spectral regime. These data are usually employed to address current astrophysical problems, e.g. in the fields of stellar and galaxy evolution and the large–scale structure of the universe. The typical problems encountered during the analysis of these data are: spatially varying cosmic background, large variety of source morphologies and intensities, data incompleteness, steep gradients in the data, and few photon counts per pixel. These problems are addressed with the developed technique. Previous methods extensively employed for the analysis of these data are, e.g., the sliding window and the wavelet based techniques. Both methods are known to suffer from: describing large variations in the background, detection of faint and extended sources and sources with complex morphologies. Large systematic errors in object photometry and loss of faint sources may occur with these techniques.

The developed algorithm is based on Bayesian probability theory, which is a consistent probabilistic tool to solve an inverse problem for a given state of information. The information is given by a parameterized model for the background and prior information about source intensity distributions quantified by probability distributions. For the background estimation, the image data are not censored. The background *rate* is described by a two–dimensional thin–plate spline function. The background *model* is given by the product of the background rate and the exposure time which accounts for the variations of the integration time. Therefore, the background as well as effects like vignetting, variations of detector quantum efficiency and strong gradients in the exposure time are being handled properly which results in improved detections with respect to previous methods. Source probabilities are provided for individual pixels as well as for correlations of neighbouring pixels in a multiresolution analysis. Consequently, the technique is able of detecting point–like and extended sources and their complex morphologies. Furthermore, images of different spectral bands can be combined probabilistically to further increase the resolution in crowded regions. The developed method characterizes all detected sources in terms of position, number of source counts, and shape including uncertainties.

The comparison with previous techniques shows that the developed method allows for an improved determination of background and source parameters. The method is applied to data obtained by the *ROSAT* and *Chandra* X–ray observatories whereas particularly the detection of faint and extended sources is improved with respect to previous analyses. This lead to the discovery of new galaxy clusters and quasars in the X–ray band which are confirmed in the optical regime using additional observational data. The new technique developed in this work is particularly suited to the identification of objects featuring extended emission like clusters of galaxies.

Zusammenfassung

In der vorliegenden Arbeit wird eine neue Methode zur Entdeckung lichtschwacher punktförmiger sowohl als auch ausgedehnter Himmelsobjekte basierend auf einer integralen Behandlung des Signals und des Untergrundes vorgestellt. Das Verfahren wird auf öffentlich zugängliche Daten angewandt, die mit bildgebenden Beobachtungsverfahren der Hochenergieastronomie im Röntgenspektralbereich gewonnen wurden, um aktuelle Fragen der Astrophysik, z.B. aus den Bereichen Stern- und Galaxienentwicklung sowie der großräumigen Struktur des Universums zu beantworten. Die entwickelte Methode widmet sich den typischen Problemen, mit denen die Datenanalyse aufwartet, die da sind: das räumlich variable kosmische Hintergrundsignal, die vielfältige Morphologie der Quellen und deren großer Intensitätsbereich, Datenunvollständigkeiten, starke Gradienten sowie wenige Photonenzählimpulse pro Bildelement. Die beiden bisher weitgehend zur Bilddatenanalyse eingesetzten Verfahren "Sliding-Window" und Wavelet-basierte Technik haben sich als unzureichend erwiesen bei großer Hintergrundvariation und bei der Detektion schwacher ausgedehnter Quellen und Quellen komplexer Morphologie. Bei diesen Verfahren sind große systematische Fehler in der Photometrie möglich und schwache Quellen können verpasst werden.

Der entwickelte Algorithmus basiert auf der Bayes'schen Theorie, die den wahrscheinlichkeitstheoretisch konsistenten Rahmen bietet, um ein inverses Problem für einen gegebenen Informationszustand zu lösen. Dabei wird das Untergrundsignal durch ein parametrisiertes Modell beschrieben und die *Prior*-Informationen der Quellintensitäten werden in Form geeigneter Wahrscheinlichkeitsverteilungen quantifiziert. Für die Bestimmung des Untergrundes werden die Bilddaten nicht zensiert. Die *Rate* des Untergrundsignals wird durch zweidimensionale Splinefunktionen beschrieben (sog. Thin-Plate Splines). Das Untergrund*modell* ist das Produkt von Untergrundsrate und Belichtungszeit, wobei letztere Variationen der effektiven Integrationszeit im Bild berücksichtigt. Daher werden Effekte wie Vignettierung, Variationen der Detektorquantenausbeute sowie große Gradienten in der Integrationszeit korrekt beschrieben, was im Vergleich zu bisherigen Methoden zu deutlich verbesserten Detektionswahrscheinlichkeiten insbesondere an den Bildrändern führt. Im Rahmen einer Multiskalenanalyse werden Quellenwahrscheinlichkeiten sowohl für individuelle Bildelemente als auch für Korrelationen benachbarter Bildelemente ermittelt. Dadurch ermöglicht die Methode punktförmige und ausgedehnte Quellen sowie deren komplexe Morphologien zu detektieren. Darüberhinaus können Aufnahmen verschiedener Spektralbereiche mit Hilfe der Bayes'schen Wahrscheinlichkeitstheorie kombiniert werden, um die Auflösung dicht benachbarter Quellen weiter zu verbessern. Alle erkannten Quellen werden durch die entwickelte Methodik automatisch hinsichtlich Position, Anzahl der Quellenimpulse, und Gestaltparametern einschließlich deren Unsicherheiten charakterisiert.

Der Vergleich mit bisherigen Techniken zeigt, dass die entwickelte Methode eine verbesserte Bestimmung des Untergrundes als auch der Quellenparameter erlaubt. Die Methode wurde auf Daten der Röntgensatelliten *ROSAT* und *Chandra* angewendet, wobei insbesondere die Detektionswahrscheinlichkeit lichtschwacher oder ausgedehnter Quellen im Vergleich bisheriger Analysen verbessert werden konnte. Dadurch wurden neue Galaxienhaufen und Quasare im Röntgenband entdeckt, die durch Heranziehen zusätzlicher Beobachtungsdaten im sichtbaren Bereich des Spektrums bestätigt werden konnten. Das hier entwickelte Verfahren eignet sich besonders für die Identifizierung von Objekten mit ausgedehnter Emission wie z.B. Galaxienhaufen.

Summary

In this thesis, a new probabilistic technique for the joint estimation of background and sources with the aim of detecting faint and/or extended celestial objects is developed. The novel probabilistic technique is applicable to astronomical images at any wavelength of the spectrum. This work exploits public imaging data from observations of high–energy astrophysics in the X–ray spectral regime. These data are usually employed to address current astrophysical problems, for instance in the fields of stellar evolution, evolution of galaxies and the large–scale structure (LSS) of the universe. In this Summary, the motivations for developing a new source detection method are addressed. The problems encountered analysing X–ray data and the difficulties experienced by previous techniques applied to these data are briefly reviewed. Successively, the technique and its capabilities are outlined.

The problem Astronomical images, collected by ground– or space–based telescopes, are frequently difficult to analyse because they consist of a diffuse background with superposed celestial objects and corrupted by effects due to instrumental complexity. The data in an image often show steep gradients due to instrumental structures, and are altered by smearing effects, vignetting effects, charge–coupled device (CCD) failures and instrumental calibrations. An astronomical image is often a combination of several individual pointings and the effects due to steep gradients in the data are cumbersome. The background, instead, is a composition of instrumental, particle and cosmic emissions. The cosmic background is not necessarily spatially constant, especially in high–energy astrophysics. Celestial objects are characterized by a large variety of (sometimes complex) morphologies and apparent brightnesses. Sources can be superposed to both, smooth and highly, varying background. Faint sources may be difficult to detect, because of background fluctuations in the data. In high–energy astrophysics, few or no photon counts per pixel frequently occur. Poisson statistics is required to analyse these data. Telescope time, i.e. the allocated time to the observations of individual astronomical topics, is limited and hence valuable. It is of great importance to make the best use of the data available.

The interpretation of observational data implies the solution of an inverse problem: From the observational manifestation of some process, one wishes to deduce what factors generated that process (Tikhonov, 1992). The data contained in astronomical images are characterized by the pervasive presence of noise. Hence, the inverse problem of extracting astrophysically interesting information from observed data is ill–posed, in the sense that

the solution is not unique or it is not stable under perturbations on the data, i.e. small changes in the observational data can entail very large changes in the solution being sought. Ill–posed problems depend in a discontinuous way on the data. Consequently, small errors (e.g., measurement errors, perturbations caused by noise) can create large deviations. Therefore, solving ill–posed problems calls for a special approach to ensure that the solution is stable, unique and close to the exact solution of the inverse problem. The numerical treatment of ill–posed inverse problems is a challenge. Often, ad hoc algorithms, as the "regularized" solutions by Tikhonov, make use of constraints to provide for a stable and unique solution (regularization). However, ad hoc algorithms may provide misleading solutions especially as the solution approaches numerical instability (Jaynes, 1984). Instead of using ad hoc algorithms, inference/decision theory methods are applied to solve ill–posed problems. The work of Jaynes (1984) shows that probability theory is the only approach allowing one to convert an ill–posed problem of deductive reasoning into a well–posed problem[1] of inference. In this thesis, Bayesian statistics is applied, providing the principles of inference required to solve ill–posed problems. An ill–posed problem which is addressed in this thesis is the detection of faint, both point–like and extended, sources.

In the environment of X–ray astronomy, standard methods, such as the sliding window and the wavelet based techniques, are employed for the detection of faint and/or extended sources. The sliding window technique is beneficial for the detection of point–like objects but has problems in detecting (mostly faint) extended sources. Wavelet based techniques have the advantages to detect point–like and extended sources employing several resolutions (or scales), but the result depends crucially on the wavelet base chosen and therefore often favour the detection of circularly symmetric sources. Sliding window and wavelet based techniques are known to suffer from: describing large variations in the background, detection of faint and extended sources and sources with complex morphologies. Consequently, large systematic errors in object photometry and loss of faint sources may occur with these techniques. Furthermore, background fluctuations give rise to false positives in source detection. In order to reduce the number of false positives, standard techniques employ a detection level (thresholding), usually at $3-5\ \sigma$ above the local background. All sources below the detection level are disregarded. It results that extended objects, which can be detected by eye, are not detected by standard techniques (Starck and Murtagh, 2006). A common practice for the detection of extended low surface brightness sources is to analyse the data in sequential steps, see e.g. the works of Pierre *et al.* (2004) and Giacconi *et al.* (2002*b*). Point–like sources are first detected with a standard algorithm and then removed from the astronomical image. The regions of the image without sources are filled with a simulated background. The resulting image, often rebinned to a larger pixel size, is successively investigated with a standard algorithm to detect extended sources. The detected extended sources suffers from biased results, because uncertainties of the experimental measurements are not properly propagated.

The problem arising for the interpretation of observational data has to consider all the

[1]Well–posed problems have the following properties: 1. A solution exists; 2. The solution is unique; 3. The solution depends continuously on the data.

information available in order to provide the most reliable answer for source detection and characterization. An accurate estimation of the background, that accounts for gradual as well as steep gradients in an image, is crucial for the detection of faint sources and for providing good estimates in object photometry. Background estimation and source detection, including a large variety of morphologies shown by the celestial objects, is achievable in a single algorithm.

The method A statistical tool to obtain unbiased results from incomplete or noisy data is provided by Bayesian probability theory (BPT), which supplies a general and consistent frame for logical inference. A suitable regularizing algorithm is developed with BPT taking advantage of all available information over a parameter set, which is described by a probability density over the corresponding parameter space. The solution of the inverse problem combines all the available information (Tarantola, 1987). The available information concern the background and the sources distributed in the image. The background is assumed to be smoother than the source signal. Background and sources are assumed to have positive values only. The properties of the source signal are described with a probability distribution. Several choices for the probability distribution of the source signal are possible and studied. Furthermore, the solution of the inverse problem entails the estimation of model parameters.

A probabilistic two–component mixture model is incorporated into the Bayesian technique. One component represents the background signal, the other component the source plus background signals. The mixture model technique is used to jointly estimate the background and to detect the sources. In this way, consistent uncertainties of background and sources are provided.

The background rate is described by a two–dimensional spline function. The thin–plate–spline (TPS) is selected to model the background rate, because the shape of the interpolating spline surface suffices a minimum curvature condition. Nonetheless, the approach can be easily adapted to other smooth functions. For the background rate estimation, the source signal is considered a nuisance parameter and it is integrated out following the rules of BPT. The background model combines the use of the background rate and the telescope's exposure time. The resulting background model is sensitive to cosmic, instrumental and exposure time variations. The image data are not censored for background estimation.

Each pixel of an astronomical image is characterized by a probability of source detection. In order to detect faint objects, independent of their size, a multiresolution analysis is employed within the developed Bayesian technique. It consists in analysing the probability of source detection correlating neighbouring pixels. It allows to analyse statistically the source structures at several resolutions. The resolution is related to the correlation length (or scale) used to group neighbouring pixels. The correlation length increases at decreasing resolutions and covers a large range of values. The outcome of the multiresolution analysis is provided by source probability maps (SPMs) at several scales. Each SPM is an image that enhances the detection of sources whose size is within the size of the used scale. Faint,

both point–like and extended, sources are revealed at decreasing resolutions and complex morphologies of celestial objects are detected.

The Bayesian algorithm gives the benefit of an additional technique intrinsic to BPT: the multiband analysis. The multiband analysis provides a statistical combination of multiple data at different energy bands improving the detection of faint sources and sources in crowded regions.

In a second step, all the detected sources are characterized automatically providing source position, net counts, morphological parameters and their errors. No explicit background subtraction is used for source characterization.

Poisson statistics is used for the analysis of the data in the X–ray spectral regime. The developed technique correctly handle Poisson statistics throughout the whole algorithm. Different statistics are easily adapted.

The results The Bayesian technique, developed in this thesis, is capable of detecting point–like and extended sources equally well and of describing variations in the background according to the diffuse emission and to spatial exposure non–uniformities. Vignetting effects, failure of pixels, instrumental structures and exposure variations are properly treated in the background model with the advantages to reduce greatly the number of false positives in source detection and to improve the photometric characterization especially for faint, both point–like and extended, sources with respect to standard techniques.

The classification of pixels into two mixture components takes into account the detection of sources without employing predefined morphologies.

The multiresolution analysis allows one to detect source features at different scales, to separate celestial objects from underlying diffuse emissions and to separate close by objects.

The multiband analysis provides improvements in the detection of faint sources and objects in crowded regions, taking into account the spectral properties of the detected sources.

The omnipresent problem of false positives in source detection due to background fluctuations is addressed with a priori information employed to describe the source and background signals and the level of detection probability selected for the identification of sources. A 99% source probability threshold is mostly effective to strongly reduce the number of false positives in source detection. Furthermore, the Bayesian probabilities of source detection are compared to p–values. The comparison is pursued in order to show the intrinsic difference in the nature of the two statistics. Consequently, the p–values cannot be calibrated with Bayesian source probabilities.

Simulated data sets are used for performance assessment of the Bayesian technique. The simulated data sets are characterized by several background intensities to cover different cases one encounters in observational data. The effects of different prior information incorporated into the algorithm are investigated. The results depend on the definition of the models for background and sources. The selected spline allows for the estimation of smooth backgrounds, which are consistent with the simulated ones. The prior information

for the source signal distributions helps to sort data, which are marginally consistent with the background model, in background and sources. Bright and faint sources are detected in a multiresolution analysis, allowing also for the detection of substructures. The estimated source parameters are consistent with the simulated ones. However, the uncertainties of parameters for faint sources can be large due to propagation of the background uncertainty. The results from the analysis of the simulated data sets with the probabilistic technique are compared with the WAVDETECT algorithm (Freeman *et al.*, 2002), a wavelet based technique. The developed technique improves on the detections of WAVDETECT especially in the low count regime. The backgrounds estimated with WAVDETECT are not as smooth as the ones obtained with the developed technique. The WAVDETECT backgrounds show rings due to the Mexican Hat function employed to filter the images. The residuals on source fluxes and positions obtained with the Bayesian technique are by a factor of 10 smaller than the ones from WAVDETECT. Furthermore, the Bayesian technique provides less contaminated samples (as much as a factor of 5) than WAVDETECT.

The Bayesian method is applied to real data from two major X–ray missions: *ROSAT* and *Chandra* satellites.

Analysing the *ROSAT* all–sky survey (RASS) data, the Bayesian technique improves the background model, the detection of faint and/or extended sources and the estimates of source parameters with respect to previous methods employed for the analysis of these data, such as the Standard Analysis Software System (SASS) algorithm (based on the sliding window technique for source detection and on the maximum likelihood approach for source characterization).
The SASS background model is not stable on the whole field, meaning that e.g. the background shows insignificant structures at the image boarders as well as the exposure non–uniformities. The background model obtained with the Bayesian algorithm, instead, is stable on the complete field even for gaps in the data where the satellite was switched off.
The developed Bayesian method allows one to detect faint and/or extended objects, such as clusters of galaxies and quasars, which could not be detected previously by the SASS method because of their low surface brightness and/or extent. Some of these new findings have a counterpart in other catalogues produced from deeper X–ray observations and/or from the optical and near–infrared bands. In addition, for cases where the SASS method detects faint extended objects, it may fail in providing the source extent: Sources may look point–like while they are extended objects. Source parameters of celestial objects embedded in a hot diffuse emission, like galactic supernova remnants (SNRs), are also shown to be improved with the Bayesian technique.

The application to the *Chandra* Deep Field South (CDF–S) data demonstrates that the Bayesian technique is suited for the analysis of images from new generation instruments.
The Bayesian algorithm is capable to cope with spatial exposure non–uniformities, large background variations, CCD gaps and images superposed. Sources located at the image edge are not distorted. The technique improves the detection of faint and extended sources and the estimates of their structural parameters with respect to conventional techniques employed for these tasks, such as WAVDETECT. The WAVDETECT technique, instead, intro-

duces systematic errors in the estimates of source parameters (source counts and extent). The BSS results are robust, allowing for the construction of reliable catalogues.
The novel Bayesian algorithm provides additional benefits. Complex or compact morphologies of faint extended sources are detected and identified as extended. A large range of surface brightnesses is explored with the BSS algorithm. Sources nearby or along the line of sight of diffuse emissions are separated with the multiresolution analysis developed with the Bayesian algorithm.
New clusters of galaxies and a filament connecting two clusters are found in the CDF–S region. Potential galaxy clusters and groups are detected, for which further work is needed to confirm their nature. The BSS technique has the power to provide a large and homogeneous sample of clusters and groups of galaxies detected in sky surveys. Consequently, the BSS technique is a suitable tool to address current astrophysical problems. Clusters and groups of galaxies, detected in the X–ray part of the electromagnetic spectrum, are important tools to evaluate cosmological models to describe the universe, to study the LSS, to determine the amount of baryonic matter in the local universe. Furthermore, the Bayesian technique allows for the analysis of the mass distribution within clusters or groups of galaxies.

Chapter 1

Introduction

1.1 Motivation

Information extraction from astronomical images is fundamental to build astrometric and photometric catalogues. In the age of new–technology telescopes and space–based missions, catalogues are employed to support observing programs. As shown in Lasker *et al.* (2008), catalogues have to provide deep (in limiting magnitude) data with multicolour and multi–epoch information. The complex project of building precise astronomical catalogues is of vital importance in astrophysical science. Analyses of astronomical catalogues allow us to study physical properties of detected objects, to test models of structure formation (as for clusters of galaxies), to explore stellar and galaxy evolution, to provide insight for the origin of the Cosmos. For instance, the distribution of galaxies throughout the universe is not uniform. Deep astronomical images show voids, filaments and clusters. The distribution of these objects constrains cosmological theories, see e.g. Rosati *et al.* (2002*b*), Brandt and Hasinger (2005) for more details.

Astronomical data are costly and therefore limited, corrupted by noise due to background fluctuations, affected by selection effects due to e.g. instrumentation, calibrations, sampling design. The detection and characterization of faint sources require precise statistical methods. In fact, statistical selection biases may arise because of data manipulation and of overestimation of the statistical significance in the data leading to wrong conclusions. Today, methods that move away from classical techniques, like Bayesian methods, are widely used to address the problem of separating data components and analysing the resulting signals (Starck *et al.*, 2008).

Independent to the wavelength employed by an observatory, the astronomical data are a composition of objects of interest superimposed on a relatively smooth signal, called background signal. Celestial objects exhibit a large variety of morphologies and apparent brightnesses. Astronomical images contain typically a large set of point–like sources (e.g. stars, active galactic nuclei (AGNs) and quasars), some quasi point–like objects (e.g. faint galaxies, double stars), and some complex and diffuse structures (e.g. galaxies, nebulae, clusters of galaxies, superclusters) (Starck and Murtagh, 2006).

The background signal arises because of instrumental, particle and cosmic emissions. The instrumental emission is due to dark current in photosensitive devices. In modern detectors, like CCDs, the background arising from instrumental emissions represents only few a percent of the total one. CCDs are the detectors of choice for most astronomical observations, because not only these detectors offer very low dark current for cooled cameras, but also they provide high quantum efficiency and linear response. Commonly CCD detectors have Poisson and/or Gaussian noise components: See Gilliland (1992), Massey and Jacoby (1992), Berry and Burnell (2005) and Starck and Murtagh (2006) for more details. More complex is the case with digitized photographic images, which show additive Poisson and Gaussian noise components plus nonlinear distortions (Lasker *et al.*, 2008; Starck and Murtagh, 2006). Note that the quantum efficiency of detectors varies over the field–of–view (fov). The particle background are due to galactic emissions. The particles contributing to the background are, for instance, cosmic rays, interplanetary rays, radiation belts around the Earth, solar activity. Calibrations of astronomical images reduce the corruption of the data due to particles. The cosmic emission is, instead, due to galactic and extragalactic photons detected by the observatory (Snowden and Freyberg, 1993). The cosmic background represents the integrated emission of unresolved (point–like) sources. For deep observations as in the X–ray spectral regime, the cosmic background is mostly due to the extragalactic background light, providing important information about galaxy formation and the LSS of the universe, see e.g. Giacconi *et al.* (1962) and Brandt and Hasinger (2005) for more details. The cosmic background is not necessarily spatially constant, especially in the high–energy range of the electromagnetic spectrum. Background estimation is essential for a proper interpretation of the data in image analysis.

The separation between background and sources is not a trivial task. Background estimation is an omnipresent problem for source detection methods in astrophysics, especially when the source signal is weak and difficult to discriminate against the background. Moreover, a reliable background model is required for the detection of extended sources[1] and of source features extending to the edge of the fov: See Snowden *et al.* (1994) for more details. An inaccurate estimation of the background may produce large systematic errors in object photometry and the loss of faint and/or extended objects (Starck and Murtagh, 2006).

The background–source separation task suffers additionally from the fact that the quality of astronomical images is corrupted by effects due to instrumental complexity. The causes for quality degradation in astronomical images are the followings:

1. Space telescopes may dither during an observation as in the X–ray spectral regime (energy range of $0.1 - 120$ keV), producing a smearing effect;

2. The quality of astronomical images may be affected by the tracking system and the telescope shake;

[1] An extended source differ from a point–like one, because its angular size is greater than the resolution of the instrument used to observe it. Hence, an extended source is a resolved object.

3. Space–based observatories are characterized by a compact geometry and mirror placement in a folded optical system. The main disadvantage of such construction is shown by an image that is brighter on axis and dimmer off axis (vignetting). The vignetting is therefore a deterioration on the quality of the image going towards the edge of the fov. It is a feature of folded telescope optics which cannot be avoided (Berry and Burnell, 2005);

4. Astronomical images may exhibit instrumental structures, such as detector window support structures as for Wolter type telescopes and gaps between adjacent CCDs;

5. Deep observations are commonly obtained by combining several individual exposures to generate a final astronomical image. The background may vary significantly within the field and steep gradients in the data are present.

These effects increase statistical (random) and systematic errors in the data.

The telescope's exposure time (exposure map) provides important information for addressing some of the causes for quality degradation in astronomical images: effects $3-5$. Exposure maps contain information on how long a given pixel was exposed to the sky. Exposure maps include factors such as vignetting, dead time (i.e. the time after each event during which the system is not able to record another event if it happens), pile–up (consequence of the sensor dead time), defective pixels (such as hot, stuck and dead pixels[2]). The exposure map accounts for instrumental structures, such as detector ribs or CCD gaps. Instrumental structures produce lack of data. The missing data must be handled consistently for the background estimation to prevent undesired artificial effects. Moreover, the data, produced by merging individual exposures, are characterized by large exposure variations. Thus, celestial objects, especially extended ones, can be superposed to both, smooth and highly varying background (Snowden *et al.*, 1994). Hence, the background modelling has to incorporate the knowledge provided by the observatory's exposure time without compromising the statistical properties. If the exposure map is not supplied, steep gradients in the data are not handled, which would yield many false positives in source detection (Damiani *et al.*, 1997) and poor estimates of source properties.

Furthermore, a source detection technique should be capable of detecting a large variety of source morphologies.
Some source detection techniques need the point–spread function (PSF) for source detection (see e.g. Stewart 2006). The PSF describes the distribution of light in the focal plane of a telescope after the light from a point source has passed through the optics of a telescope. The PSF is a measure of how well the instrument focuses all of a source's photons. Powerful astronomical systems are characterized by optical systems with a narrow PSF. The width of the PSF is important to distinguish close by objects, faint objects, discern details on the surface of a celestial object, such as a planet, a moon or an asteroid. Nonetheless,

[2] A hot pixel is a pixel which is saturated on long exposures. A stuck pixel is an extreme case of a hot pixel. It has large charge leakage, regardless of the exposure time. A dead pixel is a pixel that reads zero on all images taken. See (Gilliland, 1992) for more details.

the PSF can be spatially varying along the fov, as in high–energy astrophysics. Often, the PSF is not known precisely and some functional form of the PSF is used for background estimation and source detection. Source detection methods employing a PSF or its functional form are designed for the detection of point–like objects regardless of extended ones (Starck and Pierre, 1998). Hence, a source detection algorithm capable of detecting a large variety of source morphologies should be able to operate effectively without the knowledge of the instrument characteristics.
Other techniques employ the PSF for source characterization (see e.g. Starck *et al.* 2000), reducing systematic errors in the photometry. However, the photometric solution is not only depending on the deconvolution of the detected source flux with a known PSF. The photometric solution of detected sources depends on both, systematic and statistical, uncertainties. Both kinds of uncertainties need to be accounted for background–source separation and properly distributed in the final solution. In this thesis, a detailed PSF is not included neither in the source detection procedure nor in the source characterization routine. The developed technique described in this thesis tackle the problem of reliably detecting background as well as sources with their respective uncertainties. Nevertheless, if the instrumental PSF is known precisely for the whole fov, then the developed technique can take into account that information in a further step of source characterization within the properties of a specific observational set–up.

For a reliable detection of celestial objects and for a proper propagation of errors in background and source estimates, a source detection technique should be capable of jointly estimating the background and detecting the sources.
Many techniques subtract an estimated background from the data, leading even to negative count rate values of the signal of interest (see e.g. Śliwa *et al.* 2001). A joint background–source separation is, instead, a necessary condition for preserving the statistics throughout the whole algorithm and, therefore, for providing consistent uncertainties of background and sources. This is of major importance in astrophysics. In fact, modern astronomical instruments, from optical (wavelength range $\sim 380 - 750$ nm) to γ–ray (wavelength $< 10^{-2}$ nm) bands of the electromagnetic spectrum, can detect individual photons (Starck *et al.*, 2008). Thus, the data are discrete counts and Poisson statistics has to be used. Noise dominates the signal especially at high frequencies of the electromagnetic spectrum (Starck and Murtagh, 2006).

If all the above issues are addressed, any source detection technique improves the detection of faint sources with respect to other methods. The detection of faint sources is an hot topic in high–energy astrophysics (Burkert *et al.*, 2008). Faint sources may provide important information about the Cosmos. For instance, the detection of quasistellar objects (QSOs) allows one to improve the knowledge about the evolution of the early phase of the universe (Burkert *et al.*, 2008). However, the detection of faint, both point–like and extended, sources is limited by the pervasive presence of background fluctuations in the data. Often, source detection techniques estimate the noise in the data analysing an area of the astronomical image that supposedly contains only background. Several approaches

to estimate the standard deviation of Gaussian noise in an image have been developed. In Bertin and Arnouts (1996), for instance, the noise is estimated employing a $k-\sigma$ clipping approach on meshes of the image. Once the variability of the data around the background is known, a detection level at about $3-5\ \sigma$ above the background is chosen. Faint sources with intensities below the detection level are lost.

Noise in the data corrupts background and source signals. Thus, source detection techniques should be capable of including systematic and random errors in the analysis of both background and sources. In addition, noise in the data can not be reliably estimated (Starck and Murtagh, 2006). In order to improve the detection of faint celestial objects, multiscale (Starck and Pierre, 1998) and multiband (see Collet and Murtagh, 2004; Murtagh *et al.*, 2005; Laidler *et al.*, 2007) approaches have to be employed.
The multiscale analysis allows one to detect sources and their substructures at multiple scales. It facilitates the detection of faint objects close to the background signal and the detection of complex morphologies of extended sources. Another motivation to employ a multiscale approach to source detection, for instance, in the X–ray spectral regime, is due to the presence of a spatially varying PSF.
The multiband analysis matches sources detected at different energy bands of the electromagnetic spectrum to improve the sensitivity of source detection. Modern CCD detectors can measure not only the positions of incident photons but also their energies, as in the X–ray spectral regime. Consequently, the same portion of the sky can be observed at different energy bands by the same instrument. The information coming from different energy bands can be combined, separating more efficiently nearby objects accounting for their different spectra.

The data in astronomical images give rise to an inverse problem that is ill–posed. The inverse problem is described as follows by Sivia (1990): "*Having seeing the outcome of several 'moves' in a game, we want to infer the rules governing that game.*" Inverse problems are solvable when providing a reasoning (or inference) about the data, that are corrupted by noise. The solution of an inverse problem is not unique and, hence, is ill–posed. An ill–posed inverse problem requires the use of decision theory methods in order to provide for a unique and stable solution.

The solution of an ill–posed inverse problem is given by inferring the values of model parameters defined to describe completely the physical system arised by the data. The values of the model parameters are inferred from the observed data. Lack of data and experimental uncertainties may produce biased results. The most efficient way to solve ill–posed inverse problems is to use the calculus of probability theory as introduced by Bayes (Bayes, 1783): See Tarantola (1987) for more details. BPT allows for plausible reasoning and for unbiased results. With BPT the solution of an ill–posed inverse problem is found making the best inference based on the experimental data and any available a priori information, that are described using probability densities. The information entering the models is combined to provide a unique and stable solution. BPT allows one to combine optimally any information, because uncertainties are taken into account. In the light of

new data, the solution can be revised (Sivia, 1990).

In this thesis, the detection of faint, both point–like and extended, sources is addressed to data coming from astronomical images in the X–ray spectral regime. These images are typically containing from 0.1 to a few photons per pixel (Starck and Pierre, 1998).

In Section 1.2, conventional methods extensively applied for the analysis of X–ray astronomical images are introduced. Faint objects may be lost by these source detection methods (see, e.g., Starck and Murtagh 2006, Valtchanov *et al.* 2001 for more details), because large variations in the background are not described. The detection of extended sources, their complex morphologies and their substructures is demanding for these techniques.

In recent years, for the detection of low surface brightness sources in deep astronomical images and in surveys, alternative approaches have been used. In the works of e.g. Giacconi *et al.* (2002*b*) and Pierre *et al.* (2004), the detection of extended sources is achieved with the application of several techniques in sequential order. The employment of several techniques in sequential order does not allow to properly account for uncertainties in the data.

In Section 1.3, source detection methods employing BPT are introduced. These techniques are advanced with respect to the conventional ones, because ill–posed inverse problems are tackled from the consideration of random and systematic uncertainties. An introduction to the technique developed in this thesis is given.

In Section 1.4, an outline of the thesis structure is provided.

1.2 Conventional source detection methods

Conventional source detection methods employed in deep imaging surveys are: $k-\sigma$ clipping for background modelling, peak finding and thresholding for source detection, adaptive aperture photometry with isophotal corrections for source characterization (see, e.g., the software program SExtractor described in Bertin and Arnouts, 1996); sliding window technique (Harnden *et al.*, 1984; Gioia *et al.*, 1990) and maximum likelihood (ML) PSF fitting (see Hasinger *et al.* 1994 and Boese and Doebereiner 2001 for more details); wavelet transformation (e.g. Slezak *et al.*, 1990; Rosati *et al.*, 1995; Damiani *et al.*, 1997; Starck and Pierre, 1998; Lazzati *et al.*, 1999; Freeman *et al.*, 2002). A review of these techniques can be found in Valtchanov *et al.* (2001) and Becker *et al.* (2007).

The SExtractor software package is one of the most widely used source detection procedures in astronomy. It has a simple interface and very fast execution. It provides the morphology of any object through its list of pixels. It produces reliable aperture photometry catalogues (Becker *et al.*, 2007). The main pitfall of the SExtractor is the low accuracy in the background model. Consequently, the SExtractor does not show high sensitivity in detecting faint and extended sources. However, the SExtractor software can be applied in X–ray regime on filtered images (Valtchanov *et al.*, 2001).

The sliding window technique is a fast and robust source detection method. This tech-

nique may fail while detecting extended sources, sources near the detection limit and nearby sources (Valtchanov *et al.*, 2001). This source detection method has been refined with more elaborated techniques, such as matched filters (e.g. Vikhlinin *et al.*, 1995; Stewart, 2006) and recently the Cash method (Stewart, 2009). The Cash method is a ML technique. For source detection, the method employs a Cash likelihood–ratio statistic, that is an extended χ^2 statistic for Poisson data (Cash, 1979). Both the matched filters and Cash methods are at least by a factor of 1.2 more sensitive than the sliding–window technique (Stewart, 2009). Though, both methods are designed for the detection of point sources. The candidate sources are characterized in a further step using ML PSF fitting. The ML PSF fitting procedure performs better than other conventional techniques for flux measurements of point–like sources. However, accurate photometry is achieved if a well–determined PSF model is used (Valtchanov *et al.*, 2001). In Pierre *et al.* (2004), the ML profile fit on photon images is extended taking into account a spherically symmetric β–model (King profile, see King, 1962; Cavaliere and Fusco-Femiano, 1978) convolved with the instrumental PSF for improving the photometry of extended objects.

Wavelet transform (WT) techniques improve the detection of faint and extended sources with respect to other conventional methods (see Starck and Pierre 1998 for more details). In fact, WT techniques are able to discriminate structures as a function of scale. Within larger scales, faint and extended sources are detected. WTs are therefore valuable tools for the detection of both point–like and extended sources (Valtchanov *et al.*, 2001). Nonetheless, these techniques often favour the detection of circularly symmetric sources (Valtchanov *et al.*, 2001). In addition, artefacts may appear around the detected structures in the reconstructed image, and the flux is not preserved (Starck and Pierre, 1998). In order to overcome these problems, some refinements have been applied to the WT techniques. In Starck and Pierre (1998), for instance, a multiresolution support filtering is employed to preserve the flux and the adjoint WT operator is used to suppress artefacts which may appear around the objects. An advance on this method is provided in Starck *et al.* (2000). A space–variant PSF is incorporated in their WT technique. Object by object reconstruction is performed. For point sources the flux measurements are close to that obtained by PSF fitting.

1.3 Advanced source detection methods

A self–consistent statistical approach for background estimation and source detection is given by BPT, which provides a general and consistent frame for logical inference. The results of BPT methods are probabilities, such as the probability that a detected photon is emitted from some hot interstellar gas contributing to the background or emitted from some well defined source. Estimates of parameters and their uncertainties can be derived from the calculated probability distributions. BPT is based on the natural idea of probability as 'degree of belief' and on the rules of logic.

As James Clerk Maxwell (1831-1879) realized in 1850, the true logic is the calculus of probabilities because in science we always have to deal with incomplete information

(Jaynes, 2003). BPT provides a unique method of dealing with noisy or incomplete data and uncertainties in models, and for combining information of various types in one coincided algorithm. BPT provides an elegantly simple and rational approach for answering any scientific question for a given state of information (Gregory, 2005). Moreover, the need to extract as comprehensive information as possible from a given set of data is pressing in any physical experiment where the data sets available can not be augmented at will. Therefore, the available data should be exploited with every conceivable care and effort. For these reasons, Bayesian data analysis is becoming an established tool in astrophysics (Dose, 2003).

1.3.1 Source detection methods employing BPT

The achievement of Bayesian techniques on signal detections in astrophysics has already been shown, for example, in the works of Gregory and Loredo (1992), Loredo (1995) and Scargle (1998). In modern observational astrophysics, BPT techniques for image analysis have been extensively applied, e.g., Hobson and McLachlan (2003), Carvalho *et al.* (2009), Savage and Oliver (2007) and Strong (2003).
For the detection of discrete objects embedded in Gaussian noise (microwave regime), Hobson and McLachlan (2003) utilizes a model–fitting methodology, where the shape of the objects of interest is assumed a priori. Markov–chain Monte Carlo (MCMC) techniques are used to explore the parameter space.
An advance to this work is provided by Carvalho *et al.* (2009). For speeding up the method of Hobson and McLachlan (2003), Carvalho *et al.* (2009) proposes to use Gaussian approximation to the posterior probability density function (pdf) peak when performing a Bayesian model selection for source detection.
The work of Savage and Oliver (2007) is developed within Gaussian statistics (infrared data). At each pixel position in an image, their method estimates the probability of the data being described by point source or empty sky under the assumptions that the background is uniform and the sources have circular shapes. The Bayesian information criterion is used for the selection of the two models. Source parameters are estimated in a second step employing Bayesian model selection.
In the work of Strong (2003), a technique for image analysis is developed within Poisson statistics. The technique is instrument specific and is applied to γ–ray data. The first objective of this technique is to reconstruct the intensity in each image pixel given a set of data. The Maximum Entropy method is used for selecting from the data an image between all the available ones from a multidimensional space. The dimension of the space is proportional to the number of image pixels.

None of these techniques provides for a general formulation for the detection of faint, both point–like and extended, sources in astronomical images coming from most of the electromagnetic spectrum. In order to detect these faint sources, the requirements for a new source detection method are the followings: (1) Background model on the whole fov capable of describing large variations in the data; (2) Bayesian inference; (3) Mixture models; (4) Multiresolution analysis; (5) Multiband analysis. In Section 1.3.2, the main

properties of the technique developed in this thesis are highlighted.

1.3.2 The novel method with BPT

A new source detection method based on BPT combined with the mixture–model technique is proposed. The algorithm allows one to estimate the background and its uncertainties and to detect celestial sources jointly. The new approach deals directly with the statistical nature of the data. Each pixel in an astronomical image is probabilistically assessed to contain background only or with additional source signal. The results are given by probability distributions quantifying our state of knowledge. The developed Background–Source separation (BSS) method encounters: background estimation, source detection and characterization.

The background estimation incorporates the knowledge of the exposure map. The estimation of the background and its uncertainties is performed on the full astronomical image employing a two–dimensional spline. The spline models the background rate. The spline amplitudes and the position of the spline supporting points provide flexibility in the background model. This procedure can describe both smooth and highly varying backgrounds. Hence, no cut out of regions or employment of meshes are needed for the background estimation. The BSS technique does not need a threshold level for separating the sources from the background as conventional methods do. The threshold level is replaced by a measure of probability. In conventional methods, the threshold level is described in terms of the noise standard deviation, then translated into a probability. The classification assigned to each pixel of an astronomical image with the BSS method allows one to detect sources without employing any predefined morphology. Only, for parametric characterization of the sources predefined source shapes are applied. The estimation of source parameters and their uncertainties includes the estimated background into a forward model, where only the statistics of the original data are taken into account. The BSS method provides simultaneously the advantages of a multiresolution analysis and a multiband detection. In order to quantify the multiscale structure in the data, a multiresolution analysis is required (see Kolaczyk and Dixon, 2000; Starck *et al.*, 2000). In the BSS approach the multiresolution analysis is incorporated in combination with the source detection and background estimation technique with the aim to analyse statistically source structures at multiple scales. When multiband images are available, the information contained in each image can be statistically combined in order to extend the detection limit of the data (see Szalay *et al.*, 1999; Murtagh *et al.*, 2005).

The capabilities of this method are best shown with the detections of faint sources independent of their shape and with the detections of sources embedded in a highly varying background. The technique for the joint estimation of background and sources in digital images is applicable to digital images collected by a wide variety of sensors at any wavelength.

The BSS technique is applied to images in the X–ray spectral regime. The X–ray environment is particularly suitable to the novel Bayesian approach for a number of reasons. X–ray astronomy is characterized by small numbers of photon counts even for relatively

long exposures and the observational data are rarely reproduced. The astronomical images are affected by incomplete data due to telescope support structures, smearing effects caused by dithering of the telescope, vignetting effects and instrumental calibrations. Astronomical images provided by new generation instruments are usually a combination of several individual CCD imaging pointings. The PSF is spatially varying and it is often not known exactly on the full fov. The cosmic background is not necessarily spatially constant. X–ray astronomy primarily involves the study of plasma with thermal temperatures in the range of 10^6 to 10^8 K. Such plasma radiate the majority of their energy in the range of $(0.1 - 10)$ keV. Extended sources, like galaxy clusters and groups, with complex morphologies are detected. The background estimation directly underneath a source, especially an extended source, is a difficult task for source detection methods. In fact, there are few source detection algorithms developed so far for an automated search of faint and extended sources. A large homogeneous sample of clusters of galaxies is needed for cosmological studies.

1.4 Outline of the thesis

This thesis is organized as follows:

In Chapter 2, basic aspects of BPT are briefly reviewed (Section 2.1). A detailed description of the BSS algorithm is provided: In Section 2.2 the technique for the joint estimation of background and sources is introduced; In Section 2.3 the BSS algorithm is extended in order to obtain an automated method for source characterization.

In Chapter 3, an important issue related to false positives in source detection is addressed. A commonly used tool for signal significance testing with classical statistics is discussed and compared to the source probabilities estimated with the BSS method.

In Chapter 4, the BSS technique is applied to simulated data. The data sets are meant to test the limits and to show the potentials of the BSS method at varying background values. Results for two different choices of prior pdfs of the source intensities are provided.

In Chapter 5, the standard techniques currently employed in the X–ray regime are briefly reviewed, including those for sky surveys. Then, the BSS results on the three simulated data sets are compared with the outcome from WAVDETECT algorithm (Freeman *et al.*, 2002).

In Chapters 6 and 7, the BSS method is tested on astronomical images coming from the RASS data and on deep astronomical images of the CDF–S region, respectively. The detection of new X–ray sources is shown and a sample of galaxy clusters and groups is provided.

In Chapter 8, concluding remarks and outlook are given.

Chapter 2

The BSS technique

In this Chapter the novel method for the search and characterization of celestial sources in digital astronomical images is described. The BSS algorithm is based on BPT combined with the mixture–model technique. In Section 2.1, the basic aspects of BPT are reviewed. The principles of the background–source separation technique are introduced in Section 2.2. The source characterization method is described in Section 2.3. The BSS algorithm is published in Guglielmetti *et al.* (2009, 2005, 2004*a*,*b*,*c*).

2.1 Bayesian probability theory

In image processing, an automated system to reason, i.e. to take information about the world and to reach conclusions, is required. The expert knowledge is used to design representative models and to develop a simplified description of a complex process for reasoning. BPT allows us to investigate probabilistic models. Probabilistic models are used to deal with uncertainties in the data with a principled and definite method.

Bayesian analysis is named after Thomas Bayes (1702-1761). In his "*An essay towards solving a problem in the doctrine of chances*" (Bayes, 1783) he applied this analysis for a game of chance. In the late eighteenth and early nineteenth centuries, Pierre–Simon Laplace (1749-1827) extensively developed the Bayesian approach to statistics (Laplace, 1812). Much of Laplace's motivation in this development was the solution of problems in celestial mechanics. It remained the dominant form of statistics until the early twentieth century. Although fundamental work was still being done in astronomy and physics, it remained out of fashion as late as the 1970s (Connors, 1997). Nowadays one sees many applications, especially in image processing, as it allows to tackle problems that are ill–posed and cumbersome for classical statistics (see Berger, 1997; Connors, 1997 for more details). BPT allows one to infer an image given data constraints, prior knowledge, and uncertain information. For more on the subject see, e.g., Jeffreys (1961); Bretthorst (1988); Bernardo and Smith (1994); Gelman *et al.* (1995); Loredo (1995); Sivia (1996); Dose (2003); Jaynes (2003); O'Hagan and Forster (2004); Gregory (2005).

BPT provides a framework for scientific reasoning and rules for processing any kind of

incomplete information. The knowledge is always incomplete because of lack of data and uncertainties in the data. The information available is given by the observed data set and the expert knowledge about the physical system under investigation: priori information, statistical models and supplementary information such as first–principle physics knowledge. Each data set and parameters entering the models are subject to uncertainties which have to be estimated and encoded in probability distributions. Within BPT the so–called statistical and systematic uncertainties[1] are not distinguished. Both kinds of uncertainties are treated as a lack of knowledge.

The outcome of the BPT analysis is the pdf of the quantity of interest, which encodes the knowledge to be drawn from the information available (*a posteriori*). Any uncertainty of the physical system is accounted for and propagated in the posterior pdf. The posterior pdf comprises the complete information which can be inferred from the data and the expert knowledge. Values of model parameters and their uncertainties are directly computed from the posterior pdf.

BPT is a statistical approach based on comparisons among alternative hypotheses (or models). Probability densities are assigned to the full hypothesis space. The probability of an hypothesis covers the full range of real values from 0 to 1. In classic statistic, the probability of an hypothesis can only be 0 or 1, being an hypothesis only *true* or $false$. In addition, in contrast to classical statistics, probabilities are assigned using the single observed data set. Therefore, BPT does not need sample data drawn from a population to assess the intrinsic uncertainty in the population.

BPT provides for additional benefits with respect to classical statistics. For instance, when data from different experiments are available, BPT allows for an integrated data analysis (IDA). Heterogeneous diagnostics are individually modelled and, successively, combined probabilistically. The combination of heterogeneous diagnostics occurs accounting for interdependencies between the data sets and for uncertainties of the measured data, the calibration measurements and the physical model. Thus, the extraction of information from sets of heterogeneous data is optimized and results are improved with respect to previous techniques: Refer to Fischer and Dinklage (2004, 2007) for more details.

BPT is based on the sum and product rules of probability theory. Consequently, nuisance parameters are integrated out through marginalization. Uncertainties of nuisance parameters are accounted in the posterior pdf. BPT allows for tackling problems such as parameter estimation, uncertainty determination, model comparison with models of varying complexity, and classification of data within a mixture of models.

2.1.1 Probability axioms

BPT rests on two rules of probability theory (see, e.g., Cox, 1946; Dose, 2003):
the **sum rule**

$$p(H_\mathrm{i}|I) + p(\overline{H_\mathrm{i}}|I) = 1 \tag{2.1}$$

[1]Systematic errors reflect, for instance, uncertainties in instrumental calibration.

and the **product rule**

$$p(H_\mathrm{i}, D|I) = p(H_\mathrm{i}|I) \cdot p(D|H_\mathrm{i}, I) = p(D|I) \cdot p(H_\mathrm{i}|D, I). \tag{2.2}$$

The hypotheses (models, values for parameters) H_i are formulated in the light of some background information I. Equation (2.1) simply states that the probability that a particular hypothesis H_i is true plus the probability that the negation $\overline{H_\mathrm{i}}$ of H_i is true add up to one. Similarly, the product rule states that the joint probability for H_i and D, the data, being true given the background information I may be expressed as the probability for H_i being true conditional on I times the probability for D given that H_i is true (Dose *et al.*, 1998). Equation (2.2) shows that the decomposition can be achieved in two equivalent ways because of the symmetry in the arguments (H_i, D) of $p(H_\mathrm{i}, D|I)$. The notation employed is the one introduced by Jeffreys (1961).

In BPT the number of competing hypotheses has to be larger or equal to 2, since no hypothesis is ever regarded true until there is no plausible alternative explanation of the data. Another version of the sum rule can be derived from eqs (2.1) and (2.2):

$$p(H_1 + H_2|I) = p(H_1|I) + p(H_2|I) - p(H_1, H_2|I), \tag{2.3}$$

this is called the extended sum rule. Equation (2.3) can contain several competing hypotheses. Dealing with mutually exclusive hypotheses (i.e. if one hypothesis is true then all the other are false), the sum rule can be written as

$$p(\sum_i H_\mathrm{i}|I) = \sum_i p(H_\mathrm{i}|I) = 1.$$

This is the normalization rule (Dose *et al.*, 1998).

2.1.2 Bayes' theorem

Comparison of the two equivalent decompositions in eq. (2.2) yields Bayes' theorem:

$$p(H_\mathrm{i}|D, \sigma, I) = \frac{p(D|H_\mathrm{i}, \sigma, I) \cdot p(H_\mathrm{i}|I)}{p(D|I)}, \tag{2.4}$$

where the notation introduced by Jeffreys in eq. (2.2) is changed highlighting the errors, σ, entering the experiment. The vertical bars in eq. (2.4) denote conditionality property, based on either empirical or theoretical information.

Equation (2.4) relates the *posterior* pdf $p(H_\mathrm{i}|D, \sigma, I)$ to known quantities, namely, the *likelihood* pdf $p(D|H_\mathrm{i}, \sigma, I)$ and the *prior* pdf $p(H_\mathrm{i}|I)$. $p(D|I)$ is the prior predictive value for D, called the *evidence*. The evidence is the global likelihood for the entire class of hypotheses and is obtained by application of the sum and product rules:

$$p(D|I) = \sum_i p(H_\mathrm{i}, D|I) = \sum_i p(H_\mathrm{i}|I) \cdot p(D|H_\mathrm{i}, I). \tag{2.5}$$

Essentially, the evidence is the average likelihood for D, with the prior giving the averaging weight. In this form, eq. (2.5) has the meaning of a normalization constant.

Note that Bayes' theorem and all other rules above discussed can apply to both discrete and continuous parameters. Hence, all equations are modified accordingly. If more than one (continuous) parameter is considered, multiple integrals are used. In the case of a direct assignment of the prior density and the likelihood, the evidence is an uninteresting normalization constant. Thus, the posterior pdf is simply proportional to the product of the prior and the likelihood pdfs. Nonetheless, the evidence has two important applications: first, marginalization, that is required for the parameterization of a problem; second, model comparison. These applications are explained in the following Sections.

The posterior pdf in eq. (2.4) is the quantity to be inferred. It depends on the full data set D, on the errors σ entering the experiment and on all relevant information concerning the nature of the physical situation and knowledge of the experiment I. The likelihood pdf represents the probability of finding the data D for given quantities of interest, uncertainties σ and additional information I. It reveals the error statistics of the experiment. The prior pdf represents physical constraints or additional information from other diagnostics.

The terms 'posterior' and 'prior' have a logical rather than temporal meaning. The posterior and prior pdfs can be regarded as the knowledge 'with' and 'without' the new data taken into account, respectively.

Bayes' theorem constitutes a recipe of learning (inductive inference). The result of the learning process implied by eq. (2.4) is the posterior distribution, that constitutes the result of a Bayesian analysis (Dose, 2003). The theorem provides a formal rule for updating knowledge in the light of new data or learning from observations. In BPT, probabilities are not frequencies, although frequency arguments are often important for assigning priors and frequency estimates can be derived from Bayesian probabilities (Fischer *et al.*, 1997).

2.1.3 Marginalization rule

The marginalization rule, eq. (2.6), is a straightforward application of the sum rule (eq. 2.1) of probability theory (see Bretthorst, 1988 for more details) and of a deconvolution in the parameter variables.

In order to arrive at the pdf of any quantity x, marginalization of the multidimensional pdf can be regarded as a projection of the complete pdf on to that quantity. Marginalization is performed by integration over the quantity y one wants to get rid of:

$$\begin{aligned} p(x|D,\sigma,I,H_\mathrm{i}) &= \int p(x,y|D,\sigma,I,H_\mathrm{i})dy \\ &\propto \int p(D|x,y,I,\sigma,H_\mathrm{i}) \cdot p(x,y|I,H_\mathrm{i})dy \\ &\propto p(x|I,H_\mathrm{i}) \int p(D|x,y,I,\sigma,H_\mathrm{i}) \cdot p(y|I,H_\mathrm{i})dy. \end{aligned} \tag{2.6}$$

Equation (2.6) gives the marginal posterior pdf for x, $p(x|D,\sigma,I,H_\mathrm{i})$, in terms of the weighted average of the likelihood function, $p(D|x,y,I,\sigma,H_\mathrm{i})$, weighted by $p(y|I,H_\mathrm{i})$, the

prior pdf for y (Gregory, 2005). Marginalization of a quantity y thus takes into account the uncertainty of y which is quantified by the pdf $p(y|I, H_\mathrm{i})$. The uncertainty of y propagates into the pdf $p(x|D, \sigma, I, H_\mathrm{i})$.

Marginalization provides a way to eliminate variables (nuisance parameters) which are necessary to formulate the likelihood but otherwise uninteresting. Marginalization reduces the dimensionality of the problem.

2.1.4 Parameter estimation

Parameter estimation is a standard problem in data analysis. For given measurements, model parameters are estimated to explain at best the data (learning process). Commonly the least-squares algorithm for estimating the parameters or the ML method to estimate the parameters and their uncertainties have been used (Dose, 2003).

Bayesian analysis and the ML method analyse the problem of parameter estimation in a probabilistic framework. BPT, as the ML method, provides estimate of parameters and their uncertainties. The main difference between the Bayesian and the ML approaches to parameter estimation is that BPT makes probability statements about the parameters, while classic statistics can not. In fact, in classic statistics parameters are not allowed to be random variables (O'Hagan, 2000).

In a ML estimation approach, the mode (or maximal value) of the likelihood function, i.e. a pdf associated with the data given some parameters, is computed. Often, the Conjugate Gradient optimization technique is used for maximizing the likelihood. The ML solution maximizes the probability of the data. However, only a point in parameter space is found and no certainty is given for its uniqueness: A local maximum may be found instead of a global one. The local curvature of the likelihood function at the ML solution is used to construct error bars (*confidence intervals*). Hypothesis testing follows using a likelihood–ratio statistics. The strengths of the ML estimation rely on its large–sample properties: When the sample size is sufficiently large, then one can assume both normality of the test statistics about its mean and that the likelihood–ratio tests follow χ^2 distributions. These nice features don't necessarily hold for small samples (see, e.g., Kendall and Stuart, 1979; Eadie *et al.*, 1982; Loredo, 2004 for more details).

Bayes' theorem, instead, combines initial knowledge about the distribution of the unknown parameters entering the model with the likelihood pdf of the data given the parameters. The strengths of the Bayesian procedure in parameter estimation are due to the employment of not only prior knowledge, but also marginalization (described in Section 2.1.3): See Loredo (2004) for more details. The Bayesian solution to parameter estimation is the full posterior pdf of the parameters and not just a single point in the parameter space. Hence, BPT allows one to obtain a predictive distribution of the parameters. The values of the parameters and their uncertainties are derived from their joint posterior pdf. Probability contours (*credible regions*) in the parameter space describe uncertainties of the parameters. A credible region R of probability p is the region of highest posterior density

containing a volume in parameter space p:

$$\int_R d\theta \; p(\theta|D, I) = p, \tag{2.7}$$

where θ is a set of parameters (Loredo and Lamb, 2002). Credible regions are more robust than confidence intervals in classical statistics (Connors, 1997). In fact, with BPT there is no need to employ sample data drawn from a population to derive statements about the parameters.

BPT provides a valid approach to parameter estimation also for moderate and small data sets. A peculiarity of the Bayesian approach to parameter estimation is shown by the accuracy estimates of the parameters, which depends on the estimated noise. Everything probability theory can not fit to the model is assigned to the noise. Large uncertainties in model parameters are assigned when the noise is estimated to be large (see Bretthorst, 1988 for more details).

Note that a parameter contained within a model for the prior distribution for multiple parameters, which are themselves directly included in a model describing the data, is called *hyperparameter*.

Prior information

Physical situation always supports proper information (Fischer and Dose, 2002). Within BPT, each relevant information entering the models is explicitly stated. Priors are necessary to perform the 'probability inversion' of eq. (2.4). Priors account for the geometry of the hypothesis space, converting the likelihood from 'intensity' to 'measure' (Loredo, 2009). Prior information, encoded in probability distributions, helps to improve estimates of parameters (Bretthorst, 1988).

In order to formulate a distribution given a certain state of a priori knowledge, the principle of maximum information entropy is used (Dose, 2003). The maximum entropy (MaxEnt) principle assigns probabilities to incomplete or uncertain information, allowing one to maximize the uncertainty in the probability distribution (Gregory, 2005). With the MaxEnt principle, constraint (or testable) information is combined with Shannon's entropy measure of the uncertainty of a probability distribution to arrive at a unique probability distribution (Shannon, 1948; Jaynes, 1968, 2003). Maximizing entropy achieves the probability distribution which is most conservative and noncommittal while agreeing with the available information. One example is given when prior information is constrained to a mean value. The distribution which has maximum entropy, subject to a given average value, is an exponential function: be θ a parameter and $\hat{\theta}$ a point estimate (i.e. the only knowledge about θ), then the MaxEnt distribution is

$$p(\theta|\hat{\theta}, I) = \frac{\exp(-\theta/\lambda)}{Z(\lambda)}, \tag{2.8}$$

where λ must be determined such that $< \theta >= \hat{\theta}$ and $Z(\lambda)$ is the partition function (Jaynes, 1968). If the support range of θ is $0 \leq \theta < \infty$, then eq. (2.8) is simplified with

$\lambda = \hat{\theta}$ and $Z(\lambda) = \hat{\theta}$. On the same line of this example, the distribution with maximum entropy is given by a Gaussian function, when prior knowledge is constrained to the mean value and the variance of the distribution. Last, when no constraint is applied, then the distribution with maximum entropy is a uniform distribution. Flat priors are the least informative ones. A flat prior of a parameter gives the same probability to each model parameter value within the range of the prior. See, e.g., Jaynes (1968, 2003); O'Hagan (2000); Dose (2003); Gregory (2005) for more details.

The impact of the prior pdf on the posterior pdf can be tested employing different choices of priors. When the choice of prior pdf does not change the posterior pdf significantly, then the data (i.e. the likelihood function) contain significant information (Kass and Wasserman, 1996).

2.1.5 Model comparison, classification

Model comparison or object classification is a complementary statistical task to parameter estimation (Loredo and Lamb, 2002). Data interpretation is accomplished comparing parametrized models. Essential for model comparison is the marginal likelihood (*evidence*, *prior predicted value*) (Dose, 2003). Marginalization (integration) of the likelihood over parameter space provides a measure for the credibility of a model for given data. Ratios of marginal likelihoods (*Bayes factors*) are frequently used for comparing two models: See Berger (1985); Kass and Raftery (1995) for a comprehensive description of Bayes factors. In the literature other techniques for model comparison can be found, such as the Akaike information criterion and the Bayesian information criterion (or Schwarz criterion). An overview of these techniques is given in Kass and Raftery (1995). Bayes factors are the only penalization criteria of model complexity that take into account the full variability of parameters (and their uncertainties) by integrating over parameter space (Fischer and Dose, 2002).

Be H_i and H_j two competing models, Bayes' theorem (2.4) for model H_i can be written as follows:

$$p(H_i|D,\sigma,I) = \frac{p(D|H_i,\sigma,I)\cdot p(H_i|I)}{p(D|H_i,\sigma,I)\cdot p(H_i|I) + p(D|H_j,\sigma,I)\cdot p(H_j|I)}. \tag{2.9}$$

The posterior pdf for the competing model is given by eq. (2.9), exchanging the subscripts i and j.

The ratio between the two posterior pdfs of the competing models (odds ratio) can be written as follows:

$$O_{ij} = \frac{p(H_i|I)}{p(H_j|I)} \cdot \frac{p(D|H_i,\sigma,I)}{p(D|H_j,\sigma,I)}, \tag{2.10}$$

from model H_i to model H_j. The first factor (the ratio of the priors) is called prior odds. In most physical problems the prior odds is set to 1, since it is not known a priori which is the most preferable model. The second factor is the Bayes factor:

$$\frac{p(D|H_i,\sigma,I)}{p(D|H_j,\sigma,I)} = \frac{\int p(D|\theta,H_i,\sigma,I)\cdot p(\theta|I,H_i)d\theta}{\int p(D|\phi,H_j,\sigma,I)\cdot p(\phi|I,H_j)d\phi} \equiv B_{ij}, \tag{2.11}$$

where model parameters (θ, ϕ) can be completely independent or one can include the other. The Bayes factor is the ratio of marginal likelihoods of models H_i and H_j. The marginal likelihood is called *evidence*, in the sense that the higher this number is, the higher the evidence is that the data provide in favour of the model (Astone *et al.*, 2003).

The problem with Bayes factors is the cumbersome multidimensional integral over parameter space to be calculated for the marginal likelihood. On the one hand, an exact analytic evaluation of the integrals in eq. (2.11) is possible only for exponential family distributions with conjugate (or convenience) priors (Fischer and Dose, 2002; Gelman *et al.*, 2004), that represent a narrow class of models. On the other hand, the integrands in eq. (2.11) are highly peaked around its maximum (Kass and Raftery, 1995). Numerical methods, capable of finding the region where the integrand mass is accumulating, are: asymptotic approximation (Laplace's method and its variants); Monte Carlo integration (e.g. adaptive Gaussian quadrature); MCMC techniques simulating from the posterior (e.g. Metropolis–Hastings algorithm, Gibbs sampler, RJMCMC). A review of these techniques can be found in Kass and Raftery (1995); Fischer and Dose (2002). In this thesis, the sample size of the multidimensional integral is moderate. Therefore, the Laplace's approximation is preferable with respect to other techniques. The Laplace's approximation is described in details in the next subsection.

An important aspect of model comparison with Bayes factors is that the rule known as 'Ockham's Razor', i.e. "*Prefer the simpler model unless the more complicated model gives a significantly better fit*" (Loredo, 1995), is automatically implemented. For example, when employing the Laplace's approximation, Bayes factors are estimated by approximation of the marginal likelihood evaluated at the maximum values of the parameters multiplied by a parameter volume factor (Ockham or simplicity factor) (Dose, 2003). The Ockham factor is a quantification of the rule 'Ockham's Razor'. The Ockham factor accounts for the ratio between the volumes of the likelihoods around the maximum and the prior volumes. Model H_i will be preferred over model H_j only if the likelihood increases sufficiently to overwhelm the additional Ockham factor (see Jeffreys and Berger, 1992; Loredo *et al.*, 1997 for more details).

In classic statistics, ratios of maximum likelihoods are commonly used to compare models. More complicated models have higher likelihoods than simpler ones. Since 'Ockham's Razor' is not automatically incorporated in the likelihood ratio test (or Neyman–Pearson lemma), a specified critical value is used to provide preference for simplicity (Loredo and Lamb, 2002). Therefore, the specified critical value can be seen as a prior information, that is not included into the analysis, but it is externally prefixed. In addition, the classic hypothesis test, in contrast to Bayes factors, can not take into account model uncertainty. Model uncertainties are needed especially for comparing more than two models or nested models. Model comparison in classic statistics can lead to very misleading results (Kass and Raftery, 1995).

Laplace's approximation

The integrands in eq. (2.11) represent each the posterior pdf. For instance, at the denominator the posterior pdf is $P(\theta|D, H_i, \sigma, I)$ and it represents all the information necessary to decide how reasonable a solution θ is (Dose, 2003). The posterior pdf allows one to determine many quantities of interest, such as the posterior mode, $\max_\theta P(\theta|D, H_i, \sigma, I)$, resulting in the most probable solution, $\hat{\theta}$, the mean $< \theta_j >= \int \theta_j P(\theta|D, H_i, \sigma, I) d^N\theta$, and confidence intervals via the variance $var(\theta_l) =< \theta_l^2 > - < \theta_l >^2$.

For multivariate problems, the posterior pdf can be approximated with a Gaussian distribution. This is a commonly used method for estimating parameters. It is termed Laplace's approximation (or evidence approximation) (O'Hagan, 2000).

The posterior pdf is assumed to have a single dominant interior mode, i.e. the mode is not on the boundary of the allowed parameter space, with N parameters. The mode is indicated with $\hat{\theta}$. In the vicinity of the mode, the product of the prior and the likelihood pdfs can be approximated by a multivariate Gaussian (given by the second–order Taylor expansion of the posterior pdf around the mode), such that:

$$p(\theta|H_{\rm i}, I) \cdot p(D|\theta, H_{\rm i}, \sigma, I) \approx p(\hat{\theta}|H_{\rm i}, I) \cdot p(D|\hat{\theta}, H_{\rm i}, \sigma, I) \cdot \exp[-\frac{1}{2}(\theta - \hat{\theta})^T \mathbf{\Psi} (\theta - \hat{\theta})], \quad (2.12)$$

where the Hessian (or Fisher information) matrix $\mathbf{\Psi}$ is the matrix of second derivatives evaluated at the mode:

$$\mathbf{\Psi} = \left. \frac{\partial^2 \ln[p(\theta|H_{\rm i}, I) \cdot p(D|\theta, H_{\rm i}, \sigma, I)]}{\partial^2 \theta} \right|_{\hat{\theta}}.$$

$\mathbf{\Psi}$ is the covariance matrix. Its inverse is the model parameter covariance matrix, that provides information about the uncertainties of the determined parameters. Specifically, the Hessian matrix provides the full curvature of the posterior pdf within the Gaussian approximation.

From eq. (2.12), the marginal likelihood (evidence) can be written as:

$$p(D|H_{\rm i}, \sigma, I) \approx p(\hat{\theta}|H_{\rm i}, I)\ p(D|\hat{\theta}, H_{\rm i}, \sigma, I)\ (2\pi)^{N/2}\ \det{}^{-1/2}\mathbf{\Psi}. \quad (2.13)$$

Marginal likelihoods are necessary to solve Bayes factors (2.11). Equation (2.13) shows that the evidence is approximately equal to the posterior maximum times the volume of the posterior pdf below the peak. This representation may fail when the posterior pdf is skewed or highly non–Gaussian. For more on the subject, see refs. Kass *et al.* (1990); Loredo (1999); O'Hagan and Forster (2004).

Note that eq. (2.12) is also used to do the integrals needed to eliminate nuisance parameters. The mode of the parameters can be estimated employing the maximum a posteriori (MAP) solution to locate the mode.

Maximum a posteriori MAP is an estimate for the most probable parameter $\hat{\theta}$ found maximizing the posterior distribution of the parameters θ:

$$\hat{\theta} = \max_\theta\ p(\theta|H_{\rm i}, I) \cdot p(D|\theta, H_{\rm i}, \sigma, I). \quad (2.14)$$

The normalization factor is not considered, since only the maximum value is of interest.

2.1.6 Mixture model technique

Another important property of BPT is the capability of modelling the data by mixture distributions in the parameter space (see Everitt and Hand, 1981; Neal, 1992; Sivia, 1997; Dose, 2003; Gelman *et al.*, 2004 and references therein).

Mixture models are often useful to describe complex statistical problems. Identification of outlying observations, probabilistic classification, and clustering are some of the problems which may naturally be modelled in mixture form. Mixture distributions are, therefore, an appropriate tool for modelling processes whose output is thought to be generated by several different underlying mechanisms, or to come from several different populations.

A mixture model is a probabilistic model described by the density (Bernardo and Girón, 1988):

$$p(D|\lambda,\theta) = \sum_{j=1}^{k} \lambda_j p(D|\theta_j), \quad \lambda_j > 0, \ \sum_{j=1}^{k} \lambda_j = 1,$$

where $\lambda = \{\lambda_1, \cdots, \lambda_k\}$, $\theta = \{\theta_1, \cdots, \theta_k\}$ and k denotes the number of mixands in the mixture. Note that each $\theta_j \in \theta$ is represented itself by a vector of parameters. In this model, $p(D|\theta_j)$ describes the probabilistic mechanism of generating data D within population P_j, which is completely identified by its corresponding parameters θ_j. For instance, in image analysis the population P_j can be given by the data coming from background only or from background plus source signal. λ_j denotes the probability that a random observation comes from population P_j. The number of mixands depends on the physical problem one intends to model. The functional form of all the terms in the mixture depends on the physical models under investigation. For example, in image analysis two mixands can be employed with the two terms in the mixture represented by a Poisson and a marginal Poisson distributions, respectively.

The identification and characterization of these underlying 'latent classes' is of major importance in this thesis. The mixture model technique is employed within BPT. The Bayesian mixture model technique allows one to separate the source signal from an underlying background signal. For this, the standard Bayesian approach to this problem is followed. Hence, a prior distribution is defined over the parameter space of the mixture model, that is combined with the observed data to give a posterior distribution over the parameter space.

Several applications of mixture modelling in the framework of BPT can be found in the literature, e.g., von der Linden *et al.* (1999, 1997); Fischer and Dose (2002); Fischer *et al.* (2001, 2000). In particular, Fischer and Dose (2002) demonstrates the capability of the Bayesian mixture model technique even with an unknown number of components for background separation from a measured spectrum. The present approach follows these previous works.

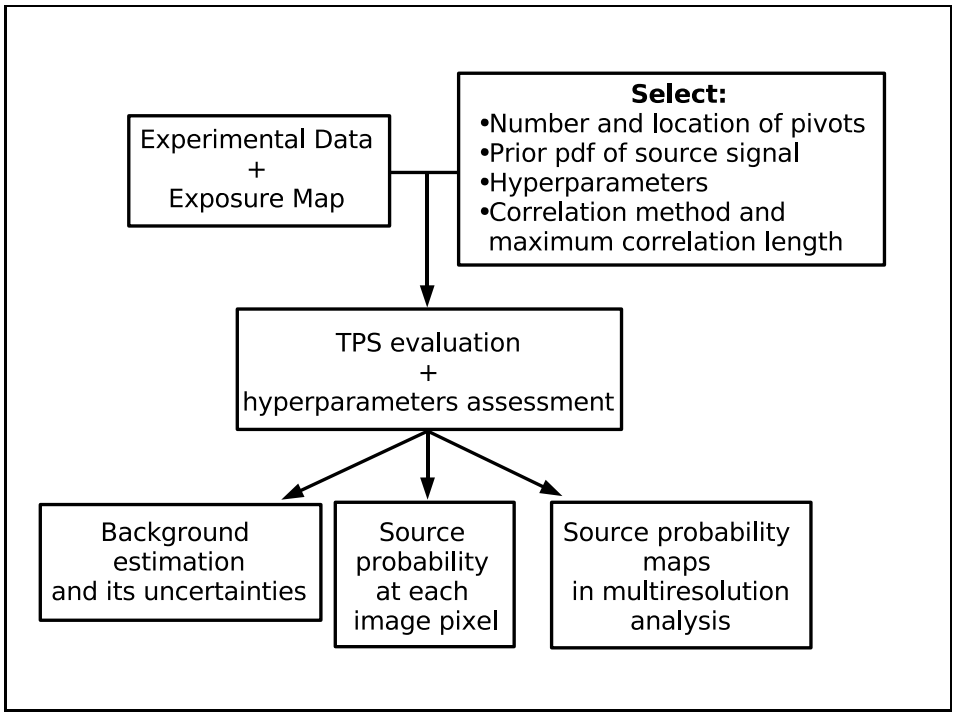

Figure 2.1: Flow chart illustrating the background estimation and source detection algorithm. The two boxes in the upper row represent the input information. The output information is provided by the boxes in the lower row.

2.2 The joint estimation of background and sources

The aim of the BSS method is the joint estimation of background and sources in two–dimensional image data. The algorithm is characterized by: background estimation and source detection; calculation of source probability maps in a multiresolution analysis. A scheme of the BSS algorithm for source detection and background estimation is provided in Fig. 2.1.

The input information of the developed algorithm is given by the experimental data, i.e. the detected photon counts, and the telescope's exposure time. Other input parameters are listed in the upper right box of Fig. 2.1. They are considered as follows.

The background rate is assumed to be smooth, e.g. spatially slowly varying compared to source dimensions. To account for smoothness the background rate is modelled with a two–dimensional TPS (Section 2.2.2). The number and the positions of the pivots, i.e. the spline's supporting points, determine what data structures are assigned to be background. All structures which cannot be described by the background model will be assigned to be sources. The number of pivots required to model the background depends on the characteristics of the background itself. Though the minimum number of pivots is four (since the minimum expansion of the selected spline has four terms), their number increases with increasing background variation.

The co–existence of background and sources is described with a probabilistic two–component mixture model (Section 2.2.1) where one component describes background contribution only and the other component describes background plus source contributions. Each pixel is characterized by the probability of belonging to one of the two mixture components. For the background estimation the photons contained in all pixels are considered including those containing additional source contributions. No data censoring by cutting out source areas are employed.

For background estimation the source intensity is considered to be a nuisance parameter. According to the rules of BPT, the source signal distribution is described probabilistically in terms of a prior pdf. The prior pdf of the source signal is an approximation to the true but unknown distribution of the source intensity in the field. Two prior pdfs of the source signal have been studied: the exponential and the inverse–Gamma function.

The background and its uncertainties (Section 2.2.3) are estimated from its posterior pdf. Therefore, for each pixel of an astronomical image an estimate of its background and its uncertainties are provided.

Moreover, the Bayesian approach introduces few hyperparameters, that are fundamental for the estimation of the posterior pdfs for the background and the source intensities. Specifically, in Section 2.2.4 the hyperparameters are shown to be estimated exclusively from the data. Alternatively, hyperparameters can be chosen in advance.

The source probability is evaluated with the mixture model technique for pixels and pixel cells[2] in order to enhance the detection of faint or extended sources in a multiresolution analysis. Pixels and pixel cells are treated identically within the Bayesian formalism. For the correlation of neighbouring pixels, the following methods have been investigated: box filter with a square, box filter with a circle, Gaussian weighting filter (see Section 2.2.1 for more details).

The BSS technique is morphology free, i.e. there are no restrictions on the object size and shape for being detected. An analysed digital astronomical image is converted into the followings:

I) the background rate image, or *'TPS map'*, is an array specifying the estimated background rate at each image pixel for a given observation;

II) the background image, or *'background map'*, is an array specifying the estimated background amplitude at each image pixel for a given observation. It is provided by the TPS map multiplied with the telescope's exposure time. The effect of exposure variations are consistently included in the spline model;

III) the source probability images, or *'SPMs'*, display the probability that source counts are present in pixels and pixel cells for a given observation in a multiresolution analysis.

[2]The image finest resolution limited by instrumental design is defined as pixel, while pixel cells are a group of correlated neighbouring pixels.

Movies are produced with the SPMs obtained at different resolutions. The moving images allow one to discern interactively the presence of faint extended sources in digital astronomical images. The size of faint extended sources is correlated to the scale of the resolution, used for their detection. SPMs coming from other energy bands can be combined statistically to produce conclusive SPMs at different resolutions with the advantage to provide probabilities for the detected sources from the combined energy bands (Section 2.2.5).

2.2.1 Two–component mixture model

The general idea of the described Bayesian model is that a digital astronomical image consists of a smooth background with additive source signal, which can be characterized by any shape, size and brightness. The background signal is the diffuse cosmic emission added to the instrumental noise and particle background. The source signal is the response of the imaging system to a celestial object. A surface $b(\mathbf{x})$ describes the background in addition to the source signal, where $\mathbf{x} = (x, y)$ corresponds to the position on the grid in the image.
Therefore, given the observed data set $D = \{d_{\mathrm{ij}}\} \in \mathbf{N}_0$, where d_{ij} is photon counts in pixel (or pixel cell) $\{ij\}$, two complementary hypotheses arise:

$$\begin{cases} B_{\mathrm{ij}}: & d_{\mathrm{ij}} = b_{\mathrm{ij}} + \epsilon_{\mathrm{ij}} \\ \overline{B}_{\mathrm{ij}}: & d_{\mathrm{ij}} = b_{\mathrm{ij}} + s_{\mathrm{ij}} + \epsilon_{\mathrm{ij}}. \end{cases}$$

Hypothesis B_{ij} specifies that the data d_{ij} consists only of background counts b_{ij} spoiled with noise ϵ_{ij}, i.e. the (statistical) uncertainty associated with the measurement process. Hypothesis $\overline{B}_{\mathrm{ij}}$ specifies the case where additional source intensity s_{ij} contributes to the background. Additional assumptions are that no negative values for source and background amplitudes are allowed and that the background is smoother than the source signal.

The smoothness of the background is achieved by modelling the background count rate with a bivariate TPS where the supporting points are chosen sparsely to ensure that sources cannot be fitted. The spline fits the background component whereas count enhancements classify pixels and pixel cells with source contributions.

In the following, pixel cells are subsumed by pixels. Pixel cells are collections of pixels where d_{ij} is the total photon count in cell $\{ij\}$. The photon counts of neighbouring pixels are added up and the formed pixel cell is treated as a pixel. In principle, any cell shape can be chosen. In practice, two methods have been developed when pixels have weight of one within the cell (box filtering with cell shape of a square or of a circle) and one method when pixels have different weights within the cell (Gaussian weighting). The box filter with cells of squared shape consists of taking information of neighbouring pixels within a box. The cell size is the box size. The box filter with cells of circular shape considers pixels with a weight of one if inside the cell size, otherwise zero. Pixels have a weight of one when the cell size touch them at least at the centre. This method allows the pixel cells to have varying shapes. The Gaussian weighting method provides Gaussian weights

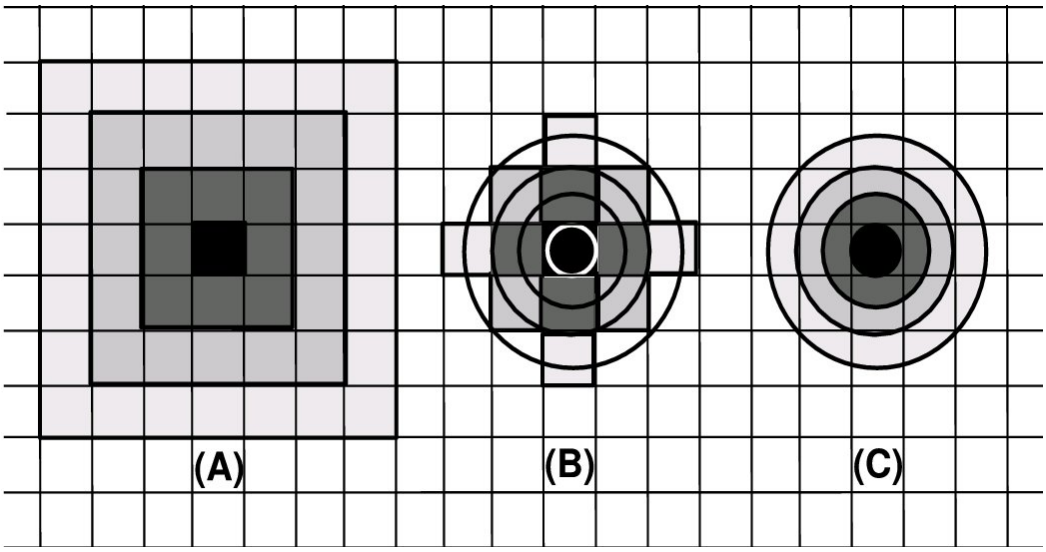

Figure 2.2: Representation of pixel cells at several correlation lengths: box filtering with cell shape of a square (A) and of a circle (B); Gaussian weighting (C).

around a centre: weights are given at decreasing values according to the distance from the centre.
In Fig. 2.2, the developed methods for correlating the information of neighbouring pixels are depicted. Four correlation lengths are used. Plot (A) shows the box filtering with cell shape of a box. The employed correlation lengths have values of $0.5, 1.5, 2.5, 3.5$ pixels, that indicate the collections of $1, 9, 25, 49$ pixels respectively. In plot (B), the box filtering with the cell shape of a circle is represented with correlation lengths of $0.5, 1.0, 1.5, 2.0$ pixels. In this case, pixel cells with $1, 5, 9, 13$ pixels are formed for each indicated correlation length. Finally, plot (C) shows the Gaussian weighting method for the same correlation lengths employed for plot (B). The grey shades indicate decreasing weights to pixel counts for increasing correlation length.

As expressed in eq. (2.4), estimates of probabilities of the hypotheses ($B_{\rm ij}$ and $\overline{B}_{\rm ij}$) are of major interest.

In this thesis, the problem arising with small number of photon counts in astronomical images is addressed. Poisson statistics has to be used. The likelihood probabilities for the two hypotheses within Poisson statistics are:

$$p(d_{\rm ij} \mid B_{\rm ij}, b_{\rm ij}) = \frac{b_{\rm ij}^{d_{\rm ij}}}{d_{\rm ij}!} e^{-b_{\rm ij}}, \tag{2.15}$$

$$p(d_{\rm ij} \mid \overline{B}_{\rm ij}, b_{\rm ij}, s_{\rm ij}) = \frac{(b_{\rm ij} + s_{\rm ij})^{d_{\rm ij}}}{d_{\rm ij}!} e^{-(b_{\rm ij}+s_{\rm ij})}. \tag{2.16}$$

This technique is easily adaptable to other likelihoods, for instance employing Gaussian statistics as given in Fischer *et al.* (2001).

The prior pdfs for the two complementary hypotheses are chosen to be $p(B_{\rm ij}) = \beta$ and $p(\overline{B}_{\rm ij}) = 1-\beta$, independent of i and j. Specifically, the parameter β is the prior probability that a pixel contains only background.

Since it is not known if a certain pixel (or pixel cell) contains purely background or additional source signal, the likelihood for the mixture model is employed. The likelihood for the mixture model effectively combines the probability distributions for the two hypotheses, $B_{\rm ij}$ and $\overline{\rm B}_{ij}$:

$$p(D|\mathbf{b},\mathbf{s}) = \prod_{\rm ij}\{\beta\frac{b_{\rm ij}^{d_{\rm ij}}}{d_{\rm ij}!}e^{-b_{\rm ij}} + (1-\beta)\frac{(b_{\rm ij}+s_{\rm ij})^{d_{\rm ij}}}{d_{\rm ij}!}e^{-(b_{\rm ij}+s_{\rm ij})}\}, \tag{2.17}$$

where $\mathbf{b} = \{b_{\rm ij}\}$, $\mathbf{s} = \{s_{\rm ij}\}$ and $\{ij\}$ corresponds to the pixels of the complete field.

The probability of having source contribution in pixels and pixel cells is according to Bayes' theorem (details can be found in Fischer *et al.* 2001):

$$p(\overline{B}_{\rm ij} \mid D) = \frac{(1-\beta)\cdot p(d_{\rm ij} \mid \overline{B}_{\rm ij}, b_{\rm ij}, s_{\rm ij})}{\beta\cdot p(d_{\rm ij} \mid B_{\rm ij}, b_{\rm ij}) + (1-\beta)\cdot p(d_{\rm ij} \mid \overline{B}_{\rm ij}, b_{\rm ij}, s_{\rm ij})} \equiv P_{\rm source}. \tag{2.18}$$

This equation enables the data contained in an astronomical image to be classified in two groups: with and without source signal contribution. Specifically, eq. (2.18) provides the probability of source detection.

Equation (2.18) is used in the multiresolution analysis. The SPM with the largest resolution is characterized by the probability of uncorrelated pixels. At decreasing resolutions a correlation length is defined. Starting from a value of 0.5 or 1, the correlation length increases in steps of 0.5 or 1 pixel for decreasing resolution. The value of 1 is used only for the box filtering with the cell shape of a box. The SPMs at decreasing resolutions are, therefore, characterized by the information provided by background and photon counts in pixel cells. Specifically, photon counts and background counts are given by a weighted integration over pixel cells. The integrated photon and background counts enter the likelihood for the mixture model. Then, the source probability is estimated for each image pixel in the multiresolution analysis. The multiresolution algorithm preserves Poisson statistics.

Source signal as a nuisance parameter

Following Fischer *et al.* (2000, 2001), the source signal in eq. (2.16) is a nuisance parameter, which is removed by integrating it out (see eq. 2.6), resulting in the marginal likelihood:

$$p(d_{\rm ij}|\overline{B}_{\rm ij}, b_{\rm ij}) = \int_0^\infty p(d_{\rm ij}|\overline{B}_{\rm ij}, b_{\rm ij}, s_{\rm ij})\cdot p(s_{\rm ij}|\overline{B}_{\rm ij}, b_{\rm ij})ds_{\rm ij}. \tag{2.19}$$

A nuisance parameter is a parameter which is important for the model (describing the data), but it is not of interest at the moment. Following BPT, a prior pdf of the source signal has to be chosen. The final result depends crucially on the prior pdf set on the source signal. In fact, in addition to the choice of the TPS pivots, the prior pdf of the source

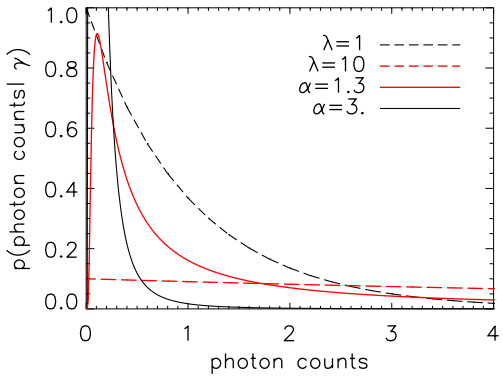

Figure 2.3: Representation of selected prior pdfs of the source signal versus the photon counts. The *exponential prior* pdf is drawn at two λ values (dashed lines). The *inverse–Gamma function prior* pdf is plotted at two α values (continuous lines). On the ordinate, γ indicates λ or α.

signal is crucial for background–source separation: All, that the prior pdf on the source signal does not allow to describe as a source, is identified as background and vice versa. Two approaches are described: the first method accounts for the knowledge of the mean value of the source intensity over the complete field (*exponential prior*), the second approach interprets the source signal distribution according to a power–law (*inverse–Gamma function prior*).

Exponential prior Following the works of Fischer and Dose (2002); Fischer *et al.* (2000, 2001), a prior pdf of the source signal has been selected such that is as weakly informative as possible. The idea follows a practical argument on the difficulty of providing sensible information. The prior pdf on the source intensity is described by an exponential distribution,

$$p(s_{\rm ij} \mid \lambda) = \frac{e^{-\frac{s_{\rm ij}}{\lambda}}}{\lambda}. \tag{2.20}$$

This is the most uninformative distribution according to the Maximum Entropy distribution for known mean value of the source intensity λ over the complete field (see eq. 2.8). In Fig. 2.3, equation (2.20) is drawn for two values of the mean source intensity: $\lambda = 1$ count and $\lambda = 10$ counts. No bright sources are expected to appear in fields with $\lambda \sim 1$. In the case of values of $\lambda \gg 1$, bright and faint sources are represented in these fields.
The *marginal Poisson likelihood* for the hypothesis $\overline{B}_{\rm ij}$ has the form:

$$p(d_{\rm ij}|\overline{B}_{\rm ij}, b_{\rm ij}, \lambda) = \frac{e^{\frac{b_{\rm ij}}{\lambda}}}{\lambda(1+\frac{1}{\lambda})^{(d_{\rm ij}+1)}} \cdot \frac{\Gamma[(d_{\rm ij}+1), b_{\rm ij}(1+\frac{1}{\lambda})]}{\Gamma(d_{\rm ij}+1)}, \tag{2.21}$$

where $\Gamma[a,x] = \int_{\rm x}^{\infty} e^{-t} t^{a-1} dt$ $(a > 0)$ is the incomplete–Gamma function and $\Gamma[a] = \Gamma[a,0]$ is the Gamma function (see refs. Fischer *et al.* 2000, 2001 for more details).

The behaviour of the Poisson and the marginal Poisson distributions is depicted with a parameter study. For the parameter study three background amplitudes b are chosen: 0.1, 1 and 10 counts. In Fig. 2.4 the Poisson distribution, eq. (2.15), and the marginal Poisson distribution, eq. (2.21), are drawn on a logarithmic scale. These plots are indicated with (a), (b) and (c), respectively. The parameter λ, which describes the mean intensity in a field, has values of: 1, 10 and 100 counts. The selected values for the background and for the parameter λ are chosen such that a large variety of cases one encounters analysing digital astronomical images are covered. For instance, $b = 10$ counts and $\lambda = 1$ count (plot c) corresponds to a field when the source signal is much smaller than the background signal. On the other side, $b = 0.1$ counts and $\lambda = 100$ counts (plot a) corresponds to a field characterized by bright sources and small background amplitude.

The Poisson distribution is always larger than the marginal Poisson distribution for photon counts lower or equal to the background intensity. Hence, hypothesis $B_{\rm ij}$ is more likely than the complementary hypothesis $\overline{B}_{\rm ij}$. This situation changes when the photon counts are larger than the background amplitude.

The decay length of the marginal Poisson distribution is determined by the expected source intensity λ. The probability to detect pixels satisfying hypothesis $\overline{B}_{\rm ij}$ is sensitive to the decay length of the marginal Poisson distribution and to the background amplitude, that is recognizable in the distance between the Poisson and the marginal Poisson distributions. Hence, the BSS method allows probabilities to be sensitive to the parameters characterizing the analysed digital astronomical image.

Let us consider plot (b) in Fig. 2.4 for photon counts in the range $(0 - 10)$. The background amplitude has a value of 1 count. If the expected mean source intensity on the complete field has a value of 1 count, i.e. $\lambda = 1$ count, 3 photon counts or more in a pixel are classified as a source, because the marginal likelihood is much larger than the likelihood. The probability of detecting a source increases with increasing counts in a pixel. This is due to the increasing distance of the marginal Poisson likelihood from the Poisson likelihood. If an analyst allows for many bright sources distributed in the field, then the relative number of faint sources is reduced. In fact, when a mean source signal 100 times larger than the background is expected, then 5 photon counts or more in a pixel are needed to identify the event due to the presence of a source. When $\lambda = 100$ counts, 5 photon counts in a pixel reveal a source probability lower than the one obtained when $\lambda = 1$ count. This situation changes for 7 or more photon counts in a pixel.

Inverse–Gamma function prior Alternatively to the exponential prior, a power–law distribution can be chosen to describe the prior knowledge on the source signal distribution.

One is tempted to claim that any physical situation contains sensible information for a proper (normalizable) prior. The choice of the prior pdf is inspired by the cumulative signal number counts distribution used often in astrophysics for describing the integral flux distribution of cosmological sources, i.e. a power–law function (see Rosati *et al.* 2002*b*; Brandt and Hasinger 2005 and references therein). The power law cannot be employed as a prior pdf, because the power law is not normalized. A normalized inverse–Gamma

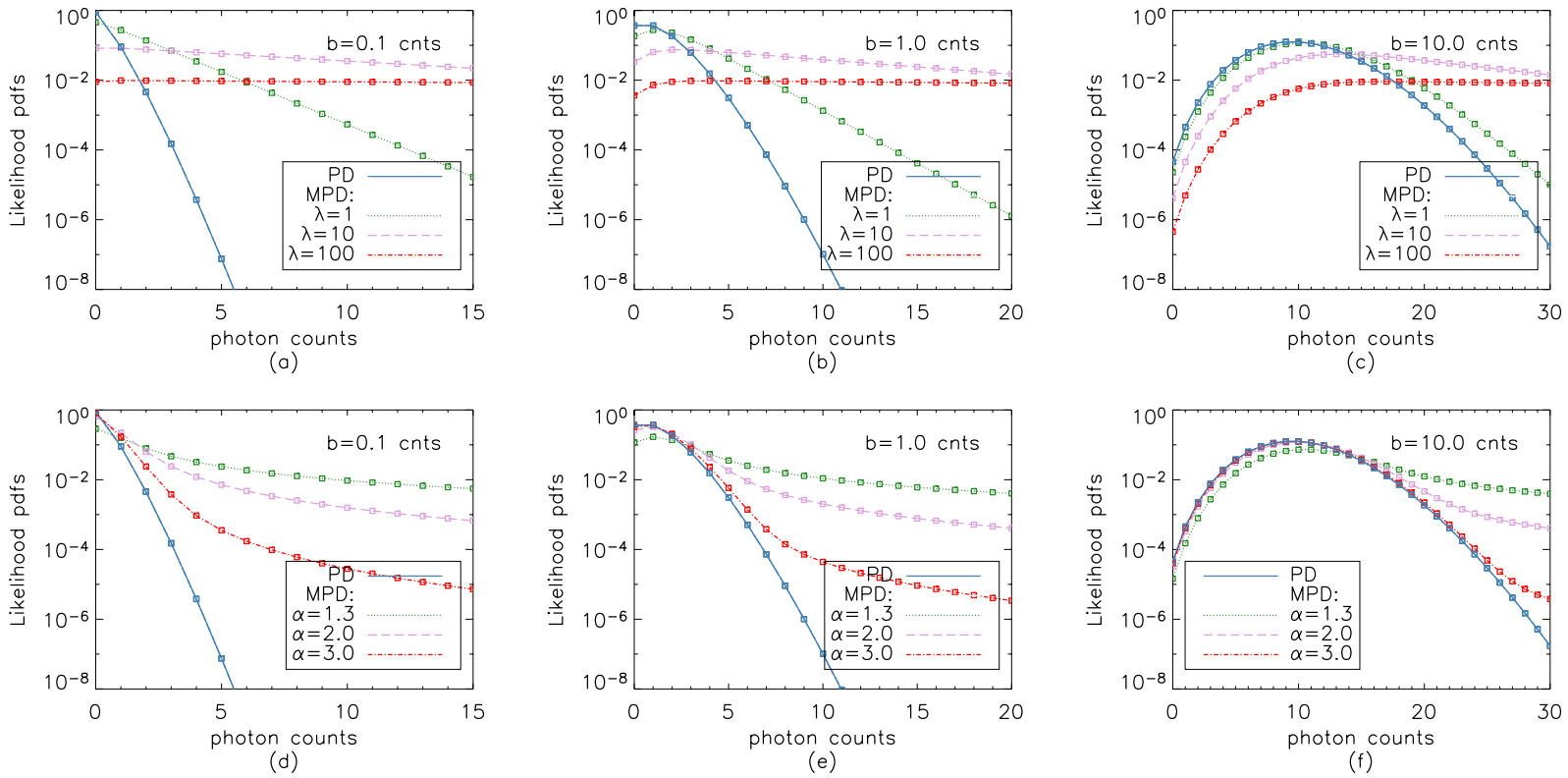

Figure 2.4: Likelihood pdfs versus photon counts. The Poisson distribution is indicated with PD. The marginal Poisson distribution is indicated with MPD. Panels $(a)-(c)$ are obtained using the *exponential prior* pdf. Panels $(d)-(f)$ are created using the *inverse–Gamma function prior* pdf.

function is instead used. It behaves at large counts as the power law, because it is described by a power law with an exponential cutoff.

The prior pdf of the source signal, described by an inverse–Gamma function, is:

$$\begin{aligned} p(s_{\rm ij} \mid \alpha, a) = &\quad e^{-\frac{a}{s_{\rm ij}}} \cdot s_{\rm ij}^{-\alpha} \cdot \frac{a^{\alpha-1}}{\Gamma(\alpha-1)}; \qquad \alpha > 1;\ \ a > 0; \\ \text{mean} = &\quad \frac{a}{\alpha-2}; \qquad \alpha > 2; \\ \text{variance} = &\quad \frac{a^2}{(\alpha-2)^2(\alpha-3)}; \qquad \alpha > 3, \end{aligned} \tag{2.22}$$

with slope α and cutoff parameter a. The location and the dispersion of the distribution depend on the values of the two parameters α and a. When a has a small positive value, the inverse–Gamma function is dominated by a power–law behaviour (see Appendix A, Section A.1 for more details).

The parameter a gives rise to a cutoff of faint sources. This parameter has important implications in the estimation of the background. If a is smaller than the background amplitude, the BSS algorithm detects sources of the order of the background. If a is larger than the background amplitude, the BSS algorithm assigns faint sources with intensities lower than a to be background only. Note that the effect of a on the selection of background and faint sources is valid also for structures, which are not due to sources but to background fluctuations.

In Fig. 2.3, equation (2.23) is drawn for two values of the parameter α. For this example the cutoff parameter a has a value of ~ 0.1 count. The distributions peak around a. The decay of each distribution depends on the value of α. When α is large, i.e. for values ≥ 2, the distribution drops quickly to zero. Instead the distribution drops slowly to zero, when α approaches 1. Hence, small values of α indicate bright sources distributed on the field.

The *marginal Poisson likelihood* for the hypothesis $\overline{B}_{\rm ij}$ is now described by:

$$\begin{aligned} &p(d_{\rm ij}|\overline{B}_{\rm ij}, b_{\rm ij}, \alpha, a) = \\ &= \frac{2}{\Gamma(\alpha-1)} \cdot e^{-b_{\rm ij}} \cdot \sum_{k=0}^{d_{\rm ij}} a^{\frac{k+\alpha-1}{2}} \cdot \frac{b_{\rm ij}^{d_{\rm ij}-k}}{\Gamma(k+1)\Gamma(d_{\rm ij}-k+1)} K_{k-\alpha+1}(2\sqrt{a}), \end{aligned} \tag{2.23}$$

where $\alpha > 1$, $a > 0$ and $K_{k-\alpha+1}(2\sqrt{a})$ is the Modified Bessel function of order $k-\alpha+1$. The proof for eq. (2.23) can be found in Appendix A, Section A.2.

In order to avoid numerical problems with the Bessel function, the following upward recurrence relation was derived:

$$\widetilde{K}_\nu(z) \equiv \frac{\widetilde{K}_{\nu-2}(z)}{(k-1)k} + \frac{2(\nu-1)}{z \cdot k} \widetilde{K}_{\nu-1}(z)$$

where $\widetilde{K}_\nu(z) := K_\nu(z)/\Gamma(k+1)$ and $\nu = k-\alpha+1$. $K_\nu(z)$ is the Bessel function of complex argument and it has the property: $K_{-\nu}(z) = K_\nu(z)$.

Figures 2.4 (d)–(f) show the corresponding parameter study for the inverse–Gamma function prior. The parameter α is chosen to be 1.3, 2.0 and 3.0 and the cutoff parameter $a \sim 0.1$ counts. The decay length of the marginal Poisson distribution, eq. (2.23), is now given by the value of α. The decay length decreases with increasing α values.

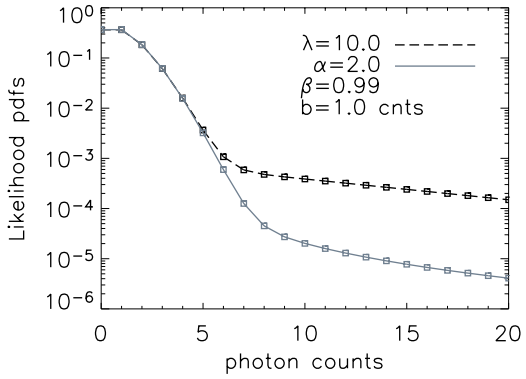

Figure 2.5: Likelihood pdfs for the mixture model using the *exponential prior* (dashed line) and the *inverse–Gamma function prior* (continuous line). The Poisson and the marginal Poisson likelihood pdfs are weighted with β and $(1-\beta)$, respectively.

The likelihood for the mixture model

The marginal Poisson likelihood pdf will be indicated with $p(d_{\rm ij}|\overline{B}_{\rm ij}, b_{\rm ij}, \gamma)$, where γ indicates λ or α. In the case of the inverse–Gamma function prior pdf, the cutoff parameter a does not appear since the value of this parameter is chosen such that the inverse–Gamma function is dominated by a power–law behaviour.

The likelihood for the mixture model, as written in eq. (2.17), now reads:

$$p(D \mid b, \gamma, \beta) = \prod_{ij} [\beta \cdot p(d_{\rm ij} \mid B_{\rm ij}, b_{\rm ij}) + (1-\beta) \cdot p(d_{\rm ij} \mid \overline{B}_{\rm ij}, b_{\rm ij}, \gamma)]; \qquad D = \{d_{\rm ij}\},\ \ b = \{b_{\rm ij}\}. \tag{2.24}$$

In Fig. 2.5 the effect of the likelihood for the mixture model on the data (semilog plot) is shown. The likelihood pdf for the mixture model is drawn for each prior pdf of the source signal employing the background value b and the prior pdf β. The value chosen for the parameter β indicates that 99% of the pixels distributed in the astronomical image are containing only background, which is frequently observed. The likelihood pdfs are composed by a central peak plus a long tail. The central peak is primarily due to the presence of the Poisson distribution. The long tail is caused by the marginal Poisson distribution. The presence of the long tail is essential in order to reduce the influence of the source signal for background estimation. The same technique was also used for outlier detections, where outliers are downweighted employing a mixture likelihood, for estimating the background contributions to measured spectra: For more details about the technique refer to Fischer *et al.* (2000). In this thesis, the source signal is considered an outlier.

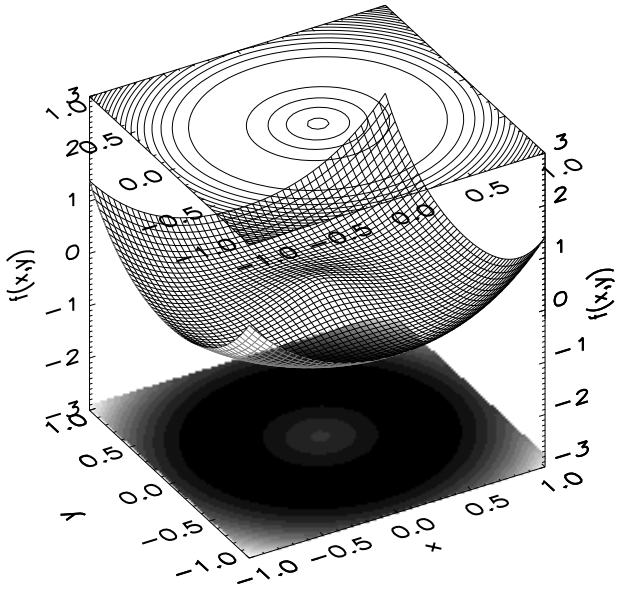

Figure 2.6: Example of thin–plate spline, $f(\mathbf{x}-\mathbf{x}_\mathrm{l}) = r^2 ln(r^2)$ is drawn with one support point centred at the Cartesian origin. The projection of $f(\mathbf{x}-\mathbf{x}_\mathrm{l})$ on the (x, y) plane is placed below and its contour plot on top of the surface image.

2.2.2 Thin–plate spline

The TPS has been selected for modelling the structures arising in the background rate of a digital astronomical image. It is a type of radial basis function (RBF).

The TPS is indicated with $t(\mathbf{x})$, where $\mathbf{x} = (x, y)$ corresponds to the position on the grid in the detector field. The shape of the interpolating TPS surface fulfills a minimum curvature condition on infinite support.

More specifically, the TPS is a weighted sum of translations of radially symmetric basis functions augmented by a linear term (see Meinguet, 1979; Wahba, 2006 for more details), of the form

$$t(\mathbf{x}) = E(\mathbf{x}) + \sum_{l=1}^{N_\mathrm{r}} \lambda_\mathrm{l} f(\mathbf{x}-\mathbf{x}_\mathrm{l}), \quad \mathbf{x} \in R^2.$$

$E(\mathbf{x}) = c_0 + c_1 x + c_2 y$ is the added plane. N_r is the number of support points (also called pivots, knots). The weight is characterized by λ_l. $f(\mathbf{x}-\mathbf{x}_\mathrm{l})$ is a basis function, a function of real values depending on the distance between the grid points $\mathbf{x}$ and the support points $\mathbf{x}_\mathrm{l}$, such that $|\mathbf{x}-\mathbf{x}_\mathrm{l}| > 0$.
Given the pivots $\mathbf{x}_\mathrm{k}$ and the amplitude $z_\mathrm{k} = z(\mathbf{x}_\mathrm{k})$, the TPS satisfies the interpolation

conditions:

$$t(\mathbf{x}_\mathrm{k}) = E(\mathbf{x}_\mathrm{k}) + \sum_{l=1}^{N_\mathrm{r}} \lambda_\mathrm{l} f(\mathbf{x}_\mathrm{k} - \mathbf{x}_\mathrm{l}) = z_\mathrm{k}, \quad k \in \{1, \ldots, N_\mathrm{k}\},\ \mathbf{x}_\mathrm{k} \in \{\mathbf{x}_\mathrm{l}\},$$

and minimizes

$$\|t\|^2 = I[f(x,y)] = \int\int_{\mathrm{R}^2} (f_{\mathrm{xx}}^2 + 2f_{\mathrm{xy}}^2 + f_{\mathrm{yy}}^2) dxdy.$$

$\|t\|^2$ is a measure of energy in the second derivatives of t. In other words, given a set of data points, a weighted combination of TPSs centred about each pivot gives the interpolation function that passes through the pivots exactly while minimizing the so–called 'bending energy'. The TPS satisfies the Euler–Lagrange equation and its solution has the form: $f(\mathbf{x} - \mathbf{x}_\mathrm{l}) \simeq r^2 \ln(r^2)$, where $r^2 = (x - x_\mathrm{l})^2 + (y - y_\mathrm{l})^2$. This is a smooth function of two variables defined via Euclidean space distance. In Fig. 2.6 an example of TPS with one pivot is pictured.

For fitting the TPS to the pivots' amplitudes, it is necessary to solve for the weights and the plane's coefficients so that it is possible to interpolate the local TPS's amplitude:

$$t_\mathrm{ij} = t_\mathrm{ij}(N_\mathrm{r}, \{\mathbf{x}_\mathrm{l}, z_\mathrm{l}, l = 1, \ldots, N_\mathrm{r}\})$$

which is the background rate. b_ij will indicate the local background amplitude, i.e. the multiplication of t_ij and the local value of the satellite's exposure time (τ):

$$b_\mathrm{ij} = t_\mathrm{ij} \times \tau_\mathrm{ij}.$$

The TPS interpolant is defined by the coefficients, c_k of the plane $E(\mathbf{x})$ and the weights λ_l of the basis functions. The solution for the TPS has been evaluated on an infinite support, since no solutions exist on a finite support (Wahba, 2006), where the requirements for this function to be fulfilled are:

1. $t(\mathbf{x})$ is two times continuously differentiable,
2. $t(\mathbf{x})$ takes a particular value z_k at the point $\mathbf{x}_\mathrm{k}$,
3. $I[f(x,y)]$ is finite.

Given the interpolation values $\mathbf{z} = (z_1, \ldots, z_{N_\mathrm{r}})$, the weights λ_l and c_k are searched so that the TPS satisfies:

$$t(\mathbf{x}_\mathrm{l}) = z_\mathrm{l}, \quad l = 1, \ldots, N_r$$

and in order to have a converging integral, the following conditions need to be satisfied:

$$\begin{cases} \sum_{l=1}^{N_\mathrm{r}} \lambda_\mathrm{l} & = 0, \\ \sum_{l=1}^{N_\mathrm{r}} \lambda_\mathrm{l} x_\mathrm{l} & = 0, \\ \sum_{l=1}^{N_\mathrm{r}} \lambda_\mathrm{l} y_\mathrm{l} & = 0. \end{cases}$$

This means that there are $(N_\mathrm{r}+3)$ conditions on $t(\mathbf{x}_\mathrm{l})=z_\mathrm{l}$ for estimating N_r λ_l weights and the coefficients c_k for the plane.

The coefficients of the TPS, λ_l, and the plane, c_k, can be found by solving the linear system, that may be written in matrix form as:

$$\begin{pmatrix} \mathbf{F} & \mathbf{Q} \\ \mathbf{Q}^T & \mathcal{O} \end{pmatrix} \begin{pmatrix} \lambda \\ \mathbf{c} \end{pmatrix} = \begin{pmatrix} \mathbf{z} \\ \mathbf{0} \end{pmatrix}, \tag{2.25}$$

where the matrix components are:

$$\mathbf{Q} = \begin{pmatrix} 1 & x_1 & y_1 \\ 1 & x_2 & y_2 \\ \vdots & \vdots & \vdots \\ 1 & x_{N_\mathrm{r}} & y_{N_\mathrm{r}} \end{pmatrix},$$

$$\begin{aligned} \mathbf{F}_\mathrm{ij} &= f(\mathbf{x}_\mathrm{i}-\mathbf{x}_\mathrm{j}), \\ \mathbf{z} &= (z_1,\ldots,z_{N_\mathrm{r}})^T, \\ \mathbf{0} &= (0,0,0)^T, \\ \lambda &= (\lambda_1,\ldots,\lambda_{N_\mathrm{r}})^T, \\ \mathbf{c} &= (c_0,c_1,c_2)^T. \end{aligned}$$

After having solved $(\lambda,\mathbf{c})^T$, the TPS can be evaluated at any point. For more information about splines, see Appendix B.

The pivots can be equally spaced or can be located in structures arising in the astronomical image. Following the works of Fischer *et al.* (2000) and von Toussaint and Gori (2007), the present work can be extended employing adaptive splines, i.e. allowing the number of pivots and their positions to vary in accordance with the requirements of the data.

2.2.3 Estimation of the background and its uncertainties

The posterior pdf of the background is, according to Bayes' theorem, proportional to the product of the mixture likelihood pdf, equation (2.24), and the prior pdf $p(b)$, that is chosen constant for positive values of b and null elsewhere. The maximum of the posterior pdf with respect to b, b^*, gives an estimate of the background map which consists of the TPS combined with the observatory's exposure map. The estimation of the background considers all pixels, i.e. on the complete field, because the source signal is tackled implicitly as outlier. In Appendix C details about the minimization procedure employed for the background model are given.

The posterior pdf for b is given by:

$$p(b \mid D) = \int p(b \mid D,z)p(z \mid D)d^{N_\mathrm{r}}z = \int \delta(b-b(z))\frac{p(D \mid z)p(z)}{p(D)}d^{N_\mathrm{r}}z.$$

This integral is complicated due to the presence of the delta function. This is, however, of minor importance since the expectation values of some functionals of b, say $g(b)$, are of

interest. Therefore:

$$\begin{aligned} E(g(b) \mid D) &= \int g(b)p(b \mid D)db \\ &= \int g(b(z))\frac{p(D \mid z)p(z)}{p(D)}d^{N_r}z \\ &= \frac{\int g(b(z))p(D \mid z)p(z)d^{N_r}z}{\int p(D \mid z)p(z)d^{N_r}z}. \end{aligned} \tag{2.26}$$

Assuming the maximum of $p(D \mid z)p(z)$ is well determined, the Laplace approximation is applied:

$$p(D \mid z)p(z) \simeq p(D \mid z^*)p(z^*)\exp\{-\frac{1}{2}\Delta\mathbf{z}^T H \Delta\mathbf{z}\}, \tag{2.27}$$

that means the integrand function is approximated by a Gaussian at the maximum z^* and the volume under that Gaussian is computed. The covariance of the Gaussian is determined by the Hessian matrix, as given by eq. (2.27), where $\Delta\mathbf{z} = \mathbf{z} - \mathbf{z}^*$ and $H_{ij} := -\frac{\partial^2 ln[p(D|z)p(z)]}{\partial z_i \partial z_j}$ is element $\{ij\}$ of the Hessian matrix. This approximation is the second–order Taylor expansion of a multivariate Gaussian around the optimized pivots amplitude's values. For more details see Section 2.1.5.
Then equation (2.26) becomes:

$$E(g(b) \mid D) = \frac{\int g(b(z))\exp\{-\frac{1}{2}\Delta\mathbf{z}^T H \Delta\mathbf{z}\}d^{N_r}z}{(2\pi)^{\frac{N_r}{2}}(\det H)^{-\frac{1}{2}}}.$$

Therefore, the posterior mean of b is:

$$E(b_{ij} \mid D) = \frac{\sqrt{\det H}}{(2\pi)^{\frac{N_r}{2}}}\int b_{ij}(z)\exp\{-\frac{1}{2}\Delta\mathbf{z}^T H \Delta\mathbf{z}\}d^{N_r}z = \mathbf{T}_{ij}^T\mathbf{z}^* = < b_{ij} >,$$

where $b_{ij}(z) = \mathbf{T}_{ij}^T \cdot \mathbf{z}$, and the variance is:

$$\begin{aligned} E(\Delta b_{ij}\Delta b_{lk} \mid D) = & \\ &= \frac{\sqrt{\det H}}{(2\pi)^{\frac{N_r}{2}}}\int (b_{ij}(z) - < b_{ij} >)\cdot(b_{lk}(z) - < b_{lk} >)\exp\{-\frac{1}{2}\Delta\mathbf{z}^T H \Delta\mathbf{z}\}d^{N_r}z \\ &= \mathbf{T}_{ij}^T H^{-1}\mathbf{T}_{lk}. \end{aligned} \tag{2.28}$$

The 1σ error on the estimated background function is therefore calculated by the square root of eq. (2.28).

2.2.4 Determining the hyperparameters

The two hyperparameters γ and β have so far been assumed to be fixed. However, these parameters can be appropriately estimated from the data.

Within the framework of BPT the hyperparameters (nuisance parameters) γ and β have to be marginalized.

Alternatively, and not quite rigorous in the Bayesian sense, the hyperparameters can be estimated from the marginal posterior pdf, where the background and source parameters are integrated out,

$$\max_{\beta,\gamma} p(\beta, \gamma \mid D) \rightarrow \beta^*, \gamma^*.$$

Hence, the estimate of the hyperparameters is the maximum of their joint posterior.

The basic idea is to use BPT to determine the hyperparameters explicitly, i.e. from the data. This requires the posterior pdf of γ and β. Bayes' theorem gives:

$$p(\gamma, \beta \mid D) = \frac{p(D \mid \gamma, \beta) p(\gamma) p(\beta)}{p(D)}. \tag{2.29}$$

The prior pdfs of the hyperparameters are independent because the hyperparameters are logically independent. These prior pdfs are chosen uninformative, because of lack of knowledge on these parameters. The prior pdf for β is chosen to be constant in $[0, 1]$. Since γ is a scale parameter, the appropriate prior distribution is Jeffrey's prior: $p(\gamma) \sim 1/\ \gamma$. Equation (2.29) can be written as follows:

$$p(\gamma, \beta \mid D) \propto p(D \mid \gamma, \beta) p(\gamma) = p(\gamma) \int p(D \mid z, \gamma, \beta) p(z) dz. \tag{2.30}$$

Assuming the maximum of $p(D \mid z, \gamma, \beta) p(z)$ is well determined, the Laplace approximation is applied

$$p(D \mid z, \gamma, \beta) p(z) \simeq p(D \mid z^*, \gamma, \beta) \cdot p(z^*) \exp\{-\frac{1}{2} \Delta \mathbf{z}^T H \Delta \mathbf{z}\} \tag{2.31}$$

where $\Delta \mathbf{z} = \mathbf{z} - \mathbf{z}^*$, $\mathbf{z}^*$ corresponds to the maximum value of the integrand in eq. (2.30), and $H_{ij} := -\frac{\partial^2 ln[p(D|z,\gamma,\beta)p(z)]}{\partial z_i \partial z_j}$ is element $\{ij\}$ of the Hessian matrix. Considering $\dim(\mathbf{z}) = N_\mathrm{r}$, where N_r is the number of support points, eq. (2.30) can be written as follows:

$$p(\gamma, \beta \mid D) = p(\gamma) p(D \mid z^*, \gamma, \beta) p(z^*) \frac{(2\pi)^{\frac{N_\mathrm{r}}{2}}}{(\det H)^{\frac{1}{2}}}. \tag{2.32}$$

$p(z^*)$ is chosen to be constant. The last term corresponds to the volume of the posterior pdf of γ and β for each γ, β estimates.

2.2.5 Probability of hypothesis $\overline{B}$

In principle, the probability of detecting source signal in addition to the background should be derived marginalizing over the background coefficients and the hyperparameters. Following the works of von der Linden *et al.* (1999) and Fischer *et al.* (2000), the multidimensional integral, arising from the marginalization, can be approximated at the optimal values found of the background coefficients and the hyperparameters.

Figure 2.7: Source probability ($P_{\rm source}$), PD and MPD versus photon counts as given by: eqs (2.21), (2.15) and (2.33) for the *exponential prior* pdf, panels (a), (b) and (c); eqs (2.23), (2.15) and (2.33) for the *inverse–Gamma function prior* pdf, panels (d), (e) and (f).

Equation (2.18) is approximated with:

$$p(\overline{B}_{\rm ij} \mid d_{\rm ij}) \approx \frac{1}{1+\frac{\beta}{1-\beta}\cdot\frac{p(d_{\rm ij}|B_{\rm ij},b^*_{\rm ij})}{p(d_{\rm ij}|\overline{B}_{\rm ij},b^*_{\rm ij},\gamma)}} = P_{\rm source}, \tag{2.33}$$

where $b^* = \{b^*_{\rm ij}\}$ is the estimated background amplitude, as explained in Section 2.2.3. SPMs are estimated employing this formula.

The BSS method does not need to incorporate the shape of the PSF. When the PSF full width at half–maximum (FWHM) is smaller than the image pixel size, then one pixel contains all the photons coming from a point–like source. Otherwise point–like sources are detected on pixel cells as large as the PSF FWHM. Extended objects are detected in pixel cells large enough that the source size is completely included. The pixel cell must be larger than the PSF FWHM and it can exhibit any shape.

Equation (2.33) shows that the source probability strictly depends on the ratio between the Poisson likelihood, $p(d_{\rm ij} \mid B_{\rm ij}, b_{\rm ij})$, and the marginal Poisson likelihood, $p(d_{\rm ij} \mid \overline{B}_{\rm ij}, b_{\rm ij}, \gamma)$ (Bayes factors). Bayes factors offer a way of evaluating evidence in favour of competing models.

Figure 2.7 shows the effect of the mixture model technique on the probability of having source contribution in pixels and pixel cells for the exponential and the inverse–Gamma function prior pdfs. For the parametric studies, the parameter β is chosen to be 0.5. This non–committal value of β arises if each pixel (or pixel cell) is equally likely to contain source signal contribution or background only. For photon counts of about the mean background intensity, $P_{\rm source}$ is small. $P_{\rm source}$ increases with increasing photon counts due to the presence of the long tail in the marginal likelihood. This allows efficient separation of the source signal from the background.

In panels (a)–(c) of Fig. 2.7, the distribution function of $P_{\rm source}$, the Poisson pdf (PD) and the marginal Poisson pdf (MPD) are drawn using the exponential prior (see also Figs 2.3 and 2.4). In the case of fields with bright sources ($\lambda > 10$ times the background intensity), $P_{\rm source}$ is nearly zero for photon counts less or equal to the mean background intensity. $P_{\rm source}$ increases rapidly with increasing photon counts. In the case of fields where the mean source intensity is similar to the mean background intensity, pixels containing photon counts close to the mean background intensity have probabilities about 50%. In these cases, $P_{\rm source}$ increases slowly with increasing photon counts, because the two Poisson distributions are similar. In the case of fields dominated by large background signal ($\lambda <$ mean background amplitude), $P_{\rm source}$ increases very slowly with increasing photon counts. In this case, the decay of the marginal Poisson distribution follows closely the decay of the Poisson distribution (e.g. for $b = 10$ counts and $\lambda = 1$ count).

In Fig. 2.7, panels (d)–(f), the distribution functions are shown using the inverse–Gamma function prior (see also Figs 2.3 and 2.4). Again, the source probability depends on the distance between the Poisson distribution and the marginal Poisson distribution. For photon counts in the vicinity of the mean background intensity, the source probability is small. This is due to the small distance between the Poisson and the marginal Poisson distributions. The source probability curves increase with increasing photon counts. The

Table 2.1: Interpretation of source probability values.

$P_{\rm source}$	<50%	50%	90%	99%	99.9%
Interpretation	Background only	Indifferent	Weak	Strong	Very strong

steepness of the slope depends on the parameter α (Fig. 2.3). The source probability curve increases faster at decreasing α values, because small α values indicate bright sources distributed in the field. In panels (e) and (f), $P_{\rm source}$ provides values close to 50% at low numbers of photon counts. This effect addresses the cutoff parameter a. In fact, in these plots the cutoff parameter a is smaller than the background amplitude. The situation is different in the simulations with small background amplitude (panel d), where the source probabilities decrease below 50% at low numbers of photon counts. In these simulations the cutoff parameter a is chosen larger than the mean background amplitude. Faint sources with intensities lower than a are described to be background.

The interpretations of the probability of having source contributions in pixels and pixel cells are shown in Table 2.1. Source probabilities <50% indicates the detection of background only. $P_{\rm source}$ is indifferent at values of 50%. In both cases, $P_{\rm source}$ might contain sources but they cannot be distinguished from the background due to statistical fluctuations. Source probability values $\gg$ 50% indicate source detections. False sources due to statistical fluctuations may occur especially for values <99%. For more details about the interpretations provided in Table 2.1, see Jeffreys (1961); Kass and Raftery (1995).

Statistical combination of SPMs at different energy bands

An astronomical image is usually given in various energy bands. SPMs, obtained with eq. (2.33), acquired at different energy bands can be combined statistically. The probability of detecting source signal in addition to the background for the combined energy bands $\{k\}$ is:

$$p(\overline{B}_{\rm ij} \mid d_{\rm ij})_{\rm comb} = 1 - \prod_{\rm k=1}^{\rm n} [1 - p(\overline{B}_{\rm ij} \mid d_{\rm ij})_{\rm k}], \tag{2.34}$$

where n corresponds to the effective energy band.

Equation (2.34) allows one to provide conclusive posterior pdfs for the detected sources from combined energy bands. It results, as expected, that if an object is detected in multiple bands, the resulting $p(\overline{B}_{\rm ij} \mid d_{\rm ij})_{\rm comb}$ is larger than the source probability obtained analysing a single band. An application of this technique is shown in Chapter 6. This analysis can be extended to study crowded fields or blends by investigating source colours.

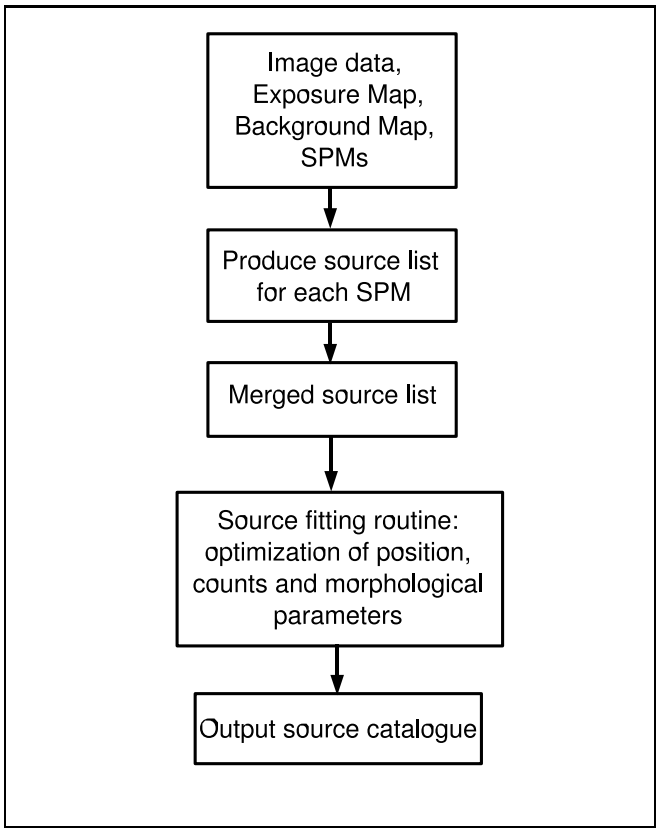

Figure 2.8: Flow chart illustrating the source characterization algorithm. The upper box represents the input information. The generated catalogue is in FITS standard.

2.3 Source characterization

Following the estimation of the background and the identification of sources, the sources can be parametrized.
SPMs at different resolutions are investigated first. Sources are catalogued with the largest source probability reached in one of the SPMs. Local regions are chosen around the detected sources. The regions size is determined by the correlation length where the maximum of the source probability is reached. A scheme of the source fitting routine is displayed in Fig. 2.8.

Although any suitable source shape can be used, the detected sources are modelled by a two–dimensional Gaussian. The data belonging to a source detection area 'k' are given by:

$$D_{\mathrm{ij}} = b_{\mathrm{ij}} + G_{\mathrm{ij}} \qquad \forall\{ij\} \in \{k\}. \tag{2.35}$$

D_{ij} are the modelled photon counts in a pixel $\{ij\}$ spoiled with the background counts b_{ij}. G_{ij} is the function which describes the photon counts distribution of the detected source:

$$G_{\mathrm{ij}} = \frac{I}{2\pi\sigma_{\mathrm{x}}\sigma_{\mathrm{y}}\sqrt{1-\rho^2}} \cdot \exp\Big\{ -\frac{1}{2(1-\rho^2)}\Big[\Big(\frac{x_{\mathrm{ij}}-x_{\mathrm{s}}}{\sigma_{\mathrm{x}}}\Big)^2 + \Big(\frac{y_{\mathrm{ij}}-y_{\mathrm{s}}}{\sigma_{\mathrm{y}}}\Big)^2 + - 2\rho\Big(\frac{x_{\mathrm{ij}}-x_{\mathrm{s}}}{\sigma_{\mathrm{x}}}\Big)\Big(\frac{y_{\mathrm{ij}}-y_{\mathrm{s}}}{\sigma_{\mathrm{y}}}\Big)\Big]\Big\},$$

where I is the intensity of the source, i.e. the net source counts, $\sigma_{\mathrm{x}}, \sigma_{\mathrm{y}}$ and ρ provide the source shape and x_{s}, y_{s} is the source pixel position on the image.

Position, intensity and source shape are provided maximizing the posterior pdf assuming constant priors for all parameters:

$$p(x_{\mathrm{s}}, y_{\mathrm{s}}, I, \sigma_{\mathrm{x}}, \sigma_{\mathrm{y}}, \rho | b, d) \propto \prod_{ij} \frac{D_{\mathrm{ij}}^{d_{\mathrm{ij}}}}{d_{\mathrm{ij}}!} \exp\{-D_{\mathrm{ij}}\} \qquad \forall\{ij\} \in \{k\}, \tag{2.36}$$

where d_{ij} are the photon counts detected on the image.

According to eqs (2.35) and (2.36) the source fitting is executed on the sources for given background. This is reasonable since the uncertainty of the estimated background is small. No explicit background subtraction from the photon counts is needed for estimating the source parameters.

Source position and size are converted from detector space to sky space. Source fluxes are provided straightforwardly.

The rms uncertainties of the source parameters are estimated from the Hessian matrix, where $H_{\mathrm{ij}} := -\frac{\partial^2 \ln[p(D|\xi)p(\xi)]}{\partial\xi_{\mathrm{i}}\partial\xi_{\mathrm{j}}}$ is element $\{ij\}$ of the Hessian matrix and ξ indicates the source parameters. The square root of the diagonal elements of the inverse of the Hessian matrix provides the 1σ errors on the estimated parameters.

The output catalogue includes source positions, source counts, source count rates, background counts, source shapes and their errors. The source probability and the source detection's resolution are incorporated.

Source characterization can be extended with Bayesian model selection. With the Bayesian model selection technique, the most suitable model describing the photon count profile of the detected sources can be found. The models to be employed are, for instance, Gaussian profile, King profile (Cavaliere and Fusco-Femiano, 1978) (i.e. the density profile of an isothermal sphere), de Vaucouleurs model, Hubble model. Such an extension to the actual method would allow an improvement in the estimation of the shape parameters of faint and/or extended sources.

Chapter 3

Reliability of detections

Statistical significance tests are used to verify whether data are consistent with the predictions of a theoretical model. Several statistical hypothesis tests are available. In this Chapter statistical hypothesis test with p–values is compared with the Bayesian solution provided within the BSS algorithm. In Section 3.1, statistical hypothesis tests are reviewed and an historical note on hypothesis testing is emphasized. In Section 3.2, the definition of p–values is provided. In Section 3.3, the general view on how this problem can be tackled with BPT is expressed. The commonly used measure of statistical significance with Poisson p–values is introduced in Section 3.4. In Section 3.5, simulations are utilized for comparing the Poisson p–values with the Bayesian probabilities. A summary of this Chapter is given in Section 3.6.

3.1 Introduction

The detection of sources is often spoiled by statistical fluctuations, which produce false detections of sources. The number of detected false sources depends on the method used and on the setting of thresholds. Thresholds are employed for tuning the number of false sources. Any chosen threshold will result in some astronomical sources being identified as background (false negative) and some false sources, due to background fluctuations, measured as real (false positives). Consequently, thresholds reduce the detectability of sources with low surface brightness, that can be most interesting for assessing cosmological theories.

Statistical hypothesis test can be described as follows. Data and models are tested for overall differences using a statistical measure of discrepancy, e.g. employing χ^2 for uncorrelated data. If the discrepancy is large enough, then there are significant differences beyond those accounted for by randomness in the data. A threshold is employed to put a cutoff to the measure of discrepancy. Classically, a test is declared significant if the discrepancy is larger than twice the standard error of the measurements (2σ approach), that means a probability of 0.05 to declare significance erroneously (Miller *et al.*, 2001). Often, a $3-5\sigma$ cutoff is used (Miller *et al.*, 2001; Starck and Murtagh, 2006), because of

multiple hypothesis tests and of noisy data.

In image analysis one wants to decide whether pixels contains background photons only or background plus source photons. The recurrent statistical problem to decide whether data belong to astronomical sources can be addressed with statistical hypothesis tests. Two competing hypothesis are used: the null hypothesis, H_0, that the pixel contains background photons only, and the alternative hypothesis, that a pixel contains source photons in addition to the background ones. A critical threshold is commonly selected to classify pixels into the two groups. The rule for classifying pixels using the data is an example of a statistical hypothesis test. Mistakes can be made in the classification process when data are insufficient to detect the discrepancy between the data and the model, because of small number of counts or of large background fluctuations. Often, statistical procedures for making a prediction about the number of false sources require only the knowledge of H_0: See Miller *et al.* (2001) for more details.

Several methods for making a prediction about the number of false sources are available, one is to use p–values from statistical significance tests (Linnemann, 2003). An example of a popular technique employing p–values is the false discovery rate method of Benjamini and Hochberg (1995). The false discovery rate technique is employed to find a significant discovery from a small set of data (Ball and Brunner, 2009). A p–value cutoff adapts to the data, since its value changes systematically as the source intensity changes (Miller *et al.*, 2001; Hopkins *et al.*, 2002). P–values are used to a great extent in many fields of science. Unfortunately, they are commonly misinterpreted. Researches on p–values (see, e.g., Berger and Sellke, 1987) showed that p–values can be a highly misleading measure of evidence.

3.1.1 Historical note on testing

Hypothesis testing with p-values was developed in the first half of the 20th century by Ronald Fisher (1890-1962). In Fisher's approach the researcher sets up H_0. A sample coming from a hypothetical infinite population with a known sampling distribution is used to provide the predicted reference distribution. The probability of the data (observed and more extreme one) given the truth of H_0 supplies an amount of evidence required to accept that an event is unlikely to have arisen by chance (Hubbard and Bayarri, 2003). This probability defines the p–value. A typical justification that Fisher would give for his procedure is that p–values can be viewed as an index of the 'strength of evidence' against H_0, with small p indicating an unlikely event and, hence, an unlikely hypothesis (Berger, 2003).

The method has been criticized by his contemporaries: Jerzy Neyman (1894-1981) and Sir Harold Jeffreys (1891-1989) (see, e.g., Berger, 2003 and references therein for more details). Both Neyman and Jeffreys were proposing different methods for hypothesis testing. Each was quite critical of the other approaches.

Neyman was founding his believing in classic statistics as Fisher did. Neyman considered alternative hypotheses to H_0 and introduced error probabilities: the Neyman–Pearson

theory of hypothesis testing [1]. Nonetheless, he recommended testing with fixed error probabilities. Jeffreys, a pioneer in Bayesian inference, proposed the use of posterior probabilities of hypotheses.

Neyman criticized p-values for violating the Frequentist Principle (i.e. in repeated actual use of a statistical procedure the average actual error should not be greater than the average reported error). Jeffreys criticized the logic of employing a 'tail area' rather than a likelihood–based measure for hypothesis testing: "*a hypothesis that may be true may be rejected because it has not predicted observable results that have not occurred*" (Jeffreys, 1961).

Note that in classic statistics, the argument of a probability is restricted to a random variable. Since a hypothesis cannot be considered a random variable, the truth of a hypothesis can only be inferred indirectly. In Bayesian inference, one can compute the probabilities of two or more competing hypothesis directly for a given state of knowledge (Gregory, 2005).

The three approaches can lead to very different results (Berger, 2003).

3.2 P-values

In hypothesis testing one is interested in making inferences about the truth of some hypothesis H_0, given a set of random variables $\mathbf{X}$: $\mathbf{X} \sim \mathbf{f}(\mathbf{x})$, where $f(\mathbf{x})$ is a continuous density and $\mathbf{x}$ is the actual observed values. A statistic $T(\mathbf{X})$ is chosen to investigate compatibility of the model with the observed data $\mathbf{x}$, with large values of T indicating less compatibility (Sellke *et al.*, 2001). The p–value is then defined as:

$$p = Pr(T(\mathbf{X}) \geq T(\mathbf{x})|H_0).$$

The significance level of a test is the maximum allowed probability, assuming H_0, that the statistic would be observed. The p–value is compared to the significance level. If the p–value is smaller than or equal to the significance level then H_0 is rejected. The significance level is an arbitrary number between 0 and 1, depending on the scientific field one is working in. However, often a significance level of 0.05 is accepted. Berger and Sellke (1987); Sellke *et al.* (2001) demonstrated that a significance level of 0.05 can indicate no evidence against H_0.

An extensive literature dealing with misinterpretations about p–values exists, see, for instance, Berger and Sellke (1987); Berger and Delampady (1987); Berger and Berry (1988); Delampady and Berger (1990); Loredo (1990, 1992); Kass and Raftery (1995); Sellke *et al.* (2001); Hubbard and Bayarri (2003); Astone *et al.* (2003); Gregory (2005) and references therein.

[1] The Neyman–Pearson hypothesis testing can be summarised in the following: Suppose one observes data $X \sim f(x|\theta)$, where θ are the parameters of the statistical model. $H_0 : \theta = \theta_0$ is tested versus some alternative hypothesis $H_1 : \theta = \theta_1$. H_0 is rejected if a test statistic $T = t(X) \geq c$, where c is a critical value. Type I (false positive) and type II (false negative) error probabilities are computed, with $\alpha = P_0$ (rejecting H_0, when H_0 is true) and $\beta = P_1$ (fail to reject H_0, when H_0 is false).

3.3 The Bayesian viewpoint

Since the state of knowledge is usually incomplete, a hypothesis can never be proven false or true. One can only compute the probability of two or more competing hypotheses (or models) on the basis of the only data available, see e.g. Gregory (2005).

The Bayesian approach to hypothesis testing is conceptually straightforward. Prior probabilities are assigned to all unknown hypotheses. Probability theory is then used to compute the posterior probabilities of the hypotheses given the observed data (Berger, 1997). This is in contrast to standard significance testing which does not provide such interpretation. In fact, in the classic approach the truth of a hypothesis can only be inferred indirectly.

Finally, it is important to underline that the observed data and parameters describing the hypotheses are subject to uncertainties which have to be estimated and encoded in probability distributions. With BPT there is no need to distinguish between statistical (or random) and systematic uncertainties. Both kinds of uncertainties are treated as lack of knowledge. For more on the subject see Fischer *et al.* (2003).

3.4 Significance testing with p–values

Several measures of statistical significance with p–values have been developed in astrophysics. A critical comparison and discussion about methods for measuring the significance of a particular observation can be found in Linnemann (2003). Following the work of Linnemann (2003), the Poisson probability p–value is defined as:

$$p_P = P(\geq d|b) = \sum_{j=d}^{\infty} \frac{e^{-b} b^j}{j!}. \tag{3.1}$$

p_P is the probability of finding d or more (random) events under a Poisson distribution with an expected number of events given by b. Note that p–values are not probabilities that H_0, in this case the 'only background' hypothesis, is true (Astone *et al.*, 2003).

Linnemann (2003) remarks that Poisson probability p–value estimates lead to overestimates of the significance since the uncertainties on the background are ignored.

3.5 Comparing threshold settings for source reliability

In order to restrain the rates of false source detections per field, a threshold on probabilities is commonly set according to the goal of a specific research. For instance, Freeman *et al.* (2002) have chosen an upper limit of 1 spurious detection per analysed *Chandra* field. This value corresponds to a false–positive probability threshold of 10^{-7}. The method developed by Freeman *et al.* (2002) is a wavelet–based source detection algorithm (WAVDETECT).

For the *XMM–Newton* serendipitous source catalogue, Watson *et al.* (2003) have chosen a detection likelihood $L = 10$, corresponding to $\approx 4\sigma$. L is given by $-\ln(1-P)$, where P is the probability of source detection obtained by a maximum likelihood method (Cruddace *et al.*, 1988). The selected likelihood threshold corresponds to the detection of < 1 spurious source per field. In any systematic investigation to source detection, the threshold level is a tradeoff between the detection power and false detections rate.

Comparison Following this idea, the Poisson probability p–value, equation (3.1), is compared to the Bayesian source probability $P_{\rm source}$, equation (2.33). Figures 3.1 and 3.2 compare the two statistics. In Fig. 3.1, the prior distribution of the source signal is chosen to be exponential, equation (2.20), where in Fig. 3.2, it is given by an inverse–Gamma function, equation (2.23).
Specifically, each plot of Figs 3.1 and 3.2 illustrates a relation between p_P (ordinate) and the background probability obtained with BPT (abscissa). The squares on each plot indicates the photon counts d chosen for calculating equation (3.1). The corresponding number counts are indicated on some of the squares. On the abscissa, the background probability is calculated as the complementary source probability provided by the Bayesian method $(1 - P_{\rm source})$. The value close to unity corresponds to a source probability, $P_{\rm source}$, which goes to zero, instead a value of 0.1 corresponds to 90% source probability and 0.01 to 99% source probability.

In Figs 3.1 and 3.2, panels $(a) - (c)$ show the relation between p_P and $(1 - P_{\rm source})$ for varying background amplitudes and source intensities. The plots are ordered with respect to increasing source intensities. Panels $(d) - (f)$ of Figs 3.1 and 3.2 display the same data but with fixed background value and varying source intensities. The background values increase from left to right.

Each plot shows a general tendency. For a given count number d, $P_{\rm source}$ and (1-p_P) increase with decreasing background intensity. However, $P_{\rm source}$ is more conservative. This is due to the dependency of $P_{\rm source}$ not only on the mean background intensity but also on the source intensity distribution. This dependency is expressed by the likelihood for the mixture model equation (2.17), that plays a central role for the estimation of the source probability equation (2.33).

An example of the different interpretations of source detection employing the two statistics is provided in Table 3.1. This example is taken from Fig. 3.1, panels (a) and (c). Illustrations A, B, C are derived from panel (a), while illustration D from panel (c). The mean source intensity in a field (λ) is 10 (A, B, C) and 1000 (D) times larger than the mean background intensity (b). *Illustration A*: For a mean background intensity of 0.1 count, 2 photon counts in a pixel are assigned with a $P_{\rm source}$ value of 0.97. Poisson statistics provides the probability of detecting 1 photon count or less equal to 0.995, stating that 5 over 10^3 pixels would show 2 or more photon counts due to Poisson random process. *Illustration B*: For a mean background value of 1.0 count, 2 photon counts in a pixel are characterized by a $P_{\rm source}$ value of 0.29. (1-p_P), instead, has a larger value of 0.74 and 26 over 10^2 pixels would show 2 or more photon counts due to background fluctuations.

Table 3.1: Bayesian source probability ($P_{\rm source}$) versus Poisson p–value (p_P).

	b (counts)	λ (counts)	d (counts)	$P_{\rm source}$	$1-p_P$	$1-P_{\rm source}$	p_P
A	0.1	1.0	2	0.97	0.995	0.03	0.005
B	1.0	10.0	2	0.29	0.74	0.71	0.26
C	10.0	100.0	2	0.01	0.0005	0.99	0.9995
D	1.0	1000.0	5	0.28	0.997	0.72	0.003

Note. This example shows the variation of $P_{\rm source}$ and p_P for detecting d photon counts in a pixel at three background levels. The mean source intensity distributed in the field is 10 and 1000 times larger than the background for illustrations from A to C and D, respectively. $P_{\rm source}$ represents the source probability for detecting 2 (A, B, C) or 5 (D) photon counts in a pixel according to the Bayesian technique. (1-p_P) is the classic cumulative distribution function (cdf). It provides the probability for detecting 1 (A, B, C) or 4 (D) photon counts or less in a pixel according to Poisson statistics, respectively. (1-$P_{\rm source}$) is the background probability estimated with the Bayesian method. p_P provides the probability for detecting 2 (A, B, C) or 5 (D) photon counts or more in a pixel according to Poisson statistics.

Both, the Bayesian solution and the Poisson p–value classify 2 photon counts in a pixel to belong to the background. However, the Bayesian solution is more conservative than Poisson p–value. *Illustration C*: When $b = 10$ counts, both statistics classify 2 photon counts in a pixel to belong to the background. *Illustration D*: For a mean background intensity of 1.0 count, the Bayesian analysis classifies 5 photon counts in a pixel to belong to the background ($P_{\rm source} = 0.28$), because the source intensity distributed in the field is 1000 times larger than the mean background intensity. Poisson statistics provides the probability of detecting 4 photon counts or less equal to 0.997, stating that 3 over 10^3 pixels would show 5 or more photon counts due to Poisson random process. In this illustration, the two statistics provide contrasting results.

In Fig. 3.3, the dependency of $P_{\rm source}$ on the source intensity distributed on a field is shown. $P_{\rm source}$ is drawn for a given number of photon counts in a pixel versus λ/b (panels $a-c$) and versus α (panels $d-f$) for fixed background values. The prior β is fixed at 0.5. In the abscissas the parameters λ/b and α are plotted in order to feature from faint to bright sources. The abscissas are drawn in logarithmic scale. For a given number of photon counts, the value of $P_{\rm source}$ varies with the source intensities expected in the astronomical image and with the background amplitude. $P_{\rm source}$ is drawn with different linestyles for given number of photon counts.

Let us consider the plot in panel (a) of Fig. 3.3, where the background has a value of 0.1 count. For 2 photon counts, $P_{\rm source}$ reaches a maximum where the mean source intensity in the field has values in the range $(1-5)$ counts. In this part of the curve, 2 photon

counts in a pixel are discriminated best from the background. Away from this range, the source probability decreases. For small λ/b values, $P_{\rm source}$ approaches 0.5 because source and background cannot be distinguished. For large λ/b values, $P_{\rm source}$ decreases since more sources with large intensities are expected relative to small intensities. Therefore, a signal with 2 counts is assigned to be background photons only.
$(1 - p_P)$ is calculated for the same values of background and photon counts as for $P_{\rm source}$. The linestyles and colours used correspond to the one employed for $P_{\rm source}$. $(1 - p_P)$ is constant, since it does not depend on the source intensities expected in the field. Its value for 2 photon counts (that is 0.995 from Table 3.1) is larger than the maximum of $P_{\rm source}$ (with a maximum value of 0.97 from Table 3.1). In general, $(1 - p_P)$ is larger than $P_{\rm source}$ for values of photon counts larger than the mean background intensity. If the values of the photon counts are lower than or equal to the mean background intensity, $(1 - p_P)$ is lower than the maximum of $P_{\rm source}$: See, for instance, panel (c) of Fig. 3.3 for a value of 8 photon counts.

Remarks on p–values versus BSS technique The comparison shows that it is not possible to calibrate p_P with $P_{\rm source}$ because of the intrinsic difference in the nature of the two statistics.

Poisson p–values are used to interpret background and sources, without including uncertainties on the background. P–values are one point estimate. Only, the null hypothesis is required for classification purposes.

The Bayesian method, instead, gives information about background and sources and their uncertainties. The BSS technique utilizes the full pdf for a predicted property, rather than simply its single scalar value as with p–values. Therefore, much more information is included in the BSS solution with respect to p–values. Threshold levels as p–values are not used in the BSS algorithm. The separation between background and sources occurs with probability distributions. The BSS technique has a built in statistical significance test, where H_0 and its alternative hypothesis are considered jointly in the likelihood for the mixture model through Bayes factors. The BSS algorithm includes a wider interpretation of background and sources with respect to Poisson p–values. The interpretation of the background model is defined by its smoothness. The source signal distributed on an image is encoded in probability distributions. Parameters describing the background model and the source signal distributed in the astronomical image are estimated from the data. The BSS technique is capable of classifying background and sources taking into account the intensities distributed in an image. Therefore, the BSS technique can adaptively select background and sources according to the properties of the analysed astronomical image. Discrepancies from the data to the model are properly accounted for and false positives in source detections are reduced. (The same effect is expected for false negatives, since both false positives and negatives are treated identically in one unique algorithm.) Last, with the BSS algorithm thresholds on source probability values can be set according to the application one is investigating. Interpretations of source probability values are given in Table 2.1. Such interpretations are used to reduce the number of false detections.

Remarks on false positives detected with the BSS technique Comparing the results shown in Figs 3.1 and 3.2, slightly different answers are arising for the two priors of the source signal. When the exponential prior is employed, fields with large intensities are less penalized by false positives caused by random Poisson noise than fields with source signal very close to the background amplitude. When the inverse–Gamma function prior is used, false positives' detections depend on the cutoff parameter a. This is because the cutoff parameter has an effect on faint sources. The same behaviour is expected on false positives in source detection. The exponential prior, instead, does not exclude small source intensities.

This result is not surprising, because the choice of the source signal prior pdf is crucial for source detection. For a reliable analysis, the source signal prior pdf chosen has to be as close as possible to the true one.

3.6 Summary

Fisher's approach to hypothesis testing employs p–values to assess the 'strength of evidence' against the null hypothesis. In Fisher's approach the argument of a probability is restricted to random variables and the truth of a probability can only be inferred indirectly. A statistic is chosen to find compatibility between a model and the observed data. The p–value expresses the probability of finding a result at least as extreme as the one obtained with the observed data, assuming that the null hypothesis is true. The significance level of a test is compared to the p–value with the result of rejecting or accepting H_0.

BPT allows one to compute the probability of two or more competing hypotheses on the basis of the only data available. Prior pdfs are assigned to all hypotheses. Bayes' theorem, eq. (2.4), is used to compute the posterior pdfs of the hypotheses given the observed data. Furthermore, the uncertainties due to the data and parameters describing the hypotheses are estimated and encoded in probability distributions.

The Poisson probability p–values are compared to the Bayesian source probability. The comparison allows one to demonstrate the intrinsic difference in the nature of the two statistics. In fact, the two statistics provide different interpretations to source detection.
Poisson p–values supply the Poisson probability of finding a certain number of photon counts (or larger) given a background value. Poisson p–values account only for H_0 and only false positives in source detection are addressed.
The Bayesian technique, instead, gives the (source) probability for detecting a certain number of photon counts given the information coming from the background, the source intensities distributed on the field and their errors. Both false positives and negatives are jointly addressed in the BSS technique. The number of false detections are drastically reduced with respect to p–values.

Finally, the two prior pdfs of the source signal provide different answers for the number of false positives in source detection. This is mainly due to the cutoff parameter in the inverse–Gamma function, that has an effect on the detection of faint sources and consequently also on false positives.

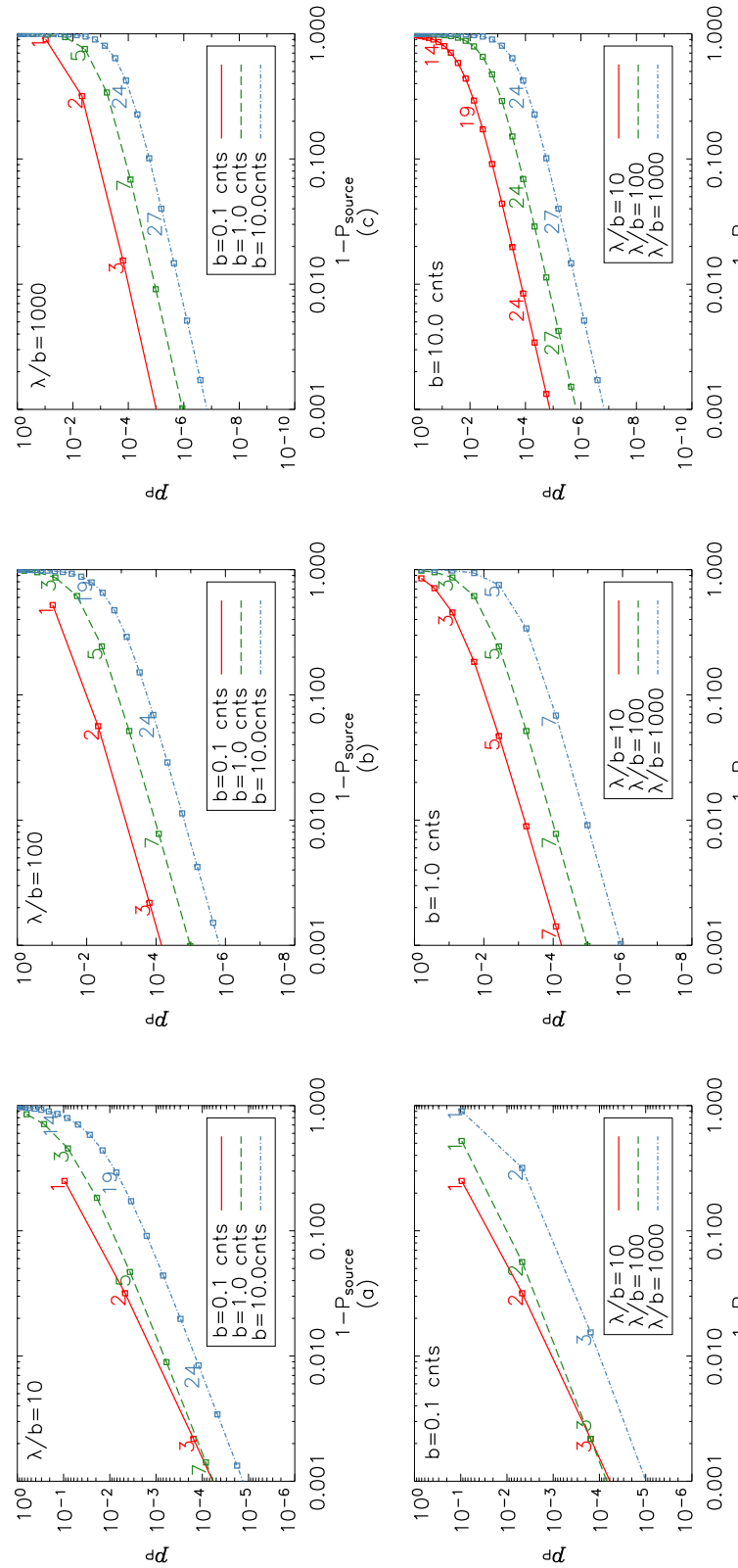

Figure 3.1: Classic hypothesis testing versus Bayesian approach. The prior distribution of the source signal is chosen to be *exponential*, equation (2.20). p_P and $P_{\rm source}$ are calculated for three background values, b. The squares represent the source number counts. Panels $(a)-(c)$ show the same data as in panels $(d)-(f)$, but with different ordering.

Figure 3.2: Same explanation as for Fig. 3.1, but employing the *inverse–Gamma function prior* pdf, equation (2.23).

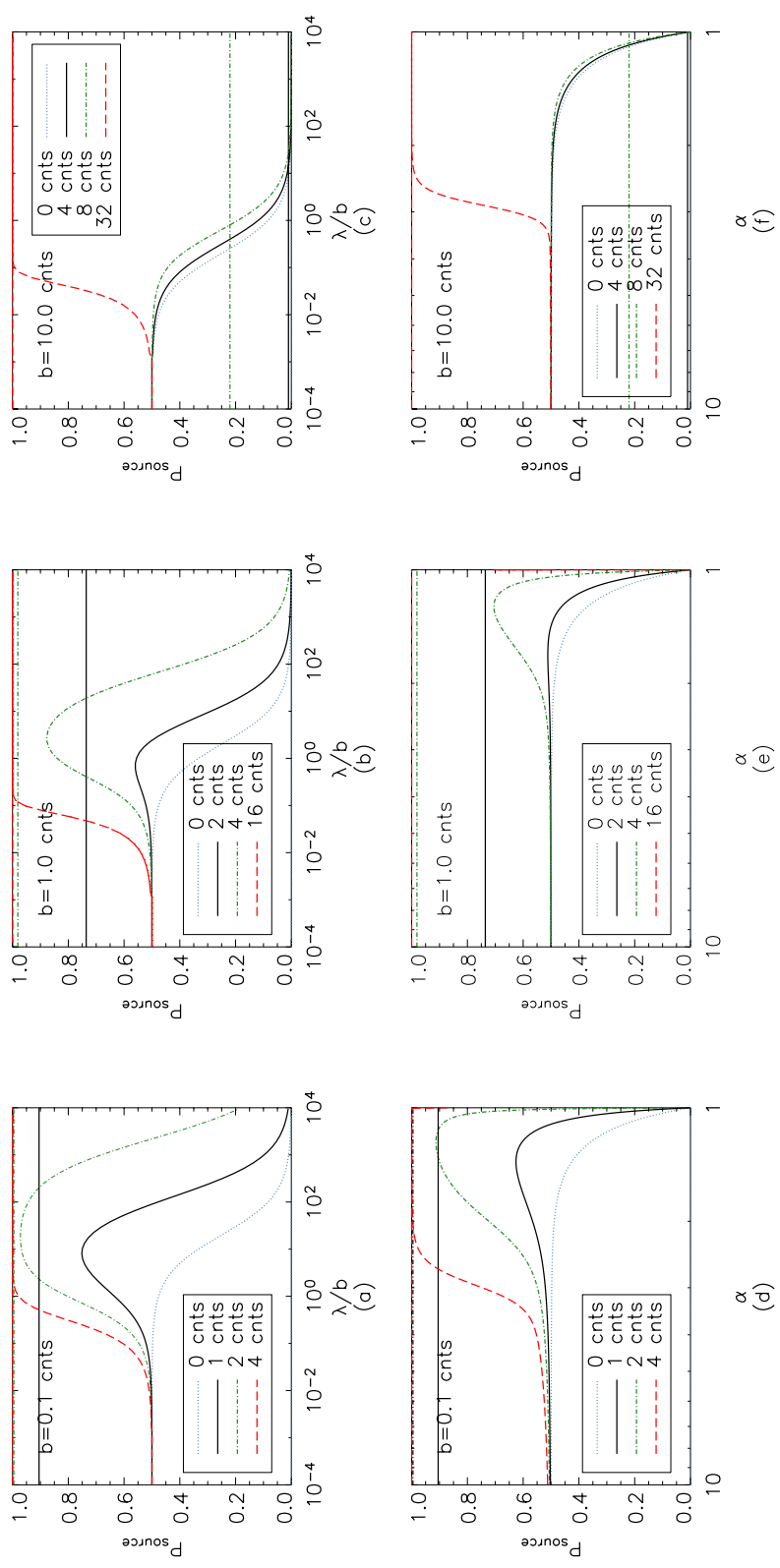

Figure 3.3: Dependency of the Bayesian source probability on the source intensities distributed on the field. Panels $(a) - (c)$: $P_{\rm source}$ for a given number of photon counts in a pixel versus λ/b (*exponential prior pdf*), the ratio between the mean source intensity and the background intensity in a field, are drawn for fixed background intensities. Panels $(d) - (f)$: $P_{\rm source}$ for a given number of photon counts in a pixel versus α, the slope of the *inverse–Gamma function prior pdf*, are drawn for fixed background intensities. In each plot $(1 - p_P)$ for a given background intensity and number of photon counts is superposed. See text for more details.

Chapter 4

Source characterization from simulated data

In this Chapter, artificial data are used for performance assessment of the BSS technique. Three simulations are analysed using the exponential and the inverse–Gamma function prior pdfs of the source signal. The data sets, described in Section 4.1, are meant to test the capabilities of the BSS method at varying background values. The idea is to cover different cases one encounters while surveying different sky regions or employing instruments of new and old generations. In Section 4.2, the outcome of the analysis on the three simulated data sets is reviewed. Last, a summary on the outcome of the analysis is provided in Section 4.3.

4.1 Simulations set–up

Three sets of simulated fields composed of 100 sources modelled on a constant background with added Poisson noise are generated. Groups of ten sources are characterized by the same number of photon counts but with different sizes. A logarithmic increment in photon counts per group is chosen ranging from 1 to 512. The shape of each source is characterized by a two–dimensional circular Gaussian. The source extensions, given by the Gaussian standard deviation, increase from 0.5 to 5.0 pixels in steps of 0.5. Sources are located equidistantly on a grid of 500×500 pixels. Initially, the simulated sources are located on the grid such that the source intensities increase on the abscissa, while the source extensions increase on the ordinate. Subsequently, the 100 sources are randomly permuted on the field. A background is added on each simulated field with values of 0.1, 1 and 10 counts respectively. A constant exposure is assumed. Note that by construction, a number of sources have intensities comparable to or lower than the background amplitude in the images. Consequently, not all sources can be recovered in every image.

In Fig. 4.1, the simulated data with small background are shown. Image (a) represents the simulated data with added Poisson noise. The image indicated with (b) is the simulated data without Poisson noise. It is placed for comparison: Sources close to or below the

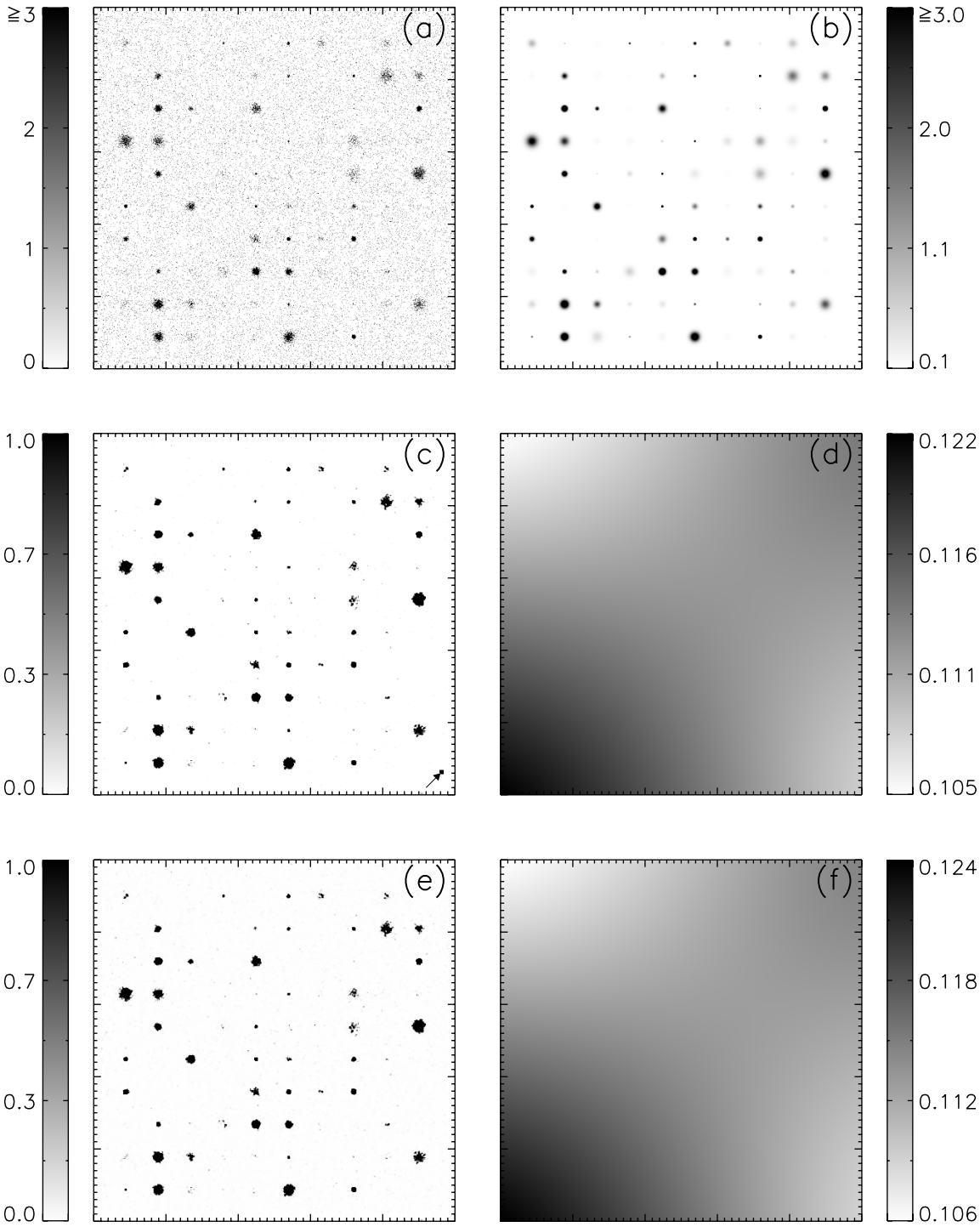

Figure 4.1: Panels $(a) - (b)$: simulated data with small background ($b = 0.1$ count): image with Poisson noise, image without Poisson noise, respectively. Panels $(c) - (d)$: results with *exponential prior* pdf: SPM with 3 pixels resolution and background map, respectively. Panels $(e) - (f)$: results with *inverse–Gamma function prior* pdf.

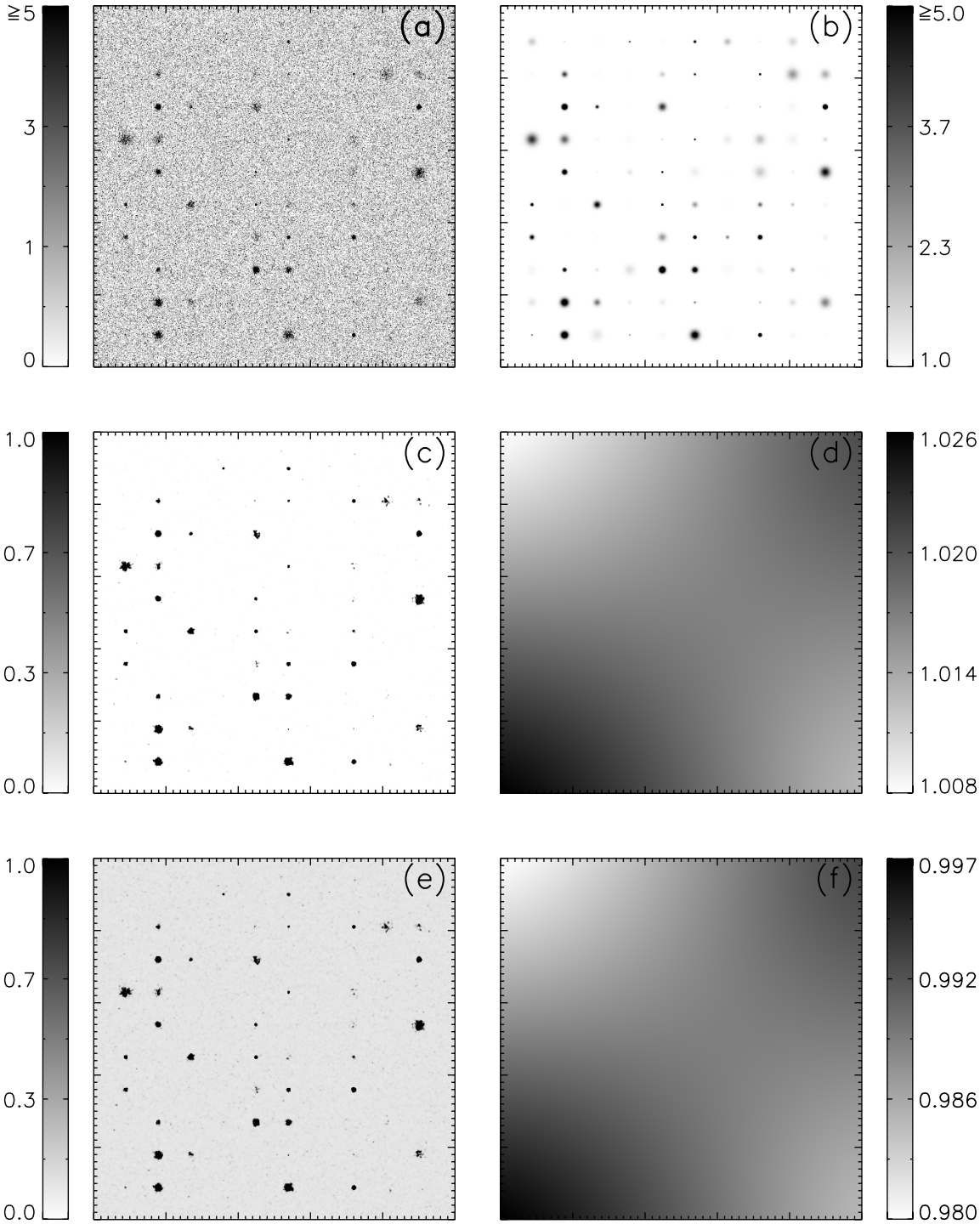

Figure 4.2: Simulated data with intermediate background ($b = 1$ count). Each panel has same explanation as given in Fig. 4.1.

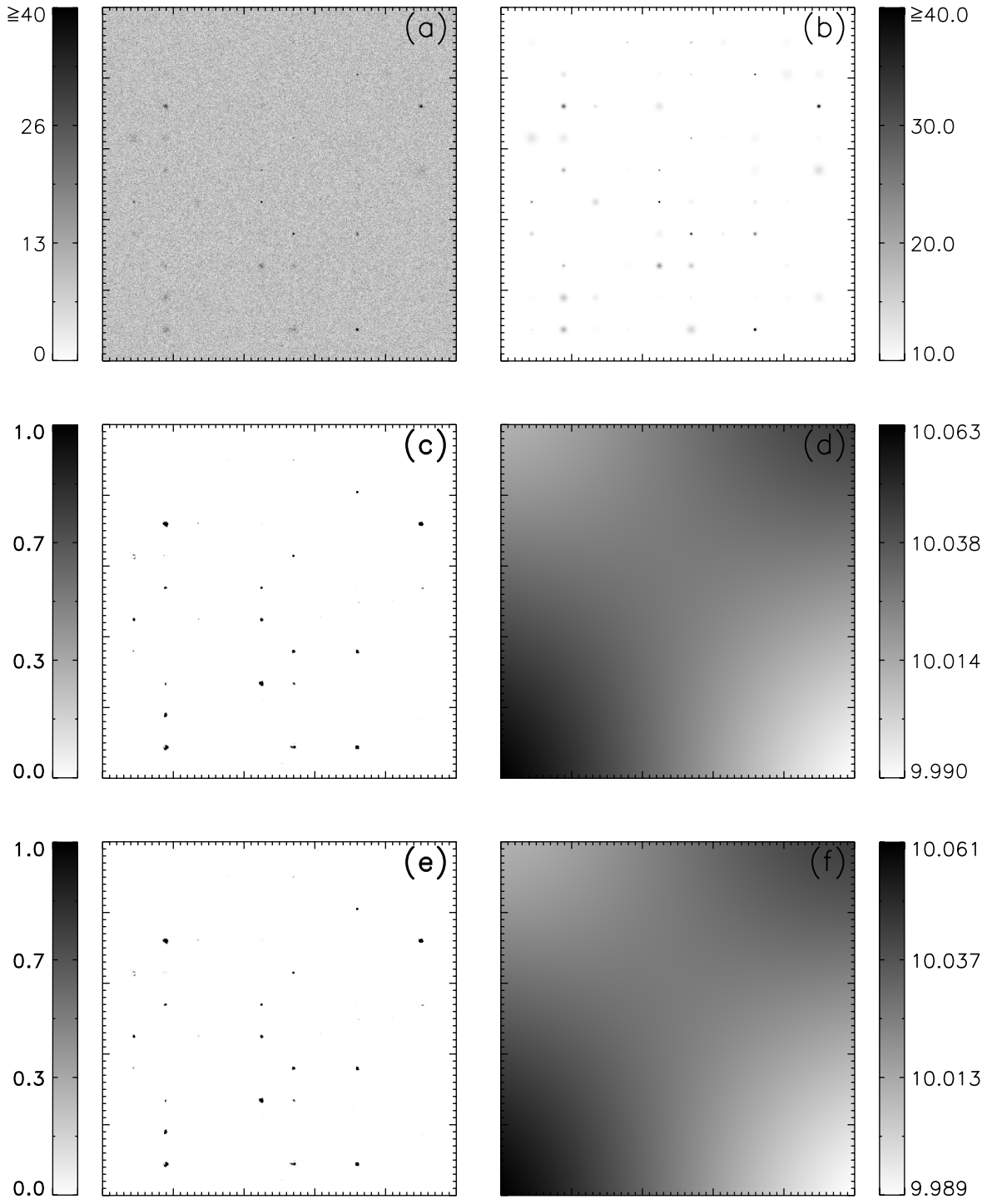

Figure 4.3: Simulated data with large background ($b = 10$ counts). Each panel has the same explanation as given in Fig. 4.1.

background amplitude become difficult or impossible to detect, even visually, when Poisson noise is added. The simulated data sets (a) and (b) are scaled in the range $(0-3)$ photon counts pixel^{-1} in order to enhance faint sources. The original scale of the simulated data with Poisson noise is $(0-317)$ photon counts pixel^{-1}. The simulated data without Poisson noise show counts pixel^{-1} in the range $(0.1-326.0)$.

The images representing the other two data sets for $b=1$ count (Fig. 4.2) and $b=10$ counts (Fig. 4.3) are similar to the one shown in Fig. 4.1. In these data sets, the number of sources to be separated from the background decreases with increasing background intensity. In Figs 4.2 and 4.3, panels $(a)-(b)$ are scaled in the range $(0-5)$ and $(0-40)$ photon counts pixel^{-1}, respectively. The original scales for the simulated data with intermediate and large backgrounds and added Poisson noise, panels (a), are $(0-334)$ and $(0-365)$ photon counts pixel^{-1}, respectively.

The cutoff parameter a is chosen to be 0.14 counts in the three simulated data sets. This is to show the effect of a when the background is smaller or larger than a.

4.2 Results

4.2.1 Background estimation

For the background modelling, only four pivots located at the field's corners are used. This choice is driven by the presence of a constant background. An optimization routine is used for maximizing the posterior pdf of having source contributions in pixels and pixel cells, eq. (2.18). The solution of the optimization routine is the pivots amplitude's estimates from which the background is calculated.

The three set–ups are designed such that half of the 100 simulated sources are characterized by ≤ 16 photon counts. Some of these simulated sources are too faint for being detected. These sources may contribute to the background model.

In Fig. 4.1, the estimated background maps are displayed when employing the exponential prior pdf (image d) and the inverse–Gamma function prior pdf (image f) for the simulated data with small background.

The two images show that the background intensity decreases slightly from the centre toward the upper left– and lower right–hand corners of about 5%, while toward the upper right– and lower left–hand corners increases up to $\sim 20\%$. The same trend is seen also in the estimated backgrounds with intermediate and large values (panels d and f in Figs 4.2 and 4.3), but with much smaller relative change. Evidently, the variations in the estimated background amplitudes are not introduced by the prior over the signal. Furthermore, these variations are not introduced by the selected pivots positions. If that were the case, then the same magnitude is expected at each image corner. Instead, these variations are an overall effect induced by the simulated sources. All simulated sources are randomly permuted. In the upper left– and lower right–hand corners are located numerous faint sources. In the lower left–hand corner many bright sources are clustered. The increment in the background intensity is due to the statistical distribution of the sources. This explains

why the same trend in background intensities is seen in all background models.

When employing the exponential prior pdf, the estimated background intensities are in agreement with the simulated background amplitudes. In the case of the inverse–Gamma function prior pdf, the estimated backgrounds are sensitive to the cutoff parameter a. When a is set larger than the mean background (i.e. simulated data with small background), the background is overestimated. The overestimated background is due to the presence of source signal below the cutoff parameter. Hence, no source intensities below 0.14 counts are allowed. It results that the estimated background is 40% larger than the simulated one. For simulated data with intermediate background value, the cutoff parameter a is fixed to a value lower than the simulated background. The background model is underestimated of only $\sim 1\%$ with respect to the simulated one. For simulated data with large background, the cutoff parameter a is much lower than the simulated mean background value. The estimated background is in agreement with the simulated one.

The background uncertainties are quite small compared with the background itself, on the order of few a percent. This effect holds because the background is estimated on the full field. However, the errors increase where the estimates deviate from the simulated background. The absolute uncertainties increase from the centre to the images' edge by a factor of ~ 4, independent to the prior pdf of the source signal used. In addition, when applying the inverse–Gamma function prior pdf, the errors are larger than those found using the exponential prior pdf. The absolute uncertainties on the estimated background amplitudes with the inverse–Gamma function prior pdf are few a percent larger than the ones obtained with the exponential prior pdf for the simulated data with small and intermediate background values. The absolute uncertainties on the estimated background intensities are, instead, very similar whether employing the exponential or the inverse–Gamma function prior pdfs for the simulated data with large background. This effect is due to the cutoff parameter.

4.2.2 Hyperparameter estimation

In Fig. 4.4 the contour plot in (λ, β) parameter space for the joint probability distribution is shown for the hyperparameters evaluated from the simulated data with small background. The contour levels indicate the credible regions, i.e. the locus of points of a constant probability which surrounds a region containing a specified probability in the joint probability distribution. The values of the estimated hyperparameters are: $\beta = (99.2 \pm 0.03)\%$, $\lambda = (3.68 \pm 0.1)$ counts. The estimated β value provides the information that only 0.8% of the pixels in the field contains sources. A similar answer is found with the other simulated data. The β value increases slightly at increasing background amplitudes. In fact, the number of pixels containing background only increases at increasing backgrounds. The λ value, instead, provides the mean source intensity in the field. The estimated value of λ increases with increasing background amplitudes because small intensities are assigned to be background. Hence, more bright sources and less faint sources are found at increasing backgrounds.

A test on the hyperparameter values is pursued with the simulated data set charac-

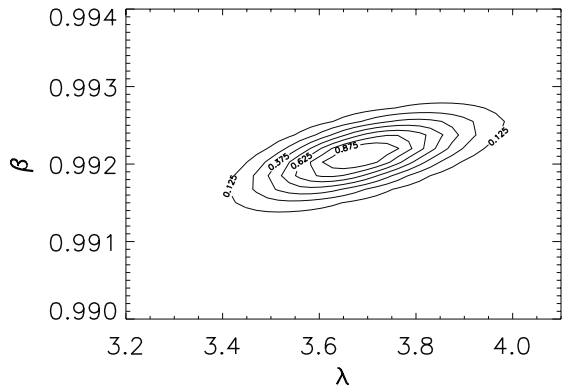

Figure 4.4: Contour plot of the posterior pdf for the hyperparameters, $p(\lambda, \beta|D)$, estimated from the simulated field with small background ($b = 0.1$ count) using the *exponential prior* pdf.

terized by small background. A value ≥ 2 photon counts per pixel is selected to indicate source detection [1]. The number of pixels with more than 1 counts are counted from the simulated field, resulting in ~ 3000 pixels with source signal in addition to the background. The respective percentage of pixels with expected signal is 1.2%. The parameter β indicates the number of pixels with background only, which has a value of 98.8% in this test. A mean source intensity value of ~ 3.5 counts is found. This quantity indicates the parameter λ. The values of each hyperparameter obtained within the test are close to the estimated ones (5% and 0.4% difference for the λ and β values are found, respectively). Realistic values of the estimated hyperparameters are found.

When employing the inverse–Gamma function prior pdf, the hyperparameter α is found with the smaller value in the simulated data with small background. The largest value of α is found in the simulated data with intermediate background. Large values of α indicates that more faint sources and less bright sources are expected in the field (Fig. 2.3). These results do not contradict our expectations on the hyperparameter estimates, since the cutoff parameter selects the source signal distribution at the faint end.

The true source signal distribution differs from both, the exponential and the inverse–Gamma functions. However, the employed models for the source signal distribution provide a realistic situation. The employed models are robust.

4.2.3 The components of the mixture model

In Fig. 4.5, the Poisson and the marginal Poisson distributions multiplied with their prior knowledge on the model are plotted over the normalized histogram of each simulated data set. The likelihoods are drawn for the exponential and the inverse–Gamma function prior

[1] The choice for ≥ 2 counts is justified by the components of the mixture model, see subsection 4.2.3

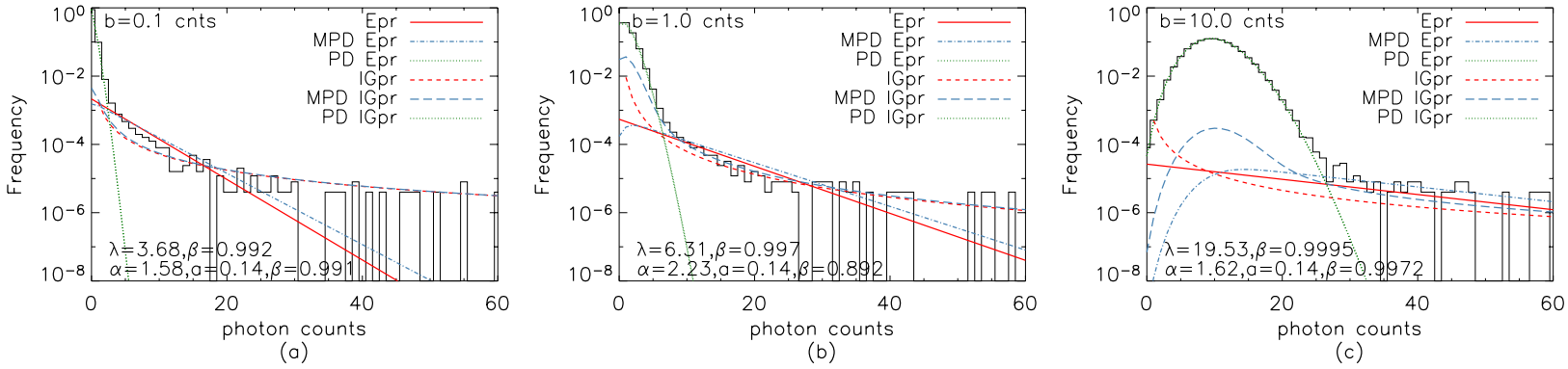

Figure 4.5: Normalized histograms of the simulated data with small (panel *a*), intermediate (panel *b*) and large (panel *c*) backgrounds are displayed. The exponential prior (*Epr*), inverse–Gamma function prior (*IGpr*) and related marginal Poisson (*MPD*) and Poisson (*PD*) distributions are plotted over the data. The ordinates are in logarithmic scale.

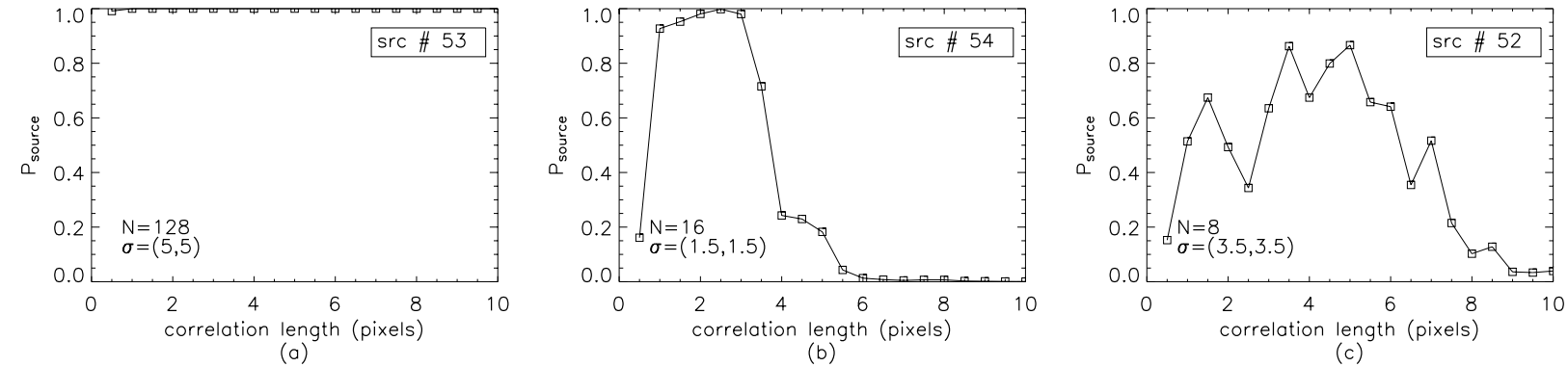

Figure 4.6: Examples of detected sources at several correlation lengths from simulated data with small background ($b = 0.1$ count), employing the *exponential prior* pdf. *src#* is the source detection sequence. N and σ provide the simulated source counts and extent in pixel units, respectively.

pdfs. The values of the estimated hyperparameters are shown in each image.

The exponential prior pdf is plotted over the histogram with a continuous line. The inverse–Gamma function prior pdf, instead, is plotted with a dashed line. The simulated data are neither distributed exponentially nor as an inverse–Gamma function. Hence, the prior pdfs of the source signal are not expected to fit the data exactly.

The marginal Poisson distribution weighted with $(1 - \beta)$ is drawn with a dash–dot line when employing the exponential prior pdf and with long dashes line in the case of the inverse–Gamma function prior pdf. The Poisson distribution (dotted line) is weighted with β for the exponential and the inverse–Gamma function prior pdfs. The same line style is used for the two Poisson distributions, because the two curves do not differ.

The intersection between the Poisson pdf and the marginal Poisson pdf indicates the source detection sensitivity. When employing the exponential prior pdf in the simulated data with small background (panel a), the exponential prior pdf enables the detection of fainter sources than the inverse–Gamma function prior pdf. This is expected since the cutoff parameter occurs at a value larger than the simulated mean background. Considering the simulated data with intermediate background (panel b), the detection is more sensitive to faint sources when employing the inverse–Gamma function prior pdf compared to the exponential prior pdf. In fact, the cutoff parameter allows to describe as source signal part of the simulated background amplitude. Note that the background is still modelled by the data and the identification of sources occurs only when $P_{\rm source}$ is large (i.e., $\gg 50\%$). For the simulated data with large background (panel c), the same sensitivity in source detection is expected when employing the two priors over the signal distribution.

4.2.4 Source probability maps

The box filter method with a circle is used in the three simulations for the multiresolution analysis. Examples of SPMs are shown in Figs 4.1, 4.2 and 4.3 for the simulated data with small, intermediate and large backgrounds, respectively. Images (c) and (e) are obtained employing the exponential and the inverse–Gamma function prior pdfs, respectively. These images represent the probability of having source contributions in pixel cells with a resolution of 1.5 pixels. At this resolution a pixel cell is composed by 9 pixels. A pixel cell with a correlation radius of 1.5 pixels is drawn in the lower right–hand corner of image (c) in Fig. 4.1. It is indicated with an arrow.

The sensitivity in source detection slightly varies with the prior pdf of the source signal employed. In the case of the inverse–Gamma function, the cutoff parameter have important implications, as already discussed throughout this Chapter. For instance, in Fig. 4.2, panel (e), the source probability map does not contain pixels with 100% probability of detecting background only. This is due to the cutoff parameter. In this simulated data set, the cutoff parameter is selected such that part of the source signal is described at the background amplitudes. Correspondingly, the background map in panel (f) of Fig. 4.2 is slightly underestimated: The percentage of difference varies only in the range $(0.3 - 2)\%$.

The multiresolution technique provides an analysis of source probabilities variation with correlation length and of source features of the detected sources.

The source probabilities variation allows one to analyse the source probability changes at different correlation length (Fig. 4.6). Different behaviours are found for bright and faint source detections. Panel (a) of Fig. 4.6 shows that the probabilities of bright sources do not vary significantly at decreasing resolutions because of the source brightness relatively to the small background value ($b = 0.1$ count). Faint sources, instead, are detected at decreasing resolutions (panel b, Fig. 4.6). The source size (or extent) of faint sources is found within the correlation length at which approximately the maximum of the source probability is reached. For increasing correlation length, the source probability decreases, because the difference between background and source signals is low. Last, source probabilities variation may provide hints on sources close to the background amplitude, as shown in panel (c), Fig. 4.6.

SPMs enable the analysis of source features. In Fig. 4.7, the photon count image and the SPMs of a bright extended source are displayed. The source probabilities variation for this source is shown in panel (a) of Fig. 4.6. This source is detected with the largest source probability (~ 1) at 2.5 pixels resolution. At this resolution the source is detected as one unique object, as given by the simulation. This object, however, is simulated as circular symmetric. Due to statistical fluctuations, source counts are grouped and the simulated geometric symmetry is lost. At correlation lengths smaller than 2.5 pixels, the BSS technique detects the data as they appear because of statistical fluctuations. At correlation lengths larger than 2.5 pixels, one unique object and its substructures are detected. In an astronomical observation, more information is needed to know if the detection represents an individual object or an object with substructures. Secondly, the maximum in source probability is reached at a correlation length that is smaller than the source size. This is due to the source brightness relatively to the small background value ($b = 0.1$ count). Within the range of resolutions studied, the source probability is constant at correlation lengths larger than 2.5 pixels.

This example shows that the multiresolution technique combined with the BSS method is particularly appropriate for the search of sources, independent to their morphologies. Statistical fluctuations may corrupt the data, but the BSS technique still provides a robust detection of these sources. This aspect of the technique is very important for real data since the majority of extended sources are not spherically symmetric.

4.2.5 Comparison between estimated and simulated source parameters

Source parameters and their uncertainties are derived as described in Section 2.3. Sources are catalogued when a probability larger than 50% is reached at least in one of the SPMs. A value of $P_{\text{source}} = 50\%$ does not provide a clear detection of a source. The explanations of the different threshold levels are supplied in Table 2.1. A threshold of 50% is chosen for these simulated data sets in order to clarify the different interpretations.

The parameters of bright sources are precisely estimated. In Fig. 4.7, an example of detection of a bright extended source employing SPMs in the multiresolution tech-

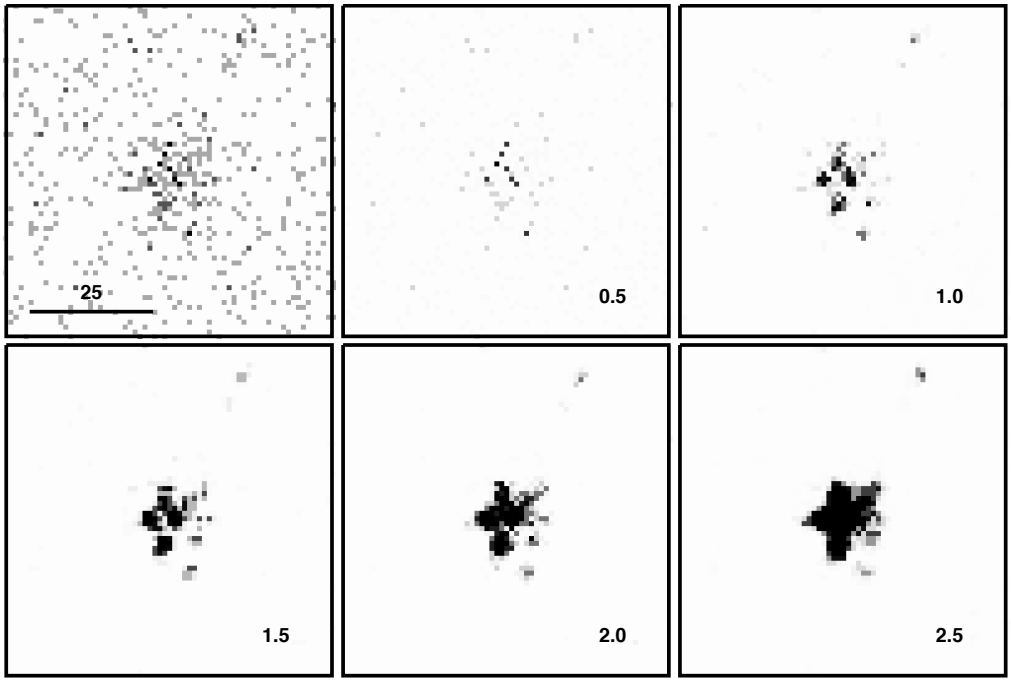

Figure 4.7: The upper left–hand image is a zoom in of the photon count image (panel a, Fig. 4.1) on a simulated source located at $(x, y) = (360, 270)$. The width of the photon count image is 65 pixels. The following images are SPMs at decreasing resolutions. The correlation length of each SPM is written on the lower right–hand corner of each image in pixel units.

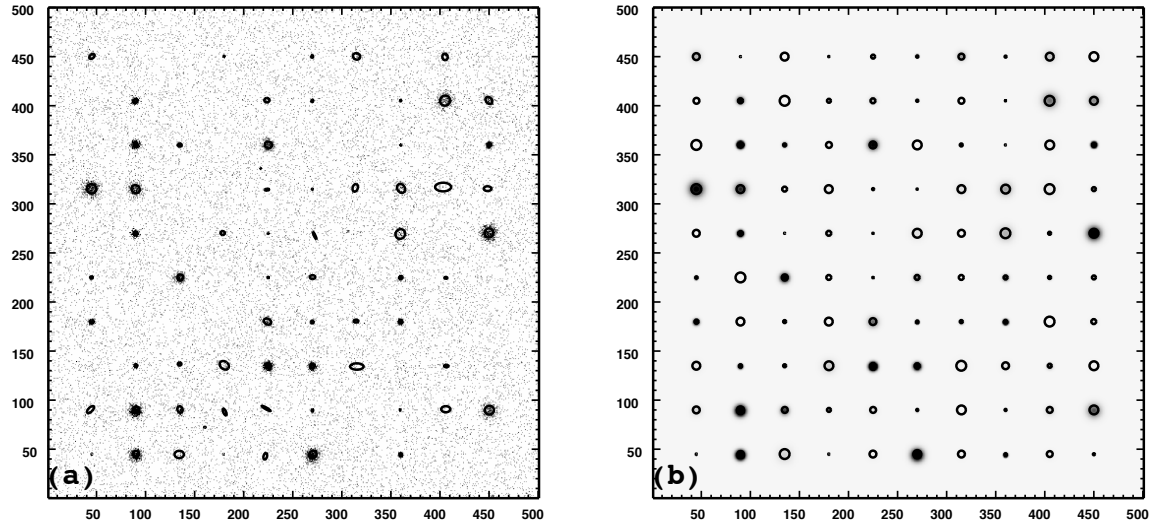

Figure 4.8: Panels (*a*)-(*b*): simulated data with small background ($b = 0.1$ count) with and without Poisson noise, respectively, and scaled in the range (0-3) counts. The catalogue obtained employing the *exponential prior* pdf (*a*) and the shapes of the region of the simulated sources (*b*) are superposed.

nique is given. The true parameters of this source are: 128 photon counts, (σ_x,σ_y)=(5,5) pixels, (x,y)=(360,270) in pixel units. The estimated parameters of this source are: (129.79$\pm$23.70) net source counts, (σ_x,σ_y)=(4.92$\pm$0.67,4.96$\pm$0.71) pixels, (x,y)=(359.57$\pm$ 0.92,269.29 $\pm$ 0.98) [pixel]. Instead, the effect of background fluctuations on faint source estimates can be quite pronounced.

In Fig. 4.8, an example of the estimated source positions and shape on the simulated data with small background is provided, using the exponential prior pdf. The errors on the estimated parameters are not considered in this plot. Some of the detected faint sources look uncentred and distorted. Four false positives in source detection are found. The simulated data without Poisson noise with the simulated source shapes superimposed are shown for comparison.

Table 4.1 reports the number of detected sources for each simulation. Different columns are used for accounting true detections and false positives separately at different source probabilities threshold values. The number of detected sources employing the inverse–Gamma function prior pdf is larger with respect to the exponential prior pdf case only when the cutoff parameter is set lower than the mean background amplitude.

In Fig. 4.9, the estimated source counts are related to the correlation length where the maximum of $P_{\rm source}$ occurs (panels *a* and *c*) and their source probability (panels *b* and *d*) for the simulated data with small background. These are log–linear plots. The results using the exponential and the inverse–Gamma function prior pdfs are shown in panels (*a*) and (*b*) and in panels (*c*) and (*d*), respectively. The asterisks indicate true sources, while the squares show spurious detections.

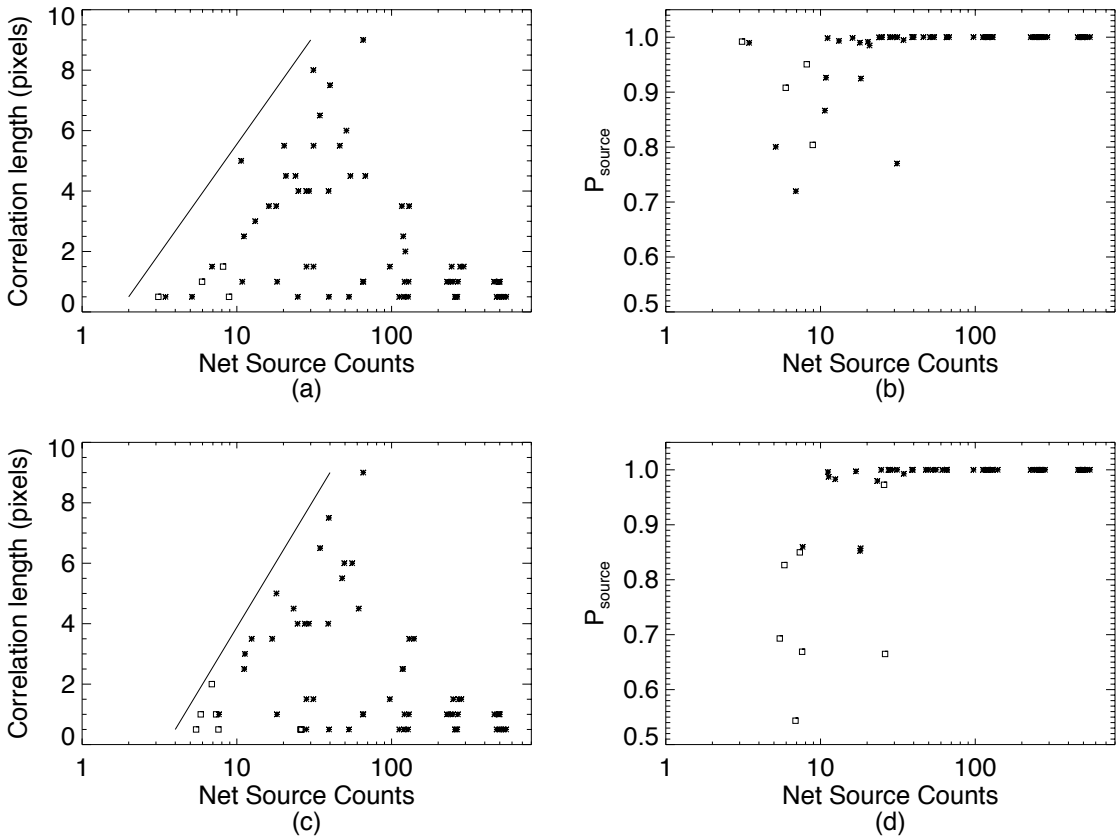

Figure 4.9: Results on simulated data with small background ($b = 0.1$ count) employing the *exponential prior* pdf (panels a and b) and the *inverse–Gamma function prior* pdf (panels c and d). Panels (a) and (c): correlation length in pixel units versus the net source counts. Panels (b) and (d): source probability versus net source counts. Sources matched with the simulated input catalogue are indicated with an asterisk. A square indicates false positives in source detection.

Table 4.1: Source detections on simulated data employing different prior pdfs of the source signal.

Simulated background	Prior pdf	≥ 50% True	≥ 50% False	≥ 90% True	≥ 90% False	≥ 99% True	≥ 99% False	≥ 99.9% True	≥ 99.9% False
0.1	Epr	64	4	60	3	57	1	52	0
	IGpr	57	7	54	1	52	0	49	0
1.0	Epr	41	6	41	3	39	0	38	0
	IGpr	42	10	42	2	40	0	37	0
10.0	Epr	25	0	24	0	22	0	22	0
	IGpr	26	2	26	2	26	2	26	2

Note. The background amplitudes of the simulated data are reported in counts pixel^{-1}. *Epr* and *IGpr* have same meaning as given in Fig. 4.5. The terms 'True' and 'False' provide the number of detected sources matched and not matched with the simulations, respectively. The number of detected sources is listed when $P_{\rm source}$ is larger then 50%, 90%, 99% and 99.9%. See Table 2.1 for the meaning of these threshold values.

The plots on panels (a) and (c) show source detections at different correlation lengths, that are resulting from the multiresolution analysis. In both plots, a line is drawn only with the purpose to guide the eye. Left to the line – sources are not detected, because very faint objects are not distinguished from the background amplitude. Right to the line – sources are found. Very faint sources with few photon counts (≤ 10) are resolved by small correlation lengths, indicating that these sources are detected when their sizes are small (within 3 pixels). In the range $(10 - 100)$ net source counts, sources are detected at decreasing resolutions. The multiresolution analysis detects efficiently sources with increasing sizes (and therefore with decreasing brightness) at increasing correlation lengths. Bright sources do not require large correlation lengths for being detected. Plots on panels (a) and (c) show that the multiresolution analysis is a robust and efficient technique for the detection of faint and extended sources.

The plots in panels (b) and (d) of Fig. 4.9 provide evidence for source selections according to their probabilities. Bright sources are all characterized by probabilities larger than 99.9%. Faint point–like sources have probabilities larger than 97%. Faint extended sources are represented by a wider range in source probability. These plots show that the detection of faint sources may be spoiled by false positives in source detection, especially for probabilities lower than 99%.

Note that the effect of the cutoff parameter a on source detection is visible in panels (c) and (d). In this example, the value of a is chosen larger than the simulated background amplitude. Hence, the inverse–Gamma function prior pdf does not allow to detect sources

as faint as the exponential prior pdf.

In Fig. 4.10, the relation between the simulated and the estimated source parameters is shown. Good estimates in source parameters are achieved. The estimated net source counts errors and source size errors can be large for faint sources.

In Fig. 4.11 a summary on the analysis of all the detected sources employing the exponential prior and the inverse–Gamma function prior pdfs on the three simulated data sets is provided. Each plot in Fig. 4.11 is used to check the reliability of the BSS technique. The plots in panels (a) and (c) show the difference between estimated and simulated net source counts, normalized with the estimated errors (residuals), versus the source probability of the merged data. Within these simulations, more than 85% of all detections occurred with probability larger than 99%, when employing one or the other prior pdf of the source intensities. The images in panels (b) and (d) are semilog plots of the residuals versus the simulated net source counts of $\sim 99\%$ true sources detected in the three simulations. When employing the exponential prior pdf, the values of two sources, detected in the simulated data with large background, are outside the selected y range. The estimated parameters of these two sources, missing from panel (b), are corrupted by background fluctuations. These two detections are included in the analysis of verification with existing algorithms (Chapter 5). When using the inverse–Gamma function prior pdf, the values of two sources are also found outside the selected y range. These two sources, missing from panel (d), are detected on the simulated data with intermediate and large background values. Their residuals values are about -15. The extreme values of these two sources are, as before, due to background fluctuations, because the optimization routine found an optimum for all sources. Comparing panels (b) and (d), the exponential prior pdf allows for the detection of fainter sources since the simulated data with small background are processed employing the inverse–Gamma function prior pdf with the cutoff parameter fixed to a larger value with respect to the background amplitude. Hence, faint sources composed by less than 8 counts are not detected with the inverse-Gamma function prior pdf with the chosen cutoff parameter.

The residuals are normally distributed, as expected. They are located symmetrically around zero. At the faint end, the results are only limited by the small number of simulated faint detectable sources. Faint and bright sources are equally well detected.

4.2.6 False positives

Until now, the detections that have counterparts with the simulated data have been discussed. The detection of false positives are now considered.

In Table 4.1 the number of detected false positives are listed for each simulation. At 50% probability threshold more false positives are found with the inverse–Gamma function prior compared to the exponential one. At a 90% source probability threshold, the analyses with the two prior pdfs provide similar results. True detections are strongly separated from statistical fluctuations for source probability values larger than 99%. Source probability values larger than 99.9% separate very strongly true detections from false positives.

When employing the inverse–Gamma function prior pdf, the number of false positives

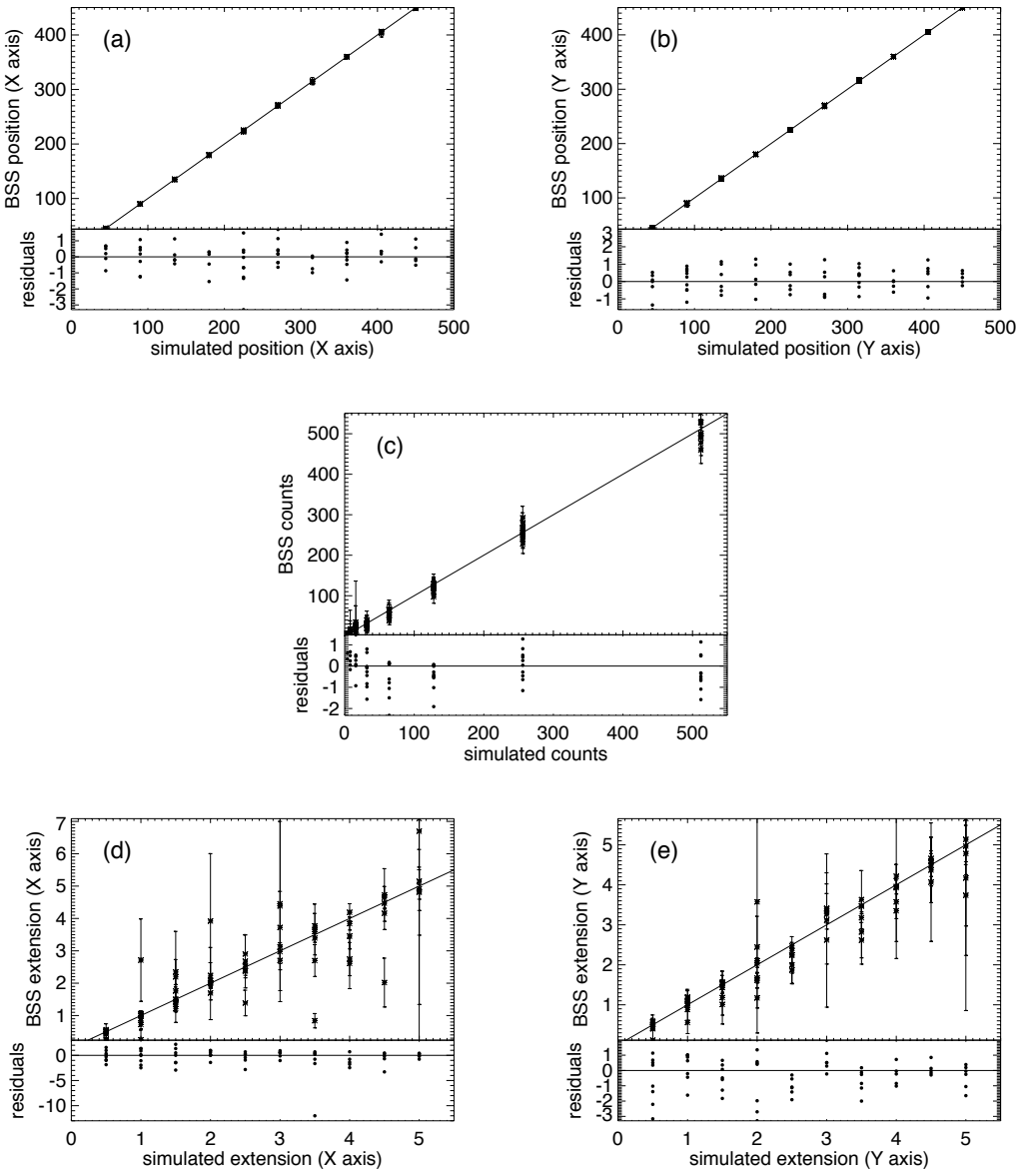

Figure 4.10: Relation between the simulated sources with small background ($b = 0.1$ count) and the measured sources as in output from the processing with the developed method employing the *exponential prior* pdf. Panels (a) and (b) show the comparison of the measured source positions with the simulated input positions on the x–axis and on the y–axis. Panel (c) displays the relation of the measured source photon counts versus the simulated intensities. A comparison of the estimated source extensions (i.e., source size) $\sigma_{\rm x}$ and $\sigma_{\rm y}$ with the input source extensions are displayed in panels (d) and (e). The errors estimated for the source parameters are superposed. The error bars on the estimated values denote the 68% confidence limit of the corresponding posterior distribution. The lower panel in each image shows the residuals.

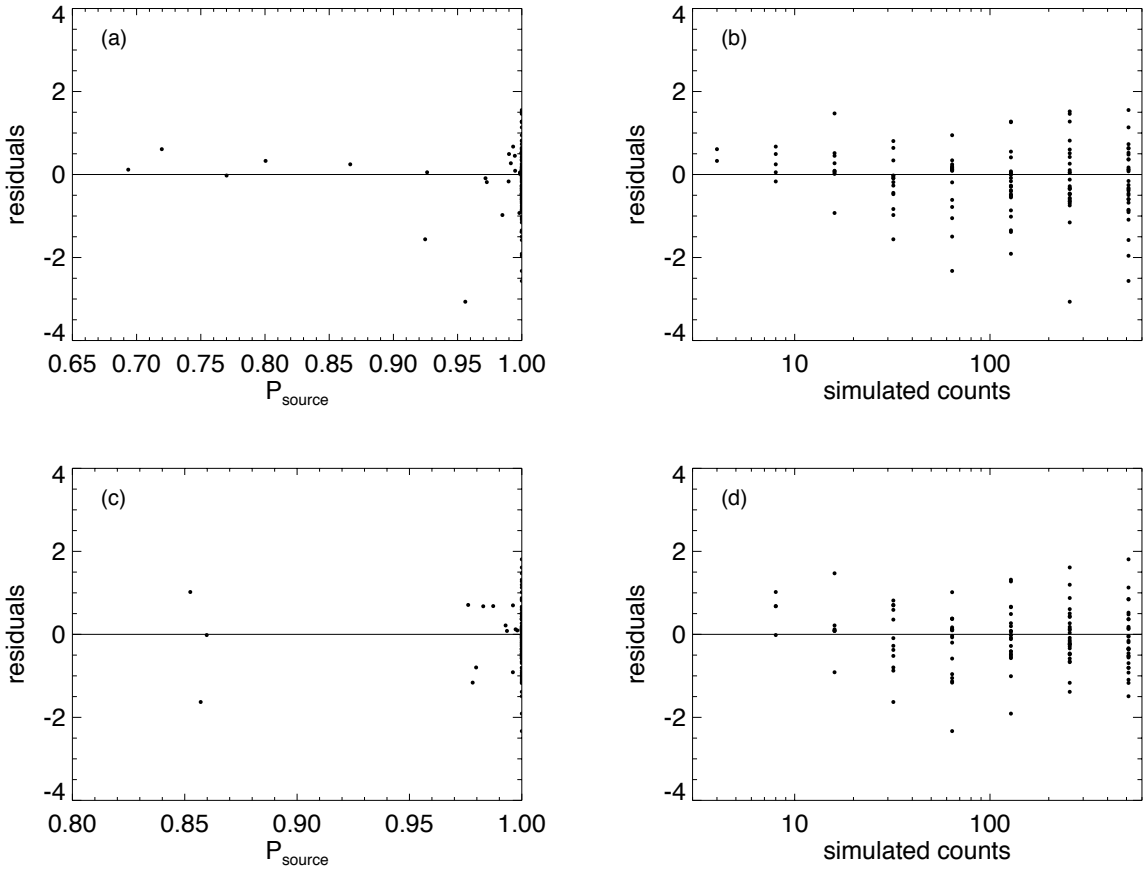

Figure 4.11: Merged information from three simulated data sets of the detected sources employing the *exponential prior* pdf (panels *a–b*) and the *inverse–Gamma function prior* pdf (panels *c–d*). Panels (*a*) and (*c*): difference between estimated and simulated net source counts normalized by the errors on the estimated net source counts versus source probability. Panels (*b*) and (*d*): difference between estimated and simulated net source counts normalized by the errors on the estimated net source counts versus the simulated counts.

is sensitive to the cutoff parameter. Less false positives are found when a is set larger than the background, because it reduces the number of detectable faint sources. It may be worth noting that even when the cutoff parameter is set larger than the background, a probability threshold $\geq 90\%$ has to be considered (see Fig. 4.9 for more details).

False positives in source detections show large errors in their estimated parameters. The source probability variations with respect to the correlation length of source detection and the source features analyses in the multiresolution technique provide hints of ambiguous detections. However, as all methods, the BSS approach is limited by statistics. Spurious detections can never be ruled out completely.

4.2.7 Choice of the prior pdf of the source signal

The big difference between the two prior pdfs of the source signal follows on from one prior pdf having one parameter and the other pdf having two.

The parameter λ, indicating the mean intensity in an astronomical image, introduced with the exponential prior pdf is estimated from the data.

The parameter α, that is the shape parameter of the power–law, given by the inverse–Gamma function prior pdf is also estimated from the data. Instead the cutoff parameter a is selected to a small value such that the inverse–Gamma function prior pdf behaves as a power–law. Astronomical images can be characterized by a small background. It results that a can be chosen from a number of alternatives, ranging from values that are above or below the background amplitude. The choice of a implies a selection on the detectable sources: sources whose intensity is lower than a are not detected; sources close to the background amplitude are detected when a is set below the background amplitude.

On real data much more prior information for the cutoff parameter is needed. The inverse–Gamma function prior pdf can be employed if a mean value of the background amplitude is already known from previous analyses.

The exponential prior pdf is preferable over the inverse-Gamma function prior pdf, since no predefined values are incorporated. This is also supported by the results obtained with the simulated data. However, the inverse-Gamma function prior pdf is a more suited model to fit the data and it has potentials for improving the detections of faint objects.

One way to improve the knowledge acquired with the inverse-Gamma function prior pdf is by the estimation of the cutoff parameter from the data. This change in the BSS algorithm is not straightforward and MCMC algorithms have to be employed. This task exceeds the scope of this thesis.

4.3 Summary

Simulated data are employed to assess the properties of the BSS technique. The estimated background and source probabilities depend on the prior information chosen. A successful separation of background and sources must depend on the criteria which define *background*. Structures beyond the defined properties of the background model are, therefore, assigned

to be sources. There is no sensible background-source separation without defining a model for the object *background*. Additionally, prior information on source intensity distributions helps to sort data, which are marginally consistent with the background model, into background or source. Therefore, prior knowledge on the background model as well as on the source intensity distribution function is crucial for successful background-source separation.

For the background model a two–dimensional TPS representation was chosen. It is flexible enough to reconstruct any spatial structure in the background rate distribution. The parameters are the number, position and amplitudes of the spline supporting points. Any other background model capable to quantify structures which should be assigned to background can be used as well.

For the prior distribution of the source intensities the exponential and the inverse–Gamma function are used for illustrations. For both distributions the source probability can be given analytically. The hyperparameters of both distributions can either be chosen in advance to describe known source intensity properties or can be estimated from the data. If they are estimated from the data simultaneously with the background parameters, properties of the source intensity distribution can be derived, but at the expense of larger estimation uncertainties. It is important to note that the performance of the BSS method increases with the quality of prior information employed for the source intensity distribution. The prior distribution of the source intensities determines the general behaviour of the sources in the fov and the hyperparameters are useful for fine–tuning.

The aim of detecting faint sources competes with the omnipresent detection of false positives. The suppression of false positives depends both on the expedient choice of prior information and on the level of detection probability accepted for source identification. Compared to, e.g., p-values the BSS technique is rather conservative in estimating source probabilities. Therefore, a probability threshold of 99% is mostly effective to suppress false positives.

The estimated background rates are consistent with the simulated ones. Crowded areas with regions of marginally detectable sources might increase the background rate accordingly.

The SPMs at different correlation lengths are an important feature of the technique. The multiresolution analysis allows one to detect fine structures of the sources.

The source parameters are well determined. Their residuals are normally distributed. In Chapter 5 it will be shown that the BSS technique performs better than frequently used techniques. Naturally, the estimation uncertainties of parameters for faint sources are large due to the propagation of the background uncertainty.

Chapter 5

Verification with existing algorithms

In this Chapter the source detection results from the developed Bayesian technique are compared with other source detection methods. In Section 5.1, actual source detection techniques implemented within the Poisson regime are reviewed. In Section 5.2, further complications encountered by the available techniques applied to X–ray surveys are addressed. The BSS results on the three simulated data sets, described in Chapter 4, are compared with the outcome from the WAVDETECT algorithm in Section 5.3. Finally, a summary of this Chapter is provided in Section 5.4.

5.1 Standard techniques

The typical observations in high–energy astrophysics feature photon fluxes in the ranges from 0.1 to a few photons per pixel. The detection and characterization of faint point–like and extended sources is a challenging task. A large sample of faint sources, e.g. AGNs, clusters or groups of galaxies and extragalactic SNRs, is required to improve the knowledge about the evolution and the origin of the Cosmos. Nonetheless, source detection algorithms in the Poisson regime suffer from the pervasive presence of (random) background fluctuations. Often, compromises for the treatment of the background estimation are taken.

Traditionally, source detection methods subtract an estimated background from the data. The background is measured on an area around the presumed detected source or on an area away from the sources, which is presumed to contain only background. Inappropriate subtraction can lead to artificial structures in the desired image. If too much is subtracted, the data constraints cannot be fulfilled by a positive image (von der Linden *et al.*, 1997). Other side–effects of this technique are the loss of faint sources during background subtraction and the statistics is not preserved. The subtraction of a background from the photon count data produces a new data set that is not anymore Poisson distributed (Skellam, 1946).

Often, a photon density distribution is used to estimate a cutoff value for describing a global background (background thresholding) or a locally determined background is used

in order to flag possibly significant density enhancements in the photon distribution (peak finding).

An example of a source detection method employing the simple background thresholding is given by the technique of Bertin and Arnouts (1996) in the SExtractor software package. In the work of Bertin and Arnouts (1996), the whole image is subdivided into a regular grid of background cells each, e.g., 200×200 pixels on the side, on which the background is estimated using $k-\sigma$ clipping for each cell. The $k-\sigma$ clipping is used to suppress the influence from outliers (i.e. sources) from the background signal. The local background histogram is clipped iteratively until convergence at $\pm 3\sigma$ around its median. The mean of the clipped histogram is used as a value for the local background in non–crowded fields, otherwise the mode is employed. In a further step, a bicubic–spline is used to interpolate from the background grid to the image pixels in order to estimate the local background. Although a median filter is applied to suppress possible local overestimations due to bright stars, the background is inevitably overestimated. The estimated background map is then subtracted from the astronomical image. Faint sources are lost.

Other techniques (e.g., Gioia *et al.* 1990; Freeman *et al.* 2002) employ a locally determined background to flag possible sources. In a second step, count enhancements above the local background are removed from the image. In a third step, the background is estimated in the censored image. Consequently, the estimated background amplitude can be too high, because of faint sources in the locally determined background. These techniques are described in the next Sections.

Methods, that employ background thresholding and/or peak finding, show very low sensitivity for variations in the background estimation. These methods do not properly account for the detection of those very extended sources, whose characteristic size is several times larger than the instrumental PSF and for which the background may vary significantly. Moreover, an inadequate estimation of the background can lead to a large number of false positives in source detection. Faint point–like objects may get lost.

A brief review on few conventional source detection methods for Poisson data, frequently used for the search of faint point–like and extended sources, is given. A short outlook of the following detection procedures is provided: sliding window technique and ML; WT techniques; Voronoi tessellation and percolation (VTP) (Ebeling and Wiedenmann, 1993); growth curve analysis (GCA) (Böhringer *et al.*, 2000).

5.1.1 Sliding window technique and Maximum Likelihood

The sliding window technique (see, e.g., Harnden *et al.* 1984; Gioia *et al.* 1990) and the ML (see, e.g., Cruddace *et al.* 1988; Hasinger *et al.* 1994; Boese and Doebereiner 2001) procedures are the standard detection algorithm of the SASS processing for *ROSAT* data (Voges *et al.*, 1999). Both procedures address mainly the analysis of point sources. SASS is also included in *Chandra* and XMM–*Newton* data analysis tools. In Chapter 6, some applications of the BSS technique on *ROSAT* data and comparisons of SASS and BSS outcomes are shown.

The sliding window technique searches locally for count enhancements relative to the

intensity in a surrounding area defining the background intensity. The source signal is derived from the pixel values inside the cell. In multiple steps the window width is changed to allow for the detection of extended sources. But extended sources, blended sources in crowded fields and sources near the detection limit may get lost (Voges *et al.*, 1999). One reason is due to the local estimation of the background in a small region around the sliding window which may provide only poor signal-to-noise ratios. In a following step, circular regions around the detected objects are removed from the image to form the so–called 'cheese' image. A coarser binning is applied to the 'cheese' image (Boese and Doebereiner, 2001). The background count distribution is often modelled with two perpendicular unidimensional cubic–splines from the resulting binned image. A consequence of the coarser binning is that no abrupt variations in the background are modelled (Boese and Doebereiner, 2001). Pitfalls due to the employed class of bivariate splines are that the background model is not stable along the whole field and the background model shows steep slopes towards the field edge: See Boese (2004), Fig. 4 and text related, for more details. The oscillatory behaviour of the SASS background model produces regions with too large or too small values (with respect to the true ones), leading to an increasing number of false positives in source detection and problems in source photometry.

The original image is investigated once more with the sliding window technique employing the background map. A second source list is created and merged with the original source list. These lists provide the input sources for the ML algorithm. The ML algorithm computes the source properties like position, flux, angular extent and significance. The ML technique works on the photon event data and the background map. The spatial distribution of the observed photons is compared with the spatial distribution of the theoretical PSF[1]. For each photon the probability to belong to source or background is calculated. A likelihood that the instrumental PSF and a two–dimensional Gaussian source distribution are matching is calculated. The parameters specifying source position in detector coordinates, source counts, extent are varied until the likelihood is maximized. The likelihood is defined as $[-ln(1-P)]$ where P is the probability of existence of the source (Cruddace *et al.*, 1988). A multi–PSF fit is also implemented to allow for deblending and reconstructing the parameters for close by sources. A confidence level for each parameter is used to reject sources with insufficient significance (Hasinger, 1985; Boese and Doebereiner, 2001). An advantage of the ML technique is the capability of taking into account the arrival time, sky and detector positions and energy of each infalling photon on the detector. The main pitfalls of the ML approach comprise: The optimum value found for the detected sources is not unique (Boese and Doebereiner, 2001), so that a local maximum may be observed instead of a global one; The background counts in addition to a source are considered constant with respect to the optimized source parameters; Background subtraction is used leading in extreme cases to negative count rates (Voges *et al.*, 1999); The uncertainties entering the optimized source parameters are based on the normal distribu-

[1] Note that for reason of computational speed, the photon space is binned and the best fit PSF density in radially symmetric Gaussian form is taken as the PSF model for point sources (Boese and Doebereiner, 2001; Boese, 2004). For extended sources, a radial two–dimensional Gaussian function is fitted to the photon distribution (Boese and Doebereiner, 2001).

tion (Boese, 2004), leading to unreliable uncertainties especially for faint sources. Last, the work of Boese (2004) shows that the ML technique provides reliable source positions for the detected sources, but fluxes for faint point–like or extended sources are often overestimated.

In Chapter 1, Section 1.2, additional benefits, pitfalls and further developments of these procedures are introduced.

5.1.2 Wavelet Transformation

Wavelet based methods have been extensively applied to astronomical image processing in the last 10 years: See Rosati (1995) as one of the pioneering works on wavelet analysis. The reasons for their success is based on their ability of detecting image structures at all spatial scales and locations and on modelling the local background in addition to a source in wavelet space (Starck and Murtagh, 2006). After providing a short presentation of WT techniques, the WAVDETECT algorithm (Freeman *et al.*, 2002), version 3.4, part of the *Chandra* Interactive Analysis of Observations (CIAO) software package is reviewed. This algorithm is employed in Section 5.3 for quality assessment of the BSS technique.

WT techniques convolve the input image with a wavelet function (e.g. Haar, Mexican Hat, Morlet functions). The solutions are wavelet coefficients at different scale parameters. Object translations are included in the solution through a position parameter. By varying the scale parameter, the original image is decomposed into wavelet images (Starck and Pierre, 1998). WTs localize the image structures associated to the maxima of the wavelet coefficients. Hence, sources are detected whose size is comparable to the employed scale. Extended sources are detected at increasing scales of the WT.

In each wavelet image, the detection threshold at a given scale is estimated through a statistical model to justify if a wavelet coefficient is significant, i.e. not due to background. The statistical significance of a coefficient is often determined by: employing a histogram of the wavelet function (Starck and Pierre, 1998); through Monte Carlo simulations (Damiani *et al.*, 1997; Vikhlinin *et al.*, 1998*a*; Freeman *et al.*, 2002).
Photons, contributing to the calculation of the wavelet coefficients, are used to compute histograms. Histograms are employed to derive threshold values. Threshold values are compared to the wavelet coefficients. Wavelet coefficients are significant if their values are larger than the estimated threshold values.
Monte Carlo techniques are commonly used on simulated images composed by a spatially uniform background with Poisson noise and convolved with the wavelet coefficients. The distribution of the local maxima in the convolved images is used to define the detection threshold. Often, the threshold level is chosen between $3-5\sigma$ (of a Gaussian distribution) above the background level.

Note that WT techniques do not require an estimation of the background on the whole image for source detection. The background in addition to a source is assumed to be constant and is estimated locally in the negative annuli of the wavelet function. The locally estimated background is biased when nearby sources are present. In addition, the parameters of extended sources are not properly accounted for, when the background amplitude is characterized by large variations.

Following the selection of the significant wavelet coefficients at each scale, the maxima of the wavelet coefficients are used to define the detected objects at each scale. Source characteristics are extracted from the detected structures, including position, flux, positional angle and deviation from sphericity.

In Chapter 1, Section 1.2, advantages, pitfalls and further developments of these techniques are discussed.

The wavdetect algorithm is a powerful and flexible software package. It has been developed for a generic detector. It is applicable to data with low background. The algorithm includes satellite's exposure variations. It estimates the local background count amplitude in each image pixel and it provides a background map.

The WAVDETECT algorithm detects candidate source pixels by repeatedly convolving the original image with a Mexican Hat function at different scales. This wavelet function employed is the second derivative of the Gaussian function. The local background is taken from the negative annulus of the wavelet function. The background estimate can be biased when sources are located within the wavelet negative annulus producing rings. The background model is improved with further iterations. Pixels identified with candidate sources are removed from the image iteratively. When very few source candidates are found or when an iteration–count limit is reached, this process stops. The background is estimated on the new censored data set (input image with source pixels extracted). The final background may still contain rings, that affect source characterization. In the background map, problems can arise also near under exposed regions or at the field edge, since the sharp gradient can be erroneously detected as a source.

The estimated background is used to set detection thresholds. These thresholds are then applied to the wavelet images to identify the candidate sources. At each set of wavelet scales, a list of candidate sources and the background image are provided. The background image is corrected for exposure variations and for sensitivity variations of the instrument at a local scale (flat–field). The background errors are also supplied.

In a second step the source lists are merged and cross–correlated. For each source, a cell containing the majority of the source flux is computed. Within that cell, source properties are computed.

5.1.3 Voronoi Tessellation and Percolation

The VTP procedure is a general method for the detection of non–Poissonian structures in a distribution of points. The VTP technique, as described in Ebeling and Wiedenmann (1993), is designed for the detection of faint and extended sources. The VTP procedure is applied on X–ray data, especially on *ROSAT* data (see, e.g., Scharf *et al.* 1997; Ebeling *et al.* 2000) and it is also included in the CIAO software package (see, e.g., Boschin 2002).

This technique works on unbinned data. No particular source geometry is assumed for the detection process. Each photon defines the centre of a polygonal cell. Each polygonal cell side is connected to the nearest neighbour photon. The photon cells form the Voronoi

tessellation of the field. The surface brightness associated with the photon in the cell equals the inverse of the product of cell area and local exposure (Scharf *et al.*, 1997). A cutoff for defining the global background is obtained by comparing the cumulative distribution of the inverse areas of the resulting Voronoi cells with that expected for a random Poisson distribution. A spatial Percolation algorithm is used to group individual cells with photons exceeding the background density. Sources are identified and removed from the field in order to revise the background estimate. A minimal number of photons required for true sources is computed in order to reduce the number of false positives. The background amplitude is then provided by the mean surface brightness calculated from all nonsource photons.

Source positions are computed as the flux–weighted mean values of photons identified as belonging to one source. A preliminary width of the sources is also provided. Source fluxes are provided with and without fitting a model profile to the detected emission (Ebeling *et al.*, 1998). The source parameters are estimated employing two kinds of source profiles: for extended emissions a β–model (Cavaliere and Fusco-Femiano, 1978), for point–like sources a Dirac's delta function (see Ebeling *et al.* 1998 for more details). The source profiles are convolved with the instrumental PSF. The convolution process provides the observed surface brightness distribution. Moreover, source count rates for the detected objects are corrected to an arbitrary fraction of the total source flux. The motivation for this correction is due to the presence of an X–ray background that always limits the emission directly detectable (unobserved flux). The correction is performed in the far wings of the source.

This method is particularly designed for the detection of extended sources in the Poisson regime. Sources with low surface brightness are found independently of their actual shape. However, this procedure is characterized neither by a well–defined background model nor by a multiresolution support. Although the estimated background accounts for the telescope's exposure, the background rate is obtained by iterations on a censored image. Large variations in the background are not modelled. Fields with very high photon densities, like the RASS fields at high ecliptic latitude, can not be processed in one go (Ebeling *et al.*, 1998). Problems in the evaluation of source positions and intensities may arise when studying fields of high source densities (Valtchanov *et al.*, 2001). Since a multiresolution analysis is missing within VTP, diffuse emissions with embedded point–like sources are combined (Ebeling *et al.*, 1998) and substructures of extended sources are not detected (Starck and Pierre, 1998). The performance of the VTP technique is best only for either small fields or low–event density regions.

5.1.4 Growth Curve Analysis

The GCA (Böhringer *et al.*, 2000) is a source characterization technique designed for the flux and width estimation of X–ray clusters of galaxies. It is applied to RASS data, processed by SASS and catalogued with a low source likelihood: $L = 7$, instead of $L = 15$ as for the Bright Source Catalogue (BSC) (Voges *et al.*, 1999): See Böhringer *et al.* (2001) for more details. The reanalysis of the source fluxes of extended objects has been necessary because the flux of these sources is underestimated by the SASS algorithm (Böhringer *et al.*, 2001). The GCA method consists in measuring background–corrected source counts as a function of an increasing circular aperture.

From the RASS data, fields with sizes of $1^\circ.5 \times 1^\circ.5$ in the sky are selected. The positions of the fields are the X–ray positions provided by the ML technique incorporated in the SASS algorithm. However, the ML approach is designed for the parameterization of point–like sources. Source positions are, therefore, estimated once more employing a moment method, i.e. a two–dimensional centre of mass of the photon distribution within an aperture of $(3 - 7.5)$ arcmin around the centre.

The background model given by the sliding window technique of the SASS algorithm is not used. The background is, instead, calculated as follows. An average background rate is derived from a ring area centred on the source, but away from the X–ray extended emission. The inner and the outer ring radii (often with values of 20 and 41.3 arcmin, respectively) are chosen large enough to cover the full field size. The ring area is divided in twelve sectors. In each sector, the count rates are accounted and averaged for providing the surface brightness (background). The background rate is corrected performing a $k - \sigma$ clipping on the twelve sectors of the ring, so that the median of the background count rates is determined in an attempt of excluding discrete sources and statistical fluctuations. For this reason, a sector is discarded if its surface brightness deviates from the average. Detected sources still contaminated by nearby sources after the $k-\sigma$ clipping are improved employing a deblending algorithm.

The cumulative source count rate as a function of radius is calculated by integrating the source counts (background corrected and weighted with the local exposure time) in concentric rings. The results are count rate profiles that allow one to estimate the total observed source count rate and to suggest the source extent (i.e., the size of the detected source). The source width is improved employing a χ^2 fit of a β–profile (Cavaliere and Fusco-Femiano, 1978) convolved with the instrumental PSF. Additionally, the estimated source profiles are tested for deviation from the count rate profile expected for a point source. A Kolmogorov–Smirnov test is used for this purpose. Furthermore, the GCA provides the following parameters: background subtracted source count rate and its Poisson error, a significance of the source detection, source extent and spectral information. X–ray fluxes are corrected for the missed flux outside the detection aperture by extrapolating to the cluster's estimated virial radius (Kocevski and Ebeling, 2006).

The GCA method ameliorates the results obtained with the sliding window technique and the ML method and with the VTP technique (Böhringer *et al.*, 2000). However,

the GCA technique works only locally[2] and does not account for large variations in the background. The GCA technique shows more clearly than other methods that an accurate estimation of the background is very important.

5.1.5 Summary of some standard techniques

Table 5.1 provides a summary of the strengths and the weaknesses of the detection techniques supplying background estimation, source detection and characterization.

Methods	Strengths	Weaknesses
Sliding window	Detection of point sources.	Coarse background estimation due to box filter and subtraction of sources, Low sensitivity in detecting faint and nearby sources, Fine tuning of parameters for extended sources, Speed decreases at increasing number of cell sizes and of detected sources.
and ML	Best performance for parameter estimates of point sources, Each individual photon is taken into account.	Extended sources may be divided into point sources.
WAVDETECT	Multi scale analysis for source detection, Source characteristics are extracted from detected structures, Closely spaced point sources are separated, Extended sources are detected at different scales, Local background is estimated in wavelet space.	Mexican Hat function is used as a filter for source detection, Circularly symmetric sources are favoured in source detection, Detection threshold given by significant wavelet coefficients, Fluxes are often not preserved, Problems at the field edge, with increasing number of false positives, Speed decreases at increasing number of scales used.
VTP	Morphology free method for source detection, Each individual photon is taken into account, Find low surface brightness features, Detected photons provide position, flux, width.	Coarse background estimation, Combines close by point sources, Combines diffuse emission with embedded point sources, Applicable to small fields or low–event density regions, Speed decreases at increasing number of cells.

Table 5.1: Summary table listing strengths and weaknesses of standard source detection methods discussed in Section 5.1. Note that the GCA technique is not listed, since it provides only source characterization.

[2]The GCA method has so far been employed only in an interactive, supervised way.

5.2 Application of standard techniques to sky surveys

X–ray sky surveys offer the possibility to study complete samples of, e.g., rare objects, such as galaxy clusters, AGNs and QSOs, in order to quantify their properties (as luminosity, temperature, space density) and to probe cosmological models (while connecting observed quantities to model predictions). The *ROSAT* data and catalogues provided the starting point to construct X–ray samples over wide areas of the sky. In the search of galaxy clusters, the largest statistically homogeneous sample drawn from the RASS is given by the works of Böhringer *et al.* (2000, 2004): the northern galaxy clusters (NORAS) and the southern clusters (REFLEX) surveys. In these works, galaxy clusters are analysed with the GCA algorithm, providing for an homogeneous sample in all its selection parameters, especially in its coverage of the sky (Böhringer *et al.*, 2001). Optical identifications and spectroscopic observations followed on the X–ray identified galaxy clusters to provide for a robust local ($z \sim 0.15$) reference frame and to measure fundamental cosmological quantities (see Böhringer *et al.* 2000, 2004; Guzzo *et al.* 2009 for more details). Several other surveys employing *ROSAT* data have been published in the past years. Utilizing *ROSAT* pointed observations, for instance, the ROSAT Deep Cluster Survey (RDCS) (Rosati *et al.*, 1998) and the 160 Square Degree Survey (Vikhlinin *et al.*, 1998*b*) extended galaxy clusters studies at higher redshifts (up to $z \sim 0.8$). For a review of X–ray sky surveys employing *ROSAT* data, see, e.g., Finoguenov *et al.* (2007); Guzzo *et al.* (2009).

With the advent of more powerful instruments, as the XMM–*Newton* satellite[3], X–ray sky surveys are carried out extending previous works in the search of evolution of the X–ray luminosity function (XLF), as well as of the luminosity–temperature relation for galaxy clusters emitting in X–ray. The XMM–Cosmological Evolution Survey (XMM–COSMOS) (Hasinger *et al.*, 2007) and the XMM–Large Scale Structure (XMM–LSS) (Pierre *et al.*, 2004) survey are performed on mosaic of images. Mosaic of images are difficult to handle. In an automated search for X–ray extended sources, some of the standard techniques previously described (Section 5.1) are combined for the analysis of a mosaic of images. The sequential application of different techniques may provide inconsistent results. Previous works (see Böhringer *et al.* 2001 for more details) have already shown that the sequential application of, e.g., the SASS and the VTP techniques (Ebeling *et al.*, 1998) produces an inhomogeneous selection function and, therefore, biased results.

In Sections 5.2.1 and 5.2.2, a summary on the data analysis performed for the XMM–COSMOS and the XMM–LSS surveys is given. In Section 5.2.3, an alternative way to analyse a mosaic of images is described employing the BSS algorithm.

5.2.1 XMM–COSMOS

The XMM–COSMOS project employs WT on a mosaic of images (Finoguenov *et al.*, 2007). Each image composing the mosaic is background subtracted and exposure corrected.

[3]Due to its sensitivity (10 times better than *ROSAT*), large fov ($\sim$ 30 arcmin) and good PSF (the on–axis PSF is $\sim$ 6 arcsec FWHM), XMM–*Newton* is ideally suited for clusters LSS surveys.

Firstly, the background is estimated on each single image before the mosaic is created. The background is estimated employing templates for instrumental and sky backgrounds. The measured background is then subtracted from the data. Problems arising from the subtraction of a background from image data have been discussed in Section 5.1. Successively, the mosaic of 'cleaned' images is created and corrected for the mosaic of exposure maps.

Clusters of galaxies are searched applying the WT method of Vikhlinin *et al.* (1998*a*) on the resulting mosaic of 'cleaned' and 'corrected' images (later on, simply, images). The search for clusters of galaxies on the mosaic of images proceeds in several steps. Initially, the wavelet transformed image with a scale of 32 arcsec is used to derive a detection threshold. An area of the detected source is selected above the detection threshold for flux measurements. A list of cluster candidates is created and cleaned for contamination from point–like sources comparing wavelet scales. The number of cluster candidates is still overestimated, so that optical data are used for straining the final cluster sample. Finally, the estimated flux of the detected clusters of galaxies is improved removing the contamination from point–like sources according to optical identifications. For the characterization of these point–like sources the instrumental PSF information is taken into account. A β–model (Jones and Forman, 1984, 1999) is used for the characterization of clusters of galaxies emission.

5.2.2 XMM–LSS

The XMM–LSS pipeline (Pacaud *et al.*, 2006) employs a mixed approach with the WT technique of Starck and Pierre (1998) and the SExtractor software package, described in Bertin and Arnouts (1996), for source detection and a ML method (Pacaud *et al.*, 2006) for source characterization.

For source detection the WT technique, based on the Multiscale Vision Model described in Starck and Murtagh (2006), is used enabling the filtering of the image, i.e. the removal of insignificant signal and the recovering of relevant structures. SExtractor is subsequently applied on the filtered image to find the sources. The detection of sources is established through sets of connected pixels above a certain threshold. Though, this scheme may fail when the characteristic scale of variation of the background is approximately the scale of the structures. This combined solution has the advantage of a fast and robust detection, as in the standard method, while keeping the ability to detect faint objects, which is not possible with SExtractor alone.

The third step consists in examining the likelihood of the detections and characterizing their extent by a ML method. The ML profile fit is performed on (single and coadded) photon images. In this step, the instrumental PSF variation with energy and off–axis radius is considered, as well as other detector characteristics (vignetting, CCD gaps, local instrument sensitivity). Two source models are used: an instrumental PSF model for point–like sources, a spherically symmetric β-model (Cavaliere and Fusco-Femiano, 1978) convolved with the instrumental PSF for extended sources.

Last, X–ray/optical overlays for every extended source candidate are employed for

quality assessment of the detected extended sources. Each overlay is inspected by eye, since instrumental artefacts could have been detected as extended features. A list of plausible extended sources is given when obvious enhancements of galaxies are shown (only for clusters at $z \leq 1$). These clusters may be confirmed from spectroscopical data. Detected extended objects with no significant optical counterpart are considered cluster candidates at $z > 1$. These candidate clusters are searched on follow–up images in the near–infrared. If confirmed, a spectroscopic follow–up is planned.

5.2.3 Analysis of mosaic of images with the BSS algorithm

In the search of extended sources in deep surveys, the analysis of a mosaic of images is particularly difficult because of the increasing uncertainties of the source and background signals towards the edge of the fov where individual images are superposed. Often, an estimated background is subtracted from individual observations for successively merging and analysing the images. The drawback of such technique is that substructures often arise in the regions of superposed images due to residuals left over after background subtraction. Large–scale residual variations in the background can be detected as spurious extended sources.

A starting point for improving the analysis of mosaic of images could be given by the BSS algorithm. An efficient way to handle mosaic of images is given by a statistical combination of each individual image. In fact, each image of the mosaic can be analysed individually with the BSS algorithm, creating SPMs with the multiresolution analysis. Successively, each SPM can be statistically combined with the multiband technique (see Section 2.2.5) for each resolution. Hence, the source signal contained in superposed regions would increase in the same way as analysing the mosaic of images.

Another critical aspect of galaxy clusters detections in deep surveys is the contamination of point–like sources on the line of sight of extended ones. The contamination of point–like sources along the line of sight of galaxy clusters is straightforwardly handled with the BSS technique due to the multiresolution analysis (examples are given in Chapter 7).

Last, the BSS source characterization algorithm (Section 2.3) can be easily adapted for the analysis of clusters survey.

5.3 Verification

In the X–ray regime, the sliding window technique and the WT techniques are widely used. However, the WT has been shown to perform better than the sliding window technique for source detection: See Freeman *et al.* (2002) for more details. The WT improvement in source detection with respect to the sliding window technique is inversely proportional to the background amplitude (Freeman *et al.*, 2002). The WT has also other favourable aspects for being compared with the BSS method developed in this thesis: The WT allows for the search of faint extended sources; The WT and the BSS methods are both based on a multiresolution analysis.

Table 5.2: Number of detected sources employing WAVDETECT on three simulated data sets.

Simulated background	Simulated sources	True detections	False positives
0.1	100	56	4
1.0	100	37	1
10.0	100	23	1

Note. For the simulation set–up see Section 4.1. The results obtained with the BSS technique can be found in Table 4.1.

Among all the available software employing WT, the WAVDETECT algorithm described in Freeman *et al.* (2002), part of the freely available CIAO software package, is chosen. Version 3.4 is used.

WAVDETECT is applied on the simulated data described in Chapter 4. The threshold setting for the significance ('sigthresh') is chosen to be 4.0×10^{-6}, in order to detect on the average 1 spurious source per image. The 'scale' sizes are chosen with a logarithmic increment from 2 to 64. Tests have been made changing the levels of these parameters, assuring that the selected values provide a good performance: This problem is already known in the literature, see e.g. Nandra *et al.* (2005).

In Fig. 5.1, the reconstructed source images and estimated backgrounds as in output from WAVDETECT are displayed. The reconstructed source images are scaled as the photon count images shown in Figs 4.1, 4.2 and 4.3, panels (a).

In Table 5.2, the number of detected sources per simulated field is reported, separating the sources correlated with the simulated one (*True detections*) to the false positives in source detection found employing the above mentioned threshold setting. The three simulated data sets are distinguished by their mean background values (counts). The simulated background values are reported in column *Simulated background*. These results are compared with the ones obtained with the BSS algorithm when employing the exponential prior pdf as shown in Table 4.1.

In Fig. 5.2 efficiency and contamination of the BSS technique, employing the exponential prior, and the WAVDETECT algorithm are compared at fixed threshold levels. The efficiency is defined by the ratio of the detected real sources and the simulated sources. The contamination, instead, is defined by the ratio of the detected false positives and the total number of detected sources. Each line in the plot connects three points. Each point indicates the estimated values of contamination and efficiency at the three simulated background values. The points at the right–hand, middle and left–hand locations of the plot are obtained with the backgrounds of 0.1, 1.0 and 10 counts respectively. The BSS

technique is more efficient (up to 3% when $P_{\rm source} = 0.99$) and provides a less contaminated sample (up to 5% when $P_{\rm source} = 0.99$) than the WAVDETECT algorithm especially in the simulated data with small background. Note that the absolute efficiency depends on the selected values of the simulated fields.

The BSS technique finds all sources detected by WAVDETECT. In the simulated data characterized by small background, the two algorithms find the same number of false positives. This occurs when a threshold level of 50% is chosen for $P_{\rm source}$. The BSS algorithm detects 8% more true detections than WAVDETECT. These sources are characterized by counts in the range $(4-8)$. Hence, the BSS technique performs better than WAVDETECT in the low number counts regime. The number of detected true sources with the two techniques on the data sets with intermediate and large background values is similar, though the BSS technique provides for a less contaminated sample.

The explanation for these results is given analysing the background estimates (see panels *b*, *d*, *f* in Fig. 5.1 for WAVDETECT and panels *d* in Figs 4.1, 4.2, 4.3 for the BSS algorithm). The WAVDETECT estimates of background values are similar to the results obtained with the BSS technique in the intermediate and high background data sets. Though, the backgrounds provided by WAVDETECT show rings due to the Mexican Hat function employed as a filter on the image data. In the simulated data with small background, the WAVDETECT background model has on the average larger values than the ones estimated with the BSS method. The plots in Fig. 5.3 support these conclusions (semilog plots). The image in panel (*a*) provides the flux recovery of WAVDETECT detections versus the simulated fluxes. WAVDETECT fluxes are underestimated for $\sim 20\%$ of all detected sources. In addition, WAVDETECT sensitivity for source detection is limited to 16 counts per source within these simulated data sets. In Fig. 4.11, panel (*b*), the flux recovery of the BSS technique versus the simulated fluxes is improved with respect to WAVDETECT. In fact, residuals of estimated and simulated source counts are normally distributed and the sensitivity achieved by the BSS method is of 4 counts. The plot in panel (*b*) of Fig. 5.3 displays a relation between the sources detected by WAVDETECT (ordinate) and by BSS (abscissa), both matched with the simulated data. Most of the WAVDETECT underestimated sources are coming from the simulated data with small background. The BSS technique provides only two sources underestimated and detected in the simulated data with large background. By chance, the triangle located at $(-8,-2)$ indicates the detection of two sources. Both sources where simulated with 256 source counts and a circular extension of 4 pixels one, 5 pixels the other. The estimated source positions are also improved with BSS (Fig. 5.4, semilog plots).

The residuals provided by the BSS technique are a factor of 10 smaller than the ones from WAVDETECT. WAVDETECT estimates have many outliers. The BSS estimates are normally distributed.

Though the comparison between the two detection methods is not yet carried out on real data, these results are encouraging. The BSS method detects at least as many sources as WAVDETECT. The simulations prove that the developed Bayesian technique ameliorates the detections in the low count regime. The BSS estimated positions and counts are improved. Finally, the BSS technique will refine WAVDETECT sensitivity on real data, because the BSS technique is designed for modelling highly and slowly varying backgrounds taking into

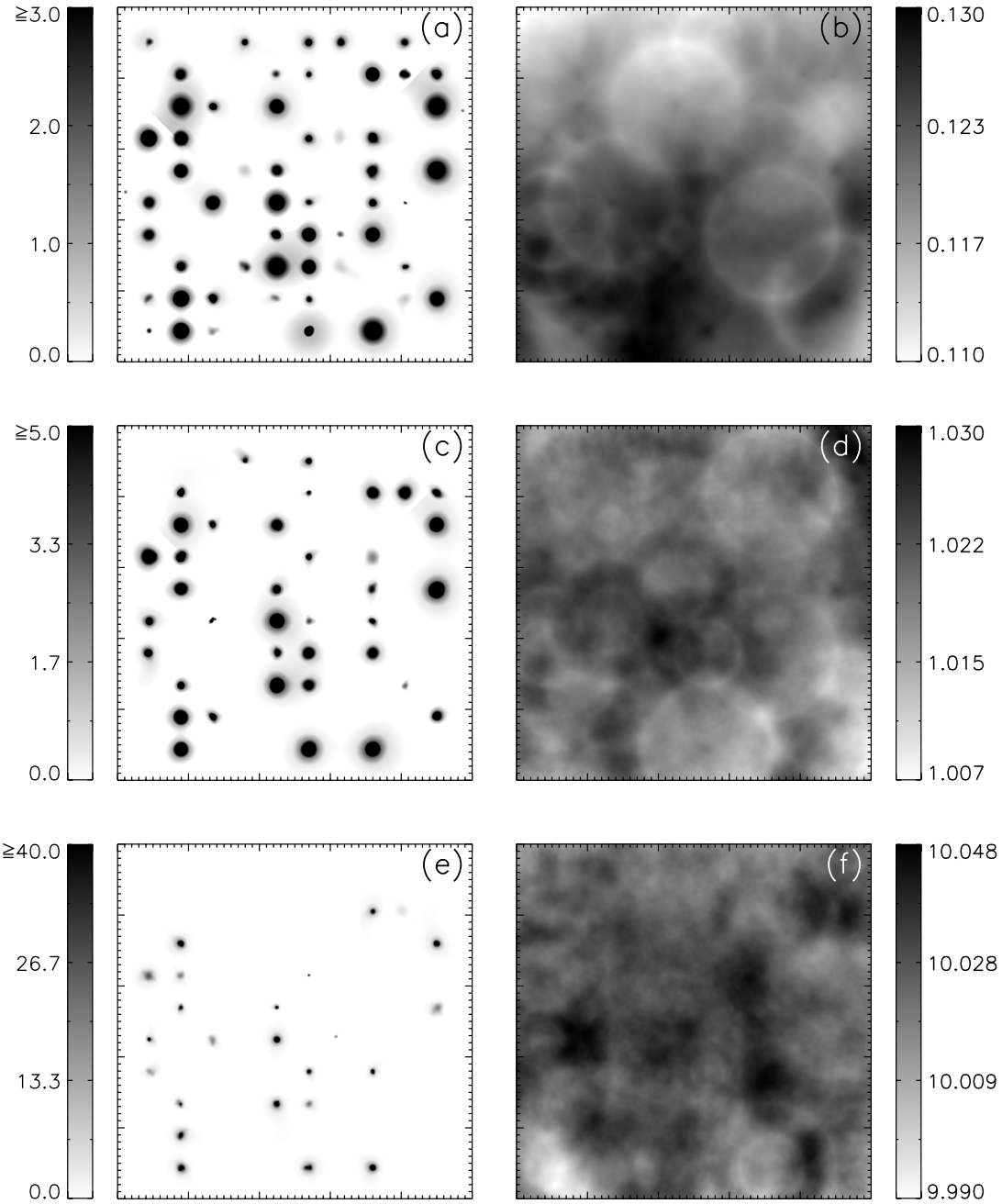

Figure 5.1: Analysis of simulated data with WAVDETECT. Panels (a), (c), (e): reconstructed source images. Panels (b), (d), (f): estimated backgrounds. From up to down: simulated data with small ($b = 0.1$ count) $(a) - (b)$, intermediate ($b = 1$ count) $(c) - (d)$ and large ($b = 10$ counts) $(e) - (f)$ backgrounds.

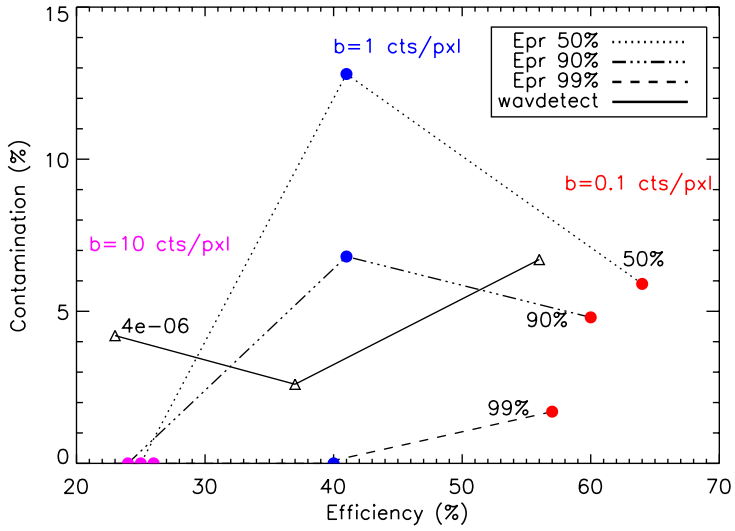

Figure 5.2: Comparison between the BSS technique employing the exponential prior ('Epr') and the WAVDETECT algorithm on simulated data. The background b is indicated in counts per pixel units.

account instrumental structures.

5.4 Summary

In high–energy astrophysics, several source detection algorithms have been developed. Each technique tackles the ill–posed inverse problem in image analysis with different strategies. It results that for deep sky surveys, standard techniques are employed in sequential order. The employment of several techniques in sequential order does not allow the uncertainties of the experimental measurements to propagate. The final result can be biased.

The results obtained from the simulated data with the BSS and the WAVDETECT (Freeman *et al.*, 2002) techniques are compared. The BSS technique improves the detections of WAVDETECT especially in the low count regime.

In the low count regime, the BSS background model with the employment of the exponential prior pdf of the source signal is closer to the true value and is on average 10% lower than the one found with the wavelet technique. Note that even employing the inverse–Gamma function prior pdf with the cutoff parameter larger than the background amplitude, the BSS background model is still lower than the one found with WAVDETECT of $\sim 5\%$. In the simulated data set with low background, sources with ≥ 4 counts are found with the BSS technique. Although scale sizes are chosen from 2 to 64 (in logarithmic increment), the wavelet based technique is sensitive only to sources with ≥ 16 counts. In order to increase the sensitivity of WAVDETECT, the significance threshold can be decreased to values $< 4.0 \times 10^{-6}$. However, the efficiency and also the contamination of the WAVDETECT

technique increase: many false positives arise at the field edge.

In the simulated data with intermediate and large backgrounds, the background models obtained with the two techniques are similar in amplitude and they differ by less than 1%. However, the BSS background models are smoother than the ones estimated with WAVDETECT. Therefore, the BSS background models reproduce a more realistic scenario than WAVDETECT background models, since the simulated backgrounds are constant.

WAVDETECT fluxes are underestimated for 20% of the sources. Biases in flux estimation with WAVDETECT are expected, because the background is not accurately estimated. The BSS residuals on source fluxes and positions are normally distributed. The BSS residuals are a factor of 10 smaller than the ones from WAVDETECT.

The BSS technique because of the reliable background estimation (that includes exposure variations), the joint background–source separation, the multiresolution reconstruction, the multiband analysis and a Bayesian approach for source characterization has a larger sensitivity than standard techniques. The search for clusters and groups of galaxies, QSOs and AGNs in sky surveys can be improved employing the BSS method.

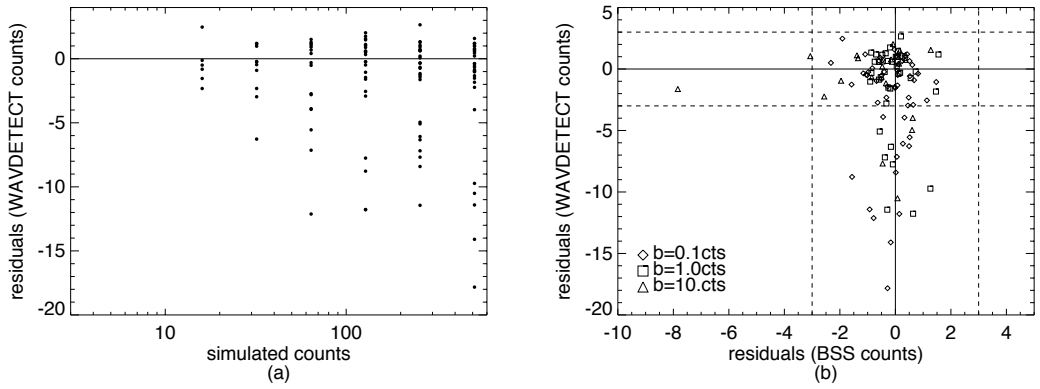

Figure 5.3: Panel (a): normalized difference between WAVDETECT estimated source counts versus simulated counts of all the detected sources in three simulated data sets. Panel (b): comparison between the normalized differences of WAVDETECT source counts and simulated counts, on the ordinate, and the normalized difference of BSS source counts and simulated counts, on the abscissa. Sources detected from the simulated data with small background are indicated with a diamond. A square is used to highlight sources detected in the data set with intermediate background. The detected sources in the simulated data with large background are indicated with a triangle. Dashed lines are drawn as a borderline of the $\pm 3\sigma$ detection. The zero line is indicated with a continuous line style.

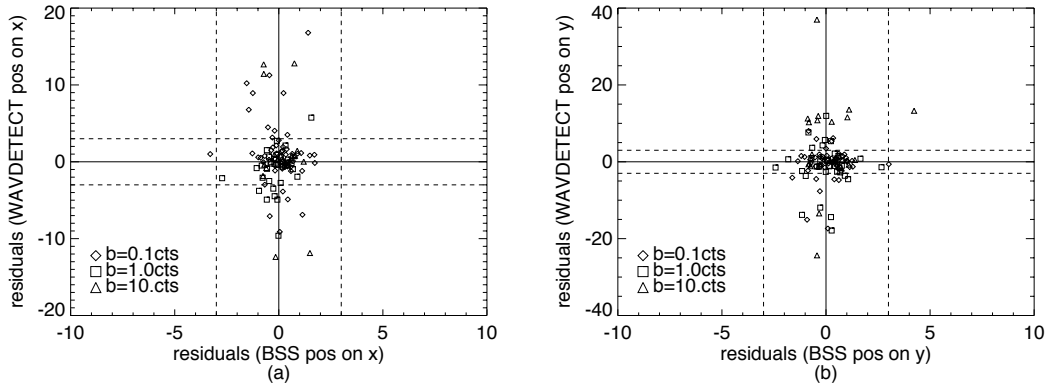

Figure 5.4: Same explanation as for panel (b) in Fig. 5.3, but comparing the estimated source positions: x–axis (panel a), y–axis (panel b).

Chapter 6

Application to observational data: ROSAT All-Sky Survey

In this Chapter, the BSS technique is applied to RASS data. In Section 6.1, the prominent aspects of the *ROSAT* satellite, its all–sky survey data and published catalogues are described. Other sky surveys and catalogues employed for the validation of the BSS detections are commented. In Section 6.2, the applications of the BSS technique to RASS data are meant to show the capabilities of this novel technique on astronomical images with large variations in the satellite's exposure and/or in the cosmic background. A comparison of the BSS method with the standard techniques employed for the analysis of the RASS data is provided. Evidence for celestial sources not previously catalogued by any detection technique in the X–ray regime is given. In Section 6.3, a summary is provided.

6.1 ROSAT PSPC Survey Mode data

The BSS algorithm is applied to a data sample measured by the Position Sensitive Proportional Counter (PSPC) on board of *ROSAT* (Röntgensatellit) in survey mode.

ROSAT, an overview: *ROSAT* was lunched on June 1, 1990. *ROSAT* operated in a circular Earth orbit with inclination of 53° and an altitude of 580 km. The orbit period was of approximately 96 minutes. The main payload of *ROSAT* is the X–ray telescope, formed by four concentric parabolic–hyperbolic mirror pairs (Wolter Type–I) with a focal length of 2.4 m. It is designed for measurements of soft X–rays ($0.1 - 2.4$ keV). In its focus were three X–ray detectors: two PSPCs and one High Resolution Imager (HRI).

The first six months of *ROSAT* operations were performed in scan mode, providing the only all–sky survey realized using an imaging X–ray telescope. A pointing mode followed the all–sky survey for a duration of 8.5 years. The telescope's sensitivity was improved in pointing mode compared to scan mode, because larger exposure time was dedicated for observing selected X–ray sources. The accuracy of X–ray object coordinate determinations was improved by a factor of 3 from scan mode to pointing mode (< 10 arcsec on axis). For

pointing mode observations, both the PSPC and the HRI detectors were used. The all–sky survey, instead, was performed employing only the PSPC. The PSPC detector has a very low intrinsic background (particle background). The particle background contribution is $\lesssim 6\%$ to the cosmic diffuse X–ray background (Snowden *et al.*, 1994), leaving a residual count rate of only $2 \cdot 10^{-5}$ count s^{-1} arcmin^{-2} (Schmitt, 1991). The PSPC combined with the wide telescope angle allows for the detection of extended sources, e.g., SNRs, clusters or groups of galaxies and the diffuse X–ray background. *ROSAT* data, from both scan and pointing mode, are publicly available[1].

RASS data and catalogues RASS was performed surveying the sky in circles of $2^\circ \times 360^\circ$, whose planes were oriented almost perpendicularly to the solar direction. The strips were merged to supply a unique map of the sky. The map of the sky was divided in 1378 fields each of $6.4^\circ \times 6.4^\circ$, corresponding to 512×512 pixels (1 pixel= 45 arcsec). Neighbouring fields were superposed by at least 0.23°. Each RASS field is provided in three energy bands: broad ($0.1 - 2.4$ keV), soft ($0.1 - 0.4$ keV) and hard ($0.5 - 2.4$ keV). The satellite's exposure time can vary between about 0.4 and 40 ks at the ecliptic equator and poles, respectively. In addition, some parts of the sky are without observations due to the satellite's crossing of the auroral zones and of the South Atlantic Anomaly. Consequently, the exposure over parts of the sky can be highly varying. It results that RASS data provide a wide range of possibilities for testing the BSS algorithm.

RASS data were analysed previously by the SASS algorithm. The SASS procedure combines the sliding window technique (Gioia *et al.*, 1990) with the ML PSF fitting method (Cruddace *et al.*, 1988) for source detection and characterization, respectively: Refer to Section 5.1.1 for more details about the SASS algorithm. SASS works well for point–like sources, but this algorithm is less suited to extended, low surface brightness sources. Extended, low surface brightness sources can consequently be missed, leading to a significant incompleteness in flux–limited cluster samples (Rosati *et al.*, 2002*b*). For each detected X–ray source, the SASS algorithm provides: detection likelihood, source positions, source and local background count–rates, exposure time, hardness ratios ($HR1$, $HR2$), source extent and corresponding likelihood. Source fluxes are provided in the broad ($0.1 - 2.4$ keV) energy band. Hardness ratios allow one to convert the source count rates in the broad energy band to the soft ($0.1 - 0.4$ keV) and hard ($0.5 - 2.4$ keV) energy bands. Specifically, the hardness ratio is defined as the normalized difference of counts in two energy bands: $HR1 = (B - A)/(B + A)$ and $HR2 = (D - C)/(D + C)$. The four energy bands indicate the following channels: $(11 - 41)$ for A, $(52 - 201)$ for B, $(52 - 90)$ for C, $(91 - 201)$ for D. Bands A and B represent the soft and the hard energy bands, respectively. Bands C and D together contain the same channels as the hard band B. Hence, $HR2$ is a hardness ratio constructed in the hard region only. Note that $HR1$ and $HR2$ have been set to a null value when the source counts have negative values. The SASS technique may provide negative net counts for faint sources, because of background subtraction (Voges *et al.*, 1999). This problem is overcome with the BSS algorithm.

[1] http://www.mpe.mpg.de/xray/wave/rosat/catalogue/index.php

SASS detections are listed in the RASS BSC (Voges *et al.*, 1999) and Faint Source Catalogue (FSC) (Voges *et al.*, 2000). The RASS BSC and FSC are derivatives of further analyses of the RASS data. The RASS–II processing, with respect to the previous version, improved mainly the spline background model and the source centroid within the sliding window technique, that provides the input list of detected sources for the ML method (see Voges *et al.*, 1999 for more details). Furthermore, a RASS–3 processing was provided. A better screening and repair of attitude data resulted in a more homogeneous sky coverage and $\gtrsim 5\%$ more exposure.

The RASS BSC (FSC) list $18,811$ $(105,924)$ sources, characterized by: a detection likelihood > 15 (≥ 7); number of source photons > 15 (≥ 6); and source count rates ≥ 0.05 count s^{-1} in the broad $(0.1 - 2.4$ keV) energy band. Although sources in BSC represent the bright sample of all X–ray sources detected by SASS, each RASS field (in three energy bands) was quality checked by detailed visual inspection in addition to the automatic processing by SASS (Gruber *et al.*, 1997; Voges *et al.*, 1999). The quality check was undertaken to guarantee a reliable source catalogue. During the visual inspection, false positives in source detection were manually removed from the final catalogue. In fact, false positives in source detection were visually identified in regions with steep gradients in the data (e.g. field and strip edges, large extended emission regions like the Vela SNR and the Cygnus Loop). About 16% of all SASS detections, that is about 17 detections per field, were identified by eye as false positives (Voges *et al.*, 1999). Furthermore, during the visual inspection, nearby sources, sources with large positional errors, extended sources, sources with complex emission structures and sources missed by SASS have been flagged (Voges *et al.*, 1999). Therefore, it is difficult to find new bright sources in the RASS data.

Other sky surveys and catalogues X–ray sources detected with the BSS algorithm, but not cross–correlated with any entry in the RASS BSC and FSC, can be validated with ROSAT data in pointing mode and with other sky surveys at the same and other wavelengths of the electromagnetic spectrum.

In addition to the RASS BSC and FSC, catalogues from the *ROSAT* data collected in pointing mode are available: *ROSAT* PSPC pointing (Voges *et al.*, 1996), WGACAT (White *et al.*, 1994), *ROSAT* HRI catalogue (ROSAT Scientific Team, 2000), *ROSAT* variable source (Voges and Boller, 1998). Both *ROSAT* PSPC pointing (Voges *et al.*, 1996) and WGACAT (White *et al.*, 1994) are derived from PSPC observations. However, the WGACAT does not use the SASS algorithm. The WGACAT was generated using an optimised sliding cell detection algorithm within the X–ray image analysis package XIMAGE (Giommi *et al.*, 1991). The source counts for WGACAT are calculated for the following energy bands: low–band $(A = 0.1 - 0.4$ keV), mid–band $(C = 0.4 - 0.9$ keV), high–band $(D = 0.9 - 2.0$ keV). The hardness ratios are defined as the ratio of counts in two different energy bands. Specifically, the following ratios are provided: softness $(SR \sim A/C)$, hardness $(HR \sim D/C)$, $SR_{hard} = C/D_1$, $HR_{hard} = D_2/D_1$. D_1 and D_2 are indicating the energy ranges $(0.9 - 1.3)$ keV and $(1.3 - 2.4)$ keV, respectively. From these spectral properties the source count rates from one energy band can be converted to another energy

band.

Images and catalogues from the XMM–*Newton* observatory (Jansen *et al.*, 2001) are also employed to compare detections obtained with the BSS algorithm analysing RASS data. The XMM–*Newton* satellite works in the energy range of $0.1 - 10$ keV. The on–axis PSF of this X–ray telescope has FWHM values of $5 - 7$ arcsec. The XMM–*Newton* satellite is, therefore, characterized by an improved resolution (at least 6 times better) with respect to the *ROSAT* PSPC PSF.

Virtual Observatories Tools, such as EURO–VO Tools[2], are employed for cross–correlating the X–ray sources detected with the BSS algorithm. Note that currently there are no other X–ray all–sky surveys besides RASS. Therefore, the amount of resources in X–ray regime is limited and some of the newly discovered X–ray detections with the BSS algorithm does not have counterparts in the above mentioned previous works. An analysis of these sources is provided with data in the optical, near–infrared, radio and γ–ray parts of the electromagnetic spectrum. Between all the available catalogues, the Sloan Digital Sky Survey (SDSS) (Abazajian, 2009) has an important role. The SDSS (optical) data reaches a much higher redshift than RASS (Schuecker *et al.*, 2004). Thus, SDSS data can be used to guide the BSS detections on RASS data.

6.2 Data analysis

This Section shows that precise statistical methods, as the BSS algorithm, are needed to provide a complete catalogue and to reduce greatly the contamination from false positives in source detection without compromising the detection of faint celestial objects. For this purpose, three RASS fields are chosen. The field identifiers are RS930625n00, RS932209n00 and RS932518n00. Each field is characterized by one of the followings: spatial variations of the background and of the telescope's exposure time; low exposure time and low surface brightness of detectable sources; sources embedded in diffuse cosmic emissions.

This Section is organized as follows. In Section 6.2.1, the background models are analysed and compared to the ones obtained with the SASS technique. In Section 6.2.2, the BSS catalogues obtained analysing the three RASS fields are compared to the RASS catalogues. For this purpose the GAVO archive[3] is employed. In Section 6.2.3, the robustness of the BSS detections is addressed. The low contamination of false positives in source detection obtained with the BSS technique is shown as illustration with SPMs derived from one of the RASS fields. The BSS results obtained combining SPMs at different energy bands are shown. The BSS algorithm capabilities on detecting sources independently of their shape, sources at the field edge and sources superposed to a diffuse emission, are demonstrated. In Section 6.2.4, the detections of X–ray sources which are not listed in the RASS catalogues are used to demonstrate the superior sensitivity of the BSS technique.

[2]EURO–VO Tools allow one to access the world's astronomical data (catalogues, images and spectra) maximising the scientific utilisation of the rich astronomical on–line resources.

[3]The German Astrophysical Virtual Observatory (GAVO) is partner of the EURO–VO. It allows one to query the whole ROSAT archive.

6.2.1 Background analysis with BSS and SASS techniques

In this Section, the results obtained with the BSS technique analysing the three selected RASS fields are shown with SPMs, TPS and background maps. The analysis of each field is organized into separate sections, whose title addresses the field's variations in the background and/or in the satellite's exposure time. Non–uniformities in background and exposure maps are consistently taken into account with the BSS technique. The background models obtained with the BSS and the SASS techniques are compared. The BSS background model is shown to be more stable than the one obtained with the SASS technique. Last, further exploitations of the background model are commented.

Varying background and exposure map

The detection capabilities of the BSS approach on an image with exposure and cosmic background non–uniformities is represented with the analysis of the *ROSAT* field id RS930625n00. This field is located at $\alpha = 17^{\rm h}49^{\rm m}5^{\rm s}$, $\delta = +61°52'30''$ (J2000), i.e. close to the north ecliptic pole region. Due to the satellite scanning restriction that each observation passes through the Earth's poles, this field is a natural one for testing large variations in the exposure map. The count rate image of RS930625n00 in the broad energy band is displayed in panel (*a*) of Fig. 6.1[4]. The photon count rates range over $0 - 0.11$ count s^{-1} pixel^{-1}. The image is scaled in order to enhance the sources. The RS930625n00 field is characterized by large variations of the satellite's exposure ranging from 1.7 to 13.5 ks (see Fig. 6.2, panel *a*).

The BSS results are shown in Figs 6.1 and 6.2 with a SPM (panel *b*, Fig. 6.1), the TPS map (panels *c*, Figs 6.1, 6.2) and the background map (panel *d*, Fig. 6.1 and panel *b*, Fig. 6.2).

In Fig. 6.1, panel (*b*), the SPM is obtained combining statistically the soft (0.1-0.4 keV) and the hard (0.5-2.4 keV) energy bands. The displayed SPM is obtained employing the exponential prior pdf. The counts of pixels are combined using the box filter method with a circle. This image corresponds to a correlation length of 1.5 arcmin. The correlation length used for this image corresponds to the width of the *ROSAT* instrumental PSF (Boese, 2000). Sources are identified in terms of probabilities. The image is in linear scale. Note the correspondence of the detected source positions with the count rate image (panel *a*). Many faint sources are already enhanced at the displayed SPM.

In Figs 6.1 and 6.2, panel (*c*), the TPS map is modelled from the broad energy band only. The TPS models the background rate. 25 support points are used and distributed equidistantly. In Fig. 6.1, panel (*c*), the color bar has units of photon count s^{-1} pixel^{-1}. The image is in linear scale. The contours are superposed for enhancing the features relative to the modelled background rate. In Fig. 6.2, panel (*c*), the cosmic background variations are shown with a surface plot. The background rate is smooth and does not depend on the large variations of the satellite's exposure time values.

[4]In each displayed astronomical image, North is up and East is to the left–hand side.

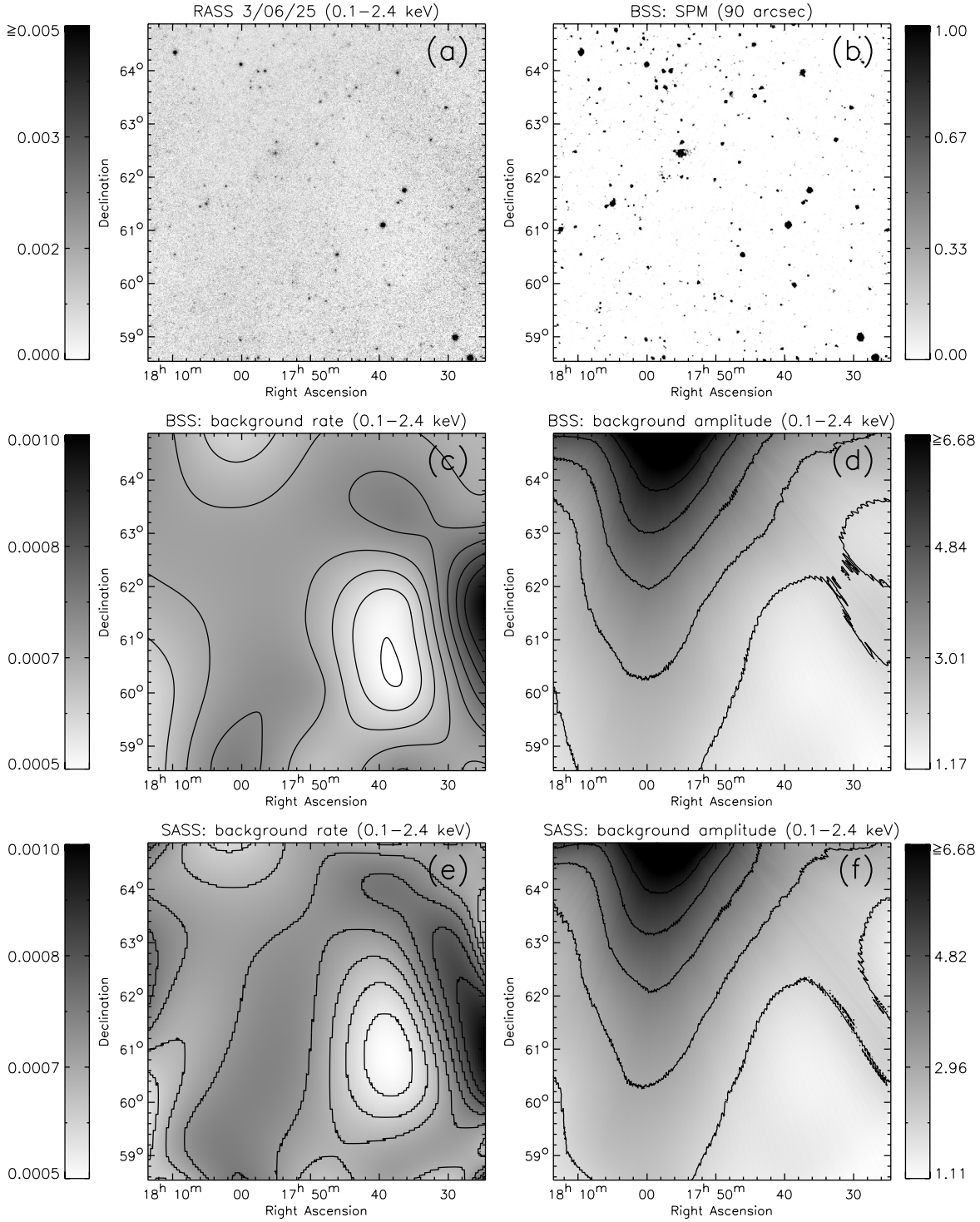

Figure 6.1: Analysis of the RASS field RS930625n00, *ROSAT* PSPC in survey mode.

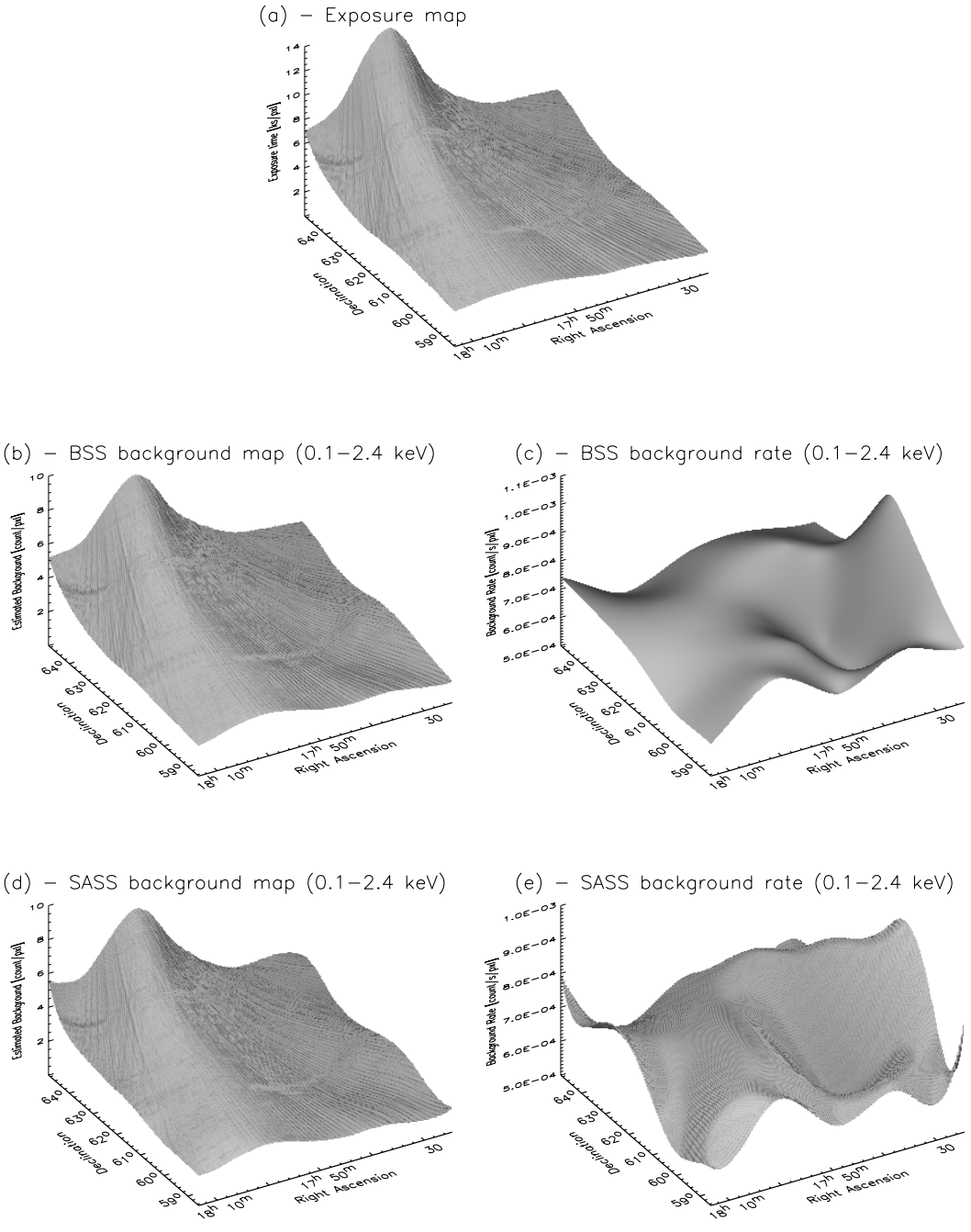

Figure 6.2: Panel (a): *exposure map* of the RASS field id RS930625n00 (Fig. 6.1). The z–axis indicates the exposure time in ks pixel^{-1}. Panels (b, d): *estimated background amplitudes* of RS930625n00 field in the broad energy band with the BSS and the SASS techniques, respectively. The z–axes show the estimated background count pixel^{-1}. Panels (c, e): the *background rates* corresponding to panels (b) and (d), respectively. The z–axes are in units of background count s^{-1} pixel^{-1}.

The corresponding background map estimated from the selected *ROSAT* field is displayed in panel (d) of Fig. 6.1. Its values are in the range $1.17 - 8.53$ photon count pixel^{-1}. In order to enhance features in the background amplitude, the image is scaled and contours are superposed. The background map shows the prominent variation due to the heterogeneous satellite exposure time (see, also, panel b, Fig. 6.2).

The lower row of Fig. 6.1 shows the background rate (panel e) and the background amplitude (panel f) as obtained analysing the broad energy band with the SASS algorithm. Note that the SASS algorithm provides only the background amplitude. The background rate is derived from the estimated SASS background amplitude normalized by the exposure map and is compared to the BSS background rate. The SASS background rate image is in the range $0.0005 - 0.00097$ photon count s^{-1} pixel^{-1}. The background amplitude image estimated by SASS has values in the range $1.11 - 8.27$ photon count pixel^{-1}. The image is scaled as the one obtained from the BSS technique in panel (d). Contours are superposed to enhance the variations in the background rate and amplitude.

In Figs 6.1 and 6.2, panels (c) are compared with panels (e). The background rate values from the BSS and the SASS techniques are similar. However, the BSS background rate (panels c) is smooth and stable along the whole field. Although main features are recovered at the field centre, the SASS background rate shows ripples along the whole field and an increasing instability towards the field edge. This oscillatory behaviour of the SASS background model and its implications are discussed in Chapter 5, Section 5.1.1.

The variations in the BSS and the SASS backgrounds (Figs 6.1, panels d and f, 6.2, panels b and d) are affected by the telescope's exposure time. Although the BSS background map is on average larger than the one estimated by the SASS algorithm, Section 6.2.2 shows that source count rates obtained with the two techniques and cross–correlated are in agreement. Furthermore, the BSS technique allows for more flexibility in the background model and the background at the field edge is more stable than the one provided by SASS. Hence, celestial objects located especially toward the field edge are not lost during source detection. In Section 6.2.4, two examples of newly discovered X–ray objects detected by the BSS technique are shown: A QSO and a potential cluster of galaxies are detected toward the field edge.

Smooth background and varying exposure map

The detection capabilities of the BSS technique on images showing strips with no exposure are tested. The *ROSAT* field id RS932209n00 is analysed. This *ROSAT* field is located at $\alpha = 3^{\rm h}31^{\rm m}$, $\delta = -28°07'08''$ (J2000). This area of the sky is known for having low Galactic neutral hydrogen column density (Giacconi *et al.*, 2001).

In Fig. 6.3, panel (a), the soft ($0.1 - 0.4$ keV) band image is shown. The image accounts for photon count pixel^{-1} in the range $0 - 9$. The image is scaled to enhance sources. The satellite's exposure map is located in panel (c). The color bar has units of second pixel^{-1}. Contours are placed in order to enhance the areas with different values.

The results from the analysis of this *ROSAT* field with the BSS technique are represented with a SPM (panel b), the background map (panel d) and the TPS map (panel f)

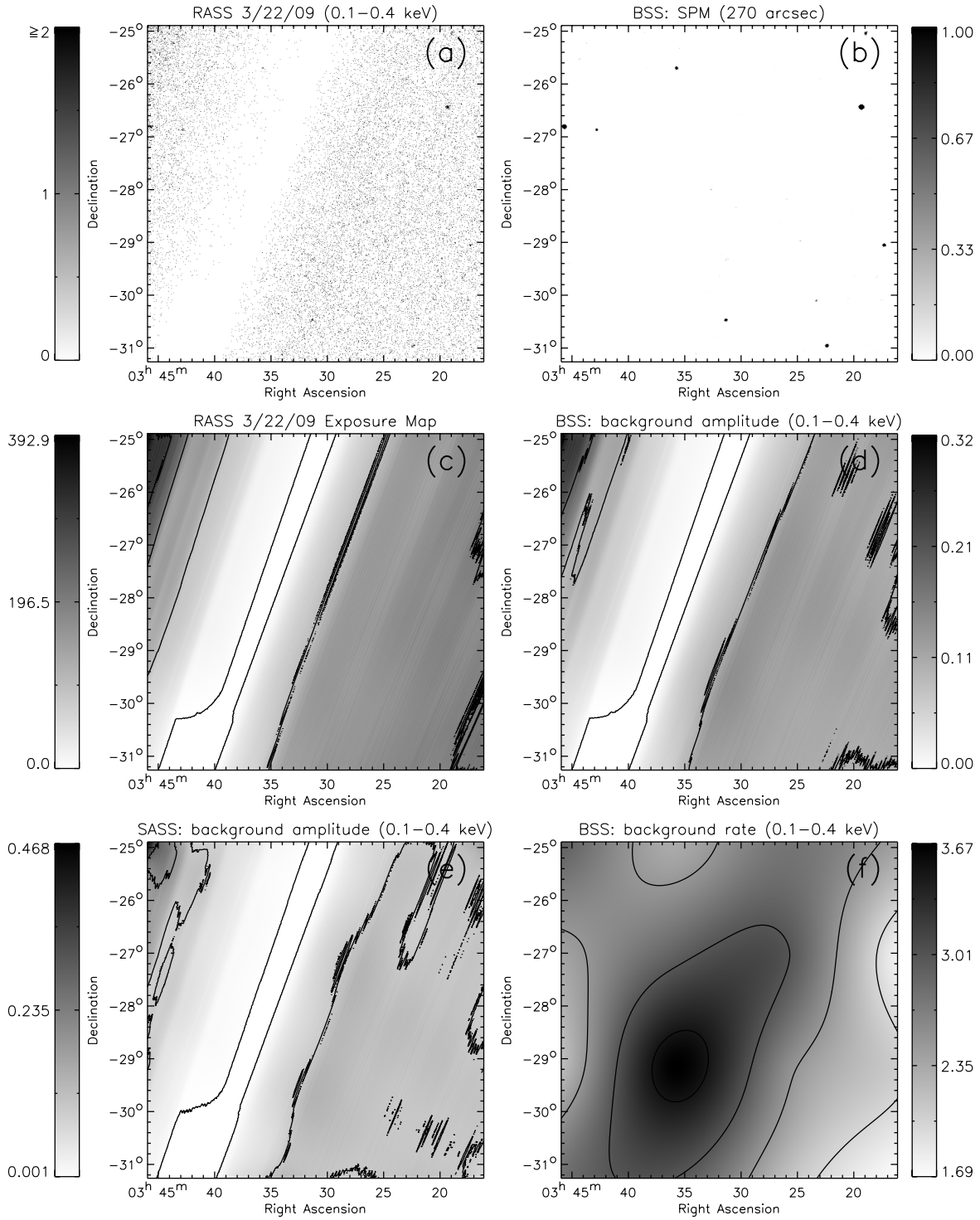

Figure 6.3: Analysis of the RASS field RS932209n00, *ROSAT* PSPC in survey mode.

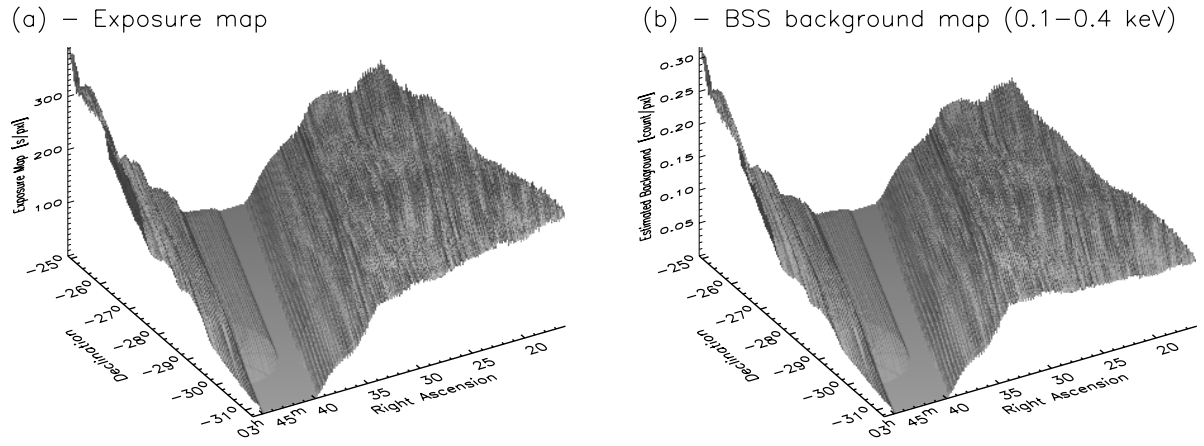

Figure 6.4: Panel (a): *exposure map* of the RASS field id RS932209n00 (Fig. 6.3). The z–axis indicates the exposure time in s pixel^{-1}. Panel (b): *estimated background amplitude* with the BSS technique of RS932209n00 field in the soft energy band. The z–axis shows the estimated background count pixel^{-1}.

in the same energy band of the photon count image in panel (a). The inverse–Gamma function prior pdf is used for source detection and background estimation.

In panel (b), this SPM is obtained with a correlation length of 270 arcsec (data resolution is 45 arcsec). The box filter method with a circle is employed.

In panel (d), the background map estimated with the BSS technique is shown. 16 pivots equidistantly distributed over the field are employed. The background amplitude ranges from 0 to 0.318 photon count pixel^{-1}. The background is estimated with a null value where no satellite's exposure information is provided. The area with an estimated null value is delineated by the contours close to white. No celestial sources can be found where the background amplitude is null. Note the agreement with the contour lines delineating null exposure and background values in panels (c) and (d), respectively .

In Fig. 6.4, the surface images of the exposure map (panel a) and of the background map estimated with the BSS technique (panel b) are provided. The estimated background map is similar to the exposure map because the distribution of the background is almost flat. The background rate, estimated with the BSS technique, is displayed in panel (f) of Fig. 6.3. The image is in linear scale. The color bar has units of count s^{-1} pixel^{-1}. Note that the background rate varies only by a factor of 2 from the minimum to the maximum estimated values (in the previous example the background rate varied by a factor of 7, see panel f in Fig. 6.1). The contours next to black delimit a region with more than 3.5 photon count s^{-1} pixel^{-1}. The contours are drawn to underline the background rate variations. The background rate estimated with the BSS technique is smooth. Furthermore, the BSS background rate does not provide a null value where there is no satellite's exposure. In fact, the background rate is estimated with a spline model, which interpolates across holes

and gaps.

The background amplitude estimated by the SASS algorithm is shown in panel (e) of Fig. 6.3. The background value ranges over $0.001 - 0.468$ photon count pixel^{-1}. The SASS background map does not provide null values where the satellite was switched off. The strip with no exposure has a constant value of 0.001 photon count pixel^{-1}. A line is drawn on the image delimiting the area with minimum value. The line emphasizes the decreased agreement with the one in panel (c) with respect to the concordance of lines in panels (c, d). The contour levels, already used in panel (d), are also drawn (except for the contour with minimum value).

The comparison of panels (d) with (e) shows that the SASS background is not as smooth as the one estimated with the BSS algorithm. The SASS background shows large structures where the exposure map has small values. These structures are emphasized by the superposed contours.

The BSS technique provides an improved background model compared to the SASS algorithm. The outcome of the well–defined BSS background model is viewable with the detections of sources employing SPMs: Panel (b) shows few detected sources, as expected comparing panels (a, b). In Section 6.2.2, the BSS source positions and fluxes are compared to the ones obtained with the SASS algorithm. In Section 6.2.3, the outcome of the multiresolution analysis is commented. The intensity of false–positives in source detection are shown to be contained. In Section 6.2.4, the discovery of a cluster of galaxies in this *ROSAT* field is shown.

Smooth exposure map and varying background

The *ROSAT* field id RS932518n00 in the hard ($0.5 - 2.4$ keV) energy band is employed to show the capabilities of the BSS technique on data with large background variations. This field is characterized by a complex structure of hot gas caused primarily by the emissions of two galactic X–ray sources: (1) Vela supernova remnant (SNR) located at $\alpha = 8^{\rm h}35^{\rm m}20.6^{\rm s}$, $\delta = -45°10'35''$ (J2000); (2) SNR $RXJ0852.0 - 4622$ located at $\alpha = 8^{\rm h}52^{\rm m}$, $\delta = -46°22'$ (J2000) (Aschenbach *et al.*, 1995; Aschenbach, 1998).

In Fig. 6.5, panel (a), the photon count image of RS932518n00 field in the hard energy band is displayed. The image shows values in the range $0 - 136$ photon count pixel^{-1}. It is scaled to enhance the X–ray emissions. The satellite's exposure map is displayed in panel (e). The exposure map shows variations in the range $0.5 - 0.8$ ks.

The analysis of RS932518n00 in the hard energy band with the BSS algorithm is shown in panels (b), (c), (d) and (f). For background estimation and source detection the exponential prior pdf is employed.

In panels (b)–(d), three SPMs are displayed. The correlation length used for their realization is written on each image. The Gaussian weighting method is employed. Point–like sources superposed to a diffuse emission are detected at small correlation lengths (see panel b). Faint sources, such as diffuse emissions and filaments, are revealed at increasing correlation length.

In panel (f) the estimated background amplitude is displayed. The color bar is in units

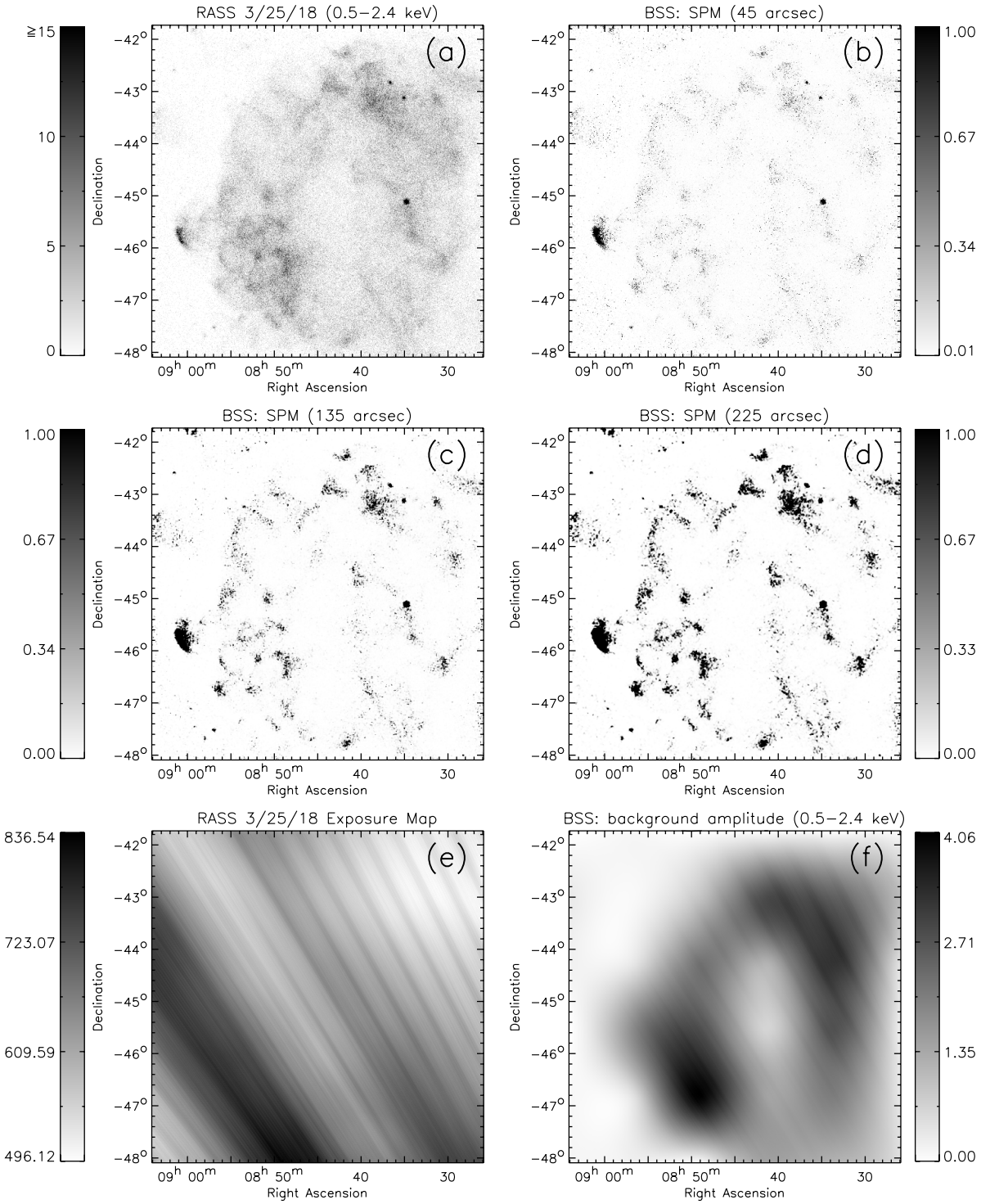

Figure 6.5: Analysis of the RASS field RS932518n00, *ROSAT* PSPC in Survey Mode.

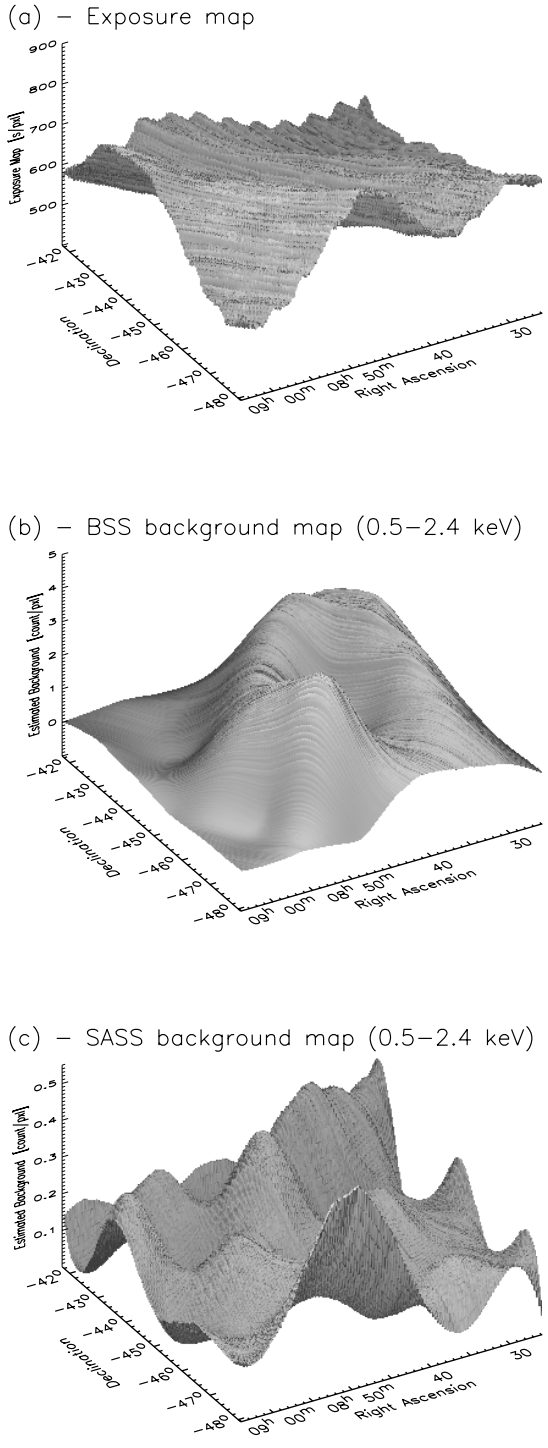

Figure 6.6: Panel (*a*): *exposure map* of the RASS field id RS932518n00 (Fig. 6.5). The z–axis indicates the exposure time in s pixel^{-1}. Panels (*b*) and (*c*): *estimated background amplitudes* of RS932518n00 field in the hard energy band with the BSS technique (panel *b*) and the SASS method (panel *c*). The z–axes show the estimated background count pixel^{-1}.

of photon count pixel^{-1}. The background map is estimated using 36 pivots equidistantly spaced along the field. The heterogeneous background is recovered.

In Fig. 6.6, two–dimensional representations of the exposure (panel a) and the background (panels $b-c$) maps are displayed. Panels (a) and (b) are already depicted in Fig. 6.5, panels (e) and (f), respectively. In panel (b), i.e. the surface plot of the estimated background amplitude obtained with the BSS technique, one can clearly spot: a foreground peak, i.e. the diffuse emission caused by the *Vela–Junior* SNR ($RXJ0852.0-4622$); a central emission, i.e. the (ring shape) shock front caused by the Vela SNR; and a background emission caused by another SNR, Puppis A. In panel (c) the background map estimated with the SASS algorithm is provided for comparison. The SASS estimated background values are in the range $0.001-0.55$ background count pixel^{-1}. The SASS background values are a factor of 10 lower than the BSS estimated background. Furthermore, the diffuse emissions caused by the SNRs are not present in the SASS background model.

In Section 6.2.2, the detected sources are cross–correlated with the RASS catalogues. Source positions and fluxes are compared. In Section 6.2.3, the BSS detections of point–like sources on top of the diffuse emissions are discussed. No point–like sources on top of the diffuse emissions are found from the RASS FSC and BSC with the exception given by the Vela pulsar, associated with the Vela SNR. The Vela pulsar fluxes and shapes obtained with the BSS and the SASS techniques are compared. The Vela pulsar flux obtained with the BSS algorithm is confirmed by XMM–*Newton* observations. The XMM–*Newton* satellite provides higher resolution images than *ROSAT*. XMM–*Newton* images are also used to strengthen the BSS capabilities in recovering extended sources observed by the *ROSAT* PSPC. In Section 6.2.4, the discovery of a potential QSO in this *ROSAT* field is shown.

Flexibility of background estimation on pivots

A careful estimation of the background is crucial for a proper assessment of source properties and for revealing sources that other techniques overlook. In this Section, the BSS background model is shown to be superior to frequently used techniques. In the next Sections, improvements in estimated source parameters and detections of new celestial objects are demonstrated.

The BSS background model depends on the number, position and amplitude of the pivots. However, only the amplitudes are estimated from the data. The number of pivots are selected according to the structures in the background. More (or less) pivots are needed if structures (or no structures) are present in the background. In principle, the pivots can be aligned on a grid or located in regions with large background variations. In practice, the pivots are automatically chosen equally spaced.

Note that the BSS technique can be improved employing adaptive splines for the background estimation. The parametric model can be extended allowing the data to select the number and location of the pivots. See Section 2.2.2 for more details.

In Fig. 6.7, four background rate models of the field id RS932518n00 in the hard energy band are shown at increasing number of support points. Different results of the TPS maps

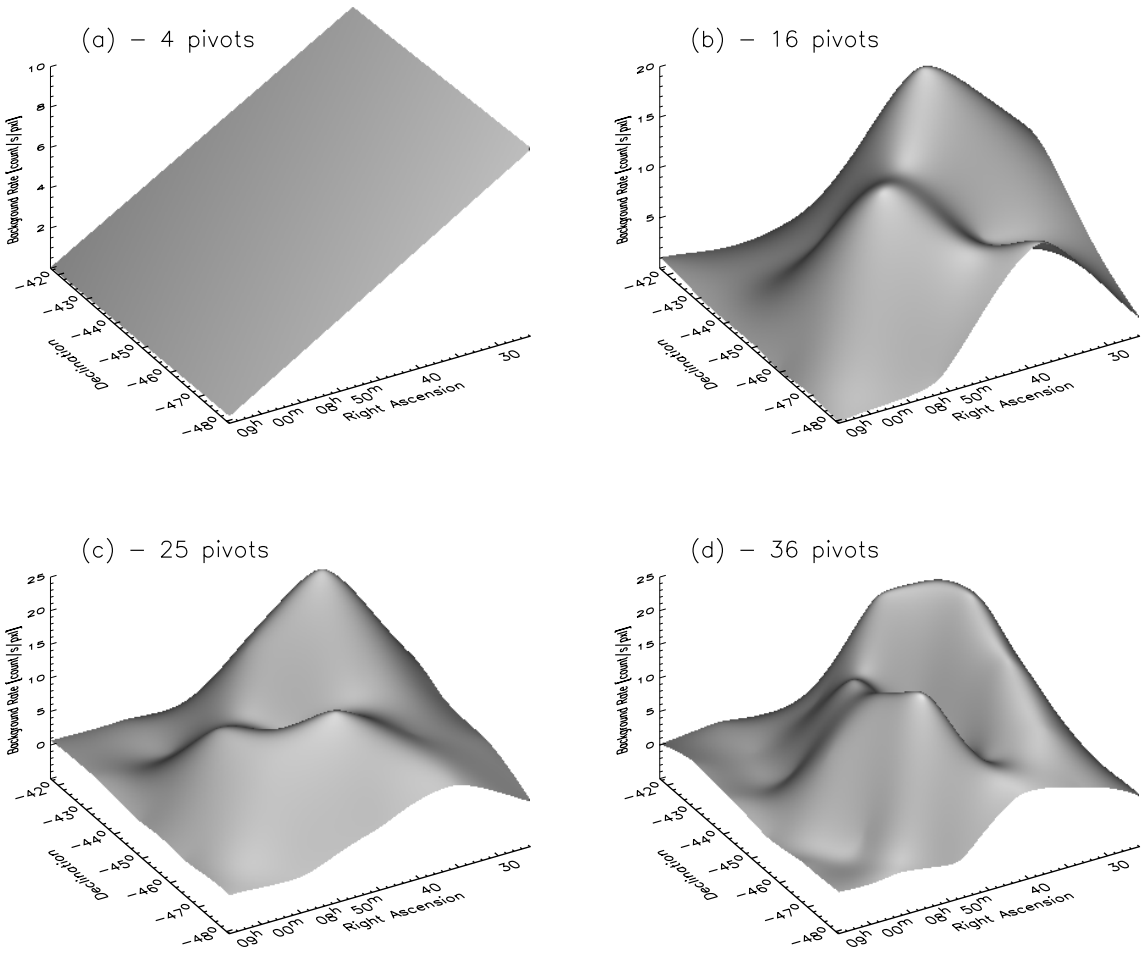

Figure 6.7: TPS maps of the field id RS932518n00 in the hard ($0.5-2.4$ keV) energy band. Panels (a)–(d): results employing 4, 16, 25 and 36 pivots, respectively.

are obtained with different number of pivots. The background rate model is close to a tilted plane with counts ranging $0-10$ if 4 pivots are used (panel a). The spline becomes more flexible at increasing number of pivots employed (panels b-d). Note that also the range of the estimated background count per pixel increases to $0-25$ at increasing number of pivots. The estimated background rates are compared to the photon count image in panel (a) of Fig. 6.5. The TPS estimated with 36 pivots, panel (d), provides the most reasonable background model.

The number of pivots influences the selection of what is source or background. On the one hand, a low number of pivots assigns more structures to be detected as source. On the other hand, a large number of pivots provides for more structures to be described as background. Therefore, the BSS technique allows the user to choose what is source or background tuning the number of pivots.

Comment on the background model

The extragalactic X–ray background (above 1 keV) is known to be largely due to accretion onto supermassive black holes, integrated over cosmic time (Hasinger *et al.*, 2002). Diagnostic of the population permeating the X–ray background emission is currently ongoing: See Brandt and Hasinger (2005) for a review and Gupta and Galeazzi (2009); Draper and Ballantyne (2009) for some recent studies. In the γ–ray energy band of the electromagnetic spectrum, instead, the origin of the diffuse background radiation is unclear (Rasera *et al.*, 2006; Dar, 2007; Inoue *et al.*, 2008; Ajello *et al.*, 2009).

The work of Snowden *et al.* (1994), applied to *ROSAT* PSPC pointed observations, proposes to separate the noncosmic background in several components, mainly: High energy charged particles penetrating the detector; Thomson and fluorescent scattering of solar X–rays in Earth's atmosphere; Short–term enhancements, i.e. low energy charged particles interacting with the atmosphere or telescope, like auroral X–rays; Long–term enhancements due to charged particles. Only the first two components of the noncosmic background are modelled, while the last two are often reduced through calibrations. Snowden *et al.* (1994) suggests to separate the different modelled components by subtraction from the estimated background.

The BSS background model is suited for investigating the nature of the cosmic background. An advance to the technique proposed by Snowden *et al.* (1994) can be given extending the BSS algorithm. When models of noncosmic and Galactic background radiation are known, the BSS technique is flexible enough to allow for a proper separation of each background radiation component. In fact, background components can be explicitly stated in the model for the background (i.e. in the *background hypothesis*). The mixture model technique is employed to separate each background component. No background subtraction is explicitly needed.

Note that the RASS data are survey mode observations. No models for the noncosmic background are available. Furthermore, the proposed extension to the BSS technique promotes a more sophisticated algorithm, that is instrument specific and not required for this thesis.

6.2.2 Catalogue comparisons

A quality assessment of the BSS source detection and characterization procedure is performed by catalogue comparisons. Specifically, the RASS catalogues and the BSS detections obtained analysing the three sample fields shown in Section 6.2.1 are compared. The results obtained from the analyses of these three fields are kept separated, because of their different variations in the background and exposure map. Sources listed in the BSS and RASS catalogues are cross–correlated. Sources from the BSS catalogue are matched with the RASS ones taking into account their angular distance. A searching radius of 1 arcmin is considered. In the *ROSAT* field id RS930625n00, a typical RASS field with background and exposure variations, the number of matched sources amount to 200. The number of matched sources in the other two fields, that are characterized by two extreme conditions of short exposure time one (RS932209n00) and large background variations the other (RS932518n00), is reduced to 12 and 6, respectively. Furthermore, in the field with the Vela SNR, i.e. RS932518n00, only sources listed in the RASS BSC are found and none of them are located on top of the SNRs shock fronts, except for the Vela pulsar itself. Sources located in the same line of sight of the diffuse emissions are analysed in Section 6.2.3.

In Figs 6.8, 6.9, 6.10 and 6.11, the BSS and the SASS results are examined with respect to source position, source count rates and source extent (i.e., the estimated size of the detected sources), source extent as a function of fluxes, probability of source detection in relation to the identification of extended sources. In the upper plots of Figs 6.8 and 6.9, a line is drawn to indicate equal values. The lower plots (residuals) display a zero line. Error bars from both techniques are placed only for the plots comparing source positions and fluxes. Error bars for source extent is placed only for the BSS algorithm, since no error bar for source extent is given in the RASS catalogues. Note that random errors provided by SASS are calculated based on the normal distribution and the 1σ standard deviations (i.e. at the 68.3% significance level) are provided for source parameters (Boese, 2004). Although in the SASS algorithm a deviation from the standard error is introduced to correct from the utilized normal to the proper Poisson distributions, the errors for source parameters of faint objects are not properly described: See Boese (2004) for more details.

In Fig. 6.8, source positions obtained with both techniques are in agreement. The BSS technique is capable to provide source positions as good as the ML technique, even if the BSS technique does not account so far for the instrumental PSF. Note the large error bars for some sources provided by the BSS algorithm. Large errors are assigned by the BSS algorithm to faint sources nearby background fluctuations due to Poisson statistics or to close by sources. Large error bars are not found in panels (c, d), that are characterized only by bright sources in uncrowded fields.

In Fig. 6.9, panels (a, b, c) show the comparison of estimated source fluxes as obtained by the BSS and the SASS techniques. The source count rates from the two techniques are similar, with few exceptions (e.g., the Vela pulsar in panel c). The residuals are normal distributed.
In panel (a), the fluxes for bright sources (> 0.15 count s^{-1}) obtained by the two techniques are in agreement within the estimated errors. The inset in panel (a) shows BSS versus

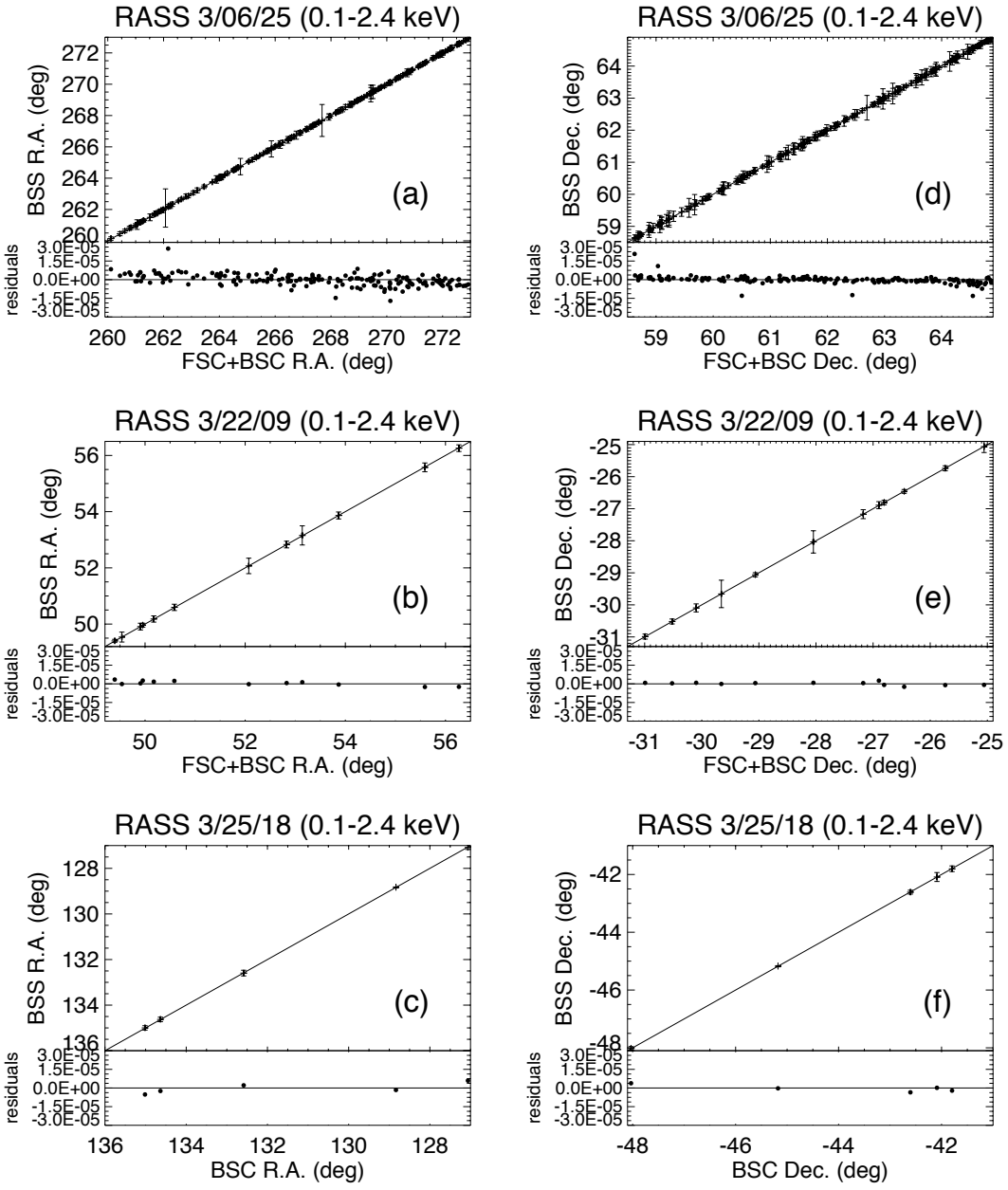

Figure 6.8: Comparison of BSS versus SASS results on source positions in celestial coordinate system (J2000): right ascension and declination on the left– and right–hand columns, respectively. Upper, middle and lower rows represent the results analysing the RASS field ids RS930625n00, RS932209n00 and RS932518n00, respectively.

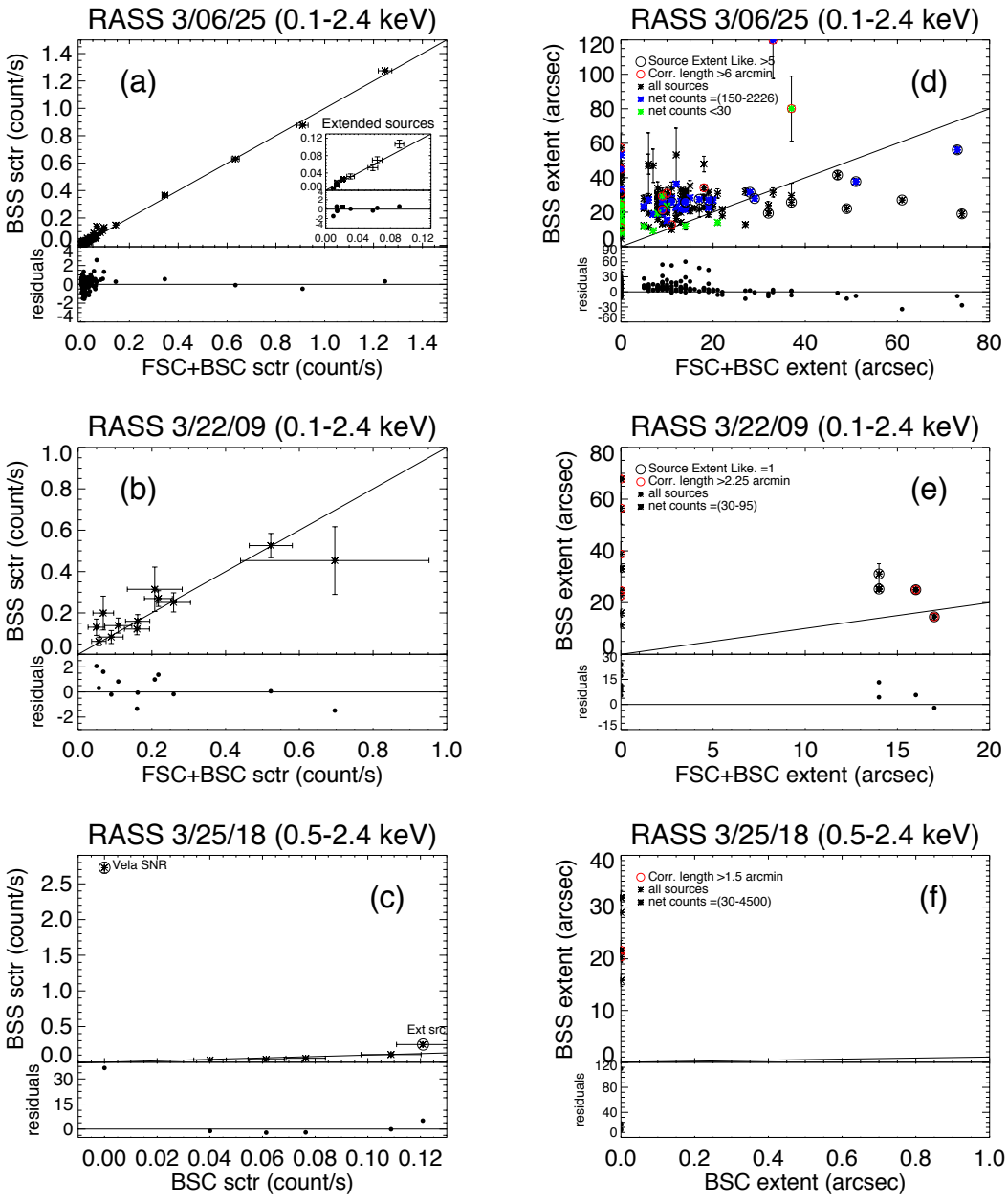

Figure 6.9: As for Fig 6.8, but source fluxes and extent at 1σ detection are compared on the left– and right–hand columns, respectively. See text for more details.

SASS source count rates for sources with < 0.12 count s^{-1} and the likelihood of source extent > 5 as given by SASS. The selected sources are investigated with the BSS technique and only the extended sources are kept (are excluded 0.4% of all sources with likelihood of source extent > 5). The BSS algorithm provides larger fluxes than the SASS technique at increasing count rates (for > 0.06 and < 0.12 count s^{-1}) for these extended sources. At increasing count rates, the ML algorithm may provide only poor fluxes for extended sources because the background in addition to a source is assumed to be constant and the background is not well–defined due to the employed class of bivariate spline (Boese, 2004). The BSS technique provides fluxes of faint extended sources (for $\lesssim 0.06$ count s^{-1}) similar and lower than the ones provided by SASS. Fluxes of faint sources and related errors are known to be overestimated by the ML algorithm (Boese, 2004).
In panel (b), large errors in source fluxes are provided by both techniques. The represented field is characterized by few photon counts and large exposure variations.
In panel (c), fluxes of sources located in the field with the Vela SNR are compared. Source count rates from the two techniques are similar only for sources located outside the shock front caused by the two SNRs. Note the detection at $0 - 2.7$ count s^{-1}. This object is the Vela pulsar (Vela SNR). The SASS technique provides a null value for the flux of the Vela pulsar. In addition, the object characterized by the SASS and the BSS techniques with 0.12 and 0.25 count s^{-1}, respectively, is an extended source (in the plot indicated with 'Ext src'). This object is known as Vela fragment A. Source parameters of the Vela pulsar and the Vela fragment A are commented further in Section 6.2.3.

In Fig. 6.9, panels (d, e, f) relate the RASS extent with the BSS extent of the detected sources. The SASS source extent is defined as the excess above the width of the instrumental PSF given in arcsec units. The SASS source extent is derived assuming: The instrumental PSF and the source surface brightness are two–dimensional Gaussian functions and independent of photon energy; The background is uniform (Voges *et al.*, 1999). A null value for the source extent is given when sources are point–like. For all the other sources, the SASS algorithm provides source extent at 1σ detection. The BSS technique, instead, gives the source extent (in arcsec units) resulting from the fitting of the multivariate Gaussian on source profiles. As shown in Section 6.2.3, the extent provided by the BSS algorithm is similar to the one obtained at 3σ detection above the local background in classic statistics. In each plot, the BSS extent is approximated to a 1σ detection. Although faint and bright sources and extended sources according to the BSS and the SASS techniques are highlighted, the discrepancy between the extent values provided by the two techniques is large. Based on the analysis of simulated data with the BSS algorithm (Chapter 4), it is not possible to infer the lack of correlation. The choice of approximating the BSS source extent to a 1σ detection in order to make the BSS extent closer to the one obtained with the SASS algorithm can be not appropriate. Although, the range of the BSS extent values are exceeding by a factor of 1.5 the range of the SASS extent values. Furthermore, in panel (f), all sources are assigned to be point–like by the SASS algorithm, that is known to be untrue as seen in panel (c).

In Fig. 6.10, the source extent versus the source count rates are plotted for the BSS (panel a, log–log scale) and the SASS (panel b, semi–log scale) algorithms separately. The

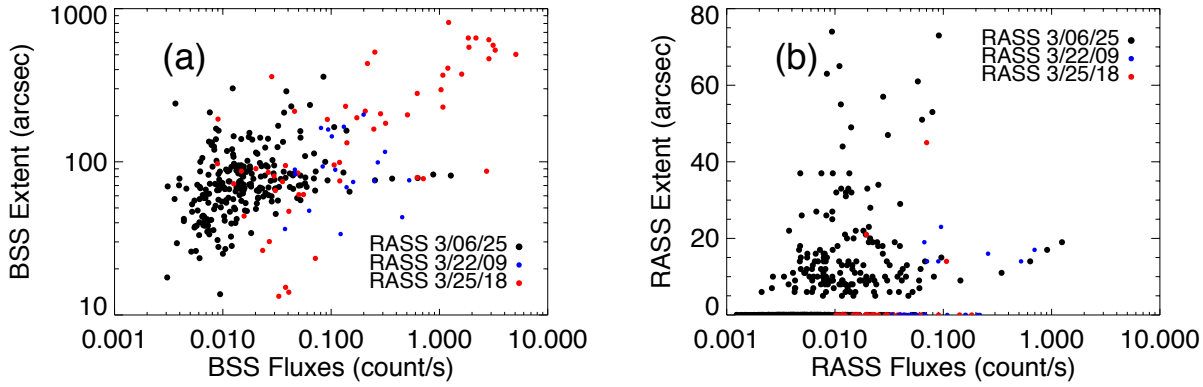

Figure 6.10: Panels (a) and (b) provide source extent as a function of source count rates according to the BSS and the SASS algorithms, respectively.

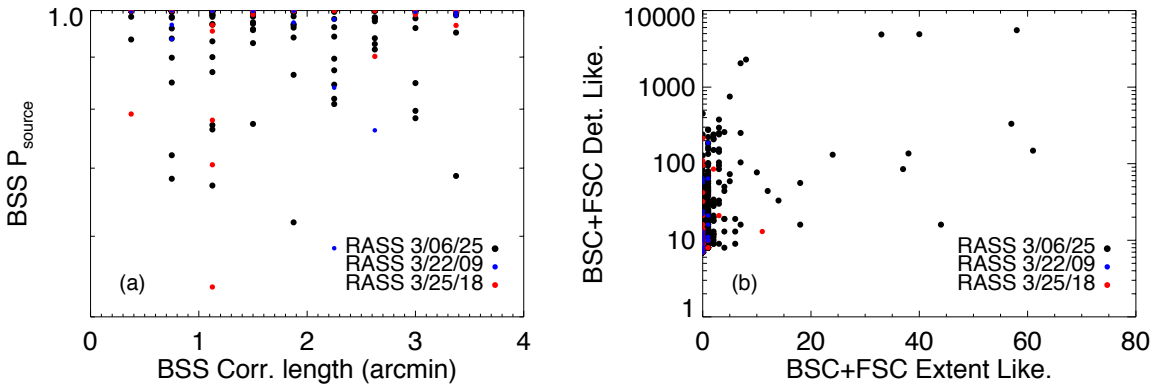

Figure 6.11: Panels (a): probability of source detection versus correlation length as in output from the BSS technique. Panel (b): source detection likelihood versus likelihood of source extent as given by the SASS algorithm.

extent is taken as given by the catalogues. In both plots, the majority of the sources are found with fluxes of about 0.01 count s^{-1}. The range of extent values with the BSS technique is larger than the one obtained with the SASS algorithm. The BSS algorithm detects several extended features in the field with the Vela SNRs. Note that so far the BSS algorithm does not set the lower limit of the source extent to be the PSF width.

In Fig. 6.11, panel (*a*) shows the source probability versus the correlation length of source detection as given by the BSS technique. Sources detected at large correlation lengths (i.e. several times the width of the instrumental *ROSAT* PSPC PSF, which is $\lesssim 2$ arcmin, see Boese 2000) are characterized by a low surface brightness and extended features. Faint point–like sources are detected at correlation lengths few times larger than the width of the instrumental PSF. Note the scale range on the y–axis $(0.5 - 1.0)$. As explained in Chapter 2, sources are strongly separated by false positives in source detection when $P_{\rm source} > 0.99$. Panel (*b*) depicts the source detection likelihood versus the likelihood of source extent, that can be used to identify extended sources, as given by the SASS algorithm. Panel (*b*) provides a more clear representation of point–like and extended sources than panel (*a*). Point–like and extended sources within the BSS formalism have been discussed in Chapter 2, Sections 2.2.5 and 2.3. A probability for a source to be extended can be implemented within the Bayesian formalism. Bayesian model comparison can be used to examine the detected source profiles with the exact instrumental PSF. Although a *ROSAT* survey PSF is available (Boese, 2000), simulated RASS fields are lacking (Boese, 2004). The development of this task can be part of a future project.

6.2.3 Robustness of the BSS technique

In this Section, details on some topics are given to strengthen the improvements obtained with the BSS technique with respect to the SASS algorithm. The considered topics are: The contamination from background fluctuations in source detection; Source extent given by the BSS technique compared to the one with classic statistics; The detections of sources affected by background fluctuations and of sources in the same line of sight of the diffuse emissions; The detections of extended sources and compared to images with higher resolution than *ROSAT*. For the discussion of these topics, fluxes of the detected sources are calculated and optical observations are used.

X–ray fluxes: $WebPIMMS$[5] (Mukai, 1993), version 3.9, is used to convert the source count rate in one band to flux in the same band. $WebPIMMS$ accounts for the instrumental response function. This physical parameter is derived for the detected sources as follows. First, the value of the interstellar hydrogen column density as measured at 21 cm for the estimated source positions is obtained following the works of Dickey and Lockman (1990) and Kalberla *et al.* (2005). The observed flux is then determined by calculating the conversion factor from count rate to flux employing a power–law source spectrum with a

[5] $WebPIMMS$ is set up as a WWW interface to the command–line version of $PIMMS$ (Portable Interactive Multi–Mission Simulator). The latter is a program available at $NASA - GSFC$.

photon index $\Gamma = 2$ (Szokoly *et al.*, 2004), where the photon spectrum is proportional to $E^{-\Gamma}$ (Henry *et al.*, 2006), for QSOs and AGNs or a Raymond–Smith-type spectrum model (Raymond and Smith, 1977) for clusters or groups of galaxies (Böhringer *et al.*, 2000) and SNRs (Aschenbach, 1998), redshift of zero (Böhringer *et al.*, 2000) if using a power–law otherwise the redshift and a fraction of global metal abundance (of solar value) whose numbers are given later in the text if using a Raymond–Smith model, and the galactic absorption according to the measured 21 cm value. No intrinsic absorption is assumed.

Optical observations Optical images are used to verify the efficiency of the BSS technique on the detected objects. The detected X–ray sources are analysed employing the optical R and I bands images of the Second STScI Digitized Sky Survey (DSS) (Lasker *et al.*, 2008). Between the available DSS images, the Palomar Observatory Sky Survey of second generation (POSS–II) are chosen for the improved resolution with respect to the ones of first generation. POSS–II fields (XP and XI plates) are sufficiently deep (Boschin, 2002) for most of the analysed celestial sources.

Contours of the surface brightness of the X–ray detected objects are superposed to the optical images. Following the work of Rosati (1995), contours are calculated convolving the RASS X–ray photon data image with a Gaussian kernel of given smoothing scale ($\sigma_{\rm g}$). The mean background value in addition to a detected source is used. The standard deviation of a Poisson distribution with mean background value ($\sigma_{\rm b}$) is changed in the standard deviation of the smoothed Gaussian image (σ), such that $\sigma = \sigma_{\rm b}/(2\sqrt{\pi}\sigma_{\rm g})$: See Rosati (1995) for more details. Therefore, the contours supply an approximation of the distribution of the X–ray background in the smoothed image, given by a normal distribution with standard deviation σ and mean background value provided by the BSS algorithm. Contours of the surface brightness of the X–ray detected objects are calculated for $n \cdot \sigma$ values above the local X–ray background. This method provides for an additional proof of and independent from the detections given by the BSS algorithm, shown through SPMs.

Contained contamination

The capabilities of the BSS technique in providing reliable detections is shown analysing the *ROSAT* field id RS932209n00 in the soft ($0.1 - 0.4$ keV) energy band: See Fig. 6.3 and Section 6.2.1 for more details. The characteristics of this field, i.e. few source counts and a strip with no exposure, are known to be challenging to conventional source detection methods. In fact, the SASS technique is known to detect false positives on strip edges. Obvious false positives, detected by SASS, have been manually removed (Gruber *et al.*, 1997; Voges *et al.*, 1999).

In Fig. 6.12, panel (a) provides the density of the photon counts in the RASS field id RS932209n00 (y–axis in log scale). The field is characterized by 93% of the pixels with a null value and few detected sources. The background is small (~ 0.2 count pixel^{-1}). Due to Poisson statistics (see Chapter 3), the number of false positives in source detection can be large. Panel (b) shows the densities of pixels with probability of source detection in bins of 0.01 for several correlation length values (y–axis in log scale). Most of the

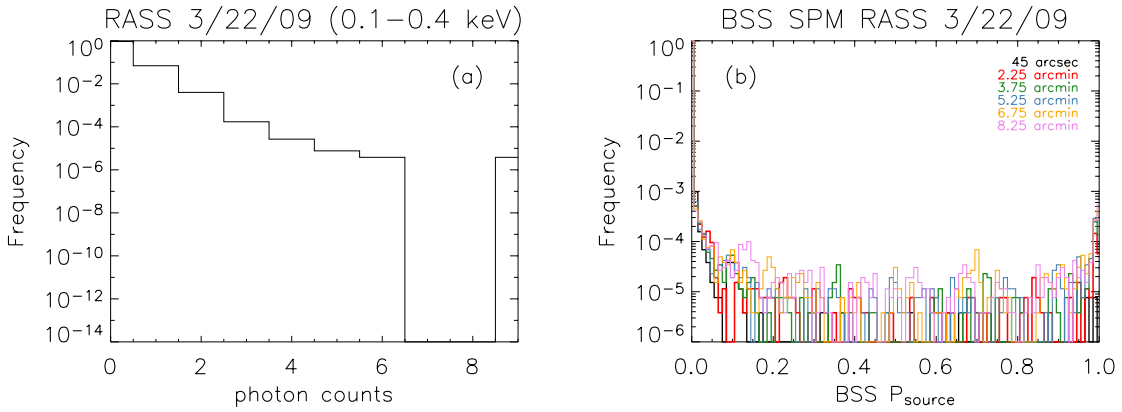

Figure 6.12: Panel (a): histogram of RASS field id RS932209n00 in the soft ($0.1 - 0.4$ keV) energy band. Panel (b): histogram of several SPMs at 6 correlation lengths, obtained analysing the field in panel (a).

pixels are assigned with a source probability ≤ 0.1, i.e. the detected background. The densities of pixels increase for values ≥ 0.99, indicating the detected sources. All values of $P_{\rm source} = (0.1 - 0.99)$ show fluctuations in the data. Less than 0.02% of the pixels may show false positives in source detection. Comparing the BSS catalogue for this field with catalogues at the same and other wavelengths, no clear evidence of false positives in source detection is found. All sources detected with the BSS algorithm are found with counterparts at the same (but deeper) or other wavelengths. More details on the detected sources in this RASS field are given in the following Sections.

BSS source extent in terms of classic statistics

The detections of a source from the RASS field id RS932209n00 (see Section 6.2.1) with the BSS and the SASS techniques are compared.

The X–ray source catalogued as 1RXSJ031938.2-250325 in the FSC (Voges *et al.*, 2000) is considered as illustration. This object is also listed in the two–degree-field Galaxy Redshift Survey (2dFGRS) (Colless *et al.*, 2001) as 2dFGRS TGS111Z214 from the optical part of the electromagnetic spectrum. It is a galaxy at redshift $z = 0.086$. No counterparts with other X–ray catalogues have been found employing the VizieR (Ochsenbein *et al.*, 2000), a database of astronomical catalogues. This source is located at $\alpha = 3^{\rm h}19^{\rm m}38.6^{\rm s}$, $\delta = -25°03'43.12''$ (J2000). The reported position is given from the BSS technique. This source is located towards the field edge: Upper left–hand corner of panel (a), Fig. 6.3.

In Table 6.1, the source parameters for 1RXSJ031938.2-250325 obtained by the BSS and the SASS techniques are summarized. The column *Sctr* indicates source count rates estimated in the broad ($0.1 - 2.4$ keV) energy band. The shape parameters are indicated with the source extent as given by SASS or with $\sigma_{\rm x}$, $\sigma_{\rm y}$, θ as given by the BSS technique. The parameters $\sigma_{\rm x}$, $\sigma_{\rm y}$ are the FWHMs (in arcsec units) derived from a multivariate

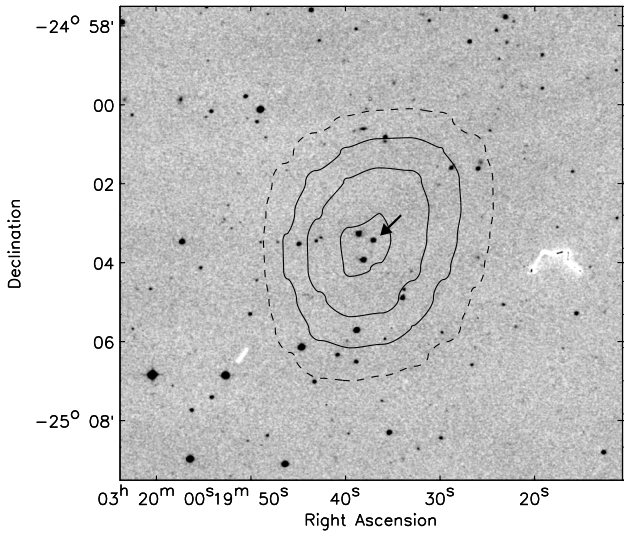

Figure 6.13: POSS–II I plate with overlaid *ROSAT* contours corresponding to 3, 5, 7 and 9 σ above the local background. In the image centre, 2dFGRS TGS111Z214, a close by galaxy, is indicated with an arrow. This object is listed in the FSC (Voges *et al.*, 2000) and reported in Table 6.1. See text for more details.

Table 6.1: Comparison of source parameters for 1RXSJ031938.2-250325 as listed in the FSC (Voges *et al.*, 2000) and the BSS technique in the broad $(0.1-2.4$ keV) energy band. This object is detected in the RASS field id RS932209n00.

Technique	Sctr	ExpTime	Source extent			Likelihood
	(count s^{-1})	(s)	(arcsec)			-ln(1-P)
SASS	0.0683±0.028	145	0.0			12
			σ_x	σ_y	θ	P_{source}
			(arcsec)	(arcsec)	(deg)	
BSS	0.114±0.039	151.3	233.4±48.5	158.2±26.9	-90	0.999995

Note. The SASS algorithm provides the Likelihood, that is related to the probability of source detection (P) obtained from classic statistics. The BSS technique provides P_{source}, i.e. the probability of source detection. See text for more details.

Gaussian profile fitted on the photon count distribution of the detected source. θ is the rotation angle in degrees from the positive right ascension axis to the positive declination. *ExpTime* indicates the observational exposure time. The last column provides a measure of certainty for the object being real according to the two techniques. The value of P, calculated from the Likelihood, is similar to $P_{\rm source}$. However, as already shown in Chapter 3, the BSS technique is more conservative than procedures based on classic statistics, which is the case for the SASS method. Therefore, the probability of source detection given by the BSS technique is larger than the one provided by the SASS algorithm. In Table 6.1, the SASS technique provides a null value for the source extent, since this galaxy is classified as point–like. When SASS detects sources as extended, the source extent is given at 1σ detection. The BSS technique, instead, detects this object with the maximum in source probability at 3.75 arcmin, indicating the detection of a faint diffuse source. In Fig. 6.13, the DSS optical image centred on this galaxy is shown. The contours of the *ROSAT* broad band image are reported. The contours confirm the extent provided by the BSS technique. In fact, the *ROSAT* contours at 3 σ above the local background corresponds to the BSS reported source extents and positional angle.

The difference in the estimated fluxes for this galaxy by the BSS and the SASS techniques is commented. The BSS technique provides the source count rates and the background count rates (not shown in Table 6.1) larger by a factor of 1.7 and 1.3, respectively, than the SASS technique. The BSS technique allows the investigation of the core and the tails of the source distribution, detecting until 3σ as above explained. Therefore, the BSS algorithm naturally increases the count rates of sources presenting extended features with respect to SASS.

BSS faint source detections and their errors

Fig. 6.14 shows the detections obtained with the BSS technique in a portion of the sky with faint point–like and extended sources. Each image is centred at $\alpha = 18^{\rm h}6^{\rm m}15^{\rm s}$, $\delta = +59°38'26''$ (J2000). The upper left–hand image is a zoom in the *ROSAT* photon count image of the field id RS930625n00 in the hard ($0.5 - 2.4$ keV) energy band. The photon counts in this field are in the range $0 - 80$. The image here displayed is scaled in the range $0 - 10$ photon counts with the purpose to enhance the sources. A 10 arcmin bar is displayed to indicate the image size. The last image depicts the estimated background with the BSS technique. The background is almost constant (~ 0.64 count) in this portion of the sky. SPMs are displayed at several correlation lengths. Ellipses are superposed to indicate the extent of the objects detected with the BSS technique. Ellipses are drawn at the correlation length of source detection. Region shapes with an ellipse are indicated from A to F. Crosses, numbered from 1 to 5, are superposed to indicate the SASS detections, listed in the FSC (Voges *et al.*, 2000).

Extended sources In this portion of the sky, the BSS technique detects an extended source. It is indicated with the letter E, located not far away from the bar indicating 4.5 arcmin resolution. At this resolution, the maximum in source probability is reached. This

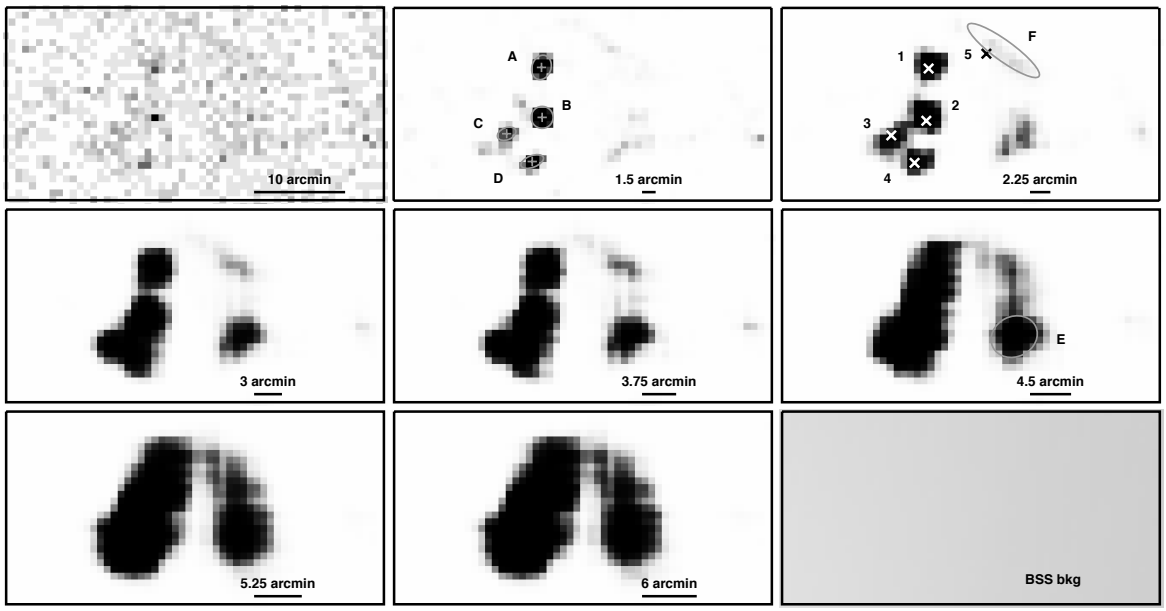

Figure 6.14: The upper left–hand image is a zoom in the RASS field id RS930625n00 in the hard $(0.5 - 2.4$ keV) energy band. The image is centred at $\alpha = 18^{\rm h}6^{\rm m}15^{\rm s}$, $\delta = +59°38'26''$ (J2000). The following images are results with the BSS technique. Seven SPMs at decreasing resolutions are displayed. The correlation length of each SPM is written in the lower right–hand corner of each image. The lower right–hand image is the estimated background amplitude.

Table 6.2: Positions and count rates for four point–like sources shown in Fig. 6.14, as given by two catalogues: BSS and FSC (Voges *et al.*, 2000). The BSS and FSC source count rates are estimated from the broad $(0.1 - 2.4$ keV) energy band.

Catalogue	Seq	R.A. (deg)	Dec. (deg)	Sctr (count s^{-1})	
BSS	A	271.84385	59.7105	0.01485 ± 0.00304	
	B	271.85464	59.6201	0.01157 ± 0.03502	
	C	271.95508	59.5811	0.00281 ± 0.00784	
	D	271.84983	59.5326	0.00604 ± 0.00250	
					RASS source name
FSC	1	271.84872	59.7049	0.01575 ± 0.00285	1RXSJ180723.7+594217
	2	271.84375	59.6089	0.01188 ± 0.00248	1RXSJ180722.5+593632
	3	271.96667	59.5776	0.00835 ± 0.00231	1RXSJ180752.0+593439
	4	271.87543	59.5303	0.00958 ± 0.00252	1RXSJ180730.1+593149

extended source is a candidate for a cluster or group of galaxies. This extended object is further commented in Section 6.2.4, Fig. 6.19. The EURO–VO Tools are used to search for counterparts. Only, few near–infrared (Jarrett *et al.*, 2000) and radio (Rengelink *et al.*, 1997) galaxies (six in total) are found in the surrounding region. However, redshift information is missing and no conclusive results can be drawn.

It is interesting to note that the extended source indicated with E in Fig. 6.14 merges with another extended feature. This secondary extended feature is indicated with F in the SPM at 2.25 arcmin. The BSS technique detects this object with a probability of only 69%. All the other objects are detected with $P_{\text{source}} \geq 0.99$. The merging of the two extended features does not provide an indication that the two objects are part of a unique celestial source. Source F has a counterpart in the FSC (Voges *et al.*, 2000). This object is indicated with a cross, number 5. The FSC id for this object is: $1RXSJ180634.2+594421$. The FSC lists this source with a source detection likelihood of $L = 9$ and source extent of null value (indicating the detection of a point–like source). No counterparts of $1RXSJ180634.2+594421$ are found employing the EURO–VO Tools at other wavelengths.

Point–like sources Four point–like sources are neighbouring the two extended features on the left–hand side: See, e.g., the SPM at 1.5 arcmin. These objects have been detected both by the BSS and SASS algorithms. The detections with the BSS technique are indicated with the letters $A - D$ in the SPM at 1.5 arcmin resolution. The source extents obtained with the BSS technique are superposed. The detections acquired with the SASS technique are indicated with the numbers $1 - 4$ in the SPM at 2.25 arcmin resolution. Crosses indicate the source positions as given by the FSC (Voges *et al.*, 2000). In Table 6.2 the source positions and count rates are shown. Following the scheme of the FSC, Table 6.2 shows count rates in the broad energy band. A column is added for the FSC to indicate the source identifier. The results, within the estimated uncertainties, are similar with the two techniques. However, the errors for sources B and C are much larger. This is due to source enhancements close by the two sources B and C. The faint source enhancements may be due to Poisson statistics or to real faint sources in the neighbourhood. The origin of these faint enhancements are not distinguished by the BSS technique. The BSS errors are informative.

Detections on top of diffuse emissions

The BSS method combined with the multiresolution analysis allows one to identify the detection of point–like sources on top of a diffuse emission and of extended X–ray features, such as the SNR $RXJ0852.0 - 4622$ and the Vela D (or Pencil Nebula) located at $\alpha = 9^{\text{h}}0.2^{\text{m}}$, $\delta = -45°57'$ (J2000). Furthermore, Vela D has been detected partially superposed to another diffuse emission, known as Vela D' (see Fig. 6.5, panels $a - d$, for more details). Aschenbach *et al.* (1995) already identified Vela fragments D and D' as two superposed objects. The BSS algorithm detects Vela D and D' at different resolutions. Vela D is detected with the maximum in source probability when pixels are not correlated, due to its brightness. Vela D' is detected at a correlation length of 3.75 arcmin. The source

fitting routine characterizes Vela D' as an extended source located 17 arcmin far from Vela D centre. The BSS algorithm detects about 50 objects analysing this *ROSAT* field.

In Table 6.3, part of this catalogue is provided. Columns *R.A.*, *Dec.*, *Sctr*, $\sigma_{\rm x}$, $\sigma_{\rm y}$ and θ are the estimated positions (right ascension and declination), source count rates and source parameters in output from the BSS technique. Each object listed is detected with a probability larger than 0.999. Source sequences (1), (3), (4) and (8) are revealed with uncorrelated pixels. Instead, the remaining objects are detected at larger correlation lengths.

The objects indicated with *Seq* (1) and (2) are the Vela pulsar and the diffuse emission provided by the central core of *Vela–Junior* SNR, respectively. The Vela pulsar, located near the centre of the remnant, originated from a massive progenitor star that exploded about 10^4 yr ago (Miyata *et al.*, 2001). The *Vela–Junior*, instead, is considerably younger ($\sim$ 680 yr as the most probable value, Aschenbach *et al.* 1999). *Seq* (3) and (4) are two objects located towards the north–west corner of image (*a*) in Fig. 6.5. *Seq* (3) and (4) are located along the line of sight of the hot diffuse emission caused by the Vela SNR. Objects (3) and (4) are low mass *X*–ray binaries, catalogued as INTREF 361 and INTREF 359 (Ebisawa *et al.*, 2003), respectively, in the γ–ray part of the electromagnetic spectrum. The remaining objects are outside the shock front caused by the two SNRs. Object (5) is a dwarf nova (CU Velorum, Downes *et al.*, 1997). Objects (6), (7) and (8) are further commented in the following Sections.

In Table 6.4, the column indicated with *Matched id* corresponds to an *id* given by catalogues created analysing *ROSAT* data and whose position coincides within the positional errors with the one obtained with the BSS algorithm. The searching radius is 1 arcmin. During this selection, priority is given to identifiers provided by the RASS catalogues (Voges *et al.*, 1999, 2000), when available. No celestial objects are found in the FSC. Sources listed in the BSC are indicated with a cross. The sources detected by SASS in *ROSAT* HRI data sets are indicated with a *b* flat. The *Matched id* names contain the following word forms: *RX* indicates *ROSAT X*–ray, *S* stands for Survey data sets and *H*, instead, for HRI pointed observations. Catalogue identifiers highlighted with an asterisk are coming from a point source catalogue, the WGACAT (White *et al.*, 1994), generated from all *ROSAT* PSPC pointed observations. These observations are deeper than the ones coming from the RASS. The remaining columns are providing the energy band employed for the catalogued source count rate (*Sctr*) and the source count rate in two bands. The source fluxes in the hard ($0.5 - 2.4$ keV) energy band are derived from the source count rates in the broad ($0.1 - 2.4$ keV) energy band employing the spectral properties given by the referred catalogues. A horizontal bar is placed when relevant information is not available from the relative catalogue. Note that RASS catalogues do not have any entry for point–like objects on top of the diffuse emissions, i.e. sources *Seq* (1), (3) and (4).

The count rates provided for source *Seq* (5) by the BSS technique, the BSC (Voges *et al.*, 1999) and the WGACAT (White *et al.*, 1994) coincide within the errors: see values in bold font in Tables 6.3 and 6.4. Source (5) is located in a region with spatially constant background. Note that source (5), see Fig 6.15, is a dwarf nova, a subclass of cataclysmic variables with non–magnetic white dwarfs. The hot corona around the white dwarf can

Table 6.3: BSS sample catalogue from the analysis of RS932518n00 field in the hard $(0.5-2.4$ keV) energy band

Seq	R.A. (J2000)	Dec. (J2000)	Sctr (count s^{-1})	σ_x (arcmin)	σ_y (arcmin)	θ (deg)
(1)	$08^h35^m20.4^s$	$-45°10'36.38''$	$2.7196\pm0.0743^{(*)}$	3.4±0.1	3.4±0.1	90.0±0.2
(2)	$08^h51^m39.60^s$	$-46°13'40.78''$	1.0326±0.1010	11.6±1.4	7.3±0.6	-78.4±0.1
(3)	$08^h37^m24.62^s$	$-42°53'55.75''$	0.6198±0.0483	3.1±0.3	2.2±0.2	-49.3±0.2
(4)	$08^h35^m55.85^s$	$-43°11'11.28''$	0.7084±0.0523	3.0±0.3	2.7±0.2	-90.0±0.7
(5)	$08^h58^m30.67^s$	$-41°48'09.86''$	**0.1069±0.0154**	3.7±0.5	2.8±0.4	47.9±0.3
(6)	$08^h57^m44.81^s$	$-41°51'51.51''$	0.251±0.0037	6.4±0.6	5.6±0.6	74.3±0.5
(7)	$08^h57^m35.64^s$	$-41°56'17.39''$	0.0378±0.0115	3.7±1.3	2.7±0.7	-24.5±0.8
(8)	$08^h56^m48.86^s$	$-47°34'33.10''$	0.1204±0.0156	2.9±0.4	2.4±0.4	-90.0±0.5

Note: (1) Vela pulsar, (2) core of Vela–Jr. SNR, (3) and (4) X–ray binaries, (5) Dwarf Nova, (6) Vela fragment A, (7) 2XMM J085736.6-415549, (8) GSC2.3 S66I031249.
$^{(*)}$ BSS technique: F_X([0.5-2.0]keV)=$(3.176 \pm 0.009) \times 10^{-11}$ erg s^{-1} cm^{-2};
XMM-Newton Survey Science Centre (2008): F_X([0.5-2.0]keV)=$(3.285 \pm 0.004) \times 10^{-11}$ erg s^{-1} cm^{-2}.

Table 6.4: Cross–correlation of public catalogues with the BSS sample catalogue shown in Table 6.3

Seq	Matched id	Energy band (keV)	Sctr $(0.1-2.4$ keV) (count s^{-1})	Sctr $(0.5-2.4$ keV)$^{(\ddagger)}$ (count s^{-1})
(1)	1RXS J083520.6-451035$^{(\dagger)}$	—	—	—
	1RXH J083520.5-451036	0.1-2.4	$1.18\pm0.0086^{(\flat)}$	—
(2)	RX J0852.0-4622	—	—	—
(3)	1WGA J0837.3-4253	0.24-2.0	$0.0507\pm0.0066^{(*)}$	0.0323±0.0043
(4)	1WGA J0835.9-4311	0.24-2.0	$0.3890\pm0.0160^{(*)}$	0.3605±0.0148
(5)	1RXS J085832.5-414745	0.1-2.4	$0.1829\pm0.0208^{(\dagger)}$	**0.1088±0.0114**
	1WGA J0858.5-4147	0.24-2.0	$0.124\pm0.0041^{(*)}$	**0.0882±0.0038**
(6)	1RXS J085748.6-415101	0.1-2.4	$0.141\pm0.0182^{(\dagger)}$	0.1206±0.0156
(7)	—	—	—	—
(8)	—	—	—	—

Note: (†) Voges *et al.* (1999); ($\flat$) ROSAT Scientific Team (2000); ($*$) White *et al.* (1994); (‡) source count rate derived from the hardness ratios.
EURO–VO software tools are used for this work.

reach temperature of $10^6 - 10^7$ K (van der Woerd, 1987). A diffuse emission around this object is detected with the BSS algorithm. Source (5) is detected at a correlation length of 2.25 arcmin (about the size of the *ROSAT* PSPC PSF). The estimated source extents are larger than the width of the *ROSAT* PSPC PSF.

The BSS count rates for point–like sources in the line of sight with the hot diffuse emission, i.e. sources (1), (3) and (4), are larger than the ones given by the other catalogues by a factor of $2 - 10$. In order to assess the capabilities of the BSS technique in estimating the fluxes of point–like sources on large background variations, the Vela pulsar is taken as example due to the recent observations of this object by the XMM–*Newton* satellite. In Table 6.3, the fluxes for the Vela pulsar are reported from the BSS technique and from the XMM-Newton Survey Science Centre (2008) catalogue. For the conversion from count rate to flux an $N_H = 3.87 \times 10^{20}$ cm^{-2} (Dickey and Lockman, 1990), a Raymond–Smith spectral model with $T = 5$ keV, a solar abundance ratio of 0.4 (Aschenbach, 1998) are used. Note that XMM-Newton Survey Science Centre (2008) catalogue reports the flux values in the $(0.5 - 1.0$ keV) and $(1.0 - 2.0$ keV), separately. The total flux in the $(0.5 - 2.0$ keV) is only approximatively the sum of each reported value. The BSS flux for the Vela pulsar on RASS data is close to the result obtained by the XMM–*Newton* satellite, characterized by higher resolution than *ROSAT*. The difference between the BSS result and the one provided by the XMM–*Newton* satellite is about 3%, that is well within the 5% expected divergence. Therefore, the BSS technique provides improved fluxes with respect to the reported values from *ROSAT* PSPC and HRI (see Table 6.4, source *Seq* 1) when applying standard techniques.

Identification of extended sources at low resolution

In Fig. 6.15, three panels covering the same sky view are shown. In these panels sources (5), (6) and (7), from Tables 6.3 and 6.4, are represented. Panel (*a*) depicts the POSS–II *R* plate with superposed *ROSAT* contours for sources (5) and (6) (left– and right–hand peaks, respectively) and for source (7) (a faint emission below source 6). Panel (*b*) is the SPM from the BSS technique corresponding to panel (*a*). The SPM is obtained analysing the hard $(0.5 - 2.4$ keV) energy band. The three represented objects are brighter in the hard $(0.5 - 2.4$ keV) than in the soft $(0.1 - 0.4$ keV) energy bands. In panel (c), the *X*–ray sky view from XMM–*Newton* satellite is depicted. The *X*–ray image shows the dwarf nova CU Velorum, i.e. source (5) in panel (*b*), and Vela fragment A, i.e. source (6) in panel (*b*). The detection of source (5) is commented in the previous Section.

Vela fragment A is a boomerang–like structure located outside the main shell of the SNR (Miyata *et al.*, 2001). Two components of Vela fragment A have been identified: a head, i.e. source (6), and a fainter extended tail (south–west direction) (Aschenbach, 1998; Miyata *et al.*, 2001). In the area where the tail of Vela fragment A is distributed, source (7) has been detected.

The BSS technique detects source (6) at a correlation length of 2.25 arcmin, indicating the detection of a low surface brightness source. Table 6.3 provides the parameters for source (6). This source is characterized by an extent larger than the width of the *ROSAT*

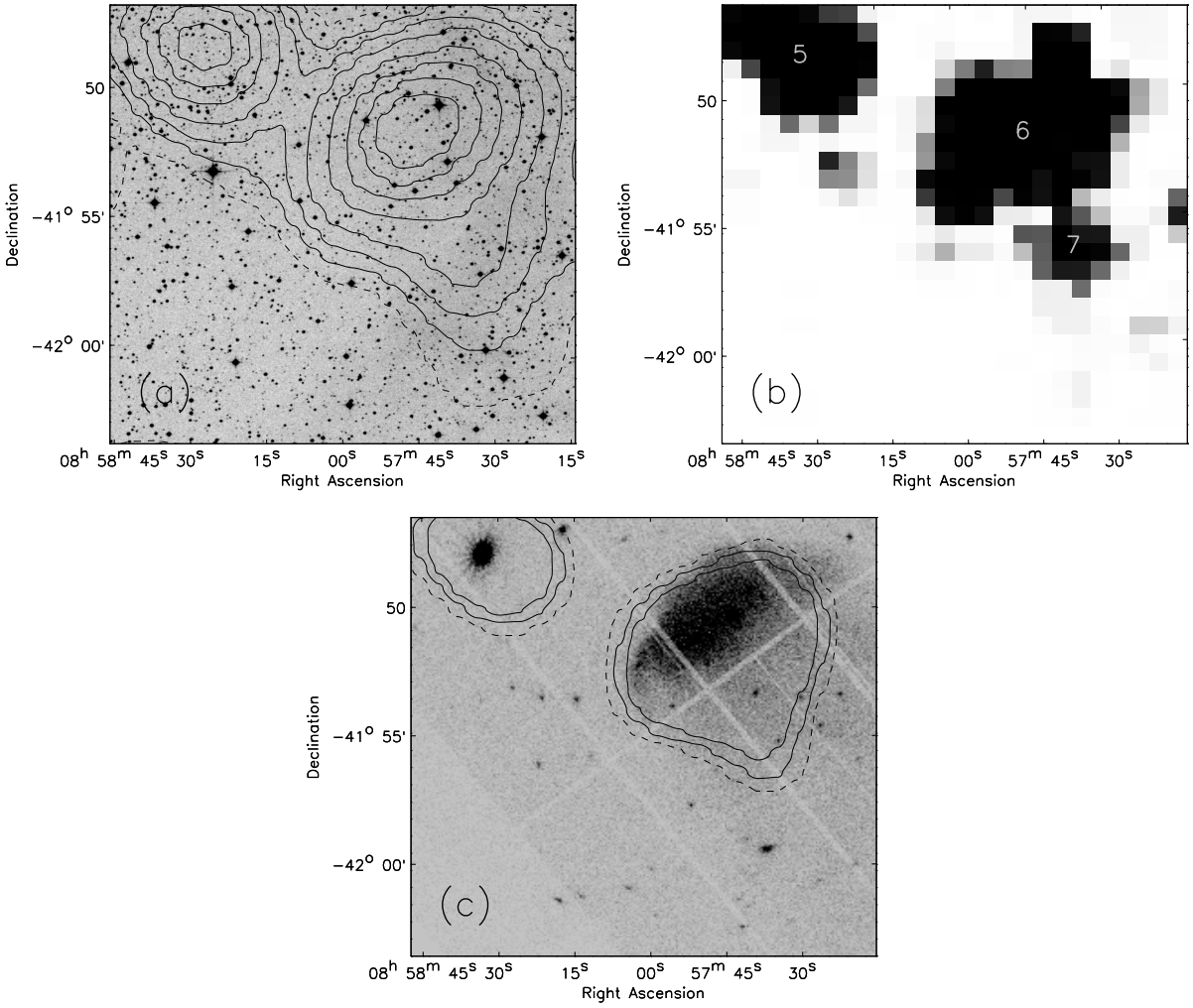

Figure 6.15: Panel (a): POSS–II R plate with superposed *ROSAT* contours corresponding to 3, 5, 7, 10, 15, 20, 25 and 30 σ above the local background for sources indicated with *Seq* (5), (6) and (7) in Table 6.3. Panel (b): SPM obtained with a correlation length of 2.25 arcmin. Detected sources are annotated with their sequence number. Source (5) is CU Velorum, a dwarf nova. Source (6) indicates Vela fragment A. Source (7) is matched with 2XMM J085736.6-415549. Panel (c): SPM contours on X–ray image from XMM–*Newton* observation. Panels (a), (b) and (c) cover the same sky view. No counterparts in FSC (Voges *et al.*, 2000) and BSC (Voges *et al.*, 1999) catalogues are found for source (7).

PSPC PSF. The FSC (Voges *et al.*, 2000), instead, reports a null extent for this object, indicating the detection of a point–like source. Even in condition of lower resolution with *ROSAT* than with the XMM–*Newton* satellite, the BSS algorithm is capable to detect the extended feature of Vela fragment A and to properly classify it.

Source (7) is cross–correlated with 2XMM J085736.6-415549 (Watson *et al.*, 2008). This source is detected at a correlation length of 2.6 arcmin, indicating the detection of a low surface brightness object. However, the estimated fluxes from the BSS technique and the one listed in Watson *et al.* (2008) do not correspond. The BSS technique provides a significantly larger flux than Watson *et al.* (2008). The unmatched fluxes is explainable by the lower resolution of *ROSAT* with respect to XMM–*Newton* satellite and by the emission of the tail of Vela fragment A, incrementing the flux of source (7). In this extreme case of faint diffuse emission ($F_X = 3.0 \times 10^{-12}$ erg s^{-1} cm^{-2}, Aschenbach 1998) with a faint point–like source ($F_X([1.0-2.0]\text{keV}) = (5.7 \pm 2.3) \times 10^{-16}$ erg s^{-1} cm^{-2}, Watson *et al.* 2008), the BSS technique fails in properly distinguishing the two emissions. The faint point–like source, cross–correlated with 2XMM J085736.6-415549, is not properly distinguished by the diffuse emission of the tail of Vela fragment A.

6.2.4 Discovery of new celestial objects

Examples of discovered X–ray sources is reported: two point–like and two extended sources. For these sources, approximate values of their physical parameters are provided: energy fluxes and luminosities in cgs units. For clusters or groups of galaxies, physical parameters are reported only when their redshift is known from previous analyses. The knowledge about the X–ray luminosity of clusters is important since it is strictly connected to their mass. For clusters or groups of galaxies, a value of their mean surface brightness is given. The mean surface brightness is essential for interpreting cosmological observations (Peacock, 1999). *WebPIMMS* is used to convert estimated count rates to fluxes: See Section 6.2.3 for more details.

X–ray fluxes: This physical parameter is derived for the newly discovered sources as already described in Section 6.2.3.

X–ray luminosities: The X–ray luminosity for the detected celestial object is provided only when knowing their redshift. A ΛCDM cosmological model for a flat universe is assumed with the parameters $\Omega_m = 0.3$ (matter density) and $\Omega_\Lambda = 0.7$ (vacuum energy density or cosmological constant), and the Hubble constant $H_0 = 70$ km s^{-1} Mpc^{-1} (Spergel *et al.*, 2003). For the values of the X–ray luminosities, the K correction is taken in consideration by converting the observed count rate into the unobserved flux in the rest–frame and computing the luminosity thereof (see Hogg *et al.* 2002 for more details).

Mean surface brightness: An approximate value of the mean surface brightness of clusters or groups of galaxies is computed. The mean surface brightness is calculated

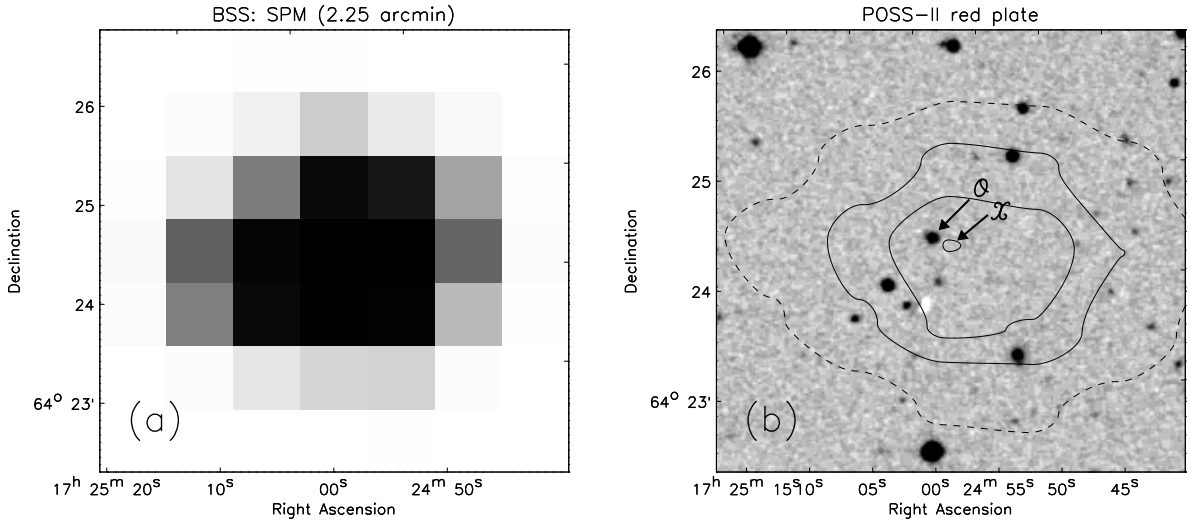

Figure 6.16: Discovery of a close by QSO with the BSS algorithm and confirmed with the SDSS. Panels (a) and (b) are centred on the QSO sky coordinates, given by the BSS technique, and cover the same fov of 5 arcmin at the side. See text for more details.

as the ratio between the flux and the elliptical area of FWHM radii in units of erg s^{-1} cm^{-2} $arcmin^{-2}$. The utilized definition of mean surface brightness follows the one given by Giacconi *et al.* (2002*b*). In Giacconi *et al.* (2002*b*), the mean surface brightness is inversely proportional to a circular area. An elliptical area given by the FWHM values corresponding to the source extents provided by the BSS algorithm is, instead, used to supply a value of the source area (Peacock, 1999), that is more appropriate than a circular one for clusters with complex morphologies.

Optical observations: In order to verify the efficiency of the BSS technique on the newly discovered objects, optical images are studied. The procedure is the same as carried out in Section 6.2.3. In this way, close by galaxies, low redshift X–ray clusters or groups of galaxies, and QSOs are identified in the optical images.

Point–like sources

Discovery of a QSO A Seyfert 1 Galaxy (Abazajian, 2003) is detected with the BSS algorithm analysing the RASS field id RS930625n00 in the hard ($0.5 - 2.4$ keV) energy band (see Fig. 6.1 for the broad band image). This QSO is located at $\alpha = 17^{\rm h}24^{\rm m}57.9^{\rm s}$, $\delta = +64°24'16''$ (J2000): Position given by the BSS algorithm. Although the observation time for this object with the *ROSAT* satellite is large (39.14 ks), no counterparts have been found in the RASS BSC (Voges *et al.*, 1999) and FSC (Voges *et al.*, 2000). A QSO is found in the SDSS, whose position coincides within the positional errors from the SDSS and the BSS algorithm. The SDSS object, matched with the BSS detection, is catalogued as SDSS J172459.31+642424.0 (Abazajian, 2004; Hao *et al.*, 2005; Vanden Berk *et al.*, 2006). The

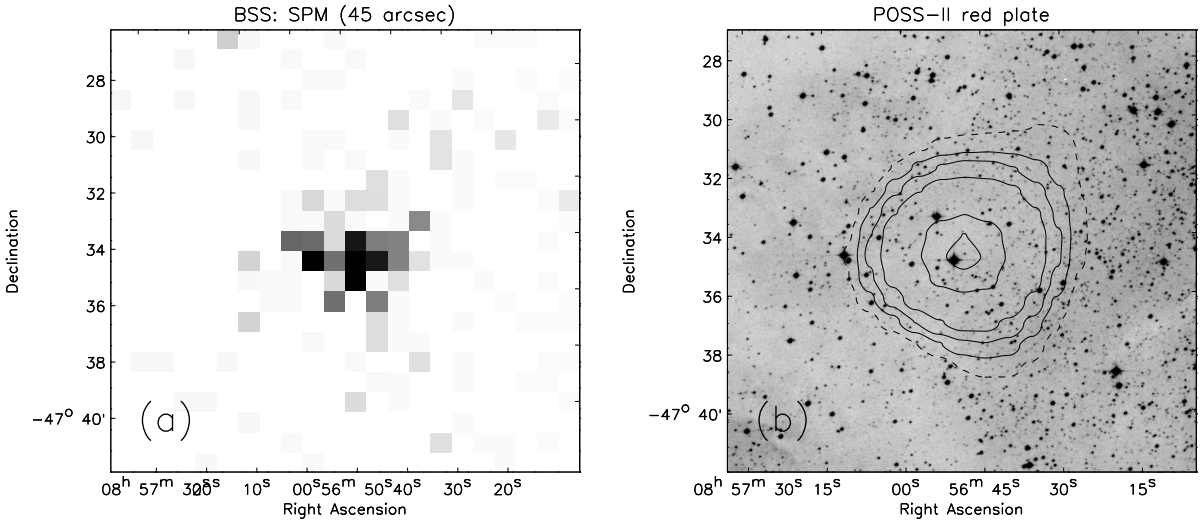

Figure 6.17: Detection of a potential AGN with the BSS algorithm. Panels (a) and (b) are centred on the discovered X–ray source in sky coordinates. Each panel covers a fov of 15 arcmin at the side. See text for more details.

redshift of this close by QSO is $z = 0.139$ (Fan *et al.*, 2001).

In Fig. 6.16, panels (a) and (b) are centred on the newly discovered X–ray object. Both panels show the same sky view. Panels (a) and (b) are an SPM from the analysed X–ray data and an optical image, respectively. Panel (a) is a zoom in the SPM obtained analysing the RASS RS930625n00 field in the hard ($0.5 - 2.4$ keV) energy band. The depicted SPM is obtained at a correlation length of 2.25 arcmin, that supplies the maximum in source probability. Black indicates $P_{\rm source} = 0.999$. Panel (b) is the POSS–II R plate smoothed with a Gaussian kernel of 2. An arrow with an 'O' indicates the optical position of SDSS J172459.31+642424.0. RASS X–ray contours in the hard ($0.5 - 2.4$ keV) energy band are superposed to the optical image. The contours correspond to 3, 4, 4.5 and 5σ above the local X–ray background. The 5σ contour is indicated with an arrow and an 'X' to point the X–ray source position.

No BSS detections are found in the soft energy band. This object is located close to the north–west corner of the field id RS930625n00 ($\sim$ 45 arcmin). In this region the SASS background intensity is 7% lower than the BSS background estimate.

In Table 6.5, the source count rates, flux and luminosity in the hard ($0.5 - 2.4$ keV) energy band are provided for this source (see source 1). For the conversion from count rate to flux, the value of the interstellar hydrogen column density as measured at 21 cm for the estimated QSO position is: $N_{\rm H} = 1.90 \times 10^{20}$ cm^{-2} (Kalberla *et al.*, 2005).

The reported luminosity is typical for Seyfert 1 galaxies (see Schwope *et al.*, 2000; Henry *et al.*, 2006; Hasinger, 2002; Brandt and Hasinger, 2005).

Discovery of an X–ray point–like source In the RASS field id RS932518n00 (Fig. 6.5) a new X–ray source is detected with the BSS technique. The estimated source parame-

ters are listed in Table 6.3, source (8). This source does not have a counterpart in any catalogue employing X–ray data. A counterpart is found in the optical and near infrared wavelengths of the electromagnetic spectrum employing the VizieR (Ochsenbein *et al.*, 2000). The matched object coincides within the positional errors provided by the BSS algorithm. It is 6 arcsec far from the BSS position. The matched counterpart is catalogued as: GSC2.3 S66I031249 (Lasker *et al.*, 2008), USNO-B1.0 0424-0200132 (Monet *et al.*, 2003), NOMAD1 0424–0202502 (Zacharias *et al.*, 2005), DENIS J085648.2–473437 (The, 2005), 2MASS 08564829–4734375 (Cutri *et al.*, 2003). This object is brightest in the near infrared band. It is characterized by a magnitude of 15.27 ± 0.15 in the J band, i.e. $1.25 \mu m$, as given by the DENIS database (The, 2005). Additionally this object is classified as a non–star (Lasker *et al.*, 2008) with no extended features (Cutri *et al.*, 2003). It is not associated with known solar system objects (Cutri *et al.*, 2003). Note that the BSS algorithm classifies this object as point–like. The RASS data, as analysed by the BSS algorithm, provide for this object a prominent X–ray emission only in the hard $(0.5 - 2.4$ keV) and broad $(0.1 - 2.4$ keV) bands.

In Fig. 6.17, panel (a) provides a zoom in the SPM, obtained with uncorrelated pixels, analysing the hard $(0.5 - 2.4$ keV) energy band of the RASS field id RS932518n00. Pixels enhancement shows source detection: Black, dark and light grey, white indicate $P_{\rm source} \sim 1, \leq 0.6, 0.16$ and 0.035, respectively. The maximum probability of source detection occurs at the depicted correlation length. Panel (b) is the POSS–II R plate, centred on the newly discovered X–ray object. The *ROSAT* X–ray contours in the $(0.5 - 2.4)$ keV are superposed. Each contour corresponds to 3, 5, 7, 10, 20 and 25 σ above the local X–ray background. The innermost contour level is centred on this faint point–like object. The flux for this object (see source 2) is listed in Table 6.5. The X–ray flux of this point–like object is calculated in the hard $(0.5 - 2.4$ keV) energy band accounting for a value of $N_{\rm H} = 7.35 \times 10^{21}$ cm^{-2} (Kalberla *et al.*, 2005), the interstellar hydrogen column density as measured at 21 cm for the position of this object. No X–ray luminosity is provided, since no redshift is known. The work of Suchkov *et al.* (2006) suggests that this point–like object is a close by AGN at a redshift ≤ 0.5. However, more studies are needed to discover the true nature of this celestial X–ray source.

Extended sources

The total flux detected from a cluster is usually corrected because part of the flux in the faint outer regions is lost in the background. The loss of flux occurs for various reasons, mainly: Large–scale variations of the background are not properly accounted for; The function used to fit the object does not properly describe the outer part of the object (see, e.g., the work of Reiprich and Böhringer 2002). In this thesis, the photometric bias is not accounted for. On the one hand, the BSS technique provides a well–defined background model. The background model accounts for large variations both in the cosmic background and in the exposure map. On the other hand, an improved parameterization for the extended sources can be added. Extended sources, in the same way as point–like sources, are fitted with a multi–variate Gaussian distribution. This assumption is not always true for

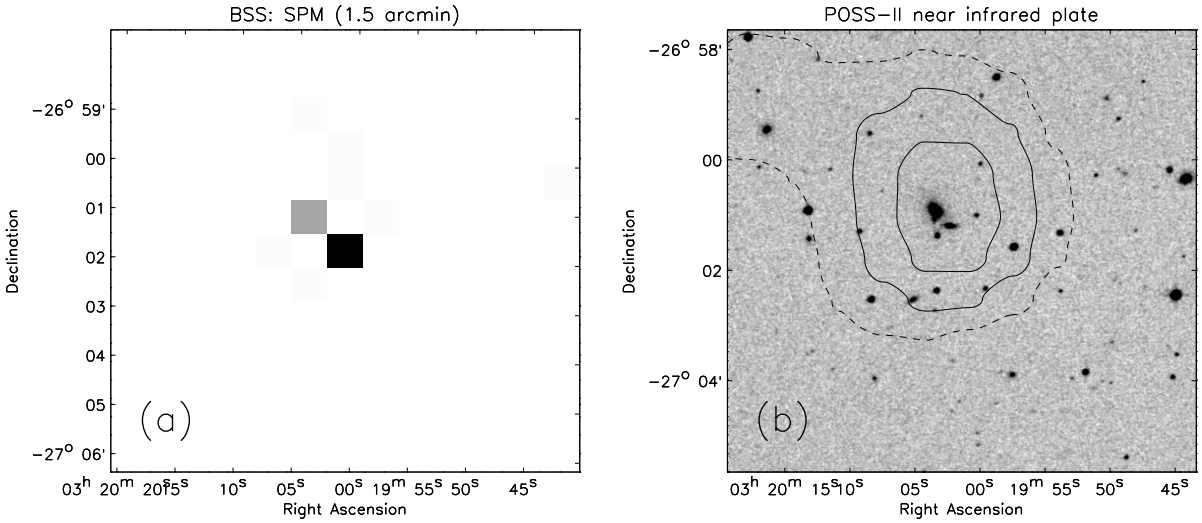

Figure 6.18: Discovery of a close by cluster of galaxies and confirmed with optical sky surveys (Abell *et al.*, 1989). Panels (*a*) and (*b*) are centred on the cluster of galaxies sky coordinates, given by the BSS technique. Each image cover a fov of 8 arcmin at the side. See text for more details.

clusters or groups of galaxies. The characterization of a cluster or group of galaxies surface brightness distribution can be improved with a β–model (Cavaliere and Fusco-Femiano, 1978): See Chapters 2 and 7 for more details. Though this is an important step for providing conclusive values on parameters of clusters or groups of galaxies, this task is beyond the scope of this thesis.

Discovery of a cluster of galaxies In the RASS field id RS932209n00, a cluster of galaxies has been detected for the first time in the X–ray band of the electromagnetic spectrum with the BSS technique. This cluster of galaxies is located at $\alpha = 3^{\rm h}20^{\rm m}1.4^{\rm s}$, $\delta = -27°01'39.17''$ (J2000), as provided by the BSS algorithm. This object is a rich cluster of galaxies and known as ACO S 340 (Abell *et al.*, 1989) from observations in the optical band of the electromagnetic spectrum. This cluster of galaxies is located at $z = 0.068$ (De Propris *et al.*, 2002).

In Fig. 6.18, panels (*a*) and (*b*) show the same fov (8 arcmin at the side). Each image is centred on the detected cluster of galaxies. Panels (*a*) and (*b*) are an SPM from the BSS algorithm analysing the X–ray RASS image in the broad $(0.1 - 2.4$ keV) energy band and an optical image, respectively. In panel (*a*), the SPM is obtained at a correlation length of 90 arcsec. At this resolution, the maximum in source probability is reached. Black, grey and white colours indicate $P_{\rm source} = 0.968, 0.338$ and ≤ 0.003, respectively. The black and grey squares cover a large portion of the sky, since each square represents the RASS pixel resolution (45 arcsec). Furthermore, the detection is difficult since the observation time for this cluster of galaxies is very low (1.8 ks). Therefore, in the hard $(0.5 - 2.4$ keV) energy band the source probability of this object is slightly lower than the value found in the broad

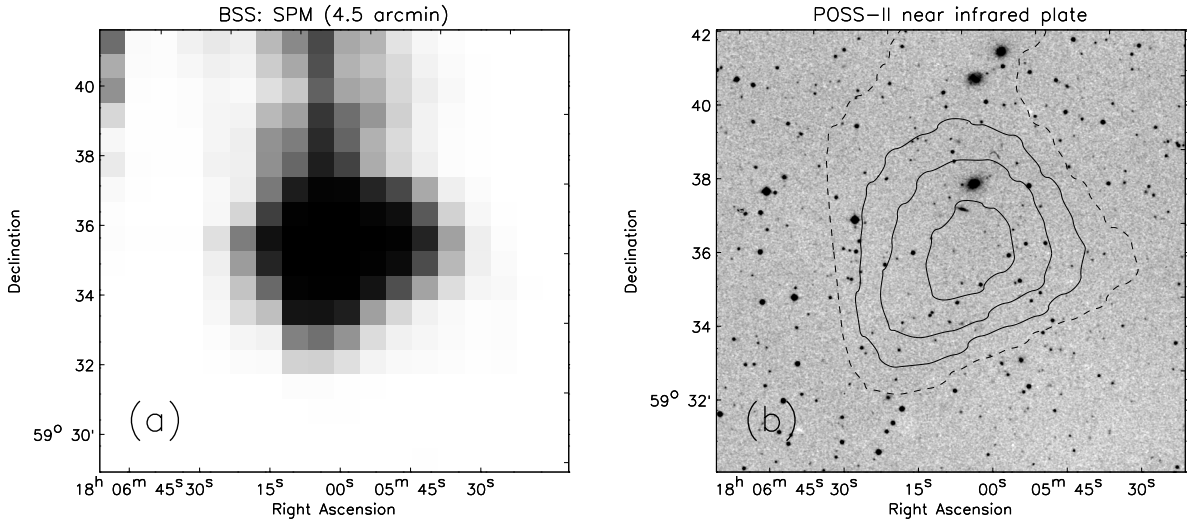

Figure 6.19: Detection of a potential cluster of galaxies with the BSS technique, but no counterparts with other catalogues have been found so far. Panels (a) and (b) are centred on the BSS position given for this object in the hard ($0.5 - 2.4$ keV) energy band. Each image cover a fov of 12 arcmin at the side. See text for more details.

band. In panel (b), the POSS–II I plate with superposed X–ray contours corresponding to 2, 3 and 4 σ above the local X–ray background is depicted. Panel (b) provides evidence that the extended source detected with the BSS technique in the *ROSAT* broad ($0.1 - 2.4$ keV) energy band is a cluster of galaxies with the central region dominated by three galaxies. Although the depicted SPM in panel (a) seems poor, the BSS source fitting routine finds the following source shapes: $\sigma_{\rm x} = (85.74 \pm 28.72)$ arcsec, $\sigma_{\rm y} = (65.21 \pm 29.01)$ arcsec, $\rho = (0.004 \pm 0.459)$. Note the large errors due to the small number of photons available. However, the estimated source shapes are in agreement with the contours reported in panel (b) at 4σ.

In Table 6.5, the flux, luminosity and surface brightness are reported for this cluster of galaxies (see source 3). The flux of this cluster of galaxies is calculated employing a galactic neutral hydrogen for the estimated position of $N_{\rm H} = 1.36 \times 10^{20}$ cm^{-2} (Kalberla *et al.*, 2005). The flux is obtained employing a thermal spectrum and a temperature of ~ 5 keV (Raymond–Smith model) (Böhringer *et al.*, 2000), a metal abundance of 0.2 of the solar value (Böhringer *et al.*, 2000), a redshift of $z = 0.068$, and an interstellar absorption according to the value of the galactic neutral hydrogen. This value is by a factor of 10 lower than the RASS flux limit ($\sim 3 \times 10^{-12}$ erg s^{-1} cm^{-2}, see Guzzo *et al.*, 2009) in the REFLEX survey (Böhringer *et al.*, 2001) for galaxies clusters and groups. The mean surface brightness for this object is by a factor of 10 larger than the faintest extended sources detected by the *ROSAT* satellite.

This cluster of galaxies is located in the RASS field id RS930625n00 at 2.7° off–axis from the centre. The location and the low X–ray brightness (due to low exposure time) of this object are the causes for being missed by the SASS technique.

Detection of an extended source A potential cluster or group of galaxies is detected with the BSS technique analysing the RASS field id RS930625n00 in the hard ($0.5-2.4$ keV) energy band (see Fig. 6.1). This detection can not be observed in the soft ($0.1-0.4$ keV) energy band. The detected X–ray emitting object is located at $\alpha = 18^{\rm h}06^{\rm m}5^{\rm s}$, $\delta = +59°35'39''$ (J2000). No counterparts are found in the RASS catalogues, although this object is observed for a high exposure time (36.5 ks).

Fig. 6.19, panel (a), is centred on the potential cluster of galaxies and displays a zoom in the SPM with correlation length of 4.5 arcmin estimated in the hard ($0.5-2.4$ keV) energy band of the RASS field id RS930625n00. At this resolution, the maximum in source detection is reached: black and white indicate $P_{\rm source} = 0.99989$ and $P_{\rm source} \leq 0.003$, respectively. The correlation length, at which this object is detected, provides evidence for the detection of an extended source. Panel (b) shows the optical sky view of panel (a): the POSS–II I plate smoothed with a Gaussian kernel of 2. X–ray contours are superposed to the optical image. Contours are obtained from the RASS photon count data in the hard ($0.5-2.4$ keV) energy band. Contours delineate the values of the detected object surface brightness at 2, 3, 4 and 5σ above the local X–ray background. The detected source appears as a cluster or group of galaxies. This detected object is bright, with 70 net source counts. The extent of this object has an estimated value of 5 arcmin. The SASS algorithm missed this extended celestial source, because of a too small box size used to slid across the image in the search of positive fluctuations with respect to the background signal measured outside the box. See Section 5.1.1 for more details about the sliding–window technique.

In Table 6.5, count rates, flux and surface brightness for this object are provided (see source 4). Note that the celestial object is distant ($z \gtrsim 0.5$, private communications with Prof.Dr. Hans Böhringer), because the POSS–II image does not provide a clear evidence of a cluster or group of galaxies in Fig. 6.19. The flux is calculated from the source count rate in the hard band to the observed flux in the same band for a source with a thermal spectrum and a temperature of ~ 5 keV (Raymond–Smith model) (Böhringer *et al.*, 2000), a metal abundance of 0.2 of the solar value (Böhringer *et al.*, 2000), and an interstellar absorption according to the value of the galactic neutral hydrogen of $N_{\rm H} = 2.92 \times 10^{20}$ cm^{-2} (Kalberla *et al.*, 2005). A test is executed considering a redshift range of $0-1$. The flux obtained with a redshift of almost zero is only by a factor of 1.04 larger than the one derived with a redshift of one. The flux, reported in Table 6.5, is calculated assuming $z = 0.5$. The estimated flux is comparable to the ones given by Henry *et al.* (2006) for clusters or groups of galaxies with redshifts in the range $0.03-0.58$. The estimated flux is by a factor of 10 lower than the RASS flux limit ($\sim 3 \times 10^{-12}$ erg s^{-1} cm^{-2}, see Böhringer *et al.*, 2000) for cluster detections. The X–ray luminosity is not provided because it depends strongly on the redshift, which is not known. The mean surface brightness for this object is reported. The mean surface brightness value is on the order of the faintest extended sources discovered by *ROSAT* (Giacconi *et al.*, 2002*b*).

Further studies, such as spectroscopic observations, are needed for a proper classification of this object.

Table 6.5: Summary table listing identification, position (J2000), redshift (z), classification, source count rates, flux, luminosity and surface brightness of discovered X−ray sources with the BSS technique

	ID	R.A.$^{(\dagger)}$ (J2000)	Dec.$^{(\ddagger)}$ (J2000)	z	Classification	Sctr$^{(\flat)}$ count s^{-1}	F_X([0.5-2.4] keV) erg s^{-1} cm^{-2}	L_X([0.5-2.4] keV) erg s^{-1}	SB_X erg s^{-1} cm^{-2} arcmin^{-2}
1	SDSS J172459.31+642424.0	17:24:57.9	+64:24:16	0.1388	Seyfert 1 Galaxy	0.0085 ± 0.0022	(2.8 ± 0.7)E-13	(0.15 ± 0.04)E+44	
2	GSC2.3 S66I031249	08:56:49	-47:34:33	?	non-star	0.1204±0.0156	(8.07 ± 1.05)E-12		
3	ACO S 340	03:20:01	-27:01:39	0.068	cl. galaxies	0.0375±0.0161	(3.6 ± 1.6)E-13	(4.05 ± 1.74)E+42	(1.87±0.80)E-14
4		18:06:05	+59:35:39	$\gtrsim 0.5^{(*)}$	cl. galaxies (?)	0.0168±0.0067	(2.41±0.96)E-13		(2.36±0.94)E-15

Note. $^{(\dagger)}$ Right ascension, coordinates (units of hours, minutes, and seconds).
$^{(\ddagger)}$ Declination, coordinates (units of degrees, arcminutes, and arcseconds).
$^{(\flat)}$ Source count rates in the hard $(0.5 - 2.4$ keV) energy band.
$^{(*)}$ assumption, private communication with Prof.Dr. H. Böhringer.
See text for more details.

6.3 Summary

The BSS technique is applied to *ROSAT* PSPC data in survey mode. Three RASS fields are chosen with different characteristics: large variations in the satellite's exposure and background; large variations in the satellite's exposure and small variations in the background; small variations in the exposure and large background variations.

The results obtained with the BSS technique are compared to the ones from the SASS method.

A background map for the complete field size (512×512 pixels $= 6.4^\circ \times 6.4^\circ$ in the sky) is inferred simultaneously with probability maps for having source intensity in addition to the background intensity in a multiresolution analysis.

Background (rate and amplitude) maps and SPMs are produced for the three *ROSAT* energy bands (broad: $0.1 - 2.5$ keV, soft: $0.1 - 0.4$ keV, hard: $0.5 - 2.4$ keV). Background maps obtained with the BSS technique are well–defined on the complete field even in extreme cases when the data are missing because the satellite was switched off or when hot diffuse emissions dominate the astronomical image. The flexibility of the BSS technique for background estimation is shown. The number of the spline's supporting points are important for addressing properly the variation in the background.

The background maps from the SASS algorithm, instead, show inconsistencies with the data towards edges (of the field or of a strip with no exposure) and where large background variations occur.

SPMs produced for the soft ($0.1 - 0.4$ keV) and hard ($0.5 - 2.4$ keV) energy bands are combined probabilistically. The source detections obtained from the combined source maps are compared with the broad ($0.1 - 2.4$ keV) energy band. The probability of source detection with the combined energy bands is improved with respect to the broad energy band alone. The detected sources are cross–correlated with existing catalogues. The BSS technique allows for improving completeness of the catalogue while decreasing the contamination from statistical fluctuations.

The BSS source positions are as good as the ones provided from the ML technique, that accounts for the source surface brightness convolved with the instrumental PSF. The BSS count rates of the detected sources and matched with the *ROSAT* FSC (Voges *et al.*, 2000) and BSC (Voges *et al.*, 1999) are similar to the ones obtained with the SASS algorithm only in regions characterized by low background variations. In regions with highly varying background, the BSS results are on the average larger. The source count rate increases by a factor of $2 - 10$ with respect to the SASS estimates. Furthermore, the BSS algorithm provides improved source parameters with respect to the SASS technique. The most interesting example of improvement in source parameters with the BSS technique is given by the Vela pulsar: see Tables 6.3 and 6.4. In fact, recent XMM–*Newton* observations of the Vela pulsar validates the flux value for this source estimated with the BSS technique. This example shows that an automated estimation of source parameters for sources embedded in a hot diffuse emission is awkward for standard techniques, like SASS. The BSS algorithm is able to overcome these problems.

Furthermore, the BSS algorithm overcomes the classical problem with SASS of faint

sources estimated with negative counts (Voges *et al.*, 1999). In addition, the BSS algorithm allows for the detection of the tails of the source profiles (until $3 - 4\ \sigma$ above the local background).

The BSS technique allows us to reveal new sources not listed in the RASS FSC (Voges *et al.*, 2000) and BSC (Voges *et al.*, 1999). Some of these sources have been found with counterparts in the WGACAT, that is a catalogue obtained from deeper *ROSAT* PSPC data in pointing mode (White *et al.*, 1994); the SDSS catalogue (a deep optical survey) (Abazajian, 2004); the XMM–*Newton* catalogue (X–ray) (Watson *et al.*, 2008) and the 2dFGRS in the optical band (Colless *et al.*, 2001; De Propris *et al.*, 2002). The Bayesian method allows, therefore, to detect faint and extended objects, like QSOs and groups of galaxies, which could not be detected previously by SASS. The newly discovered X–ray objects are characterized by fluxes up to 10 times lower than the RASS source detection limit ($\sim 3 \times 10^{-12}$ erg s^{-1} cm^{-2}) as given by the works of Böhringer *et al.* (2000, 2004). The BSS technique provides a more complete sample when analysing astronomical images with respect to the SASS algorithm. No counterparts with other catalogues have been found for some of the discovered X–ray sources. These sources are potential clusters or groups of galaxies and AGNs. Further studies are required to verify the true nature of these X–ray sources.

Chapter 7

Application to observational data: Chandra Deep Field South

In this Chapter, results obtained with the BSS technique applied to one of the deepest astronomical images and the most well studied part of the sky across a wide range of photon energies is provided. The studied field is the CDF–S. In Section 7.1, an overview of the *Chandra* X–ray observatory, a discussion of the CDF–S data and of the major X–ray catalogues in the CDF–S region are given. In Section 7.2, the CDF–S data are used for showing the capabilities of the BSS technique in improving source detection with respect to previous methods and in detecting sources of any shape and of a wide range of brightness values. The detection of clusters and groups of galaxies and of sources superposed with an extended one are considered. Last, a summary of this Chapter is provided in Section 7.3.

7.1 The CDF–S region

The CDF–S represents one of the deepest X–ray surveys to date (Giacconi *et al.*, 2001, 2002*b*; Rosati *et al.*, 2002*a*), improving by a factor of ~ 20 the deepest *ROSAT* survey (Giacconi *et al.*, 2002*b*). Deep surveys allow one to study the nature of celestial objects, that could not be studied otherwise, for instance the evolution of the AGN population (space density and properties such as obscuration). The nominal aimpoint of the CDF–S region is $\alpha_{\rm J2000.0} = 03^{\rm h}32^{\rm m}28^{\rm s}.0$, $\delta_{\rm J2000.0} = -27^{\circ}48'30''$ (Giacconi *et al.*, 2002*b*). The field was selected for a deep X–ray survey due to its high Galactic latitude, low Galactic neutral hydrogen column density ($N_{\rm H} = 8.8 \times 10^{19}$ cm^{-2}, Stark *et al.* 1992) and lack of bright stars: See Rosati *et al.* (2002*a*) for more details. The energy range of the CDF–S data sets varies between $0.5 - 7.0$ keV.

The *Chandra* X–ray telescope's angular resolution and the CDF–S sensitivity are ideal for the discovery and study of clusters of galaxies with complex morphologies. In addition, the CDF–S data are characterized by a very small background (i.e., the background counts follow Poisson distributions) and large exposure variations, and by images from several pointings superposed and with CCD gaps. Hence, the CDF–S data are particularly suited

for using the BSS algorithm. The optimal energy band to detect the emission from extended sources is between $0.5 - 2.0$ keV (Boschin, 2002).

The *Chandra* X–ray observatory (CXO) The *Chandra* satellite (Weisskopf *et al.*, 2000) was named after the late astrophysicist Subrahmanyan Chandrasekhar. CXO provides for sub–arcsecond imaging, spectrometric imaging and high–resolution dispersive spectroscopy over the X–ray part of the electromagnetic spectrum in the energy range of $0.1 - 10$ keV. CXO's capability for high–resolution imaging allows for the studies of structures of extended sources, including SNR, astrophysical jets, hot gas in galaxies and clusters of galaxies (Weisskopf *et al.*, 2000).

CXO was launched on July 23, 1999 and propelled into an elliptical orbit around the Earth with apogee and perigee values of 133×10^3 and 16×10^3 km, respectively. The time to complete an orbit is 63.5 hours, allowing for a high observing efficiency (uninterrupted observations lasting more than 2 days are possible). The observatory has three major modules: the X–ray telescope, the science instruments and the spacecraft (see Weisskopf *et al.* 2000 for more details). The telescope optical system has a Wolter–1 design with four paraboloid and hyperboloid pairs of nested mirrors with 10 m focal length. CXO provides high–resolution imaging with an instrumental PSF of 0.5 arcsec (FWHM) on axis. CXO has two focal plane instruments: the High–Resolution Camera and the Advanced CCD Imaging Spectrometer (ACIS). Each of these instruments has two detectors, that operate in photon counting mode and have low internal background. The appropriate instruments are placed at the focus of the telescope with a slide mechanism.

For the observation of the CDF–S region, the ACIS instrument is used. ACIS is composed of ten CCDs (each of 1024×1024 pixels) designed for source detection and spectroscopy (Lehmer *et al.*, 2005). The CCDs are distributed in a 2×2 array (ACIS–I) and a 1×6 array (ACIS–S). All four ACIS–I chips and the ACIS–S3 chip were used for the CDF–S observations. The telescope aimpoint was centred on the ACIS–I3 chip for each exposure.

CDF–S data The public released data of the CDF–S is a combination of several individual *Chandra* ACIS–I imaging pointings. Each pointing covers a field of about 0.08 deg^2. Due to different roll angles of individual pointings, the final image covers a total of 0.109 deg^2. Three images are extracted from the CDF–S data: the soft image ($0.5 - 2.0$ keV), the hard image ($2.0 - 7.0$ keV), and the total image corresponding to the soft and hard energy bands together.

Two allocated sets of observations were executed: See Giacconi *et al.* (2002*b*); Luo *et al.* (2008). The first survey (Giacconi *et al.*, 2002*b*) was performed from October 1999 until December 2000 with a total of 11 individual pointings and a total exposure time of 0.94 Ms. The image is binned in 1600×1650 pixels, which gives an image scale of 0.982 arcsec pixel^{-1}. A second survey (Luo *et al.*, 2008) was performed in 2007 September–November adding 12 pointings to the previous observations and bringing the total exposure time to 1.911 Ms. These additional data were part of an effort to create still deeper X–ray surveys.

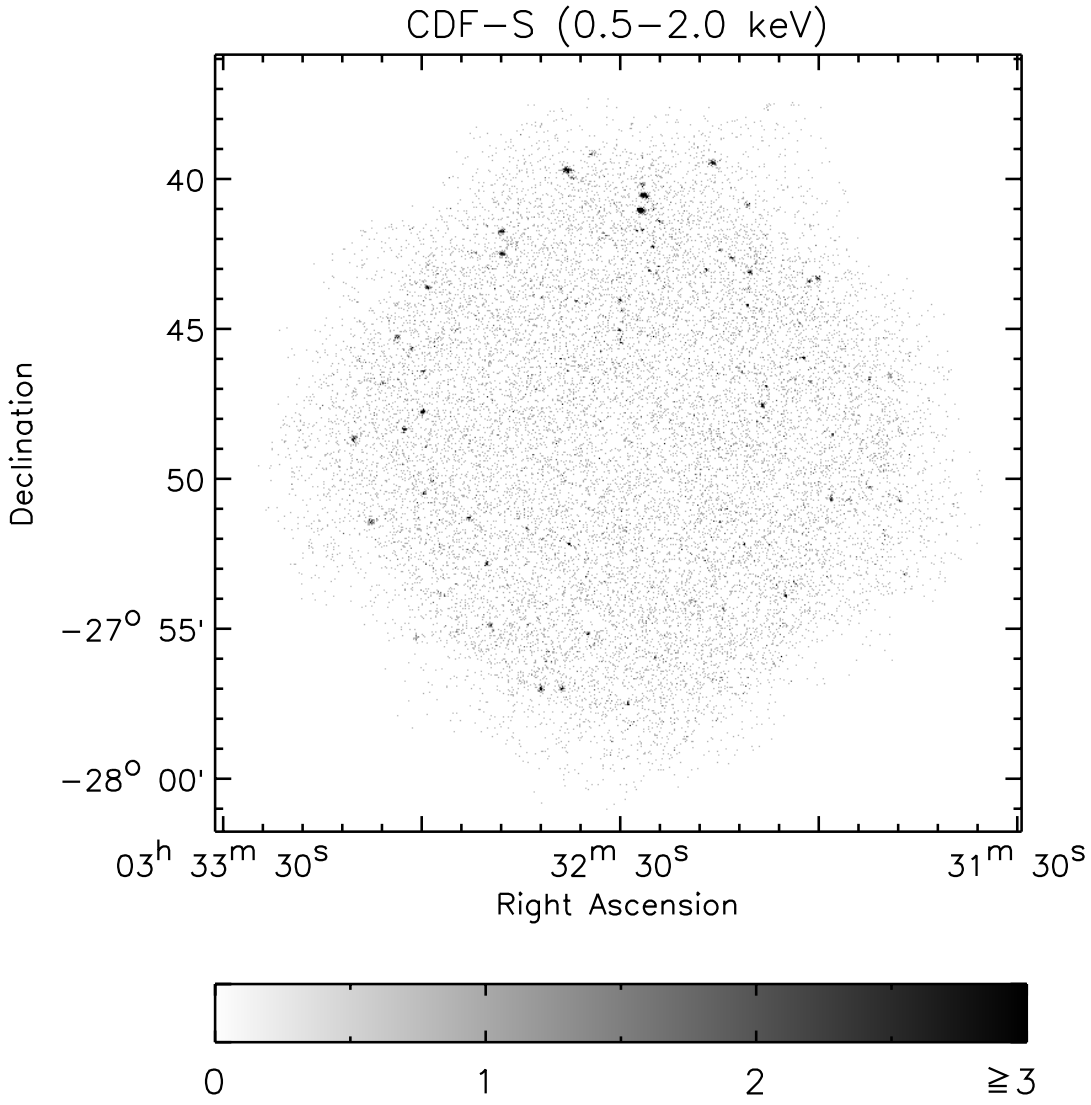

Figure 7.1: CDF–S 2Ms photon count image in the soft $(0.5-2.0$ keV) energy band. The colorbar has units of count pixel^{-1}. The original scale of this image is in the range $(0-959)$ count pixel^{-1}.

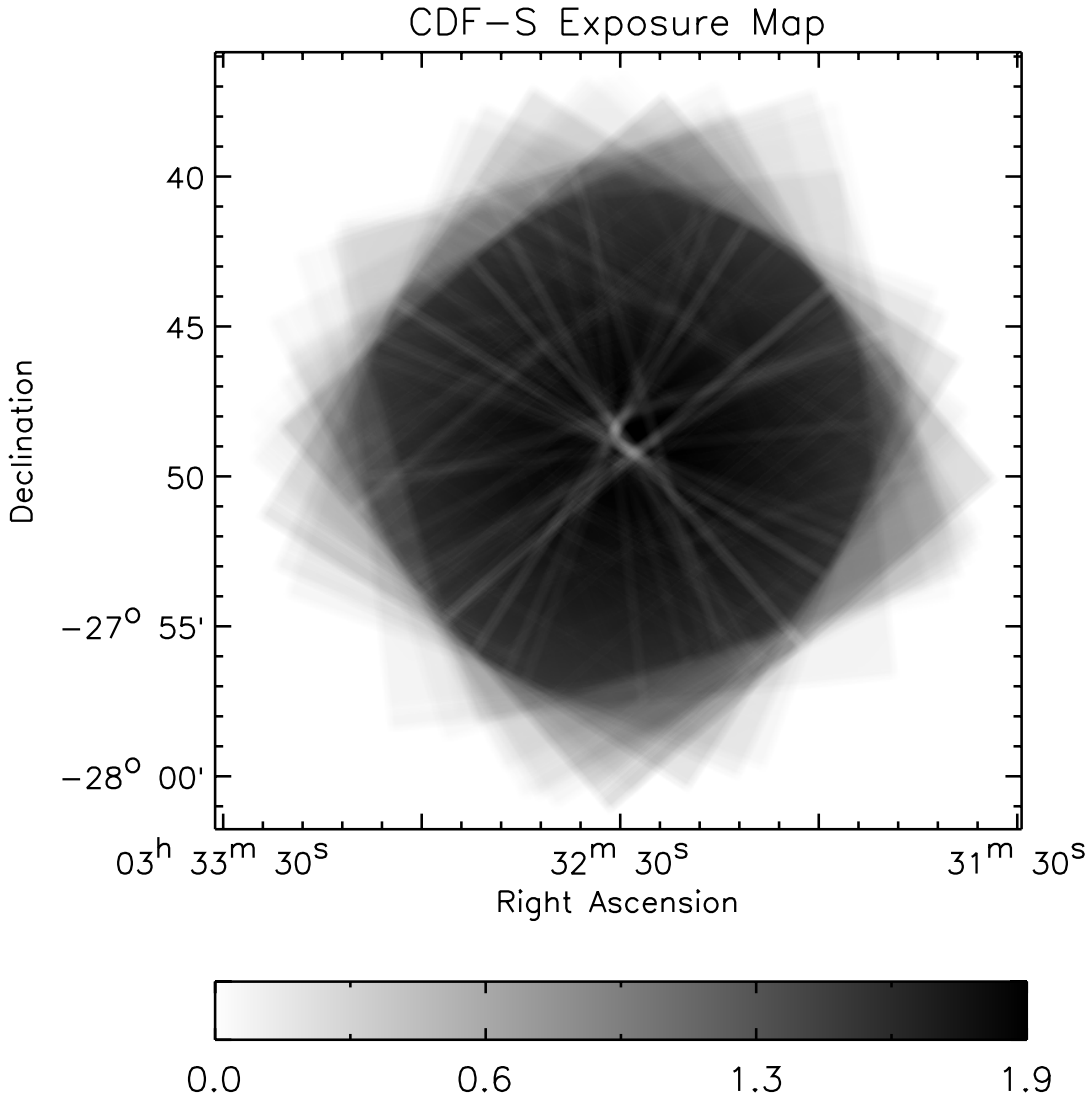

Figure 7.2: Exposure map of the CDF–S 2Ms in the soft ($0.5 - 2.0$ keV) energy band (Fig. 7.1). The colorbar has units of Ms pixel^{-1}.

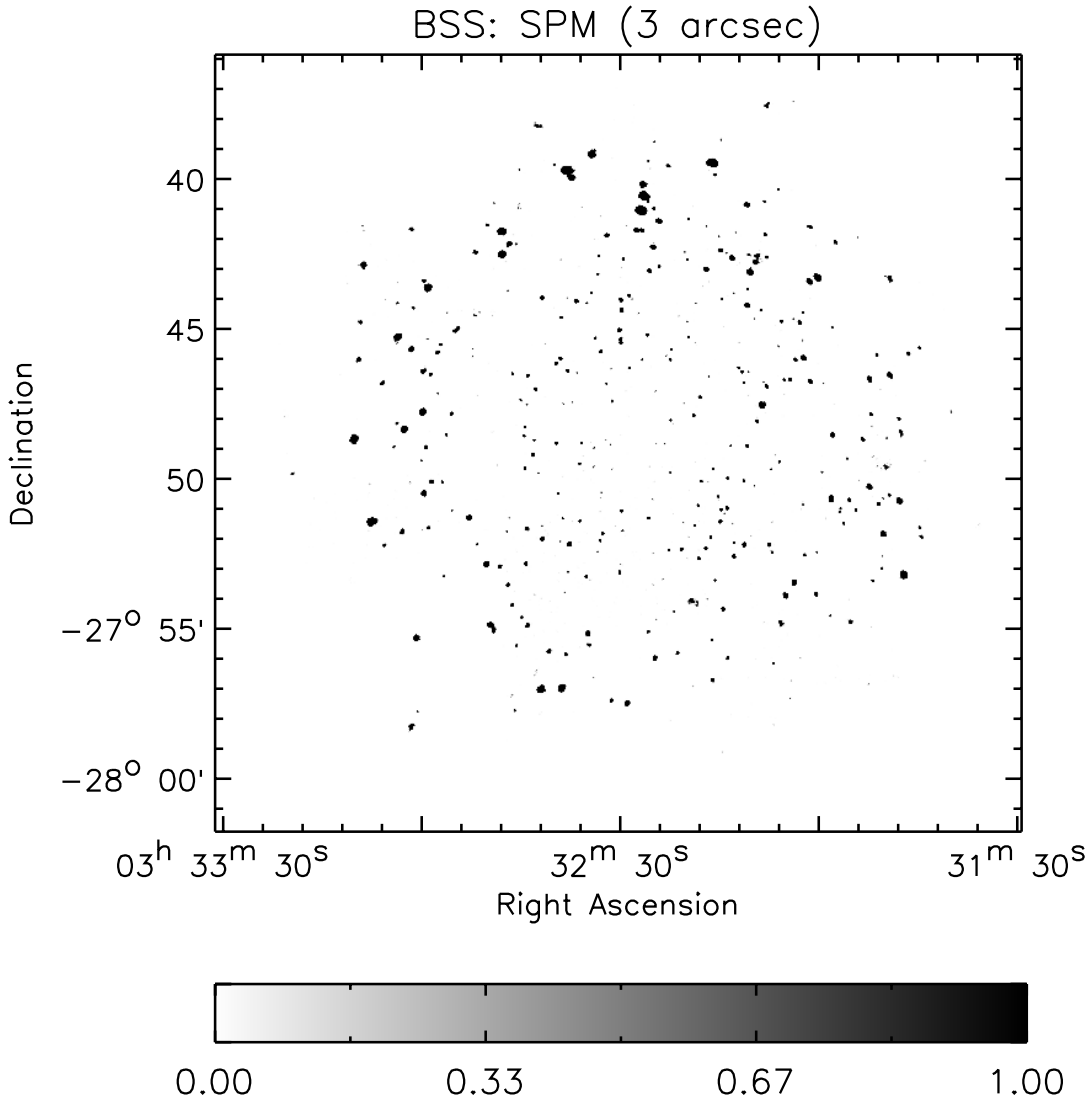

Figure 7.3: SPM at 3 arcsec resolution of the CDF–S 2Ms in the soft ($0.5-2.0$ keV) energy band as given by the BSS technique. The grey scales are linear. The colorbar indicates source probabilities per pixel. The image can be compared to Fig. 7.1.

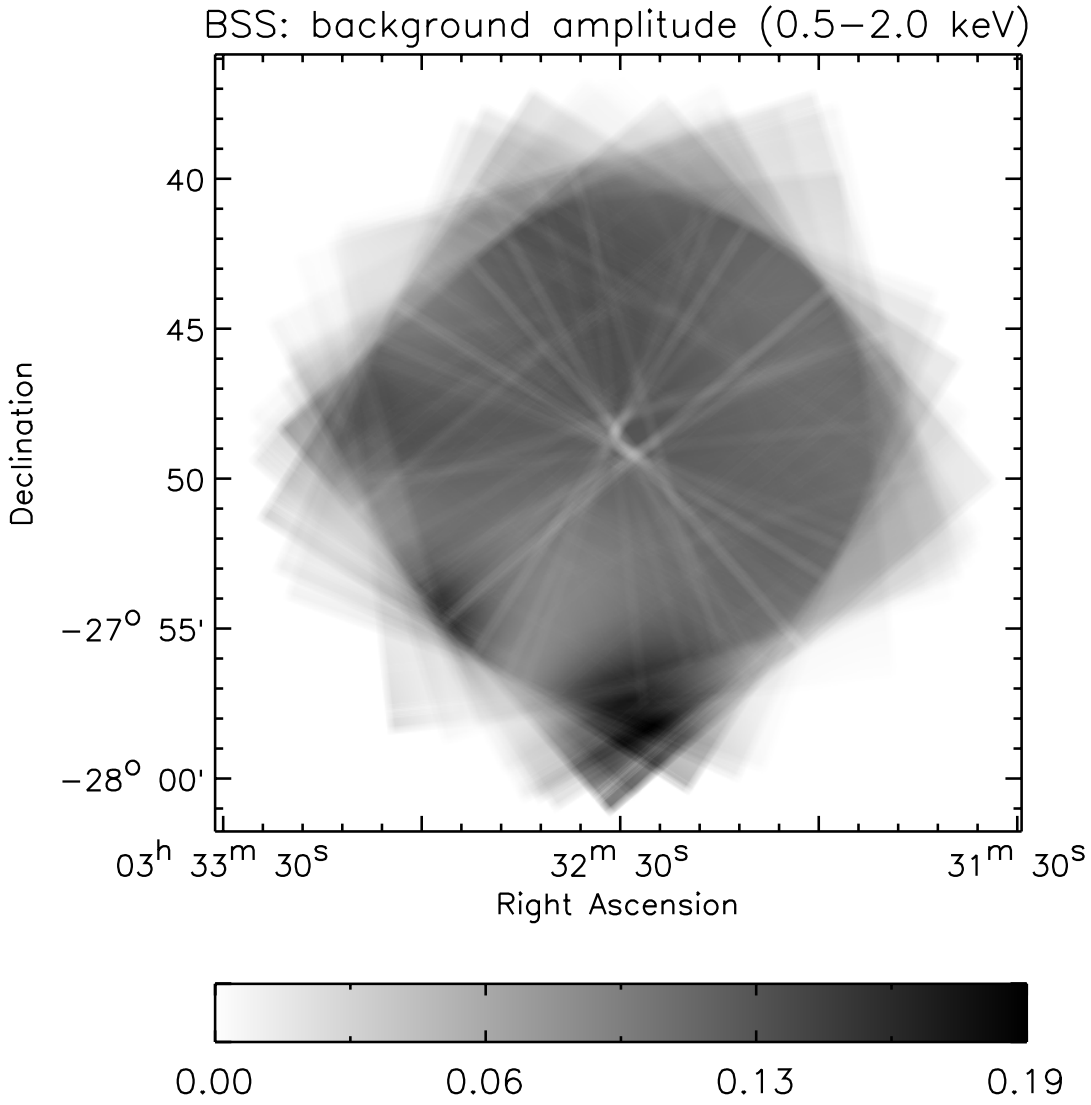

Figure 7.4: Estimated background intensity of the CDF–S 2Ms in the soft $(0.5-2.0$ keV) energy band as given by the BSS technique. The grey scales are linear. The colorbar gives background count pixel^{-1}. The background map takes into account the variation in the exposure map, shown in Fig. 7.2.

The new survey was performed with all observations in Very Faint mode to increase the sensitivity of faint source detections (Luo *et al.*, 2008). Note that most of the observations in the first set (Giacconi *et al.*, 2002*b*) were taken in Faint mode. The image data given by Luo *et al.* (2008) are provided in an array of 3280×3160 pixels (i.e., 0.492 arcsec pixel^{-1}). From now on the surveys given by Giacconi *et al.* (2002*b*) and Luo *et al.* (2008) are indicated as CDF–S 1Ms and CDF–S 2Ms, respectively.

In Figs 7.1 and 7.2, the CDF–S 2Ms image and exposure map are shown in the soft ($0.5 - 2.0$ keV) energy band, respectively. The maximum exposure time is 1.884 Ms but varies across the detector(s), with a minimum of 0.15 s at the edge of the field where there is only single exposure due to rotation of the fov. Effective area and spatial resolution of the telescope vary inversely with the off–axis angle (Giacconi *et al.*, 2002*b*).

The CDF–S catalogues The CDF–S 1Ms X–ray source catalogue and the details of the detection process are described in Giacconi *et al.* (2002*a*,*b*) and references therein. In the works of Giacconi *et al.* (2002*a*,*b*), modified versions of SExtractor (Bertin and Arnouts, 1996) and wavdetect algorithms (Freeman *et al.*, 2002) are used. SExtractor is utilized for source detection and characterization of point–like sources. Due to the small background amplitude detected in the CDF–S ($\sim 0-1$ count pixel^{-1}), SExtractor fails in providing a reliable background map. Therefore, in each energy band the background amplitude is computed externally removing from the data sources down to a very low threshold (Tozzi *et al.*, 2001). A local background is estimated in an annular ring around the detected sources and its value is used to model the background in addition to the removed sources. Last, the background map is obtained smoothing the resulting image. wavdetect is employed in two steps for the detection of point–like and extended sources. For the detection of point–like sources, wavdetect is applied with a false–positive probability threshold of 1×10^{-6} (i.e., ~ 1 false positive per field) and wavelet scales with values from 1 to 8 pixels in steps of $\sqrt{2}$. The detections obtained with SExtractor and wavdetect algorithms are compared and joined in the resulting CDF–S catalogue (Giacconi *et al.*, 2002*b*). Very extended low surface brightness sources may be missed by these standard detection algorithms (Giacconi *et al.*, 2002*b*). To search for very diffuse sources a complementary approach is adopted. wavdetect is ran with a small characteristic scale to preferentially select point–like sources. These objects are removed from the (soft) image by replacing the source region with a simulated background. The resulting image is rebinned to a larger pixel size ($4''$) and the wavdetect algorithm is used to search for extended sources: See Giacconi *et al.* (2002*b*) for more details. The flux limit in source detection achieved in the CDF–S 1Ms at the aimpoint for the soft ($0.5 - 2.0$ keV) energy band is 5.5×10^{-17} erg s^{-1} cm^{-2}.

The CDF–S 2Ms X–ray point source catalogue is published in Luo *et al.* (2008, 2009). Sources are detected utilizing the wavdetect algorithm (Freeman *et al.*, 2002), only. The false–positive probability threshold is chosen with a value of 1×10^{-6}, providing a number of false positives in source detection ≤ 3 per field in the three energy bands (Luo *et al.*, 2008). A "$\sqrt{2}$ sequence" of wavelet scales from 1 to 16 pixels is used to search for sources. Although

the large range of wavelet scales utilized, the WAVDETECT algorithm fails in detecting faint and extended sources. Therefore, only lists of point–like sources are provided. The resulting source lists for each field in the three energy bands are merged to construct the main catalogue. Furthermore, the WAVDETECT source positions are improved in two steps. Firstly, matched–filter positions are used. The matched–filter position is the position provided correlating sources in the full–band image with the instrumental PSF weighted by the number of detected counts. The matched–filter technique accounts for the complex PSF at large off–axis angles, where the X–ray source position is not always located at the peak of the X–ray emission. The matched–filter positions are generated with a software for visualizing and analysing X–ray astronomical data, known as Tools for ACIS Real–time Analysis[1]. This tool requires a visual inspection of each source. Secondly, the absolute X–ray source positions are refined by matching the X–ray detected sources to optical sources. The comparison of X–ray and optical sources permit the derivation of an empirical relation for the positional uncertainties of the X–ray sources as a function of the off–axis angle.

Note that the CDF–S is one of the best studied fields in the sky. The CDF–S region has been target of other space– and ground–based observatories. The deep imaging data and spectroscopic follow up of the CDF–S region are gathered in the Great Observatories Origins Deep Survey (GOODS) (Dickinson *et al.*, 2003). GOODS provides the deepest data across the electromagnetic spectrum, allowing the exploration of the distant universe. Furthermore, the CDF–S survey was extended (E–CDF–S) (Lehmer *et al.*, 2005). Four contiguous 250 ks *Chandra* observations covering an approximately square region of total solid angle ≈ 0.3 deg^2 have been added. The CDF–S data covers only 35% of the E–CDF–S survey. The E–CDF–S data are utilized in the works of Luo *et al.* (2008, 2009) to improve sensitivity in the outer regions of the CDF–S. In the soft $(0.5-2.0$ keV) energy band, the CDF–S 2Ms data provides for a flux limit of 1.9×10^{-17} erg s^{-1} cm^{-2}, that is ~ 3 times deeper than the one achieved with the CDF–S 1Ms data in the same band.

7.2 Performance of the BSS algorithm on the CDF–S region

In this Section, the BSS technique is tested on the CDF–S 1Ms and 2Ms data. Firstly, the statistical detection of sources and the background model are considered. Successively, the detections of sources at the field edge are shown. The well–defined background model allows for reliable detections also at the field edge where steep gradients in the data occurs. Furthermore, a test is run on real sources for four samples extracted from the CDF–S 2Ms data set. The BSS technique is shown to be a robust method for background estimation, source detection and parameterization. In addition, the BSS technique is shown to outperform previous techniques for the detection of low surface brightness sources, as clusters or groups of galaxies. Therefore, astrophysical implications of these rare objects are commented. Examples of clusters and groups of galaxies detections are shown.

[1]http://www.astro.psu.edu/xray/docs/TARA/TARA_users_guide/

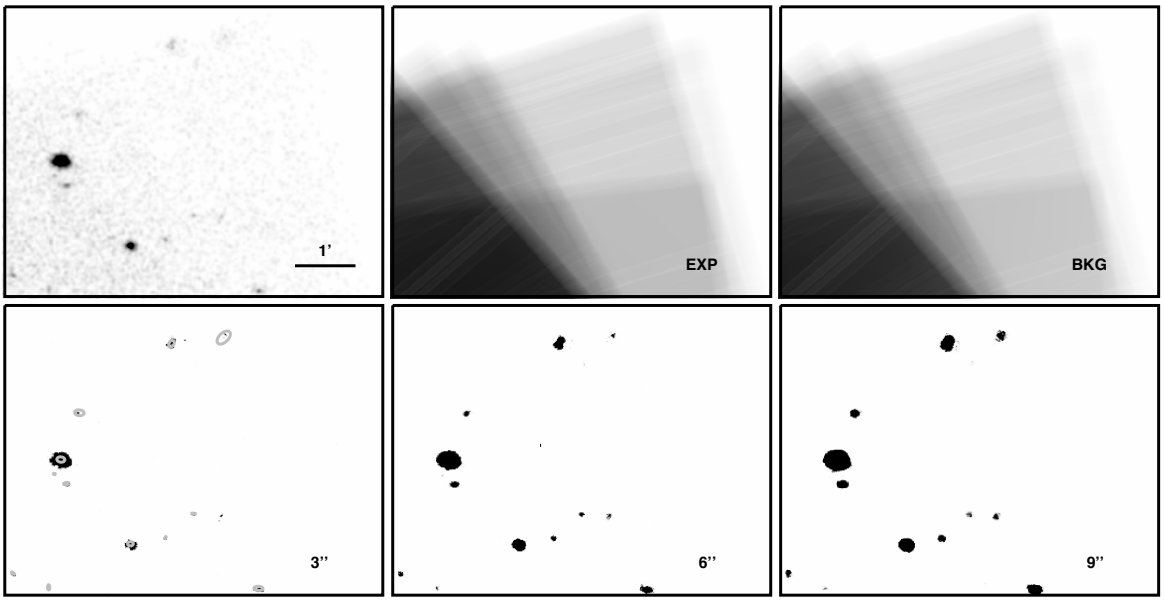

Figure 7.5: Example of source detection at the edge of the fov and with superposed observations in the CDF–S 1Ms data. Each image is centred at $\alpha_{\rm J2000.0} = 03^{\rm h}32^{\rm m}07^{\rm s}.0$, $\delta_{\rm J2000.0} = -27°39'32''$ and has $\sim 6'$ width and $\sim 4.5'$ height. See text for more details.

7.2.1 Products of the BSS technique

The capabilities of the BSS technique, in separating the background from the celestial sources on images of a new generation instrument, are tested on the CDF–S data in the soft $(0.5-2.0$ keV) energy band. For background–source separation, both prior pdfs of the source signal are examined. In Figs 7.3 and 7.4, products of the BSS technique analysing the CDF–S 2Ms data are shown: an SPM and the background map, respectively. These results are found employing the exponential prior pdf of the source signal.

The displayed SPM (Fig. 7.3) is obtained with a correlation length of 3 arcsec. At this resolution, a searching radius of 3 pixels (with a pixel scale of 0.5 arcsec pixel^{-1}) is used for correlating neighbouring pixels. The Gaussian weighting method is employed. No contaminations due to CCD gaps or to the steep change in the exposure time map are shown in any SPM. Part of the extended features of some known clusters of galaxies are starting to appear at this resolution, e.g. at $\alpha_{\rm J2000.0} = 03^{\rm h}32^{\rm m}09^{\rm s}.0$, $\delta_{J2000.0} = -27°42'43''$.

In Fig. 7.4 the estimated background amplitude is shown. The number of pivots employed for the background rate estimation amounts to 25. The pivots are chosen equally spaced. The background map is strongly dominated by the satellite's exposure time.

7.2.2 Field edge detection

The detection capabilities of the Bayesian approach at the field edge is shown in Fig. 7.5. Six co–centred images are covering the same fov. The upper left–hand image is a zoom in

the CDF–S 1Ms data, smoothed with a Gaussian kernel of 3 arcsec in order to increase details in the data. The satellite's exposure is located next, indicated with "EXP". In the exposure map image, black and white correspond to 590 and 0 ks pixel^{-1}, respectively. The estimated background image ("BKG") is placed for comparison: black and white stand for 0.22 and 0 background count pixel^{-1}, respectively. In the lower row three SPMs with decreasing resolution (black labels) are showing source detections. No artifacts are found neither in the background map nor in the SPMs. The detections depicted in the SPMs are very similar to the smoothed CDF–S 1Ms data. The multiresolution analysis allows one to detect sources at different scales. Regions of catalogued sources are superposed to the SPM located below the CDF–S 1Ms smoothed image. The regions indicate source position and extents at 1σ detection.

7.2.3 Comparison on real sources

An analysis is performed to test the sensitivity and the internal consistency of the BSS algorithm when detecting sources on real fields from pointed observations. The main advantages of testing real data with respect to simulated ones (as shown in Chapter 4) resides on the fact that real data are characterized by a complex background, a complex PSF dependence across the field, source confusion and a wide range of source properties. These characteristics intrinsic to real observations are not easily elaborated within artificial data. Therefore, four independent realization of the same observed data set are created. No artificial sources are added in the data.

A set of four images are extracted from the CDF–S 2Ms soft ($0.5 - 2.0$ keV) energy band. The four fields are shown with the photon count data and the exposure maps in Figs 7.6 and 7.7, respectively. Each image is characterized by the same fov of the CDF–S region and by 500 ks exposure, reducing the sensitivity by a factor of 4 compared to the full CDF–S 2Ms. Due to rotation of the telescope during the surveys, the four fields are covering the same fov only in the central region (within ~ 10 arcmin from the aimpoint). From now on, these four CDF–S fields are indicated with numbers $1 - 4$ CDF–S 500ks. Furthermore, the following blind test is performed: the analysis of the four CDF–S 500ks fields with the BSS algorithm is compared to the one obtained with the WAVDETECT technique (Freeman *et al.*, 2002).

The BSS algorithm is applied on the four fields. The exponential prior pdf of the source signal is chosen and 25 pivots equally spaced are used for the background rate estimation. Scales in the range values $0.5-13$ arcsec are used in the multiresolution analysis. Moreover, a threshold value of $P_{\rm source} \geq 0.9$ is chosen to separate false–positives in source detection from true sources. A test verifies the number of detected sources when a threshold value of $P_{\rm source} \geq 0.5$ is selected. For such low threshold value, the number of detected sources increases only up to 2% in these sets of data.

For the analysis of the four CDF–S 500ks fields with the WAVDETECT technique, the software CIAO, version 4.1.2, is used. The false–positive threshold setting ('sigthresh') is chosen to be 10^{-6}, in order to detect ≈ 1 false positive per field. The 'scale' sizes chosen are only 2 and 4. Following the work of Luo *et al.* (2008), the number of scales are increased

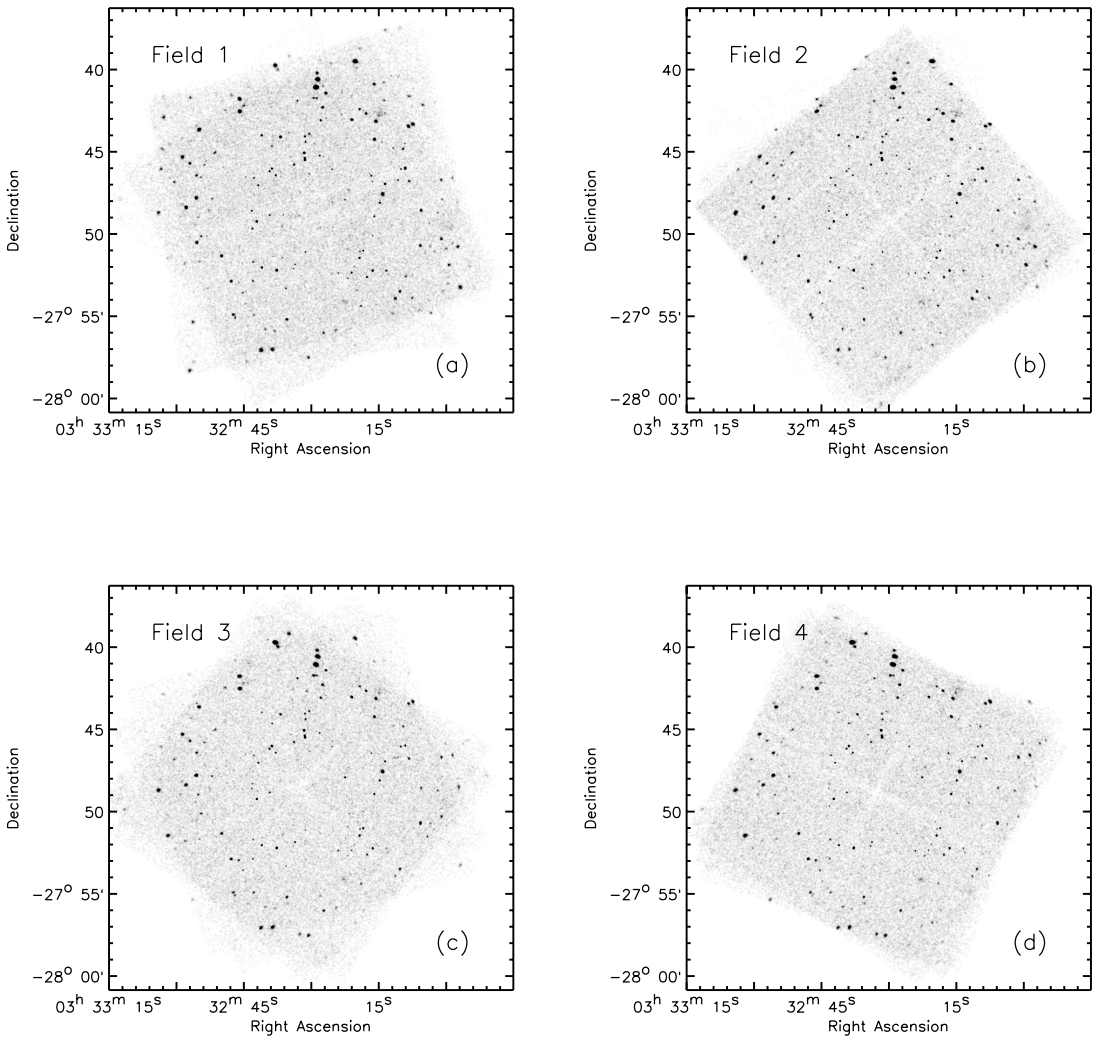

Figure 7.6: Each panel shows the four CDF–S 500ks photon count data in the soft ($0.5-2.0$ keV) energy band and smoothed with a Gaussian kernel of $3''$. Each image is enhanced in the range values $0-1$ photon count pixel^{-1}. The original images have values in the ranges: $0-638$, $0-769$, $0-646$, $0-657$ photon count pixel^{-1} for fields $1-4$ in panels (a)-(d), respectively.

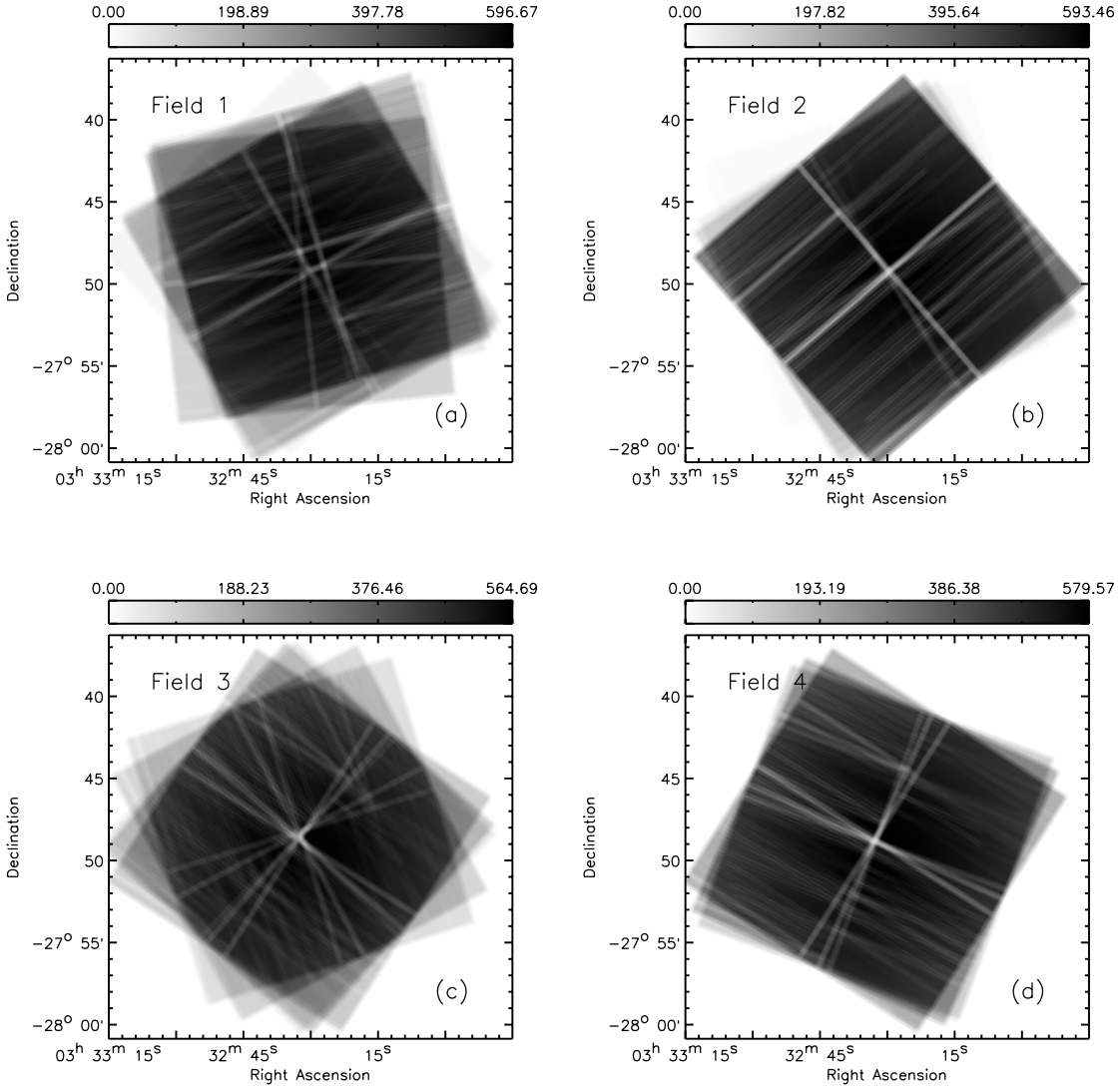

Figure 7.7: As for Fig. 7.6, but showing the corresponding exposure maps. The colorbars have units of ks pixel^{-1}.

Table 7.1: Test on CDF–S region in the soft $(0.5-2.0$ keV) energy band.

Field	Max photon count (count pixel^{-1})	<photon> (count pixel^{-1})	<background> (count pixel^{-1})	Detected sources	Flux limit erg s^{-1} cm^{-2} $\times 10^{-17}$
1	638	0.122	0.106	208(194*)	7.3(8.5*)
2	769	0.117	0.099	192(182*)	7.3(9.4*)
3	646	0.110	0.097	154(159*)	6.9(10.*)
4	657	0.111	0.097	155(160*)	7.8(10.*)

Note. Characteristics of each CDF–S 500ks field $(1-4)$. Average photon and background counts per pixel calculated within 10 arcmin far from the aimpoint. Number of detected sources and flux limit obtained with the BSS algorithm are listed for each field. In brackets $(*)$: number of detected sources and flux limit in the soft $(0.5-2.0$ keV) energy band from the WAVDETECT algorithm. See text for more details.

to 16, allowing for the detection of more point–like sources but also of extended ones. The WAVDETECT algorithm applied with scales $2-16$ detects $2-10\%$ more sources than with scales $2-4$. The value 10% of additional detected sources is found in the field 3, that is characterized by the lowest mean source intensity compared to the other three fields. In addition, the WAVDETECT algorithm is known to not properly detect the size of extended sources (private communications with Dr. Paolo Tozzi). Therefore, the standard wavelet scale values of $2-4$ are preferred above the scale values $2-16$.

In Table 7.1, field properties are reported. Specifically, Table 7.1 reports for each field the maximum number of photon counts, the average intensity and background calculated within 10 arcmin from the aimpoint and the number of detected sources on the full fov. The average background and the number of detected sources are given from the analysis with the BSS algorithm of the four CDF–S 500ks fields. In addition, the number of sources detected by the WAVDETECT technique are listed in brackets. The flux limit[2] reached by the two techniques in the four CDF–S 500ks fields is reported. Energy fluxes are extrapolated from the observed count rate assuming a conversion factor $c_{\rm f} = (4.6 \pm 0.1) \times 10^{-12}$ erg cm^{-2} from count rate to flux in units of erg s^{-1} cm^{-2} (Giacconi *et al.*, 2002*b*; Rosati *et al.*, 2002*a*). This conversion factor is calculated assuming a power–law source spectrum with a photon index $\Gamma = 1.4$, absorbed by a Galactic column densities of 8.8×10^{19} cm^{-2} (see Rosati *et al.* 2002*a* for more details). The flux limit values are commented at the end of this Section. Note that the number of detected sources decreases with decreasing mean intensity in the field, as expected. This statement is true for both algorithms employed in the source detection. Contrariwise, when wavelet scale values $2-16$ are chosen with the WAVDETECT algorithm, an increasing number of detected sources is found from field 4 to

[2]Note that with the term 'flux limit' is here intended as the flux of the weakest detected source, instead of being quoted for a certain completeness.

3.

BSS analysis of the four CDF–S 500ks fields

In Fig. 7.8, the internal consistency of the BSS algorithm analysing the four data sets is reported. In panels $(a-d)$, the four CDF-S 500ks fields are arranged in pairs. Fields 1 and 3 are compared to fields 2 and 4, respectively. The radius used for cross–correlating the catalogues is of 2 arcsec.

From panel (a) to (d), source positions (right ascension and declination), fluxes and extent (i.e. the estimated size of the detected sources) are taken into account. In each panel, two plots are given. In the upper plots, a line of equal values is drawn. Error bars are superposed at $\pm 1\sigma$. Vertical error bars indicate the uncertainties on the parameters relative to fields 2 (black) and 3 (red). Horizontal error bars provide the measured error for the parameters on the other fields. The lower plots provide the residuals, i.e., the difference between the estimated values for each paired field. In panels $(a-b)$ and $(c-d)$ the residuals are the absolute difference and the relative error, respectively. Specifically, when A and B indicate the estimated parameter values for each paired field and σ_A and σ_B the errors on the parameters A and B, the absolute difference is given by $A-B$ and the relative error is $(A-B)/\sqrt{\sigma_A^2+\sigma_B^2}$. The zero and the ± 1 arcsec lines (panels $a-b$) and $\pm 3\sigma$ lines (panels $c-d$) are superposed with continuous and dashed linestyles, respectively. Insets are added in panels $(a-d)$ on the lower right–hand corner. In each of these insets, the histogram plot of the residuals is drawn. The histograms show that the residuals are normally distributed. In addition, in panel (c) a zoom into the data in the range value $[0, 500]$ net counts is shown in the upper left–hand corner.

In panels $(a-b)$, the estimated positions are consistent within each data set with a precision of ~ 1 pixel (with 1 pixel ~ 1 arcsec in the sky). Note that also when utilizing relative errors (this result is not shown), the residuals on the estimated positions are within the $\pm 1\sigma$ lines. Meaning that the centre of mass of detected sources is well defined also in extreme conditions of poor signal-to-noise ratio.

A larger scatter is found for the estimated fluxes (i.e., net counts) and extents (in terms of FWHM and units of arcsec) for each paired field, see panels $(c-d)$. The range of residuals extends to $\pm 3\sigma$. Poisson fluctuations in the background and contaminations by other sources in the field can increase the uncertainties estimated for the background model and, consequently, also the uncertainties estimated for the source flux and extent measurements. Therefore, the dispersion given by the residuals in panels $(c-d)$ is further investigated.

The estimated source flux and extent uncertainties versus the corresponding flux and extent are plotted in panels $(e-f)$, respectively, in logarithmic scales.

In panel (e), a black line is drawn to indicate the Poisson errors for given number of source counts, independent of the background value. The reported BSS flux errors for each CDF-S 500ks field are close to the Poisson error line with bright sources less affected by the background estimate. This result is expected since the uncertainties on the estimated source fluxes account for the propagation of errors due to background and

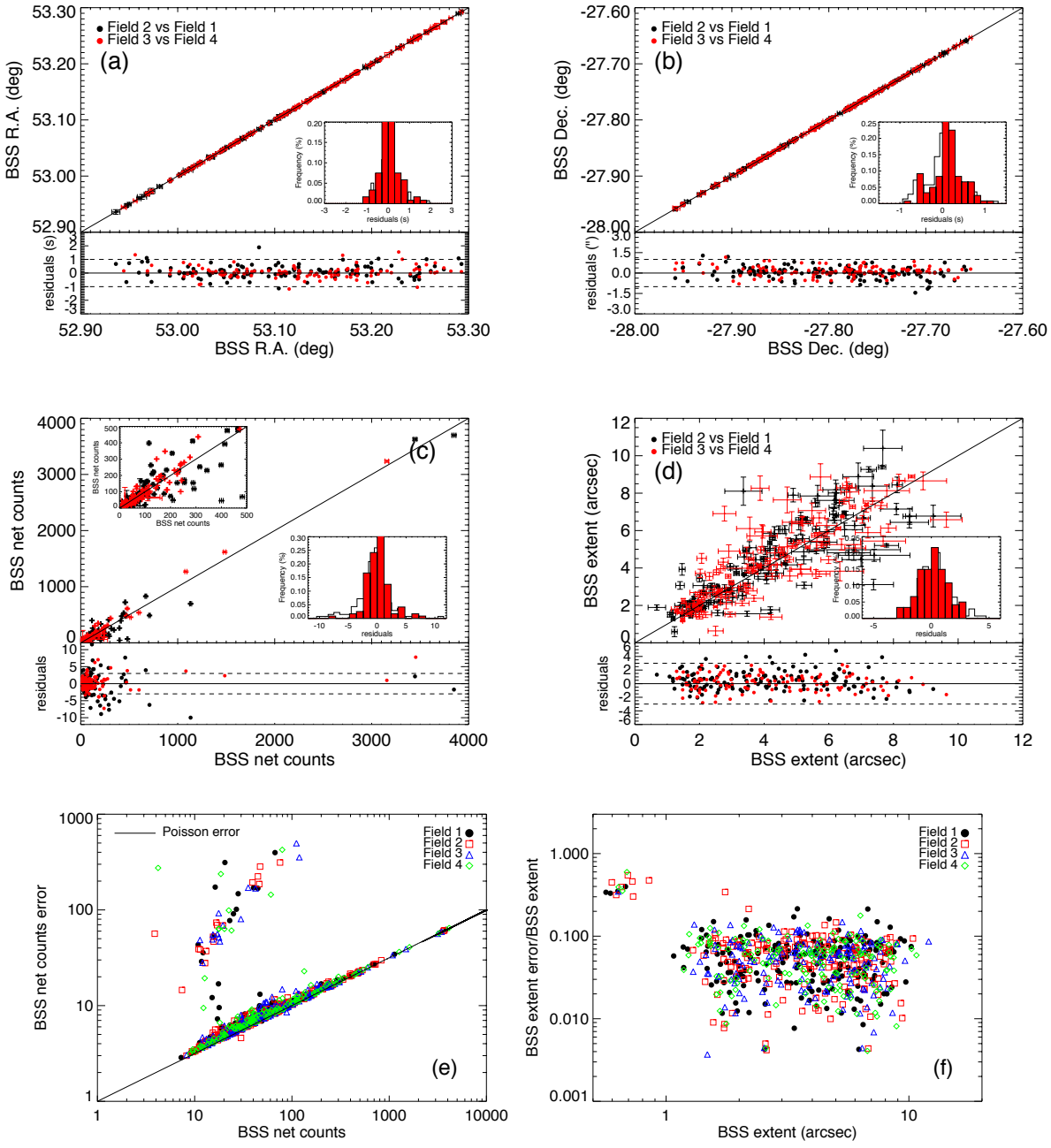

Figure 7.8: Comparison of the four CDF–S 500ks catalogues analysed with the BSS algorithm (see also Table 7.1). Panels $(a-d)$: comparison of right ascension, declination, fluxes and size, respectively. 1σ errors are superposed. Panels $(e-f)$: source flux and size compared to error and relative error, respectively.

source signals (i.e., $\sigma^2 = \sigma_S^2 + \sigma_B^2$, where σ_S, σ_B and σ indicate uncertainties on source signal, background and propagated error on detected source, respectively). Furthermore, a small number of data (8%) deviates from this trend. The scattering occurs for values of counts below fluxes of ≈ 100 counts and for net counts error larger than ≈ 6 counts. These sources have been visually inspected. Large errors in source counts are found for both point–like and extended sources. The causes for the large errors with point–like sources are: 1. Faint point–like source partially superposed to a bright point–like source; 2. Faint point–like source located at the edge of the fov; 3. Faint point–like source with nearby count enhancements of undetectable sources. Case 3 is verified with the CDF–S 2Ms data and the photometry of those sources can not be improved further when taking into account each CDF–S 500ks field individually. The large errors indicate in this case a natural fluctuation. Cases 1 and 2, instead, show that the knowledge of the instrumental PSF at varying off–axis angles included in the source fitting routine can improve the photometry especially of these sources. As already commented previously, the BSS source characterization routine can be adapted to specific instruments. Last, extended sources are affected by natural fluctuations in the data more than point–like sources. This is due to the larger area covered by extended sources with respect to point–like ones. Moreover, extended sources are currently parametrized with a multi–variate Gaussian. As already discussed, extended low surface brightness source parameters can be improved employing a β–model (Cavaliere and Fusco-Femiano, 1978). This task is not part of the current thesis.

In panel (f), the relative errors are considered. All data show extent errors lower than the extent parameter. A small group of data (2%) is characterized by an extent < 1 arcsec, i.e. the image pixel resolution. The relative error of this small group of data is much larger than with the rest of the sample. The sources belonging to this small group are visually inspected. These sources are faint point–like sources located within 5 arcmin from the aimpoint. These sources are also listed in the CDF–S 1Ms and the CDF–S 2Ms catalogues.

Selection of extended sources The results of the multiresolution analysis are a good indicator for separating point–like from extended sources for two reasons. First, SPMs provide for a visual identification of extended sources. Second, in an automated identification of extended sources, these objects are distinguished from point–like sources by the correlation length of source detection and the width of the instrumental PSF.

In Chapter 6, the RASS data were analysed. The width of the *ROSAT* RASS PSF is constant on the full fov (Boese, 2000) and it is easily accounted for on the full image for the separation of point–like and extended sources.

In pointed observations, as for the CDF–S region, the instrumental *Chandra* PSF degrades going towards the edge of the fov. In an automated search for extended sources associated with hot halos of galaxies, groups and clusters, the method described in Rosati (1995); Giacconi *et al.* (2002*b*) for the selection of the extended sources is well–known in astronomy. Therefore, this method is used.

The separation of extended and point–like sources occurs comparing the measured

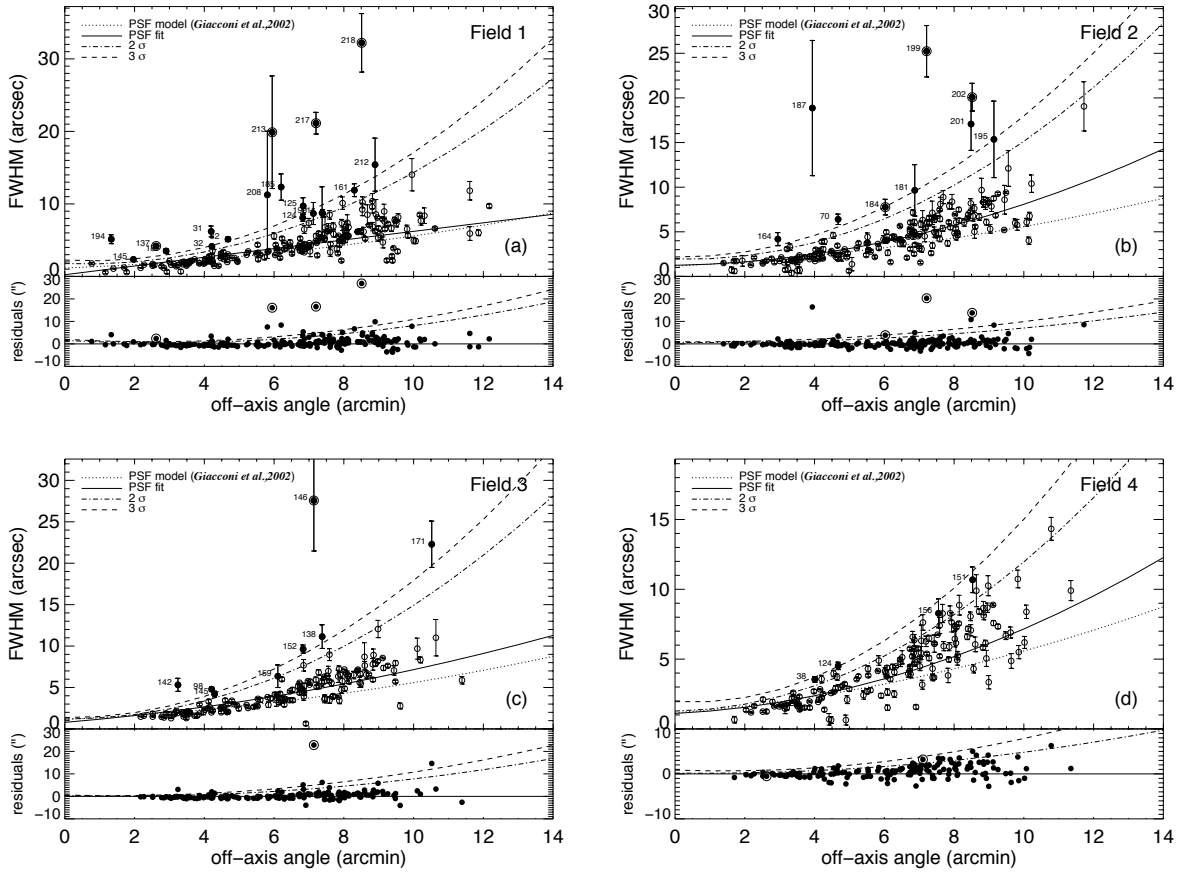

Figure 7.9: Selection of extended sources in the FWHM versus off–axis angle plane for each CDF–S 500ks data. Panels $(a-d)$ show the complete catalogues for Field $1-4$, respectively. Line curves are models and best fits of the PSF dependent. See text for more details.

FWHM of the detected sources with a local PSF width. The instrumental PSF model at varying off–axis angle is obtained empirically from each CDF–S 500ks catalogue (fields $1-4$) analysed by the BSS technique. The best fit of the PSF FWHM as a function of the off–axis angle is obtained as follows. The measured source extents, in terms of FWHM and in units of arcsec, are separated in four different off–axis angle bins ($0'-3'$, $3'-6'$, $6'-9'$, $9'-12'$). Histograms of the data in each bin are created and a Gaussian distribution is fitted to the histogram. A $k-\sigma$ clipping procedure is applied to reject sources with significantly large extent. By iterating, a subset of data in each bin is created that contains only sources with extent $< k\sigma_{\rm s}$, where $\sigma_{\rm s}$ is the standard deviation of the subset and k is chosen equal to 3. A polynomial fit to the mean values of the subset data in each bin defines the best fit of the PSF FWHM as a function of the off–axis angle. The mean and the standard deviation values of the subset data in each bin are used to create the confidence limits of $95-99.8\%$. The 3σ upper limit defines the cutoff line for extended sources.

In Fig. 7.9, four plots are given for each analysed CDF–S 500ks field. In the upper panels, the FWHM versus the off–axis angle plane is drawn for all detected sources. For each source the error bars (1σ) on the estimated sizes are drawn. The solid line is the parabolic best fit to the *Chandra* PSF as described above. Dashed and dot–dashed lines are the 3σ and 2σ limits of the PSF FWHM distribution. Sources which are likely to be extended are plotted as filled circles above the 3σ limit. The catalogue identification number is reported for each potential extended source. Known clusters or groups of galaxies are highlighted by filled circles. Note that in the upper panels, the dotted line (PSF model) is the best fit of the *Chandra* PSF FWHM in the soft ($0.5-2.0$ keV) energy band as provided in the work of Giacconi *et al.* (2002*b*). The difference of the two PSF models is mainly due to different techniques employed for the data analysis and for the number of data points used. The work of Giacconi *et al.* 2002*b* employed a larger sample (346 sources). In fact, two deep fields in the *Chandra* Archive additional to the CDF–S 1Ms are used for the PSF fit. The lower panels show the distribution of the FWHM residuals (absolute difference in units of arcsec) for the CDF–S 500ks sources. The 3σ and 2σ limits of the FWHM distribution are plotted with the same linestyles used in the upper plots. The histograms of the residuals (not shown) are composed by a distribution close to normal plus a right–sided long tail. The normal distributions are characterized by mean of ~ 0 and variance of 3 and 1.5 arcsec in the fields $1-3$ and 4, respectively. The one–sided tail indicates the presence of outliers, i.e. mainly sources whose surface brightness deviates from the one of a point–like source. Most, but not all, of the known clusters or groups of galaxies exceed the 3σ limit. This classification technique may fail primarily because the $k-\sigma$ procedure assumes an unjustified Gaussian distribution of the data, the results depend on the choice of the bins size and the source extent error is not taken into account in the classification process. The SPMs reveal, instead, that all known clusters or groups of galaxies are characterized by extended emissions.

Furthermore, the uncertainties on the source extent and the 3σ limit are now accounted for estimating the deviation of the source extents from the empirical PSF fit. Specifically,

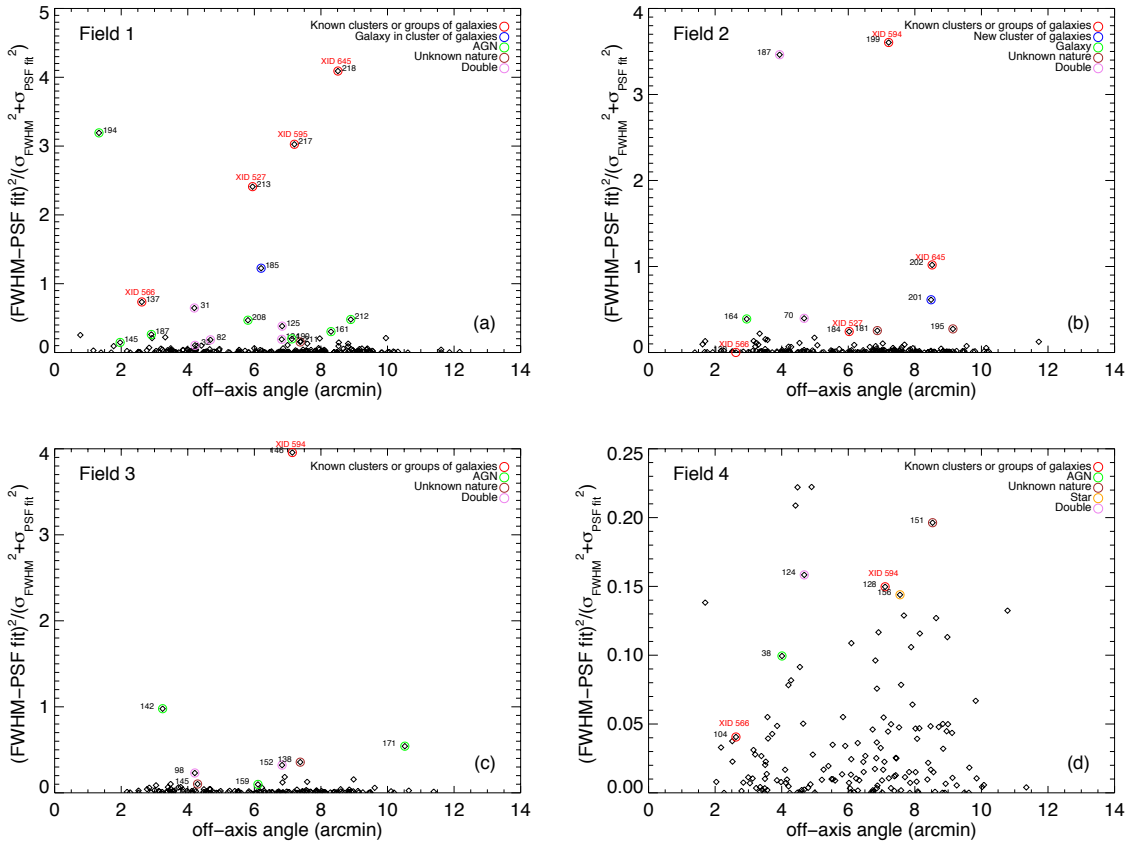

Figure 7.10: χ^2 distribution of source extent compared to the empirical instrumental PSF fit versus off–axis angle. See also Fig. 7.9 and text for more details.

a χ^2 distribution is considered, that is given by: $(X-Y)^2/(W^2+Z^2)$, where X, Y, W and Z are the source size, the PSF fit, the estimated error on the source size and the 3σ limit, respectively.

In Fig. 7.10, the results of the χ^2 distributions on the four fields are shown. In each plot, small values of χ^2 indicate that the estimated extent values agree with the one of point–like sources. Alternatively, sources associated with large values of χ^2 deviate from the empirical *Chandra* PSF fit and, therefore, one often assumes that large values of χ^2 indicates the detection of extended sources. In the four panels, all sources above the 3σ limit (results shown in Fig. 7.9) are highlighted. In addition, all known clusters or groups of galaxies listed in Giacconi *et al.* (2002*a*) (red labels) are highlighted with red circles independent to the 3σ limit. Most of the known clusters or groups of galaxies are above the selected threshold. However, in panels (*b*) and (*d*), a known compact group of galaxies (XID 566 in Giacconi *et al.* 2002*a*) is characterized by small values of χ^2. In the same way, XID 594 (Giacconi *et al.*, 2002*a*) in panel (*d*). Blue circles indicate potential clusters or groups of galaxies not listed in Giacconi *et al.* (2002*a*). In panel (*a*), the source ID 185 is catalogued as galaxy in cluster of galaxy by Moy *et al.* (2003). The work of Moy *et al.* (2003) provides an H–band survey of the CDF–S region. In panel (*b*), a blue circle indicates a new cluster of galaxies, that is confirmed by the BSS algorithm analysing the CDF–S 1Ms and 2Ms. AGNs are highlighted with green circles. Brown, orange and violet circles indicate sources of unknown nature, stars and nearby sources, respectively. Note that when the BSS multiband analysis is applied, detections affected by source confusion are improved. Additionally, field 4 CDF–S 500ks provides the most biased sample. This is due to the assumption that the data are normally distributed in each bin for the $k-\sigma$ procedure. This assumption is highly violated in this case. In Fig. 7.11, the sampled data for field 4 CDF–S 500ks are shown with histograms and a superposed Gaussian distribution fitted to each histogram.

Last, a probability of a source to be extended is desired for a proper source classification. Often, an extent likelihood is provided and used in classic statistics. The extent likelihood is a statistical statement determining whether the extent of a source is significant: See for instance the ML procedure (Cruddace *et al.*, 1988). In classic statistics, when only the PSF fit model is taken into account, it will never be possible to provide a probability for a source to be extended. At best, it is possible to provide the likelihood that the source deviates from a point–like source. For instance, the p–value can be calculated using the χ^2 fit. H_0 is set such that the PSF fit describes the width of point–like sources at varying off–axis angle and any deviation from the PSF fit is due to randomness in the data. Therefore, the χ^2 p–value (commonly known with the term χ^2 probability) provides the probability[3] that a function which does genuinely describe a set of N data points would give a value of χ^2 as large, or larger, than the one already estimated. The χ^2 probability requires a certain number of user selected parameters. The χ^2 probability is calculated as follows. A cutoff

[3]In classic statistical inference, the probability $p(A)$ is the long–run relative frequency with which A occurs in identical repeats of an experiment (Gregory, 2005).

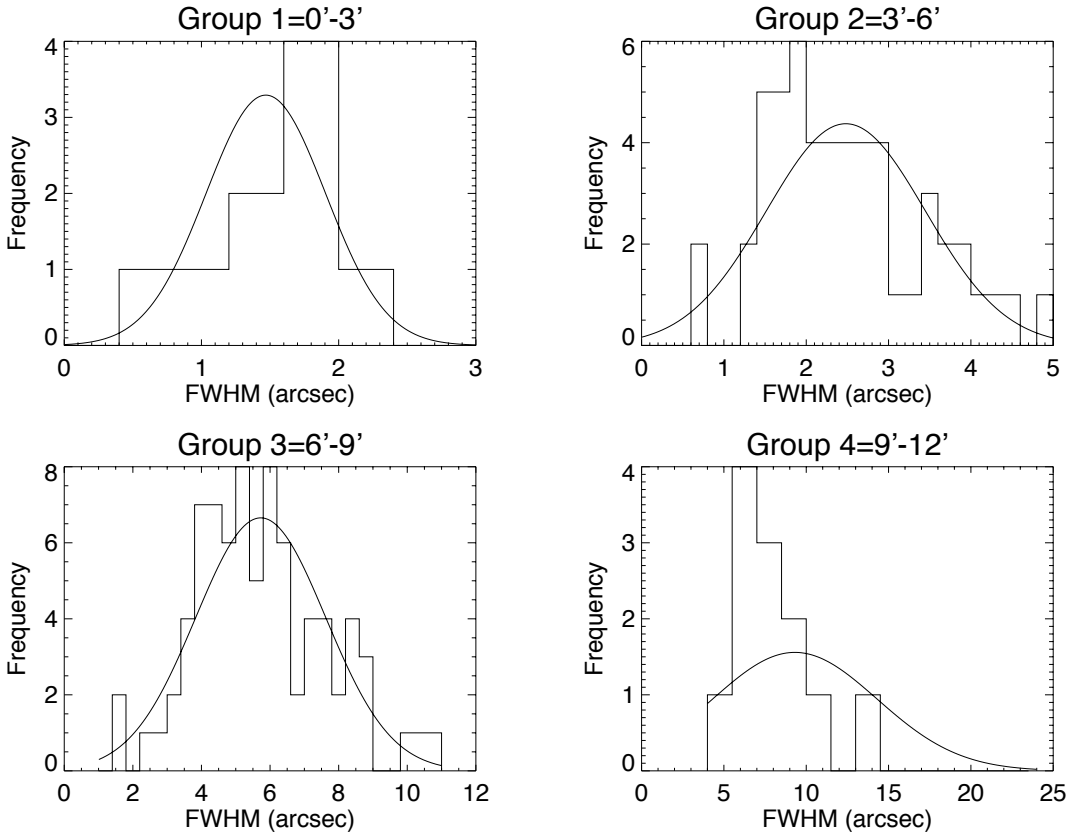

Figure 7.11: Example of normality condition for the $k - \sigma$ procedure in Field 4 of the CDF–S 500ks. Each histogram show the frequency of the source extent values, in terms of FWHM and in units of arcsec, divided in four groups. Each group collects data at different off–axis angles (in units of arcmin). The data in each group is fitted with a normal distribution.

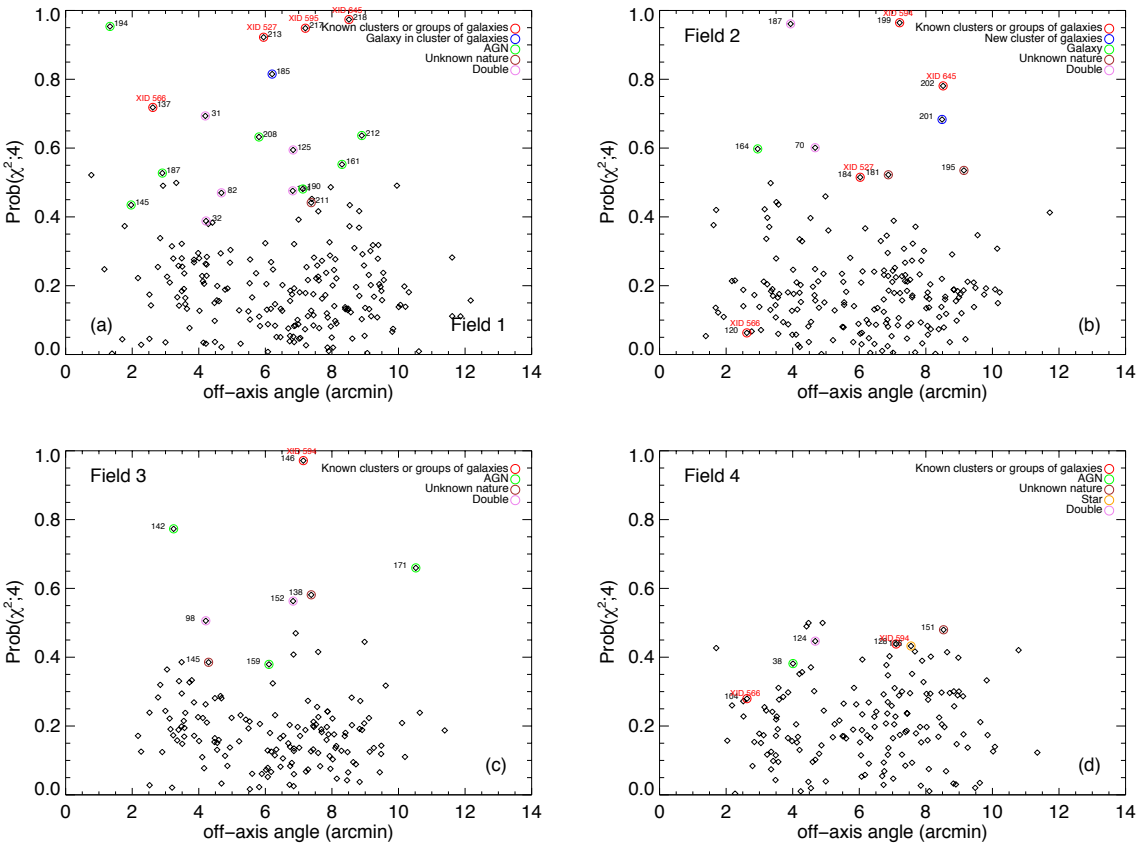

Figure 7.12: χ^2 p–value for an object to deviate from point–like versus off–axis angle. See also Figs 7.9 and text for more details.

value V in the χ^2 distribution with 4 degrees of freedom is used to specify a probability of occurrence or success. The number of degrees is chosen to be 4 because all the data are used to create the PSF fit and one additional data in each bin is utilized. The probability of occurrence or success is set to 0.95, due to the classically accepted significance level of 0.05. In Fig. 7.12, the χ^2 probability calculated for each detected source in each of the four fields is shown. Note that the properties of p-values have been already commented in Chapter 3. In other works, as for the $2XMM$ catalogue pipeline[4], an extent likelihood is calculated comparing the best fitting point–like source model with the best fitting extended source model. Also in this case, the probability that the extent detection is due to randomness in the data is calculated.

The technique proposed by Rosati (1995); Giacconi *et al.* (2002*b*) can be extended on two directions. First, sources are characterized by two sizes (i.e., major and minor axes). The two sizes can be exploited and compared to the instrumental PSF. Second, a probability of a source to be extended can be provided. In order to accomplish this goal, a new algorithm can be developed within the BPT formalism.

Survey selection function and source number counts In this test, there is no explicit interest in the nature of the detected sources, since this result is published in the works of Rosati *et al.* (2002*a*); Luo *et al.* (2008). However, the sensitivity of source detection can vary significantly across the survey area. On the one hand, bright sources can be detected over the entire solid angle of the survey. On the other hand, the effective area for the detection of faint sources decreases towards the edge of the fov. Therefore, the survey selection function and the source number counts are computed employing the BSS catalogues obtained analysing the four CDF–S 500ks images.
The following conditions are taken into account: (1) The four CDF–S 500ks fields are part of the same sky region; (2) Each CDF–S 500ks image is observed with the ACIS–I instruments onboard of the *Chandra* satellite. Although it is known that about 70% of the sources in the CDF–S region are characterized by X–ray variability (Paolillo *et al.*, 2004), the CDF–S 500ks data can be used to learn about the consistency of the developed method to obtain the same results in terms of the sky coverage and the source number counts. The sky coverage, or survey selection function, describes the sensitivity and the coverage of a survey. The sky coverage allows one to compute the source number counts. The source number counts (or $\log N$–$\log S$ distribution) provides information about the completeness and the reliability of a survey. The sky coverage and the source number counts depends on the algorithm employed for source detection (Rosati *et al.*, 2002*a*). Therefore, the sky coverage and the source number counts can be used as diagnostic tools for the BSS technique. Last, it is known that the $\log N$–$\log S$ distribution for point–like sources differs from the one for extended sources: See Rosati *et al.* (1995) for more details. In this test, the source number counts for point–like sources is taken into account and compared to the ones published for the CDF-S 1Ms and 2Ms catalogues (Giacconi *et al.*, 2002*b*; Luo *et al.*,

[4]http://xmmssc-www.star.le.ac.uk/Catalogue/2XMM/SSC-AIP-TN-003.ps

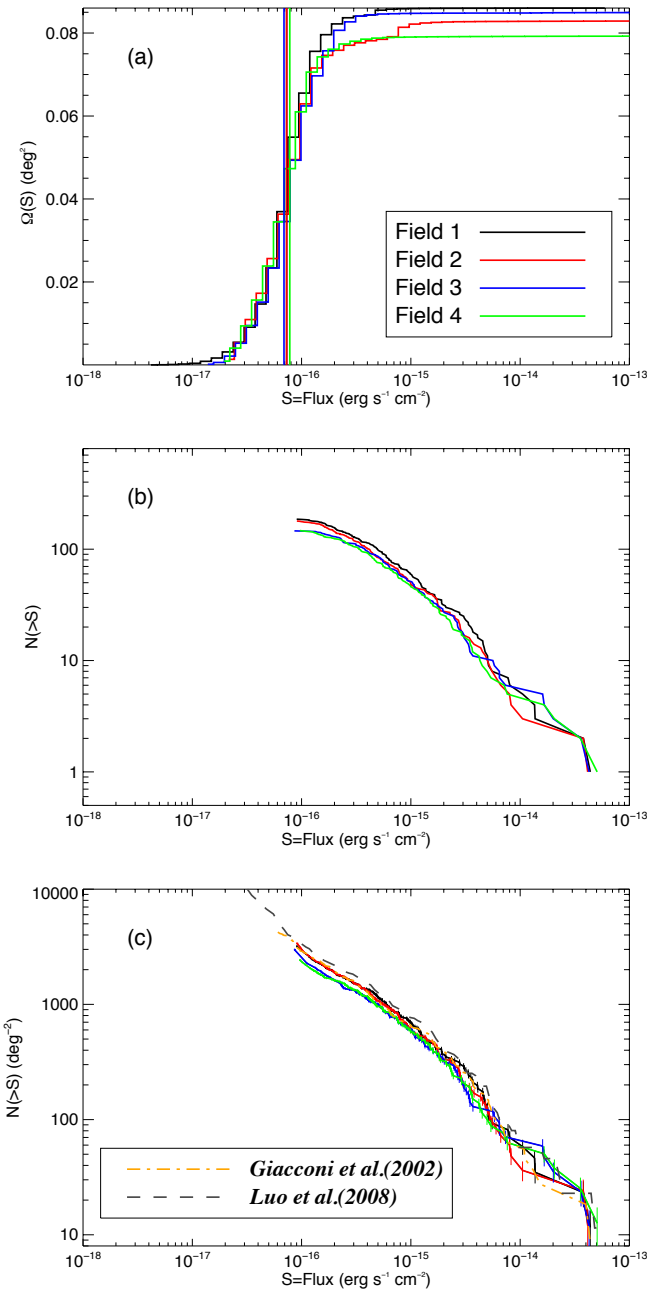

Figure 7.13: Sensitivity analysis of the BSS algorithm analysing the four CDF–S 500ks images: Panels (*a*), (*b*) and (*c*) provide the sky coverage (area covered vs. flux limit), the raw number counts and the log$N$-log$S$ distributions, respectively.

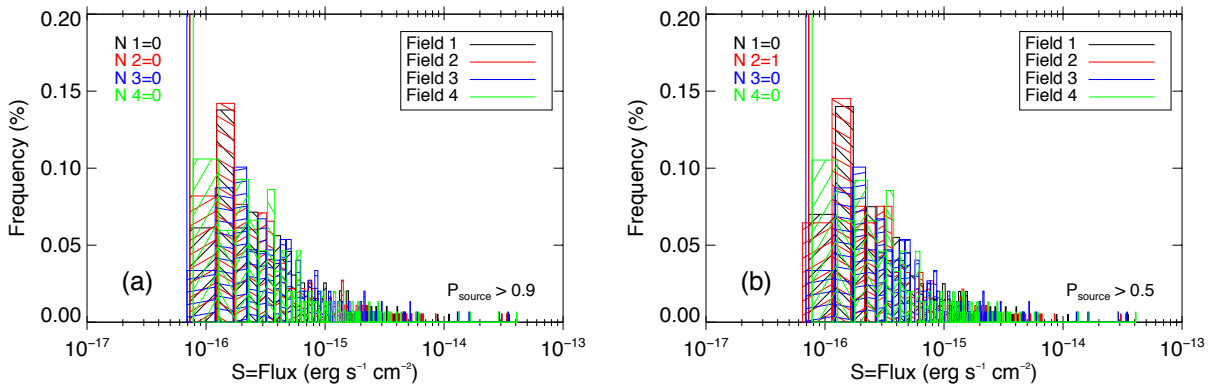

Figure 7.14: Relative frequency of detected sources in flux units of erg s^{-1} cm^{-2}: Panels (a, b), all sources detected with a source probability ($P_{\rm source}$) greater than and equal to 0.9 and 0.5, respectively. The abscissas are in logarithmic scale. See text for more details.

2008). To ensure compatibility of the absolute flux scale when comparing with previously published results the conversion factor to turn source count rate into observed flux in the soft $(0.5-2.0$ keV) energy band has been bootstrapped using the soft flux reported in the catalogue of Giacconi *et al.* (2002*b*). Requiring high signal–to–noise and non–variability, the relatively bright ($f_{\rm X} = 4 \cdot 10^{-14}$ erg s^{-1} cm^{-2}) source labelled XID 63 in Giacconi *et al.* (2002*b*) has been identified as the best flux calibrator in the field because its measured signal remains constant within $\pm 3\%$ amongst the different epochs of observation defined by the four CDF–S 500ks data sets. In this way a flux calibration accurate to about 3% and consistent with previous measurements has been established. The corresponding flux conversion factor for the $0.5-2$ keV energy band is 5.7×10^{-12} erg cm^{-2} from count rate to flux in units of erg s^{-1} cm^{-2}. The sky coverage and the source number counts are calculated on the full fov.

The sky coverage, $\Omega(S)$, is the survey solid angle within which the flux limit S is reached. The flux limit map is usually constructed to take into account PSF variations, vignetting effects and the background variations. The background maps from the BSS technique, obtained analysing the four CDF–S 500ks images, are used. Therefore, vignetting effects and background variations are already accounted for in the coverage. The PSF fit, i.e. the FWHM as a function of the off–axis angle (θ), is obtained empirically with a $k-\sigma$ technique. For a description of the technique, see previous paragraph. The polynomial fits obtained for each CDF–S 500ks field are used.

The sky coverage is studied employing the following steps. Considering each pixel of an astronomical image, a map containing the flux limit (flux limit map) is computed. The flux limit map is based essentially on a threshold value for the background, the exposure map and the PSF variation along the fov. The threshold value for the background is chosen with a value of 3σ, because this value corresponds approximately to the limit

in sensitivity of the BSS technique. A PSF area is considered, in which the number of background photons on the PSF area follows Poisson statistics. From the flux limit map, the cumulative distribution with respect to the flux is obtained.

In Fig. 7.13, panel (a), the sky coverage for each of the four CDF–S 500ks fields is drawn. The sky coverage for each analysed field is highlighted with different colors: black, red, blue and green correspond to fields 1, 2, 3, 4, respectively. The same pattern is kept in panels (b, c).

The flux limit of each survey can be derived where the curve changes in concavity. The vertical lines indicate, instead, the flux limit obtained by the faintest detected source listed in each BSS catalogue as given in Table 7.1. The flux limit given by the catalogues coincides with the one provided by the sky coverage. The four CDF–S 500ks fields are very similar in terms of depth. For flux values larger than 10^{-15} erg s^{-1} cm^{-2}, the four fields are characterized by different effective area. A dispersion of $> 20\%$ is shown, which is due to the different geometric area of each field (see Fig. 7.6). The different geometric area arises because of the different roll angles in the observations and, consequently, of different exposure times.

In the literature, often sources with fluxes below the flux limit map are found. For instance, in the work of Luo *et al.* (2008), 14 sources are found in the soft $(0.5 - 2.0$ keV) energy band that have fluxes below the flux limit map. Luo *et al.* (2008) attributes the presence of these sources to the fact that detected sources are not filtered out with the flux limit map. In this work, the BSS background model is used for the calculation of the flux limit map. A different result is expected with respect to the one of, e.g., Luo *et al.* (2008). In Fig. 7.14, histograms are used to compare the flux densities of the detected sources at two source probability ($P_{\rm source}$) thresholds with respect to the flux limit. Sources with fluxes lower than the flux limit are counted. The labels $N1, 2, 3, 4$ indicates the number of detected sources with fluxes fainter than the one given by the vertical bar (i.e. the flux limit). Only in the field 2 of the CDF–S 500ks data, one source with $P_{\rm source} < 0.9$ is found. The flux of this source is only 1% lower than the flux limit given by the vertical bar. This is another benefit of the BSS technique when studying survey data analysis with respect to previous algorithms employed for background estimation and source detection.

In panel (b) of Fig. 7.13, the cumulative distributions of the number of sources are shown for each field. The plot indicates the raw number count function. This function depends on the instrument and the observed field. The details of the raw number count function is determined by the technique employed for source detection. In fact, each curve provides the number of sources detected in each field. The raw number count function is similar for the four fields.

The distributions in panels (a, b) of Fig. 7.13 are used to derive the cumulative distribution of number of sources corrected for the sky coverage, shown in panel (c) of the same figure. Panel (c) provides the number of sources per square degree of sky, $N(> S)$, versus the minimum detectable flux S (erg s^{-1} cm^{-2}). Hence, panel (c) shows the real density of sources. The log$N$–log$S$ distribution allows one to set constrains on the cosmological

evolution of the surveyed population.

In panels (b, c) of Fig. 7.13, the cutoff at low fluxes arises because the surveys are flux limited and a cut is set as a detection limit. At large fluxes, the limit is due to the geometrical area. The flux limits shown in panels (b, c) are similar to the ones shown in panel (a). Uncertainties (1σ) are superposed to the cumulative distributions in panel (c) following Poisson statistics. The errors are, therefore, given by $1/\sqrt{N}$, where N is the source number counts per square degrees, that is e.g., on 100 sources observed, an error of 10% is added for not having detected expected sources.

The four CDF–S 500ks images show very similar sensitivity. Nonetheless, at low fluxes ($S < 10^{-16}$ erg s^{-1} cm^{-2}) the log$N$–log$S$ distributions increase rapidly. This steep increment is due to sources with net counts ≤ 15. Faint fluxes of detected sources are characterized by larger errors than the ones encountered with bright sources. Consequently, in panel (c) one would expect increasing errors in the source number counts deg^{-2} at decreasing fluxes. This effect is due to systematics, that are not accounted for by Poisson statistics alone. An additional systematic error enters in the log$N$–log$S$ distribution from the sky coverage. It is another cause for the steepening in the data, due to the fact that the number of detected sources is corrected for the survey area. Therefore, the flux limit and the survey area at a given flux limit is underestimated with the consequent overcorrection of the four log$N$–log$S$ distributions derived from the analysis of the CDF–S 500ks data. The uncertainty from these systematic errors to report in the analysis is not easily quantifiable. In classic statistics, the quantification of systematic errors occurs employing supplementary analyses, e.g. simulations. In Bayesian statistics, the quantification of systematic errors occurs employing the rules of probability theory. Considering the many advantages that BPT provides with respect to classic statistics (listed or described through the whole thesis), a new method for estimating the source number counts while taking into account systematic and random errors can be developed: More information is given below and in Chapter 8.

Furthermore, the log$N$–log$S$ distributions published in Giacconi *et al.* (2002*b*) and Luo *et al.* (2008) are plotted with dot–dashed (orange) and dashed (dark grey) linestyles in panel (c) for comparison. The log$N$–log$S$ distributions obtained with the four CDF–S 500ks images are in agreement with the ones published for the CDF–S 1Ms and 2Ms data. The source number counts distribution employing all the data sets available (Luo *et al.*, 2008) is deeper than the ones derived with the four CDF–S 500ks data sets and the one published in Giacconi *et al.* (2002*b*). In the work of Luo *et al.* (2008), the cumulative number counts deviation from the CDF–S 1Ms data to the CDF–S 2Ms data is justified by the different selection of the count–rate–to–flux conversion factor used in these two surveys and by sky–to–sky variations. Note that also in the work of Luo *et al.* (2008), a steepness in the data is found for fluxes below 10^{-16} erg s^{-1} cm^{-2} even if effects of incompleteness and selection bias are quantified through Monte Carlo simulations. Since measurement errors distort the shape of a distribution of source observables (scatter distortion) (Jeffreys, 1938; Loredo, 2004), it is very important that any claimed evolutionary effect has to be properly quantified. In order to properly quantify the shape of the distribution, a new method for survey data analysis can be developed within the BPT framework. The new

technique has to incorporate in one unique algorithm the survey selection function and the cumulative source number counts, including selection effects and measurements errors. The application and further studies of the proposed technique is not part of this thesis.

Wavdetect analysis of the four CDF–S 500ks fields

The four WAVDETECT catalogues are analysed as executed with the BSS algorithm in the previous paragraph. The results are shown in Fig. 7.15. The description of the plots follows the one given for Fig. 7.8. Nonetheless, the 1σ error (or Gaussian level) associated with the estimated source parameters is now describing the *confidence limit* reported at a 68.3% confidence level. Note that the plot on the estimated source extent does not report errors. Errors on source extent are not listed in the WAVDETECT catalogues even if source extent errors are estimated by the WAVDETECT algorithm. Therefore, the absolute difference between the estimated source extents are considered when comparing the four WAVDETECT catalogues.

Panels $(a-b)$ of Fig. 7.15 show that the accuracy of the WAVDETECT source positions is ~ 1 arcsec. However, the scatter between the absolute difference of the estimated positions in each pair of field is by a factor of 3 larger than the one found with the BSS algorithm (compare to Fig. 7.8).

In panel (c), the values on the estimated net source counts are similar within each field. The relative errors on the estimated net source counts for each paired field show a larger scatter than the one given by the BSS technique.

In panel (d), the estimated source extent provided by the WAVDETECT catalogue is shown at 3σ. The WAVDETECT source extent is given, as for the BSS algorithm, by a multi–variate Gaussian parameterization of the detected sources. Different to the BSS technique, the parameterization is computed from a wavelet transform analysis of the counts in a region of source detection. In the mean, the extent values reported by the two techniques are similar, although the range of values provided by WAVDETECT is larger than the one obtained with the BSS algorithm. The residuals report the absolute difference between the estimated values. A scatter of 10 arcsec is found. Meaning that objects detected in one field may be found with an extent parameter value differing by 10 arcsec in the other field. Moreover, a systematic error inserted by the WAVDETECT technique is found in the estimate of the extent parameter. This systematic effect is not found with the BSS algorithm (see Fig. 7.8, panel d).

In panel (e), the estimated source net counts and their errors are considered. On the plot, the Poisson and Gehrels' error lines are drawn. The Gehrels' error line provides an approximate expression for the error on the source net counts. The Gehrels'error is defined as $1 + \sqrt{N + 0.75}$, where N indicates the source net counts (Gehrels, 1986). The work of Gehrels (1986) provides the upper confidence level equivalent to 1σ Gaussian error with small number statistics. In WAVDETECT technique, the errors are calculated with both methods. In panel (e), the errors on the net counts are well fitted by the Gehrels' error line for net source counts > 50 counts. For fainter sources, the Poisson and Gehrels' error lines are the lower and upper limits of the net counts errors. The same trend is

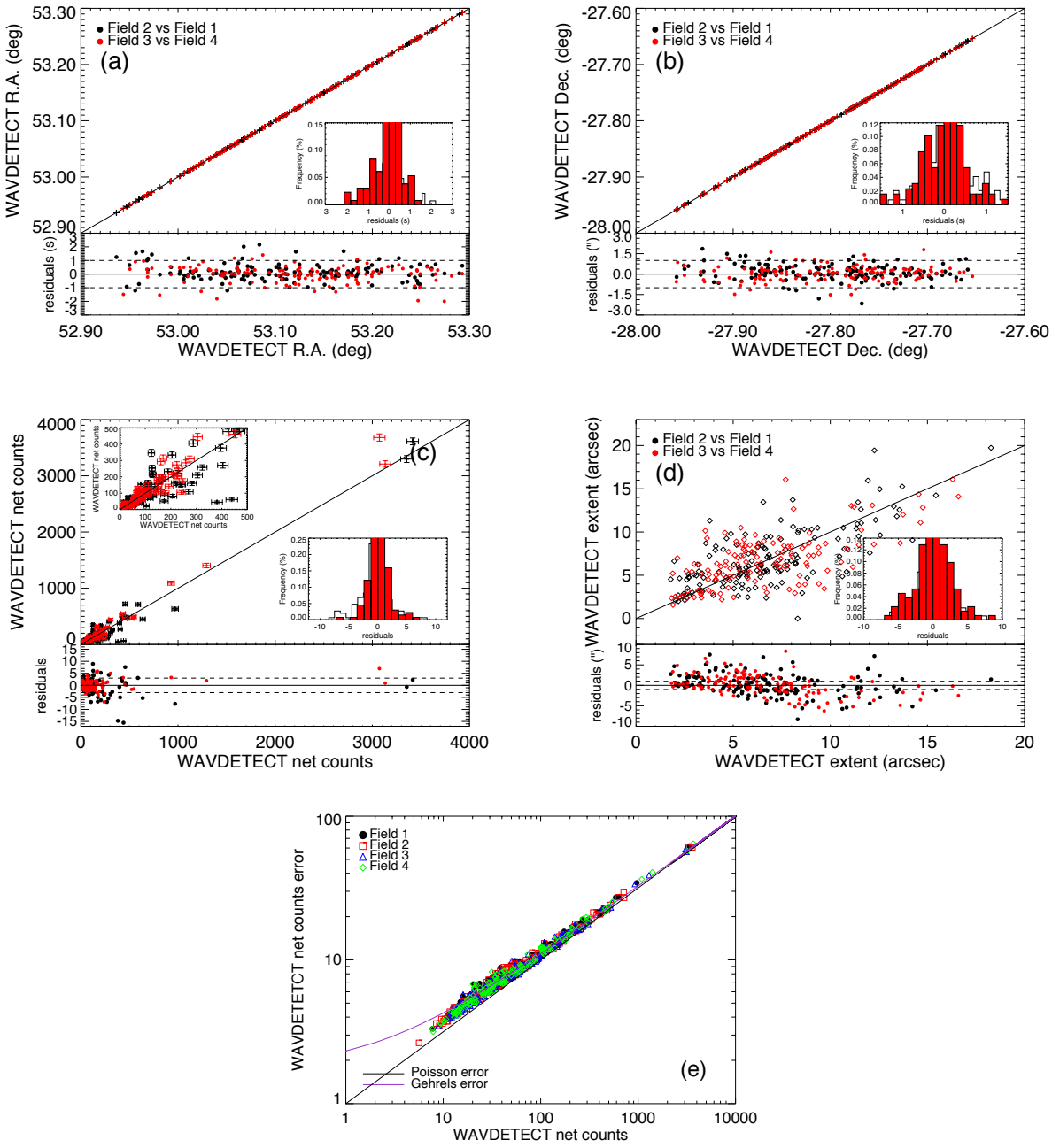

Figure 7.15: As Fig. 7.8, but employing the WAVDETECT algorithm. No errors on the source extent are reported in the WAVDETECT catalogues.

found in the simulated data analysed with the WAVDETECT algorithm in Chapter 5. The deviation from the Poisson error line may be due because background counts are taken into account. Hence, another bias (systematic error) is found when employing the WAVDETECT algorithm.

Comparing BSS and wavdetect catalogues

In Fig. 7.16, the catalogues obtained with the BSS and the WAVDETECT techniques are compared. In panels $(a-c)$, the residuals are the difference in values weighted by the sum of their squared variances. In panels $(a-b)$ the estimated source positions are compared. Agreement in source position with the two techniques is achieved. Panel (c) relates the detected net source counts with the WAVDETECT technique versus the ones obtained with the BSS algorithm. Often larger values for the net counts are found with the BSS algorithm. As shown in Chapter 5, the BSS background model allows for improved source counts with respect to the WAVDETECT algorithm. In panel (d), the probability of source detection given by the BSS technique is compared to the BSS estimated source fluxes in units of count ks^{-1}. The same relation is shown in panel (e), but for the WAVDETECT algorithm. In panels $(d-e)$, the abscissas are in logarithmic scales. The WAVDETECT algorithm provides the source significance instead of the probability of source detection as the BSS technique does. The source significance of a detection, provided by WAVDETECT, is the ratio of the net source counts and the Gehrels'error of the sum of the estimated background counts in each pixel of the source detection region. Therefore, the source significance increases at increasing source count rates. The description of a "source significance" is very different from the BSS technique. As already discussed in Chapters 2 and 3, the BSS algorithm provides a probability of source detection that is intrinsically connected with the mean intensity distributed in the field, the detected source counts and the background counts in addition to the detected source. Therefore, large values of source probability can be given to faint point–like sources: See, for instance, Table 3.1. Faint objects are often missed with the WAVDETECT technique. An example is given by a source detected in field 1 CDF–S 500ks with $P_{\mathrm{source}} = 0.95$. This object is listed in the CDF–S 1Ms catalogue (source XID 516 in Giacconi *et al.* 2002*a*), that is an AGN–I at $z = 0.667$. This AGN is detected by the BSS algorithm with net counts lower by a factor of 2 than the ones provided in Giacconi *et al.* (2002*a*). This AGN is not listed in the catalogue provided by WAVDETECT. The WAVDETECT source significance for faint objects results less reliable than the one obtained with the BSS technique.

In Table 7.2, the number of sources detected in one field but not another of the CDF–S 500ks data are summarized for the two algorithms separately. Only sources within 10 arcmin from the average aimpoint are considered, due to the different geometries of the four fields. Therefore, sources located at the edges of the four fields are excluded from the comparison. Looking at the reported numbers, the WAVDETECT algorithm seems to behave better than the BSS method (due to smaller numbers) especially when comparing fields $1-2$ with fields $3-4$. However, nondetected sources are faint objects whose brightness varies not only because of background fluctuations but also for X–ray variability (Paolillo *et al.*,

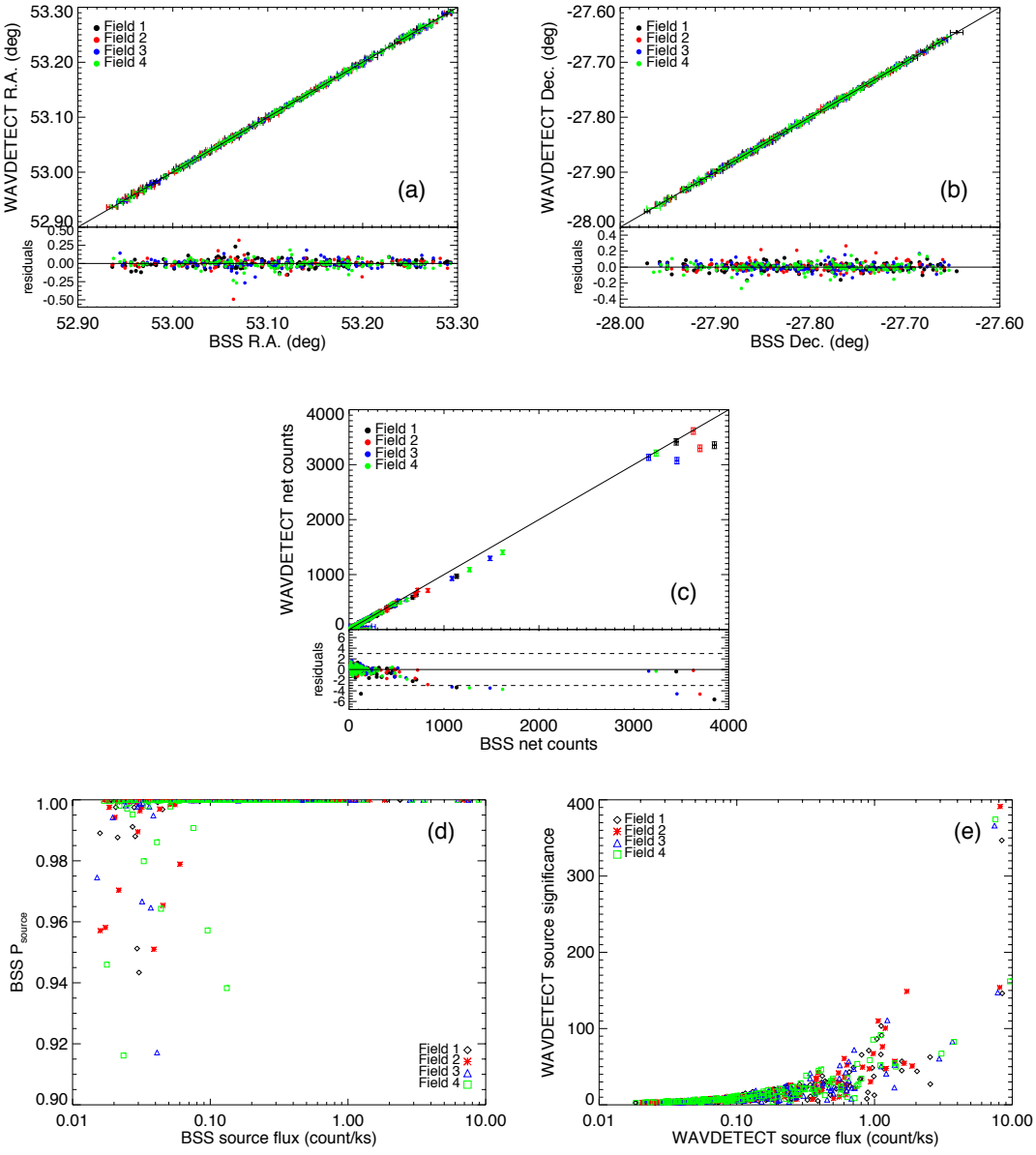

Figure 7.16: Comparison between BSS and WAVDETECT algorithms. Panels $(a-c)$, as given in Figs 7.8 and 7.15. Panels $(d-e)$ significance of source detection versus fluxes according to the two techniques.

Table 7.2: Sources detected in one field of the CDF–S 500ks data but not another, according to the BSS and WAVDETECT techniques separately. Only sources within 10 arcmin from the aimpoint are considered.

		NONDETECTION						NONDETECTION			
	Field	1	2	3	4		Field	1	2	3	4
BSS	1	$\cdots$	44	63	67	WAVDETECT	1	$\cdots$	40	59	58
	2	36	$\cdots$	60	60		2	30	$\cdots$	48	49
	3	20	25	$\cdots$	21		3	27	25	$\cdots$	23
	4	26	27	19	$\cdots$		4	27	27	22	$\cdots$

Note: e.g., there are 44 sources detected in field 1 with the BSS technique that are not detected in field 2 with the same algorithm.

Table 7.3: Sources detected in each field of the CDF–S 500ks data with one technique but not the other (BSS vs. WAVDETECT).

	NONDETECTION	
Field	BSS	WAVDETECT
1	20	7
2	24	12
3	4	10
4	8	11

Note: e.g., there are 20 sources detected in field 1 with the BSS technique that are not detected with the WAVDETECT algorithm.

2004). 70% of the sources in the CDF–S region are characterized by X–ray variability. The observations of fields $1-2$ are taken in the time range of 1.2 year, while images of fields $3-4$ are taken ~ 7 years later than fields $1-2$ and within 3 consecutive months of observations. In fact, the number of nondetected sources increases when comparing fields $1-2$ with fields $3-4$. No conclusive statement can be given on this respect.

In Table 7.3, the number of sources detected with one algorithm and nondetected with the other algorithm are listed for each analysed field. These detections are faint sources. In order to exclude the presence of false positives in source detection, previous researches on the CDF–S region are considered. For both algorithms, almost all sources are found in the CDF–S 1Ms and the CDF–S 2Ms catalogues. A small number of sources ($< 1\%$) has no counterpart with these two major X–ray catalogues on the CDF–S region. These sources are further investigated employing supplementary optical, near infrared and X–ray

catalogues, suggesting that these objects are likely true X–ray sources. The WAVDETECT technique detects 3 sources (two galaxies and one object of unknown nature) listed in the works of Groenewegen *et al.* (2002) (optical and near infrared bands), Grogin *et al.* (2003) (optial band), Grazian *et al.* (2006) (near infrared band). The WAVDETECT positions of these sources are ~ 2.2 arcsec far from the positions given by the listed catalogues. The BSS algorithm detects 4 sources (one star, one object of unknown nature, two galaxies), whose counterparts are found within 1 arcsec far from the positions given by Groenewegen *et al.* (2002) (star in the optical and near infrared part of the electromagnetic spectrum), Grogin *et al.* (2003) (object of unknown nature in the optical band), Alexander *et al.* (2003) (X–ray galaxy), Moy *et al.* (2003) (galaxy, H–band study).

The BSS algorithm outperforms the WAVDETECT technique in detecting extended objects. The four known clusters and groups of galaxies listed in the CDF–S 1Ms catalogue (Giacconi *et al.*, 2002*a*) (XID 527, 566, 594, 645) are detected by the BSS algorithm. Problems are found with the WAVDETECT algorithm in detecting these sources. More is reported about some of these objects in Section 7.2.4.

A cluster of galaxy close to a point–like source, XID 527, is detected by the BSS algorithm in the fields $1-2$ CDF–S 500ks. The WAVDETECT algorithm detects this object only in the field 2 CDF–S 500ks, but with distorted extent and much larger than the one found with the CDF–S 1Ms data.

XID 566 is a compact cluster of galaxy with emission similar to point–like objects. In the $1-2-4$ CDF–S 500ks fields, the BSS and the WAVDETECT techniques detect this object. Only the BSS algorithm identifies this object as extended. In the 3 CDF–S 500ks field the BSS and the WAVDETECT algorithms do not detect this object.

A bright cluster of galaxies, XID 594, is composed by a cD galaxy and a diffuse emission. The BSS algorithm detects the cD galaxy and the diffuse emission of the cluster of galaxies in the four CDF–S 500ks data. Substructures, that can be due to background fluctuations in the data, are additionally detected. The WAVDETECT algorithm detects the cD galaxy, but the detection is often misplaced and with larger extent than the one given with the CDF–S 1Ms data.

A very low surface brightness object, XID 645, is detected by the BSS algorithm as extended source in the fields $1-2$ CDF–S 500ks. Substructures are also detected by the BSS algorithm. In field 2 CDF–S 500ks, the BSS algorithm detects another extended feature not listed in the work of Giacconi *et al.* (2002*b*), but confirmed by the BSS algorithm analysing the CDF–S 1Ms and 2Ms and by photometric data. No detections of this object occurred with the WAVDETECT algorithm in the four CDF–S 500ks fields.

Last, the flux limit reached in each four CDF–S 500ks fields by the two techniques is considered. In order to give an estimate of the sensitivity reached in each field by the two techniques, the minimum source count rate (in units of count s^{-1}) is converted to flux (in units of erg s^{-1} cm^{-2}). Following the work of Giacconi *et al.* (2002*b*), the conversion factor c_f is used: See Section 7.2.3 for more details. In Table 7.1 the estimated flux limits are reported. The CDF–S 2Ms catalogue (Luo *et al.*, 2008) is by a factor of 3 more sensitive than the CDF–S 1Ms catalogue (Giacconi *et al.*, 2002*b*). The BSS algorithm on the four CDF–S 500ks fields provide flux limits that are 4 and 1.3 times less sensitive than

the CDF–S 2Ms and 1Ms catalogues, respectively. The WAVDETECT technique on the four CDF–S 500ks fields is 5 and 1.7 times less sensitive than the CDF–S 2Ms and 1Ms catalogues, respectively. The BSS technique improves, therefore, the sensitivity reached by the WAVDETECT algorithm.

Summary

The CDF–S region was observed during two surveys. The first and the second surveys lasted from October 1999 until December 2000 and from September 2007 until November 2007, respectively. The total exposure time is of 2 Ms. Official catalogues in the X–ray regime of the CDF–S region are given by the works of Giacconi *et al.* (2002*b*); Luo *et al.* (2008).

The CDF–S 2Ms data in the soft ($0.5 - 2.0$ keV) energy band are separated in four images of 500 ks exposure time each in order to test the capabilities of the BSS algorithm on pointed observations. Additionally, the results obtained with the BSS algorithm are compared to the ones given by the WAVDETECT technique.

The BSS algorithm provides a robust technique. The BSS estimates in source parameters are internally consistent. No systematic errors are found within the BSS results. The residual errors are within 1σ and 3σ for estimated parameters in source positions and source counts (and extent), respectively. However, large errors in source counts are found for 8% of all detected sources. Large errors in source counts are found for: 1. faint sources partially superposed to bright sources; 2. faint sources embedded in large background fluctuations, 3. extended sources. Further developments of the BSS technique are proposed to improve the estimates of these sources. The proposed developments are not part of this thesis.

The catalogued sources, extracted with the BSS algorithm from each CDF–S 500ks image, are also explored in source classification (i.e., an automated technique to classify point–like and extended sources) and in survey data analysis. Standard techniques in the X–ray regime are employed, whose result is depending on an empirical PSF fit. The PSF fit is executed on each field with a $k - \sigma$ procedure.

For the separation of point–like and extended sources, the classification technique described in Rosati *et al.* (1995); Giacconi *et al.* (2002*b*) is used.
All scientific applications require an automated machine capable to provide a list of clusters or groups of galaxies or at least sources associated with hot halos from the analysis of an astronomical image. In the works of Rosati *et al.* (1995); Giacconi *et al.* (2002*b*), the distance of the detected source FWHM from the local PSF fit is taken into account. This technique succeeds in classifying clusters or groups of galaxies as extended sources, only for those clusters or groups of galaxies whose extent is several times larger then the local PSF size. Compact groups of galaxies, as the Cimatti's (XID 566), are not properly classified. In addition, the sample of potentially extended sources is contaminated by AGNs, stars, close by galaxies and sources affected by source confusion. The pitfalls of this technique

reside mainly in the assumption of a Gaussian distribution for binned data. The bin size depends on the user choice and the source extent measurement error is not taken into account for the binning process.
The residual errors of the distance from the source FWHM and the local PSF fit are additionally calculated taking into account the FWHM error and the 3σ limit of the PSF fit. A classical χ^2–fit is performed. The χ^2 statistic is employed because it is widely used in many fields of science as goodness of fit. However, the technique of Rosati *et al.* (1995); Giacconi *et al.* (2002*b*) is not improved with a χ^2–fit and no statistical result is given.
Ideally, an astrophysicist aims to a probability of an object to be extended. Classic statistics is further explored to obtain a χ^2 p–value. Additionally user selected values for acquiring the final result of the χ^2–fit are needed. The result of this procedure provides a number that tells us how much the celestial object deviates from a point–like source due to randomness in the data. BPT has, instead, the potentials for providing the probability of an object to be extended. Further studies are proposed as future work.

Current procedures for the survey data analysis are tested. The sky coverage and the source number counts from the analysed CDF–S 500ks fields with the BSS algorithm are studied. The BSS technique is capable to obtain the same results of the sky coverage and the source number counts from the four analysed fields. The results are in agreement to the ones obtained with the CDF–S 1Ms and 2Ms data, published in Giacconi *et al.* (2002*b*); Luo *et al.* (2008).
The background model provided by the BSS algorithm is shown to be superior to the ones given by previous methods. The BSS background model is used for the calculation of the flux limit map. However, an empirical PSF fit and a user selected threshold for the background level are also accounted in the flux limit map. Both, the PSF fit and the selected threshold level, may introduce a bias on the final result of the log$N$–log$S$ distribution. In addition, the log$N$–log$S$ distribution is calculated without accounting for the source flux error. Consequently, the shape of the distribution is distorted especially for very faint fluxes. A new technique within the BPT framework for survey data analysis could improve the log$N$–log$S$ distribution: See Chapter 8 for more details.

The WAVDETECT technique is tested for internal consistency as performed with the BSS algorithm. The BSS algorithm is capable to supply an improved internal consistency with respect to the WAVDETECT technique. The WAVDETECT residuals errors on source positions are found 30% larger than the ones with the BSS algorithm. WAVDETECT does not provide the uncertainty measurement on the source extent. The range of the WAVDETECT source extent values are by a factor of 3 larger than the ones provided by the BSS algorithm. Systematic errors are found in the estimate of the source extent and counts.

The comparison of the BSS and the WAVDETECT catalogues shows that the BSS algorithm improves in the source count estimates. In addition the Bayesian $P_{\rm source}$ provides for more reliable results than the WAVDETECT source significance.

Sources detected with one and not the other algorithm for each field are analysed. In this specific case, the BSS algorithm detects by a factor of 1.4 fainter sources than the WAVDETECT technique. Nonetheless, faint sources are not detected with one or the other

algorithm, because of background fluctuations and of the selected threshold levels (i.e., 'sigthresh' and $P_{\rm source}$ values with the WAVDETECT and the BSS algorithms[5], respectively). 99.6% and 99.4% of all sources detected with the WAVDETECT and the BSS algorithms, respectively, are found in the CDF–S 1Ms and 2Ms catalogues. The remaining sources are found in additional surveys: optical, near infrared and supplementary X–ray catalogues. For these remaining sources, the distance from the positions given by the additional surveys and the BSS source positions is within 1 pixel (i.e., 1 arcsec). Instead, the distance from the positions given by the additional surveys and the WAVDETECT source positions is of 2.2 pixels. Furthermore, the efficiency in source detection with the BSS algorithm is improved with respect to the WAVDETECT technique only for fields $1-2$ CDF–S 500ks, that are characterized by larger mean source signal in the field: Take into account that 1% of the X–ray sources in WAVDETECT catalogues of the CDF–S 500ks fields are considered true sources, although counterparts at other wavelengths are ~ 2.2 arcsec far from the X–ray position. Note that the BSS technique on the CDF–S 500ks fields is exactly 4 times less sensitive than the CDF–S 2Ms, as expected. The WAVDETECT technique is by a factor of 1.3 less sensitive than the BSS algorithm on the four fields.

Last, the BSS algorithm outperforms the WAVDETECT technique for the detection of extended sources. Extended sources are detected by the BSS algorithm also at low signal–to–noise ratio. Structures of these clusters or groups of galaxies are detected at multiple scales. Substructures detected with extended sources might be due to background fluctuations in the data. Those substructures could increase the contamination with false–positives in source detection. Compact groups of galaxies are identified by the multiresolution analysis as extended objects. Last, an extended source not listed in the CDF–S 1Ms catalogue (Giacconi *et al.*, 2002*b*), is found. This extended source is confirmed by the BSS algorithm, analysing the CDF–S 1Ms and 2Ms data, and by photometric data.

7.2.4 Clusters and groups of galaxies

Combining the BSS technique with the presently most sensitive X–ray data from the *Chandra* Observatory, morphologies and physical properties of clusters and groups of galaxies also in the distant universe can be analysed (Maughan *et al.*, 2003). The motivations for surveying a population of these rare massive objects reside mainly in evaluating cosmological models to describe the universe, to study LSSs, to determine the amount of baryonic matter in the local universe and to measure the mass distribution within these systems (Böhringer *et al.*, 2010). In order to achieve these goals, a large sample of clusters and groups of galaxies is needed.

In the followings, an introduction to clusters and groups of galaxies is given. The introduction includes a brief decription of hot topics related to the study of these systems. Last, the BSS detection of a sample of galaxy clusters and groups with different characteristics (e.g., compact or complex morphologies and filaments connecting two galaxy clusters) is

[5]Note that the $P_{\rm source}$ threshold value is selected at the end of the analysis, while 'sigthresh' is an input parameter for the WAVDETECT algorithm.

shown.

Introduction

Clusters and groups of galaxies arise from the rare highest peaks of the primordial density perturbations in the hierarchical clustering scenario for the formation of cosmic structures (Big Bang cosmology[6]): See, e.g., Rosati *et al.* (2002*b*) and references therein. In the early universe, initial density perturbations grow under gravity and eventually form the massive structures visible today. Firstly, less massive systems are forming. Secondly, larger systems of galaxies, groups, and clusters of galaxies are formed through a combination of merging of the less dense surrounding regions (Maughan *et al.*, 2003). Fluctuations (or perturbations) in the primordial density field evolved into a complex structure of sheets and filaments with clusters of galaxies at the intersections of the filamentary structures (Werner *et al.*, 2008). Properties of clusters and groups of galaxies are sensitive to the nature of such fluctuations (Boschin, 2003). Voids and filaments (also known as cosmic web) have been revealed through galaxy surveys in the optical part of the electromagnetic spectrum: See, e.g., Croom *et al.* 2000. Detection of these filaments in the X–ray regime is difficult and few works revealed a reliable detection of these systems (e.g., Werner *et al.* 2008; Zappacosta *et al.* 2010). Detection of filaments in the X–ray regime is important for improving our understanding on the baryonic dark matter. Unambiguous tracers for the search of filaments in the X–ray regime are clusters and groups of galaxies: More details are dedicated on the subject in a following paragraph.

Galaxies, the hot thin gas that fills the space between the galaxies and the dark matter are gravitationally bound in the common gravitational potential of the cluster. Therefore the hot diffuse X–ray emission is the direct manifestation of the existence of a potential well within which the hot gas and the dark matter are in dynamical equilibrium. The thin hot gas permeating the cluster gravitational potential well is fully ionized and emits via thermal bremsstrahlung in the X–ray band. Since the galaxy cluster mass function (as a function of redshift) is predicted by theoretical models for cosmic structure formation (Rosati *et al.*, 2002*b*), X–ray studies of clusters and groups of galaxies are fundamental for assessing cosmological models. The cluster mass is never directly observable. However, the temperature and the density of the hot intergalactic medium are directly related to the cluster mass. Temperature and density of the hot intergalactic medium can be measured from the X–ray emission. The temperature of the hot thin gas is related to the depth of the potential well and its distribution is related to the dynamical state of the system (Böhringer *et al.*, 2010). Typically, clusters of galaxies are characterized by temperatures of several 10^7 K for cluster mass of $10^{14}-10^{15}$ $M_\odot$ and X–ray luminosities of $L_{\rm X}\sim 10^{43}-10^{45}$

[6]Between others, the work of Spergel *et al.* (2003) provided strong observational evidence that the ΛCDM model is a good approximation to reality: the universe is flat and its dynamics is dominated by 73% of dark energy (expressed by the cosmological costant Λ, representing an accelerating force) and by 27% of matter. All matter in the universe is composed by 22% of nonbaryonic dark matter (exotic, unknown particles) and by 5% of baryonic matter (p, n). Less than 1% of the baryonic matter is visible (e.g., stars, nebulae) and the remaining fraction is baryonic dark matter (Fukugita and Peebles, 2004).

erg s^{-1}. Hence, clusters and groups of galaxies are among the most luminous objects in the sky. Their luminosity does not show variabilities. Clusters and groups of galaxies are observationally accessible also at large cosmological distances due to their luminosity.

A quantitative analysis of the abundance of clusters and groups of galaxies as a function of redshift, z, allows one to constrain cosmological parameters and to test the models of structure formation. In fact, the large scale distribution of galaxy clusters and groups and their number density depend on the geometry of the universe and hence on the dark energy. The dark energy gives rise to the acceleration of the cosmic expansion, but its nature is so far unknown. X–ray observations of galaxy clusters and groups are essential for improving our knowledge about the rate of expansion of the universe and the amplitude of the primordial fluctuations that originated the whole structure of the universe.

The BSS technique is an efficient method for the search of clusters and groups of galaxies over a wide range of redshifts. The BSS algorithm allows one also for the detection of filaments along the line–of–sight between clusters or groups of galaxies. However, the estimation of the mass of these systems and a method to compute the survey volume, within which clusters or groups are found, require further studies within the BPT formalism.

Space density of X–ray galaxy clusters and groups A quantitative analysis of the abundance of clusters and groups of galaxies as a function of z allows one to constrain cosmological parameters and to test the models of structure formation.

In Section 7.2.3 of this Chapter, the survey selection function is described and applied to the CDF–S 500ks data only for point–like sources, where the flux limit is expressed with a function known as sky coverage. The sky coverage is the effective area covered by the survey as a function of flux. This function is measured because exposure time, background and PSF are not uniform across the fov of X–ray telescopes.

The survey selection function for clusters or groups of galaxies follows mainly the one of point–like sources, but the sky coverage function depends also on the surface brightness of galaxy clusters and groups and on selection bias. Clusters or groups with low surface brightness can often be missed when their signal–to–noise ratio is below the detection threshold (as for many conventional methods discussed in Chapter 5, in particular for the sliding window technique). Consequently, especially at high redshifts[7] the decrement in source brightness gives rise to an incomplete cluster sample at the faintest flux levels. A diagnostic procedure is usually employed for assessing the survey flux limit above which the sample is truly flux–limited and free of surface brightness effects (usually this is taken a factor $2-3$ higher than the minimum detectable flux in given survey) (Rosati *et al.*, 2002*b*). Concerning the selection bias, the sample of detected clusters can be contaminated by clusters hosting X–ray bright AGN or by unrelated point sources projected along the line of sight of diffuse cluster emission. The effect of bright AGNs is found in less than 5% of the cases. The effect of objects along the line of sight is significant for

[7]The z limit for detecting X–ray clusters is today at $z \sim 1.6$ (see, e.g., Rosati *et al.* 2009; Tanaka *et al.* 2010), utilizing multi–wavelength studies.

up to 50% flux contamination in some cases: See Rosati *et al.* (2002*b*) for more details. As a result, the sky coverage becomes increasingly inaccurate at very faint detection limits.

The surveyed population as a function of flux (log$N$–log$S$ distribution) for extended sources can be used to measure actual physical quantities, e.g. the surface density of galaxy clusters. Hence, the log$N$–log$S$ distribution allows one to set constrains on the cosmological evolution of clusters or groups of galaxies. Note that since the sky coverage becomes increasingly inaccurate at very faint detection limits, the faint end of the cumulative distribution of number counts is very uncertain.

Following the determination of the log$N$–log$S$ distribution, the luminosity function of X–ray galaxy clusters and groups can be estimated when z is known. The XLF allows one to investigate properties (e.g., mass, temperature), space–density and evolution of galaxy clusters and groups.

The cluster XLF is commonly modelled with a Schechter function, that takes into account the faint end slope, the characteristic luminosity, the space–density of clusters brighter than a minimum luminosity value: See Rosati *et al.* (2002*b*) and references therein for more details. Using the detected clusters sample in the survey, often a binned representation of the XLF is obtained by adding the contribution to the space density of each cluster in a given luminosity bin and a total search volume. The volume of the survey sky coverage depends on the survey sky coverage as a function of flux, on the luminosity distance as a function of z, and on the Hubble constant as a function of z.

Statistical significance of claimed evolutionary effects is not properly quantified when selection bias and measurement errors are not accounted. For improving the recovery of the information contained in any flux–limited cluster sample, new methods have been developed. For instance, the work of Rosati *et al.* (2000) demonstrated that when the XLF is analysed from an unbinned data distribution with a ML approach, the XLF is consistent with models predicting no evolution only for faintest fluxes.

In Fig. 7.17, the log$N$–log$S$ distribution obtained merging the information from several surveys is shown, as provided by Rosati *et al.* (2002*b*). At bright fluxes, the slope is close to the Euclidean value of -1.5, as expected for a homogeneous distribution of objects. At faint fluxes, the slope flattens to almost -1. As explained in Rosati *et al.* (2002*b*), the slope is mainly determined by the faint–to–moderate part of the XLF. The slope is insensitive to the abundance of the most luminous, rare massive systems. The observed counts are consistent with no–evolution predictions. It indicates that a significant fraction of the cluster population does not evolve with z. At the faint end, the *Chandra* Deep Fields North (labelled with "CDFN") and South (labelled with "CDFS") data have extended to very faint fluxes the number counts. Serendipitous surveys with *Chandra* and XMM–*Newton* satellites are filling the gap between these measurements and the *ROSAT* surveys. Measurements from *ROSAT* surveys are all the data points plotted at values of $S > 10^{-14}$ erg cm^{-2} s^{-1}. The *ROSAT* satellite provided the sample necessary to compute the space density of clusters in the local universe and its evolution. Further studies on the

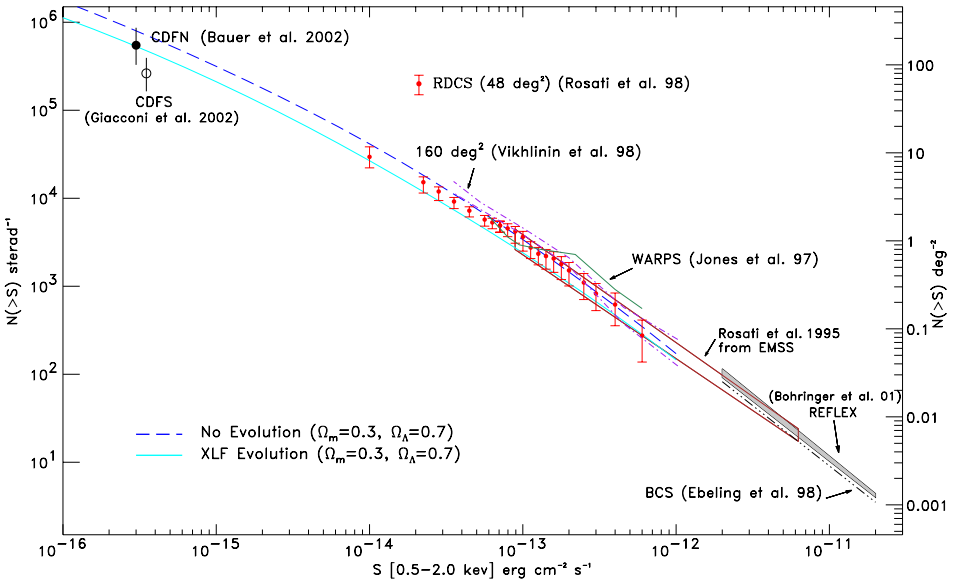

Figure 7.17: The cluster cumulative number counts as a function of X–ray flux (log$N$–log$S$) as measured from different surveys. This plot appeared in Rosati *et al.* (2002*b*).

sample supplied the evidence that the majority of the cluster population has not evolved significantly since $z \sim 1$. The *Chandra* satellite supplied the first view of the gas distribution in clusters at $z > 1$. X–ray studies of clusters and groups of galaxies are in agreement with hierarchical models of cosmic structure formation in a flat low–density universe with the density parameter $\Omega_m \sim 0.3$ and dominated by cold dark matter (Rosati *et al.*, 2002*b*).

Detection algorithms designed to examine a broad range of cluster parameters (X–ray flux, surface brightness, morphology) and to deal with source confusion at faint fluxes are particularly required for the search of clusters and groups of galaxies at several z (Rosati *et al.*, 2002*b*). The BSS technique, that is particularly sensitive in detecting faint sources and in separating sources superposed to a diffuse emission, may help to increase the sample of very distant clusters and to reduce selection bias due to contamination of sources located along the line of sight of galaxy clusters and groups. Due to the currently small sample available, the evolution of clusters and groups of galaxies at high z is not yet well understood. A Bayesian technique for the estimation of the log$N$–log$S$ distribution can be developed in order to take into account measurement uncertainties of source fluxes, sky coverage, and selection effects when making inference about the population of X–ray galaxy clusters and groups. Note that the sky coverage for cluster surveys is different from the one obtained for point–like sources (Rosati, 1995). Instead of accounting for the PSF variation, a median for the extent of clusters or groups of galaxies is often considered. This information can be properly accounted for the proposed clusters analysis.

Mass distribution in galaxy clusters The morphology of the X–ray emission of clusters or groups of galaxies can provide important insight into the nature of the hot gas. Usually, bright clusters have regular morphologies and show an (optical) luminous elliptical galaxy located near the dynamical centre of the cluster (Ebeling *et al.*, 1994; Mulchaey *et al.*, 1996; Mulchaey and Zabludoff, 1998). Irregular morphologies are often found at lower luminosities and the hot emission is distributed around several (optical) galaxies (Diaferio *et al.*, 2008). Irregular morphologies of an X–ray emission may indicate strong galaxy interactions. The physics of the hot intracluster gas is not well understood. No physical models are currently predicting the density and temperature distribution of the gas and the interplay between heating and cooling mechanisms (Rosati *et al.*, 2002*b*).

Statistical measures of substructures observed in X–ray images have been developed: See Böhringer *et al.* (2010) and references therein. Studies of substructures allows one to characterize the cluster or group of galaxies mass and the dynamical state of the system and, thereof, to create a ranking order of these systems. The most recent work on the subject, given by Böhringer *et al.* (2010), is based on a statistically representative bright and homogeneous sample of closeby clusters of galaxies, allowing for a reliable analysis.

The BSS technique is capable of providing a large sample of clusters and groups of galaxies and their substructures, allowing for a refinement of these studies. Further developments of the BSS algorithm within the BPT formalism would yield to an extension of the work of Böhringer *et al.* (2010) when the sample is small and/or composed by faint clusters or groups of galaxies.

The missing baryons in the local universe An open question in cosmology is the problem of the missing baryons in the local ($z < 1$) universe (Lieu and Bonamente, 2009). The problem manifests itself as a deficit in the mass budget. Observationally, the total baryonic content in stars, galaxies and clusters of galaxies is only about half of the amount required by the Big Bang nucleosynthesis models or from measurements of the cosmic microwave background. Cosmological hydrodynamical simulations predict that virialized halos (e.g., galaxies, groups and clusters of galaxies) are connected by a warm–hot intergalactic medium (WHIM). The WHIM is characterized by a low density ($n_{\rm b} = 10^{-6} - 10^{-4}$ cm^{-3}) and warm–hot ($T = 10^5 - 10^7$ K) intergalactic gas (Werner *et al.*, 2008; Zappacosta *et al.*, 2010) and by a filamentary shape. The filamentary shape originates in the kinematics of collapsing structural overdensities in the universe (as described in the Zeldovich pancake scenario, Zeldovich 1978). Filaments are predicted to contain about 50% of all baryons in the local universe (Zappacosta *et al.*, 2010). Thus, filaments are the best candidates to host baryons missing in the local universe, but seen at high redshifts (Fukugita and Peebles, 2004).

The detections of the WHIM in the X–ray regime is difficult due to the low surface brightness, the low density and the low temperature of the intergalactic gas. Nonetheless, the temperature of the WHIM increases up to 10^7 K when close to clusters or groups of galaxies. Hence, the WHIM is detectable in the soft (< 1 KeV) X–ray regime only in the neighbourhood of clusters or groups of galaxies. X–ray images, extracted in the soft

energy band, may reveal the WHIM as a bridge between clusters or groups of galaxies (Werner *et al.*, 2008). Up to date, a small sample of filaments between clusters or groups of galaxies have been discovered (see, e.g., Werner *et al.* 2008). Evidence of WHIMs in the LSSs is given by the works of, e.g., Zappacosta *et al.* (2010); D'Elia *et al.* (2008) employing primarily X–ray spectroscopy. The detection of a large sample of these filaments is needed in order to improve our understanding of the missing baryons in the local universe.

Detection of clusters and groups of galaxies

The detections of three clusters and one group of galaxies with the BSS technique are shown with the aim of demonstrating the superior capabilities of the BSS technique with respect to previous methods for properly detecting and classifying galaxy clusters/groups also in extreme cases of very low signal–to–noise ratio or contaminated by galaxies located nearby or superposed. The selected clusters and group of galaxies are located at high redshifts and contribute to two LSSs of the universe discovered in this region at redshifts 0.679 and 0.735 (Gilli *et al.*, 2003). The selected clusters and group of galaxies are characterized by different properties in the mass distribution: complex morphology; complex morphology contaminated by two galaxies along the line of sight; cD galaxy not at the centre of the X–ray potential well and contaminated by nearby galaxies; very low and compact surface brightness distribution. Therefore, a large range of surface brightnesses are explored with the BSS algorithm. The selected clusters and group of galaxies are listed in the work of Giacconi *et al.* (2002*a*), except for one object. All extended sources listed in Giacconi *et al.* (2002*a*) are not characterized by an automated procedure. In fact, as shown in previous Sections, the WAVDETECT algorithm is not capable to provide a reliable source extent for low surface brightness sources. A comparison of the detection of these clusters and the group with the BSS algorithm and the ones listed in Giacconi *et al.* (2002*a*) is given.

In Fig. 7.18, the two LSSs are schematically outlined. In panel (*a*), the plotted points indicate the $\alpha_{\rm J2000}$,$\delta_{\rm J2000}$ positions (degree units) of galaxies from all spectroscopic redshifts publicly available in the CDF–S region: Cristiani *et al.* (2000); Croom *et al.* (2001); Bunker *et al.* (2003); Dickinson *et al.* (2004); Stanway *et al.* (2004*b*,*a*); Strolger (2004); Szokoly *et al.* (2004); van der Wel *et al.* (2004); Doherty *et al.* (2005); Le Fèvre *et al.* (2005); Mignoli *et al.* (2005); Ravikumar *et al.* (2007); Vanzella *et al.* (2008); Popesso *et al.* (2009); Balestra *et al.* (2010). These spectroscopic campaigns are gathered in the ESO–GOODS website[8]. The red and blue filled circles highlight the galaxies located at the two redshifts bins contributing to the discovered LSSs. Four black crosses indicate the positions of the analysed sample. As shown in panel (*b*), the frequency distribution of the detected galaxies has two predominant peaks centred at the two redshifts contributing to the two LSSs. In panel (*a*), the structure at $z = 0.735$ shows a filament crossing the image and characterized by one knot at the centre of the image. At this position, a group of galaxies is located. The X–ray emission of this group of galaxies has a very compact structure. A cluster of galaxies, located most North in the image, is characterized by the same redshift as the

[8]http://www.eso.org/sci/activities/projects/goods/MasterSpectroscopy.html

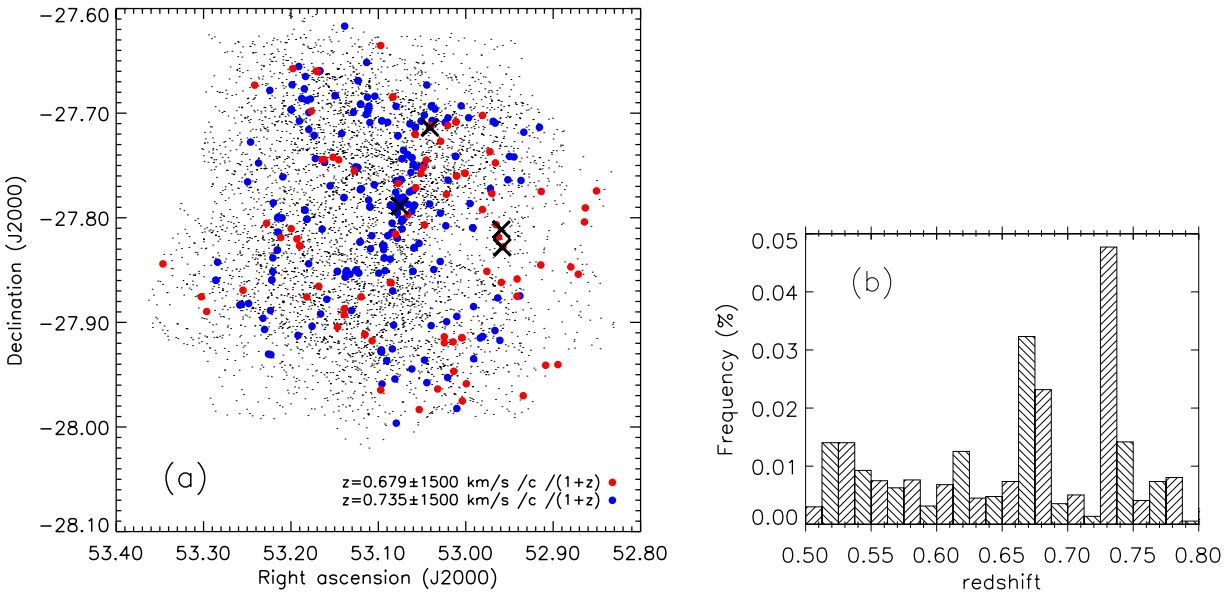

Figure 7.18: Panel (a): Sources with spectroscopic redshifts in the CDF–S region. Points, red and blue filled circles indicate all data, data with $z \sim 0.679$ and $z \sim 0.735$, respectively. Panel (b): histogram of data in panel (a) in the redshift range $[0.5 - 0.8]$. The two highest peaks indicate the density of galaxies in the two LSSs, located at redshifts 0.679 and 0.735.

previous one and lies on the same filament structure as the cluster located at the image centre. This cluster, located most North, is contaminated by neighbouring galaxies that are characterized by different redshifts. The other LSS at $z = 0.679$ does not show any knot. The clusters of galaxies analysed at this redshift are located in the centre-right–hand side of the image. The morphology of these two clusters is complex. Hence, these clusters are dynamically young and in a phase of formation.

The fluxes and the luminosities in the soft ($0.5 - 2.0$ keV) energy band are computed for these extended sources. The same scheme described in Sections 6.2.3 and 6.2.4 is followed. Specifically, galaxy clusters and groups are assumed to exhibit a thermal Raymond–Smith spectrum (Raymond and Smith, 1977) with the temperature $kT = (1.0 - 1.7)$ keV (Lehmer *et al.*, 2005; Giacconi *et al.*, 2002*b*) and solar abundance ratio of $0.2 - 0.3$ (Mushotzky, 1996; Giacconi *et al.*, 2002*b*). Note that the instrumental response function is encoded in $WebPIMMS$. However, the quantum efficiency of ACIS CCDs varies with time and for each observation (Virani *et al.*, 2006). Hence, only approximate values of fluxes and consequently of luminosities are provided.

The mean surface brightness is computed for the selected sample of clusters and group of galaxies. The computation of the mean surface brightness is explained in Section 6.2.4.

Color composite images combining optical imaging are used to give evidence of the BSS detection of the selected clusters and group of galaxies (Figs 7.20, 7.23 and 7.25). Composite images in optical band are used to enhance the contrast of (red) group galaxies against

the background (blue) galaxy distribution (Rosati *et al.*, 2002*b*). Specifically, optical data from the *Wide Field Imager* (WFI) at the MPG/ESO 2.2m–telescope on La Silla, Chile, are used in Figs 7.20, 7.23 and 7.25 (panel *a*). Each image is obtained combining B, R and I filters. Panel (*b*) of Fig. 7.25, shows instead an image from the advanced camera for surveys (ACS) on board of the Hubble Space Telescope, combining b, v, i, z filters. The comoving size in units of parsec is provided in square bracket. The comoving size is calculated as a function of the given angular scale, known redshift, $H_0 = 70$ km s^{-1} Mpc^{-1} and the cosmological parameters $\Omega_m = 0.3$ and $\Omega_\Lambda = 0.7$ (Spergel *et al.*, 2003). Contours from SPMs, obtained analysing the CDF–S 2Ms data with the BSS algorithm, are superposed to the color composite images to unequivocally prove the detection of a real, gravitationally bound cluster or group. In each image, square and diamond symbols provide the position and the value of spectroscopic (see Fig. 7.18 and related text for the full list of references) and photometric (Wolf *et al.*, 2004, 2008) redshifts measurements, respectively. Green and magenta symbols highlight member galaxies of groups and clusters. In white are drawn X–ray detections which are not members of the cluster and group of galaxies.

The BSS technique shows to be a powerful and unbiased tool suited for the search of galaxy clusters and groups in sky surveys.

Clusters of galaxies with complex morphology In Fig. 7.19, the detection with the BSS algorithm of two extended low surface brightness sources employing images with different depth is shown. Each image is centred at: $\alpha_{\rm J2000.0} = 03^{\rm h}31^{\rm m}50^{\rm s}$, $\delta_{\rm J2000.0} = -27^\circ 49' 13''$.

In panel (A), a cutout of the smoothed CDF–S 1Ms photon count image is placed for comparison with the corresponding exposure map, background map and SPMs estimated with the BSS algorithm employing the exponential prior pdf. A bar of one minute of arc length is placed in the smoothed image as indication of the image scale. In the exposure and background maps, dark and light grey indicate a range over $170-600$ ks and $0.06-0.21$ count pixel^{-1}, respectively. The SPMs at three resolutions (black labels) are displayed.

In panel (B), the upper left–hand image is part of the CDF–S 2Ms data, characterized by the same pixel scale of ~ 1 arcsec as the CDF–S 1Ms data in panel (A). In panels $A - B$, the SPMs show how the morphologies of the two clusters are detected at different resolutions and that the BSS algorithm consistently detects these clusters also if the signal–to–noise ratio is low (i.e., in panel A). At increasing exposure time (i.e., in panel B), more sources are detected as well as more structures of the two clusters of galaxies.

The cluster of galaxies located most South is listed as XID 645 in Giacconi *et al.* (2001). This cluster is detected with the largest source probability at a resolution of 15 arcsec with the BSS algorithm when analysing the CDF–S 1Ms data. In panel (A), at 15 arcsec resolution two regions are drawn. The regions indicate the location of object XID 645 (more details about these regions are given in the following lines). An increment in cluster features is evident at decreasing resolutions. The hot X–ray emission of the cluster is clearly detected. At the largest displayed correlation length, the hot medium is connected by a filament with the other extended feature located to the North of XID 645. The new cluster of galaxies is indicated with an arrow. Note that the filament is resolved by the BSS technique

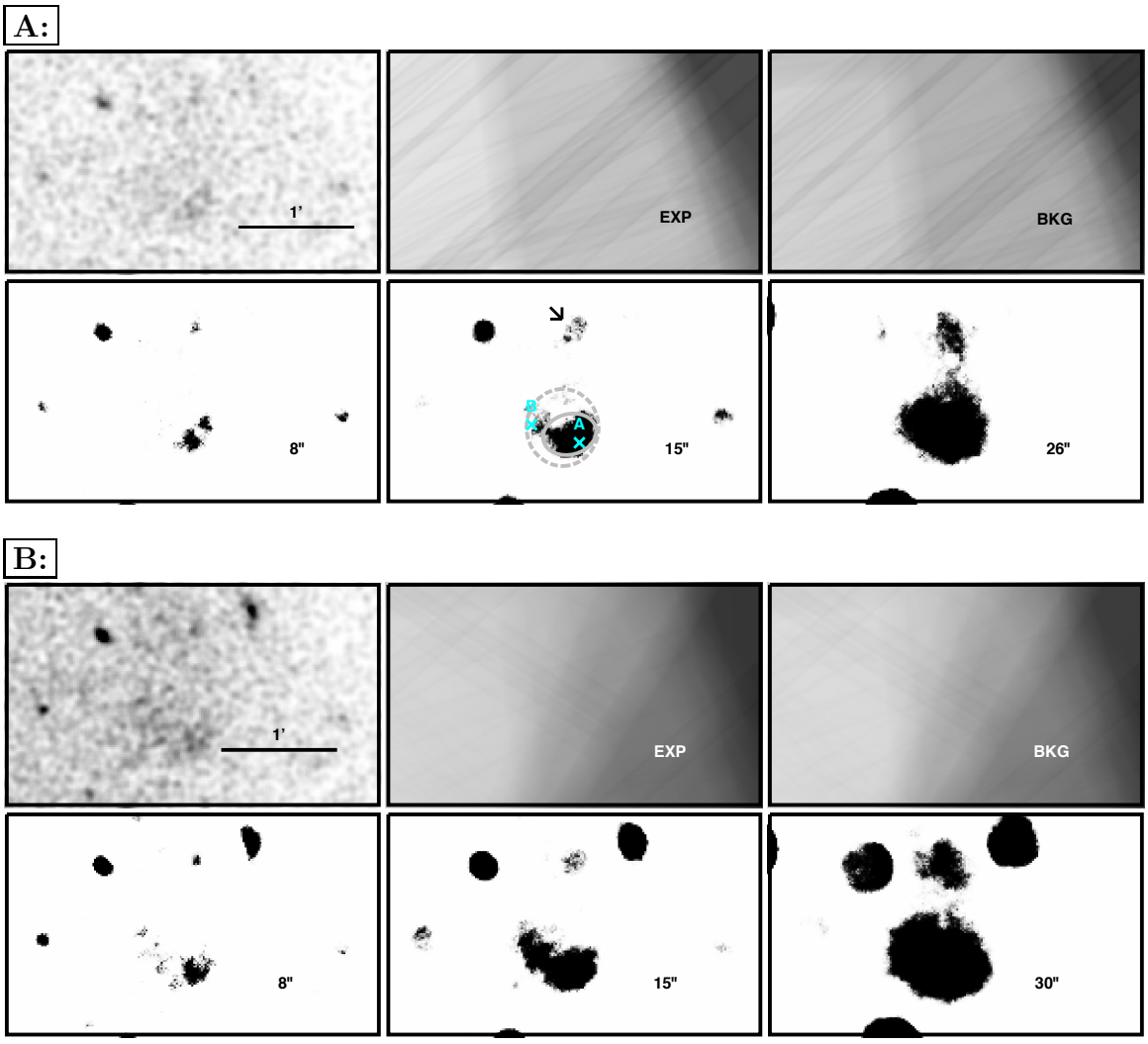

Figure 7.19: Panel *(A):* Example of detection with the BSS algorithm of two clusters of galaxies linked by a filament. The clusters of galaxies are XID 645 (Giacconi *et al.*, 2001), located most South, and a newly discovered, located most North, respectively. The plot in the upper left–hand side is a zoom in the CDF–S 1Ms image (Fig. 7.1), smoothed with a Gaussian kernel of $3''$ (soft energy band: $0.5 - 2.0$ keV). The corresponding exposure map and the estimated background map are indicated with 'EXP' and 'BKG', respectively. The images in the lower row are SPMs at decreasing resolutions (black labels). All images are co–centred, covering a fov of $\sim 3'$ width and $\sim 2'$ height.
Panel *(B):* As plot *A*, but analysing with the BSS algorithm the CDF–S 2Ms data (pixel resolution as CDF-S 1Ms in plot *A*: 1 arcsec pixel^{-1}).

analysing the CDF–S 1Ms and the CDF–S 2Ms data sets (panels $A - B$). The filament was not visible during the analysis of the four CDF–S 500ks images with the BSS algorithm.

The parameters for the cluster of galaxies located at the position of XID 645 as in output from the BSS algorithm employing the exponential prior pdf are listed in Table 7.5. The values from the exponential prior pdf are highlighted with an asterisk symbol at the end of the row. Source parameters of the detected cluster as in output from the BSS technique are superposed in the SPM at 15 arcsec resolution (panel A) with a continuous line.

In the CDF–S catalogue (Giacconi *et al.*, 2002*a*), the modified version of SExtractor did not detect this object. The wavdetect algorithm detects partially this cluster of galaxies: catalogued as CXO CDFS J033150.0-274941. The parameters for this object as given by Giacconi *et al.* (2002*a*) are listed in Table 7.6. An asterisk is used to highlight these values. The parameters for this extended object are improved when employing a modified version of the wavdetect algorithm (see Section 7.1). As reported in Giacconi *et al.* (2002*b*), XID 645 has parameters listed in Table 7.6 and highlighted with a bflat symbol. No extent parameter for this object is reported.

The net source counts for XID 645 estimated with the BSS technique (employing the exponential prior pdf) and the modified wavdetect algorithm are similar. The source extent parameters, given by the BSS technique, take into account only the brightest region of the detected cluster of galaxies. The multiresolution analysis, with the BSS algorithm when employing the exponential prior pdf, shows us that the hot gas extends in a larger region than the one given from the estimated parameters. Therefore, the detection of XID 645 is further investigated employing the inverse–Gamma function prior pdf with the cutoff parameter selected to a value of 0.01 count. The value of the selected cutoff parameter is at least by a factor of 10 smaller than the average background. The substructures arising in the multiresolution analysis are fully detected. The resulting parameters for this cluster of galaxies are listed in Table 7.5 and are highlighted with a bflat symbol. In Fig. 7.19, panel (A), the SPM at 15 arcsec resolution provides a region drawn with a dotted line. It indicates the position and shape parameters for XID 645 employing the inverse–Gamma function prior pdf. The BSS technique with the inverse–Gamma function prior pdf provides estimates in source parameters suitable to the extended feature resolved in the multiresolution analysis. The resolved feature is confirmed not only by the analysis of the CDF–S 2Ms data with the BSS algorithm (when employing the exponential prior pdf) but also by, e.g., the work of Szokoly *et al.* (2004). In fact, two galaxies are found with spectroscopic redshift of $z = 0.679 \pm 0.005$ in the following locations (see crosses on SPM at 15 arcsec resolution): (A) $\alpha_{\rm J2000.0} = 03^{\rm h}31^{\rm m}49.79^{\rm s}$, $\delta_{\rm J2000.0} = -27^{\circ}49'40.0''$; (B) $\alpha_{\rm J2000.0} = 03^{\rm h}31^{\rm m}51.66^{\rm s}$, $\delta_{\rm J2000.0} = -27^{\circ}49'30.7''$. The galaxy located in (A) is included in both regions drawn in Fig. 7.19, while the galaxy in position (B) is only included in the region obtained with the inverse–Gamma function prior pdf, i.e. it is located within the region with dotted lines but outside the region with a continuous line. The two prior pdfs are known to have different sensitivity. The inverse–Gamma function prior pdf improves, in this case, the parameterization of this object than the exponential prior pdf.

In Fig. 7.20, the color composite image from WFI telescope, that includes XID 645, is shown. All spectroscopic data with redshifts similar to the one of the known cluster of galaxies are indicated with a green square.

The new cluster of galaxy, indicated with an arrow in Fig. 7.19, is located at $\alpha_{\rm J2000.0} = 03^{\rm h}31^{\rm m}49.996^{\rm s}$, $\delta_{\rm J2000.0} = -27°48'40.62''$. This cluster is not listed in Giacconi *et al.* (2002*a*); Luo *et al.* (2008). For the estimated source parameters provided by the BSS technique when employing the exponential prior pdf, see Table 7.5. This object is indicated with "new". In Fig. 7.20, the X–ray emission of the new cluster of galaxies is corrupted by the presence of two foreground galaxies located at $z = 0.179$ and $z = 0.416$, respectively. The extra emission of those galaxies is detected by the BSS algorithm in the CDF–S 1Ms and 2Ms data sets: See in Fig. 7.19, the SPM at 8 arcsec correlation length. Three galaxies are found with photometric redshift of $z = 0.64 \pm 0.02$ (Wolf *et al.*, 2004, 2008). The combination of the X–ray detection shown with the SPM contours and the identified red galaxies unequivocally proves a real, gravitationally bound cluster. The X–ray intrinsic luminosity of this new cluster of galaxies is calculated considering the known photometric z. The resolution for which the source detection occurs indicates that this object is fainter than XID 645. This is supported by the estimated luminosities. In fact, this extended source is ~ 4 times less luminous than XID 645.
Furthermore, in Fig. 7.21, the very recent observation of the CDF–S region with *Chandra* 4 Ms observing time is shown and zoomed on the two clusters. The 4 Ms data set confirms the presence of the second cluster of galaxies. The BSS technique is capable to clearly detect the fainter galaxy cluster already employing the CDF–S 1Ms data set. This is due to the unique capability of the BSS algorithm of providing a high contrast between background and sources. Note that the contours of XID645 follow closely the X–ray emission given by the new observed data set.

The two clusters of galaxies are separated by ~ 0.5 arcmin on the sky, which corresponds to a projected distance of 195.1 ± 2.5 kpc. An observational evidence of X–ray emission from the WHIM connecting the two clusters is provided. Due to the lower precision of the photometric redshifts than the spectroscopic ones (by at least a factor of 10), a precise determination of the physical separation along the line of sight is not feasible. In Table 7.4, morphological parameters, X–ray flux and luminosity of this filament are provided analysing the image and taking into account the two z avaliable separately. Nevertheless, the observational evidence of the X–ray emission from the filament connecting the two clusters of galaxies need further assessments employing spectral data. Spectral data allows one to estimate the temperature of the gas associated with the filament and, consequently, the density, the entropy and the total mass of the gas in the filament (Werner *et al.*, 2008). The determination of the mass of the WHIM is essential for improving our understanding on the "missing baryons" in the universe. Furthermore, properties of the gas can be compared for consistency with simulations of the densest and hottest parts of the WHIM (Werner *et al.*, 2008).

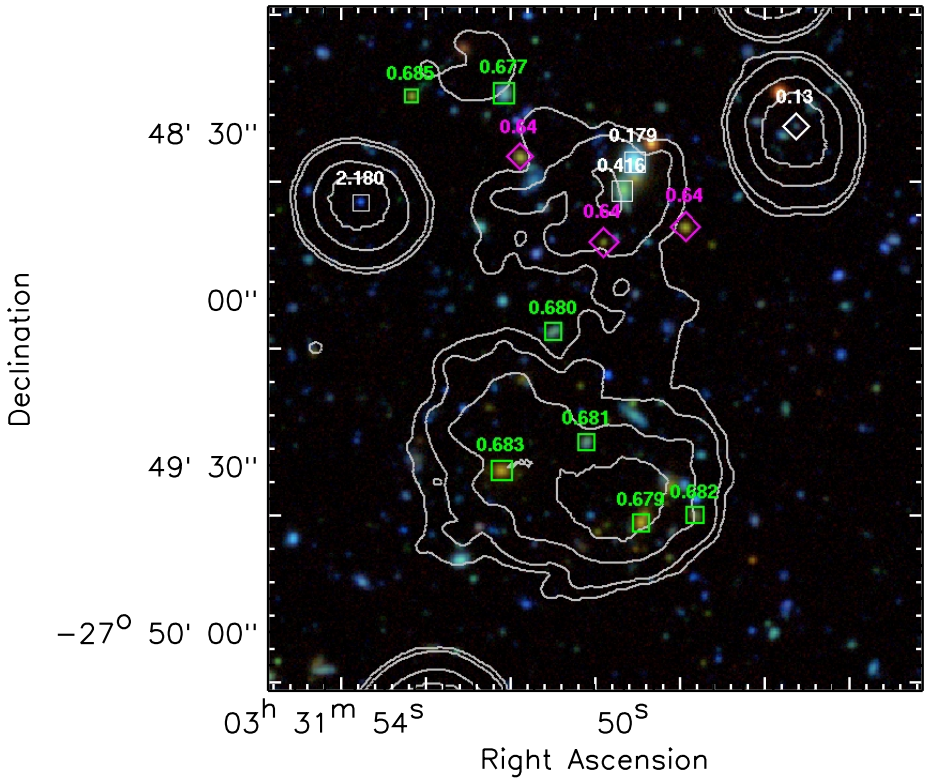

Figure 7.20: Color composite image combining B, R and I optical filters (WFI telescope) of the X–ray diffuse emission shown in Fig. 7.19. X–ray contours of the SPM at 20 arcsec resolution, analysing the CDF–S 2Ms data with a pixel scale of ~ 0.5 arcsec, are overlaid. Squared regions are public and Silverman *et al.* (in preparation) spectroscopic redshifts at $0.676 \lesssim z \lesssim 0.683$. Diamonds indicate photometric redshifts from Wolf *et al.* (2004, 2008). The photometric redshifts confirm that the newly revealed extended source is a cluster of galaxies located at $z = 0.64 \pm 0.02$. A filament is visible connecting the two clusters of galaxies. The existence of the filament is not confirmed yet by data in addition to the X–ray ones. The image covers ~ 2 arcmin length on the side [~ 800 kpc]. See text for more details.

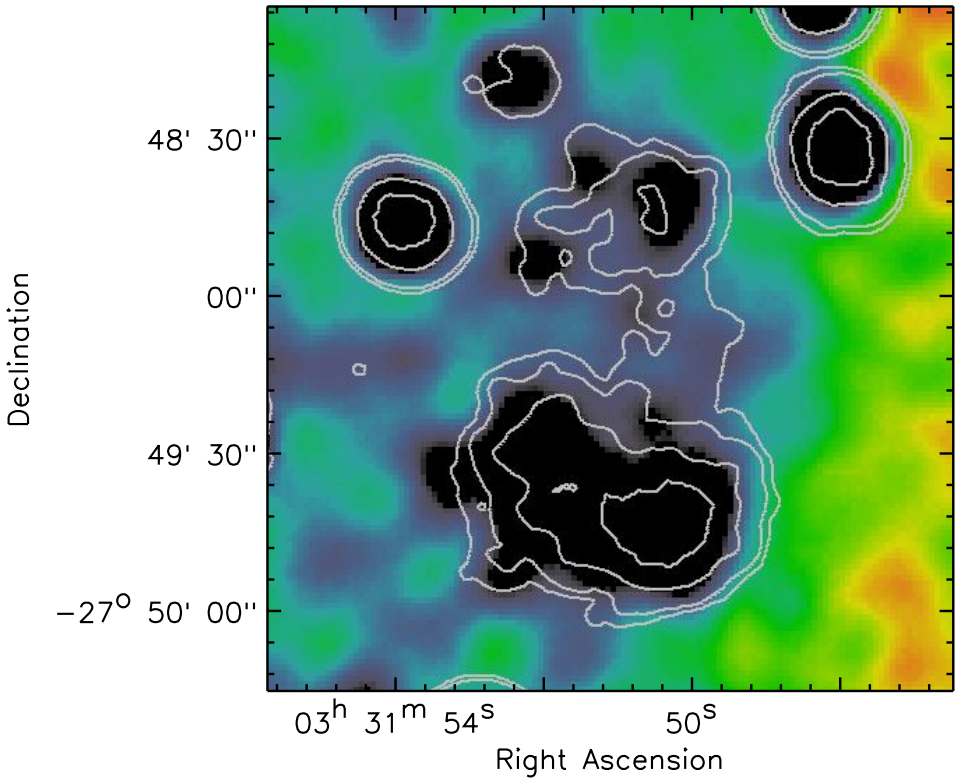

Figure 7.21: CDF–S 4Ms photon count image in the soft ($0.5 - 2.0$ keV) energy band, covering the same fov of Fig. 7.20. The image is scaled to $0 - 1$ count pixel^{-1} (the original data range is $0 - 3901$ count pixel^{-1}) and smoothed with a Gaussian kernel of 9". The superposed contours are given by the BSS technique, analysing the CDF–S 2Ms data as reported in Fig. 7.20.

Table 7.4: Filament characteristics (size, $F_{\rm X}$, $L_{\rm X}$ and surface brightness) extracted from the soft ($0.5-2.0$ keV) energy band image of the CDF–S 2Ms data at the photometric ($z=0.64$) and spectroscopic ($z=0.682$) redshifts available. See also Fig. 7.19 and text for more details.

z	length (Kpc)	width (Kpc)	$F_{\rm X}$ (erg/s/cm^2) $\times 10^{-15}$	$L_{\rm X}$ (erg/s) $\times 10^{44}$	SB (erg/s/cm^2/arcmin^2) $\times 10^{-13}$
0.64	165	82	1.4 ± 0.1	2.44 ± 0.17	1.39 ± 0.09
0.682	170	85	1.4 ± 0.1	2.85 ± 0.2	1.39 ± 0.09

Note: Length and width are the projected distances on the sky. The reported unabsorbed flux ($F_{\rm X}$) is calculated assuming a Raymond–Smith spectrum (Raymond and Smith, 1977) with the temperature $kT = 0.9$ keV (Werner *et al.*, 2008).

Cluster of galaxies contaminated by nearby galaxies The BSS technique is tested on an area of the CDF–S region where a cluster of galaxies (XID 594, Giacconi *et al.* 2001) exhibits a cD galaxy (Fig. 7.22). In the case of XID 594, the cD galaxy is not located at the centre of the cluster. Additionally, more galaxies are surrounding the cluster of galaxies. The detection of this cluster of galaxies with the BSS algorithm on the CDF–S 2Ms data is very similar to the one obtained analysing the CDF–S 1Ms data. The CDF–S 1Ms results are displayed in Fig. 7.22.

All images in Fig. 7.22 are co–centred and have the same size. The upper left–hand image is the CDF–S 1Ms photon count data smoothed with a Gaussian kernel of 3 arcsec. A bar of 0.5 arcmin length is placed to indicate the image scale. Following the CDF–S smoothed image, five SPMs are located. Their resolution is indicated in the lower right–hand corner. The output from the BSS catalogue is superposed to the SPM where the source detection occurred. Evidently, these sources reach a maximum in source probability at different resolutions emphasizing distinct detections.

In Fig. 7.23, a color composite optical image with superposed the X–ray contours from the SPM at 20 arcsec obtained with the BSS algorithm analysing the CDF–S 2Ms data (~ 0.5 arcsec pixel^{-1}) is shown. Known spectroscopic (see Fig. 7.18 and related text for the full list of references) and photometric (Wolf *et al.*, 2004, 2008) redshifts are highlighted for the galaxies member of the LSS at $z = 0.735 \pm 0.003$ (3σ).

In Table 7.7, the estimated source parameters are reported for the sources listed in Fig. 7.22 as in output from the BSS technique. Note that source 6 is the merging of sources 3 and 5. The net source counts for source 6 as in output from the BSS technique results to be the sum of the net source counts estimated for sources 3 and 5. The fluxes for sources $1-4$ are calculated employing a conversion factor $c_{\rm f}$, explained in Section 7.2.3. The fluxes for sources $5-6$ are instead calculated as explained in Section 7.1.

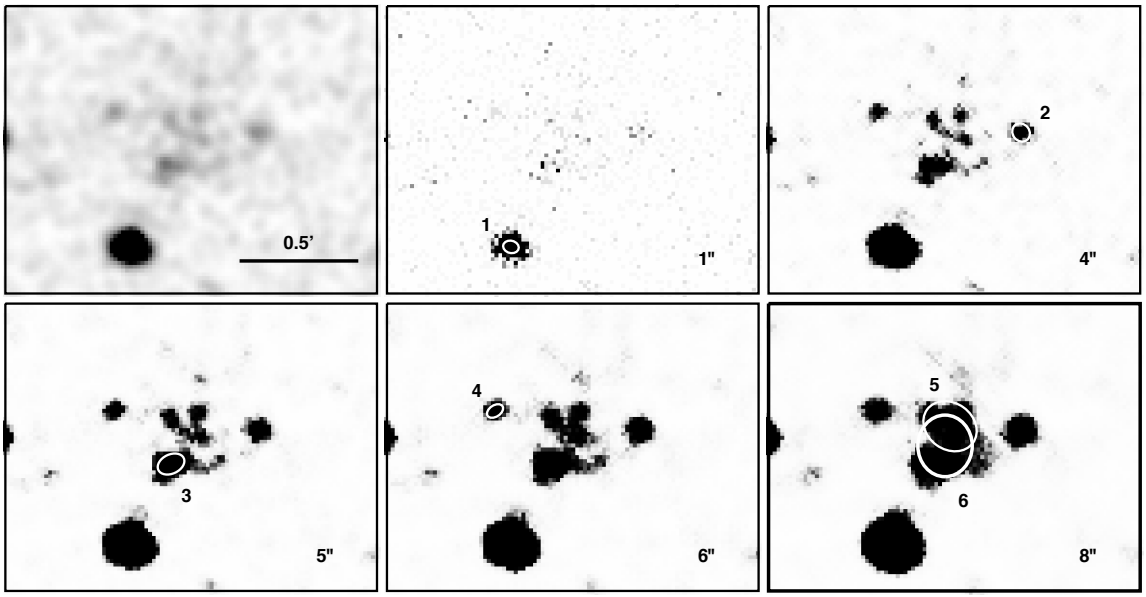

Figure 7.22: Example of detection with the BSS algorithm of a cluster of galaxies (XID 594, Giacconi *et al.*, 2001) in a crowded region. The upper–left hand image is a zoom in the CDF–S 1Ms photon count data, smoothed with a Gaussian kernel of $3''$. The following images are SPMs at several correlation lengths (black labels). Each image is centred at $\alpha_{\rm J2000.0} = 03^{\rm h}32^{\rm m}09^{\rm s}.4$, $\delta_{\rm J2000.0} = -27°42'38.5''$. The images cover a fov of $1.6' \times 1.3'$. The BSS catalogue is superposed to the SPM where sources are detected with the largest source probability. See text for more details.

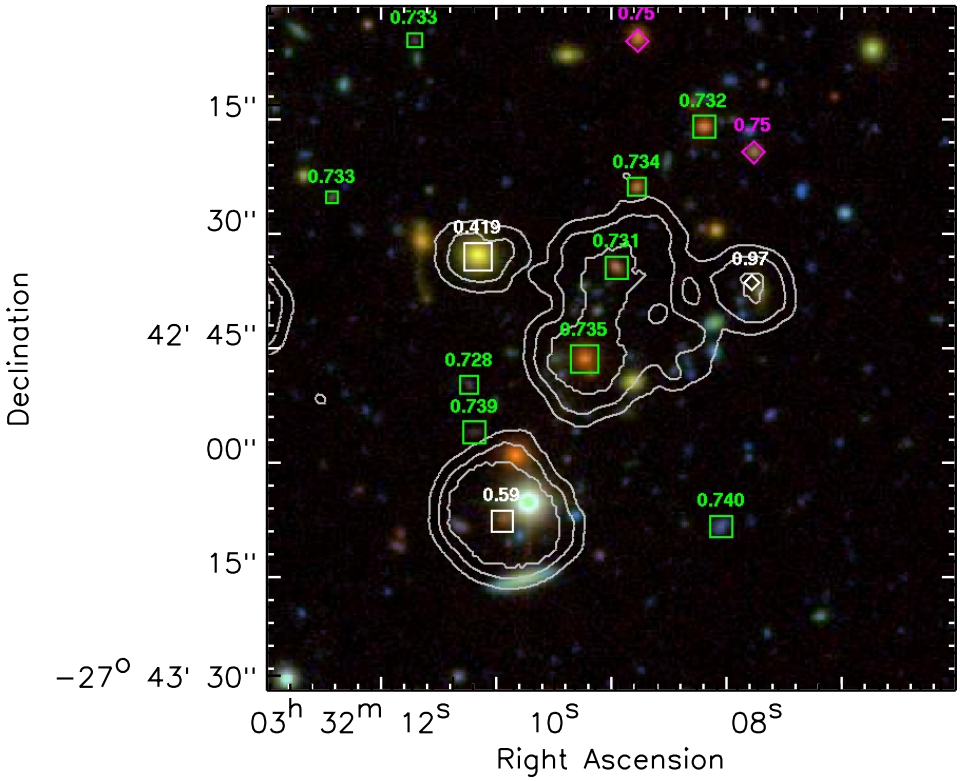

Figure 7.23: Same explanation as for Fig. 7.20, but centred on XID 594 (Giacconi *et al.*, 2002*b*) (see also Fig. 7.22). Optical sources that are members of the cluster of galaxies are characterized by redshifts of $0.732 \lesssim z \lesssim 0.738$. The image covers 1.5 arcmin length on the side [638 kpc]. See text for more details.

In Table 7.8, the output from the CDF–S catalogue (Giacconi *et al.*, 2002*a*) is provided for comparison with Table 7.7. Source 5 is not listed in this table, because this object is a substructure of source 6, i.e. XID 594. Source 3 instead is listed. In fact, the cD galaxy is detected by their standard algorithms. Source 6 is instead detected by the modified version of WAVDETECT. Note that the net source counts of the listed objects in the two tables are comparable within the errors. However, the FWHM provided for XID 594 by Giacconi *et al.* (2002*a*) is by a factor of two lower than the one provided by the BSS algorithm. The luminosity of XID 594 is reported with a value of $4 \times 10^{42} h_{50}^{-2}$ erg s^{-1} by Giacconi *et al.* (2002*b*). This value is similar to the one estimated with the BSS technique.

Very low and compact surface brightness distribution of a group of galaxies The capabilities of the BSS algorithm is now tested on one of the faintest and more compact group of galaxies so far detected in the CDF–S region: XID 566 (Giacconi *et al.*, 2001). This known group of galaxies is confirmed by the K20 survey (Cimatti *et al.*, 2002; Mignoli *et al.*, 2005). The K20 survey is an optical and near–infrared spectroscopic survey down to $K < 20$ using ESO Very Large Telescopes and instruments: See Cimatti *et al.* (2002) for more details.

In Fig. 7.24, the upper left–hand image is a zoom in the CDF–S 1Ms count image smoothed with a Gaussian kernel of 3 arcsec. Smoothing is essential in this image in order to allow an easy visual identification of the Cimatti's cluster. The original image shows pixels with values in the range $0 - 6$ count in this region. The followings two images are the corresponding observatory's exposure map and the estimated background map with the BSS algorithm. In these two images, dark and light grey indicate values in the range $416 - 644$ ks and $0.15 - 0.23$ count pixel^{-1}, respectively. Six SPMs at decreasing resolutions (black labels) are provided. The displayed background map and SPMs are results of the BSS technique employing the exponential prior pdf. For the correlation of neighbouring pixels, the box filter method with a circle is utilized. The analysis of the CDF–S 2Ms data with the BSS algorithm is not shown. The results with the CDF–S 2Ms data are similar to the ones obtained with the CDF–S 1Ms data.

XID 566 is located at the image centre. Note two point–like objects close to the group of galaxies. These point–like objects are not detected any longer at resolutions lower than 5 arcsec. These objects are a Seyfert 2 galaxy (CXOCDFS J033220.6-274733) at $z = 0.670$ (Giacconi *et al.*, 2002*a*; Luo *et al.*, 2008) and a source known in the infrared part of the electromagnetic spectrum (CDF:[SGC2001] 263; Saracco *et al.*, 2001), located towards the lower left– and upper right–hand corners of the image, respectively. CDF:[SGC2001] 263 is detected with the BSS algorithm both in the CDF–S 1Ms and in the CDF–S 2Ms data sets. Source CDF:[SGC2001] 263 is for the first time catalogued as X–ray source. In the multiresolution analysis, the central source (i.e., the Cimatti's cluster) shows the typical features of an extended low surface brightness object. Its source probability reaches a peak (in this case at 5 arcsec resolution) and then decreases at large correlation lengths. Source features increase until 15 arcsec resolution. The parameters for this object as in output from the BSS technique are reported in Table 7.5. The region shapes (without uncertainties)

are drawn in the SPM of source detection with the largest source probability.

The source parameters reported by Giacconi *et al.* (2002*b*) for XID 566 (or CXO CDFS J033218.1-274719) are given in Table 7.6. The estimated net counts and FWHM are similar to the ones provided by the BSS technique.

Fig. 7.25 provides two color composite images obtained with optical observations. Each image is centred on the BSS position provided for XID 566. The image widths are given in arcminute sizes: 2.5 and 0.5 arcmin for the images in panels (A) and (B), respectively. The contours of the SPM at 15 arcsec resolution are used to highlight the detected X–ray emission. The core of the group of galaxies is dominated by red, early–type galaxies. Green squares are placed to indicate the positions of galaxies at the same redshift of the group centre. Galaxies at redshift $z = (0.735 \pm 0.003)$ are found out to ~ 1 arcmin far from the central X–ray emission. Note in panel (A), the SPM contours highlight also the Seyfert 2 galaxy (towards the lower left–hand corner) already commented in Fig. 7.24 and related text.

In contrast to the cluster of galaxies XID 645 with the most extended surface brightness distribution, XID 566 is one of the most compact extended object in the CDF–S region. Nonetheless, the surface brightness of XID 645 is at least by a factor of 10 larger than the one of XID 566. The *Chandra* Observatory allows one to study low mass clusters or groups of galaxies and reveals complex morphologies of the hot gas between the galaxies. The BSS technique provides for the investigation of the wide range of physical parameters and the characteristics of the surveyed population with the *Chandra* satellite.

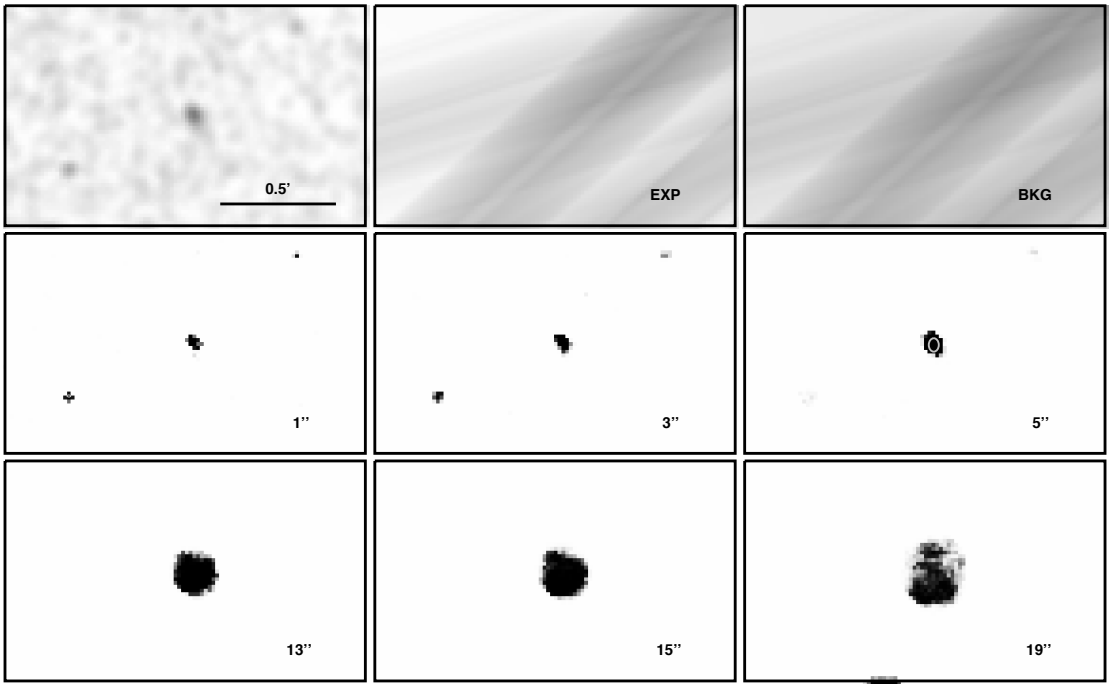

Figure 7.24: Example of detection with the BSS algorithm of a compact group of galaxies (XID 566; Giacconi *et al.*, 2001). The sequence of images follows the same explanation given for Fig. 7.19, panel (*A*). Each image is centred at $\alpha_{\rm J2000.0} = 03^{\rm h}32^{\rm m}18.02^{\rm s}$, $\delta_{\rm J2000.0} = -27°47'19.46''$. The images cover a fov of $1.5' \times 1'$. A region is superposed to the SPM at 5 arcsec resolution. The region's shape indicates position and source extents of the group of galaxies as in output from the BSS catalogue. The group of galaxies is detected with the largest source probability at 5 arcsec resolution.

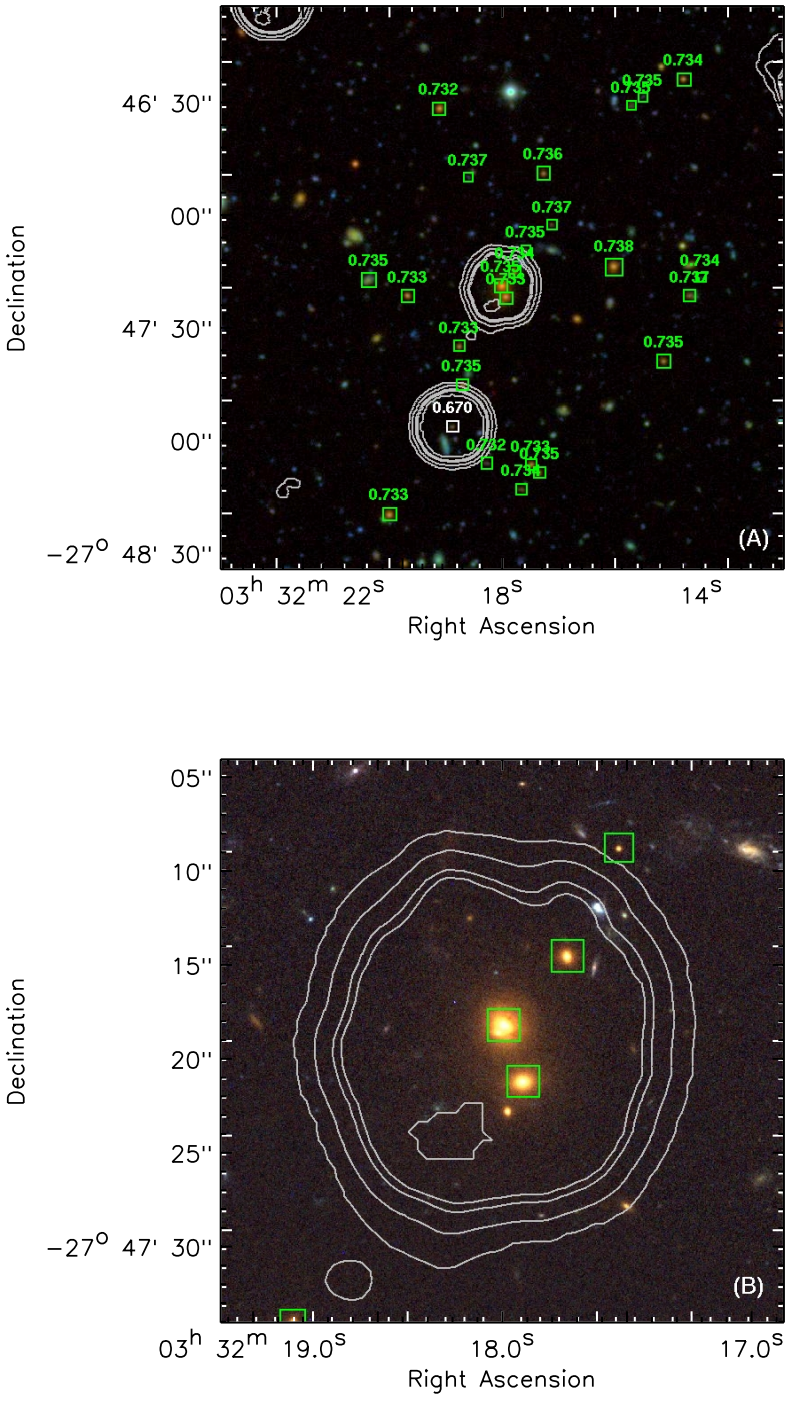

Figure 7.25: Panel (A): Same explanation as for Fig. 7.20, but centred on XID 566 (Giacconi *et al.*, 2002*b*) (also shown in Fig. 7.24). This compact group of galaxies is characterized by optical galaxies at redshifts of $0.732 \lesssim z \lesssim 0.738$. The image covers 2.5 arcmin length on the side [1 Mpc]. Panel (B): Detailed ACS image of the central part of panel (A). The image covers 0.5 arcmin length on the side [126 kpc]. See text for more details.

Table 7.5: Estimated parameters with the BSS algorithm on a sample of three clusters and one group of galaxies.

XID	R.A. (J2000)	Decl. (J2000)	Soft counts (count)	Ave bkg (count)	Exp (ks)	Sctr (count ks^{-1})	FWHM$_{\rm M}$ (arcsec)	FWHM$_{\rm m}$ (arcsec)	Soft Flux $\times 10^{-15}$	L$_{\rm X}$ $\times 10^{42}$	SB $\times 10^{-15}$	z
645	52.959042	-27.826567	239.4 ± 54.5	0.169	487.26	0.491 ± 0.079	28.0 ± 4.6	21.1 ± 3.7	3.1 ± 0.5	6.27 ± 1.01	1.51 ± 0.24	0.679 ± 0.005 ($*$)
645	52.960208	-27.825589	443.5 ± 83.3	0.175	498.28	0.833 ± 0.167	39.9 ± 5.7	37.4 ± 5.4	5.3 ± 1.1	10.6 ± 2.1	1.01 ± 0.20	0.679 ± 0.005 ($\flat$)
new	52.958292	-27.811283	70.4 ± 38.1	0.173	512.48	0.134 ± 0.047	29.7 ± 13.4	5.5 ± 1.9	0.86 ± 0.3	1.7 ± 0.6	1.5 ± 0.5	0.64 ± 0.02 ($*$)
594	53.0349	-27.71213	245.5 ± 39.9	0.207	580.6	0.423 ± 0.049	18.85 ± 2.16	15.11 ± 2.01	2.70 ± 0.31	6.62 ± 0.76	2.7 ± 0.3	0.735 ± 0.003 ($*$)
566	53.0751	-27.788656	34.12 ± 10.19	0.165	455.2	0.075 ± 0.016	4.10 ± 0.74	3.06 ± 0.88	0.48 ± 0.1	1.15 ± 0.24	0.11 ± 0.02	0.735 ± 0.003 ($*$)

Note: *XID* indicates the source identification number given by Giacconi *et al.* (2001). *R.A.* and *Decl.* are right ascension and declination in degree units. *Soft counts* are the net source counts in the soft $(0.5-2.0$ keV) energy band. *Ave bkg* is the average background estimated within the source detection area. *Exp* is the effective exposure time in the soft $(0.5-2.0$ keV) energy band in kiloseconds. *Sctr* is the estimated source count rate in the soft $(0.5-2.0$ keV) energy band. $FWHM_{\rm M}$ and $FWHM_{\rm m}$ are the full-width at half maximum in arcsecond unit of the estimated source profile with a two–dimensional Gaussian, major and minor axis respectively. *Soft Flux* is the flux in the soft $(0.5-2.0$ keV) energy band in units of erg cm^{-2} s^{-1}. No increment is incorporated to account for photometric bias as done in Giacconi *et al.* (2002*b*). $L_{\rm X}$ is the estimated X–ray luminosity, in units of erg s^{-1}. *SB* is the surface brightness in units of erg cm^{-2} s^{-1} arcmin^{-2} (see Section 6.2.4 for definition of surface brightness). z indicates the redshift (see text for more details). The ($*$, $\flat$) indicates source values obtained with the exponential and the inverse–Gamma function prior pdfs, respectively.

Table 7.6: Estimated parameters listed in Giacconi *et al.* (2002*b*).

XID	R.A. (J2000)	Decl. (J2000)	Soft counts (count)	Ave bkg (count)	Exp (ks)	Sctr (count ks^{-1})	FWHM$_{\rm M}$ (arcsec)	FWHM$_{\rm m}$ (arcsec)	Soft Flux $\times 10^{-15}$	L$_{\rm X}$ $\times 10^{42}$	SB $\times 10^{-15}$
645	52.958125	-27.794917	66.5 ± 13.0	$\cdots$	688.3	$\cdots$	$\cdots$	$\cdots$	0.462 ± 0.09	$\cdots$	$\cdots$ ($*$)
645	52.958125	-27.794928	262.1	$\cdots$	$\cdots$	$\cdots$	$\cdots$	$\cdots$	1.75	$\cdots$	$\cdots$ ($\flat$)
594	53.040958	-27.7138	237	$\cdots$	$\cdots$	$\cdots$	$\cdots$	$\cdots$	1.36	$\cdots$	$\cdots$ ($\flat$)
566	53.075458	-27.78875	32.50 ± 7	$\cdots$	668.8	$\cdots$	3.4	3.4	0.232 ± 0.05	$\cdots$	$\cdots$ ($\flat$)

Note: Each column has same explanation as for Table 7.5. The ($*$, $\flat$) symbols indicate parameters estimated with WAVDETECT and with a modified version of WAVDETECT, respectively.

Table 7.7: Properties of the sources listed in Fig. 7.22 as in output from the BSS algorithm.

Seq	R.A. (J2000)	Decl. (J2000)	Soft counts (count)	Ave bkg (count)	Exp (ks)	Sctr (count ks^{-1})	FWHM$_{\rm M}$ (arcsec)	FWHM$_{\rm m}$ (arcsec)	Pos. Angle (deg)	Soft Flux (erg cm^{-2} s^{-1})
1	53.04371	-27.71912	815.01 ± 41.46	0.20995	586.9	1.3887 ± 0.0499	4.75 ± 0.15	3.70 ± 0.12	75.14 ± 0.08	(6.39 ± 0.23)E-15
2	53.03335	-27.71096	45.26 ± 13.61	0.20204	574.1	0.0788 ± 0.0169	5.63 ± 1.11	4.77 ± 1.39	-37.78 ± 1.05	(3.63 ± 0.78)E-16
3	53.04027	-27.71342	96.54 ± 18.85	0.20545	576.8	0.1672 ± 0.0234	9.06 ± 1.27	6.40 ± 0.85	90.00 ± 0.04	(7.69 ± 1.08)E-16
4	53.04499	-27.70961	29.42 ± 9.98	0.21194	589.2	0.0499 ± 0.0119	5.26 ± 1.15	3.34 ± 0.83	-56.32 ± 0.39	(2.30 ± 0.55)E-16
5	53.03912	-27.71062	160.58 ± 68.09	0.20648	580.4	0.2767 ± 0.0835	15.53 ± 5.02	14.73 ± 5.66	73.07 ± 3.98	(1.77 ± 0.53)E-15
6	53.03949	-27.71213	245.47 ± 39.93	0.20662	580.6	0.4227 ± 0.0485	18.85 ± 2.16	15.11 ± 2.01	65.65 ± 0.36	(2.70 ± 0.31)E-15

Note: Same explanation as for Table 7.5, but *Seq* indicates the source number as given in Fig. 7.22.

Table 7.8: Properties of the sources listed in Fig. 7.22 as in output from the CDF–S catalogue (Giacconi *et al.*, 2002*a*).

Seq	XID	CXO CDFS	R.A. (J2000)	Decl. (J2000)	Soft counts (count)	Exp (ks)	Soft Flux (erg cm^{-2} s^{-1})
1	61	J033210.6-274309	53.044042	-27.719369	826.60 ± 29.4	845.3	(4.68 ± 0.17)E-15
2	155	J033208.0-274240	53.033458	-27.711139	26.30 ± 10.1	831.0	(1.51 ± 0.58)E-16
3	594	J033209.8-274249	53.040958	-27.7138	60.40 ± 11.8	838.7	(3.45 ± 0.67)E-16
4	536	J033210.9-274235	53.045375	-27.709839	32.20 ± 9.6	848.9	(1.81 ± 0.54)E-16
—	—	—	—	—	—	—	—
6	594		53.040958	-27.7138	237.0		1.36E-15

Note: Columns have same meaning as for Table 7.7. In addition, *XID* is the unique detection identifier as given by Giacconi *et al.* (2002*b*), *CXO CDFS* is the IAU registered name. Source parameters of Seq 3 are provided by the standard detection algorithms employed. Source parameters of Seq 6 are provided by the modified WAVDETECT algorithm for the search of extended objects. A FWHM of 8.1 arcsec is reported for this object.

7.3 Summary

The BSS algorithm is applied to the CDF–S data sets. The CDF–S region was surveyed by CXO with 23 pointed observations. All combined observations reach an exposure time of 2 Ms and cover a sky area of ~ 0.109 deg^2. CCD gaps and the edge of the fov produce large background variations. The high resolution and the sensitivity of the *Chandra* Observatory allows for the detection of faint surface brightness sources. Some of the low surface brightness sources show complex morphologies. The CDF–S region has been previously studied in the X–ray regime by Giacconi *et al.* (2002*b*); Luo *et al.* (2008); Alexander *et al.* (2003), and by several other surveys (mostly, optical, near–infrared and infrared parts of the electromagnetic spectrum). Therefore, the CDF–S data provide a test case for assessing the capabilities of the BSS technique on pointed observations.

The BSS technique analysed the CDF–S 1Ms, CDF–S 2Ms and four CDF–S images of 500 ks each. The four CDF–S 500ks data sets have been extensively analysed. The BSS algorithm is fully exploited. A large range of correlation lengths are used.

The BSS background models of the CDF–S data sets are assessed on the image without data censoring. Each background model is well–defined on the whole fov and is strongly dominated by the satellite's exposure time. No contaminations due to CCD gaps or to the steep change in the exposure time map are shown in any background map or SPM. The dynamic searching technique of the multiresolution analysis provides for the detection of a wide range of source fluxes. SPMs at several correlation lengths clearly reveal the detections of point–like or extended sources and their morphologies.

The BSS analysis of the four CDF–S 500ks images is compared to the one with the WAVDETECT technique. The WAVDETECT technique is commonly used for image analysis of CXO data sets. The WAVDETECT technique is run with very conservative values of both scales and significance threshold, in order to provide for a clean sample.

In contrast to the WAVDETECT algorithm, the BSS technique gives the following benefits: 1. well–defined background model; 2. no systematic errors on estimates of source parameters; 3. the residual errors are 30% smaller than the ones found with the WAVDETECT technique especially for source positions and extent; 4. errors on extent parameters are reported; 5. source counts are improved. This is supported also by simulated data: See Chapter 5 for more details; 6. detection of 40% more faint sources than the ones found with the WAVDETECT technique for the test run on real data; 7. detection of clusters and groups of galaxies. No false–positives in source detection are found for both techniques.

The detection of clusters or groups of galaxies is an hot topic in astrophysics. The importance of detecting clusters or groups of galaxies in the X–ray regime on a large sample and their morphologies is explained. The BSS technique is shown to outperforms the currently used techniques for the detection of these rare massive objects.

A wide range of fluxes for clusters or groups of galaxies are investigated with the BSS technique analysing the CDF–S data. The BSS technique is capable to detect clusters and

groups of galaxies with complex morphologies (as XID 645, Giacconi *et al.* 2002*b*), with a cD galaxy not located at the centre of the cluster of galaxies and with contaminations from close by galaxies (as XID 594, Giacconi *et al.* 2002*b*), with compact morphology (as XID 566, Giacconi *et al.* 2002*b*). The BSS technique detects also a filament connecting XID 645 to a secondary cluster of galaxies. Previous to this analysis, the second cluster of galaxy and the filament were unknown.

Moreover, the BSS algorithm is tested applying two prior pdfs of the source signal. The inverse–Gamma function prior pdf improves the detection of complex morphologies and their substructures, as for XID 645, with respect to the exponential prior pdf. Previous analyses in the X–ray regime did not detect these morphologies and their substructures. Spectroscopic studies (e.g., Szokoly *et al.* 2004) support the conclusion that the detected substructures are part of the same X–ray emission.

The BSS technique is a suitable tool for the analysis of data coming from a new generation instruments. So far, the BSS algorithm provides information of source properties, such as position and fluxes. From these observables, one wants to investigate the nature of the surveyed population. The space density of a surveyed population, e.g. clusters or groups of galaxies, as a function of flux ($\log N$–$\log S$) is needed to set constraints on the cosmological evolution.

Classic techniques are employed to study the sky coverage and the $\log N$–$\log S$ distributions from the BSS catalogued data of the CDF–S 500ks images only for point–like sources. The resulting $\log N$–$\log S$ distributions are similar to the ones obtained by previous analyses on the CDF–S 1Ms and CDF–S 2Ms data. However, selection effects and measurements errors are not accounted into the analysis. Consequently, the distributions of the source number counts are distorted especially at the faintest fluxes. A forward technique is proposed in survey data analysis for accurately accounting the uncertainties in source parameters and selection distortion: See Chapter 8. The proposed technique, for deriving the source number counts per deg^2, is applicable for both point–like or extended sources. This proposed technique and the entire catalogue of clusters or groups of galaxies can be part of a future project.

Chapter 8

Concluding remarks & Outlook

In this Chapter, comments drawn from the main results obtained in this thesis are given in Section 8.1 and an outlook is provided based on the given work in Section 8.2.

8.1 Concluding remarks

A general, powerful and flexible Bayesian technique for background and source separation is developed. The technique is general since it is applicable to astronomical images coming from any count detector. The aim of providing more reliable results, with respect to previous techniques, for faint and/or extended sources is achieved and makes for a powerful algorithm. The technique is flexible, because it can easily be extended to other statistics (e.g., Gaussian statistics) and astronomical problems in image analysis (e.g., data cubes of spectral analysis).

Employing BPT, an algorithm is created to obtain, under appropriate assumptions, the optimal solution of the ill–posed inverse problem encountered in image analysis. The BSS algorithm tackles the problem of source detection straightforwardly. In contrast to previous source detection methods, the BSS technique does not censor the data for background estimation and source detection. Hence, the BSS algorithm does not need thresholding to reduce the number of expected spurious detections (as the WAVDETECT algorithm) and a punctured image (as the sliding window technique) for the background estimation. The BSS algorithm is capable to cope with steep gradients in the data. For the detection of point–like and extended sources, images are not analysed in sequential steps. The BSS technique detects point–like and extended sources on the original image data, providing a proper propagation of uncertainties of the experimental measurements.

The BSS background model is more reliable than the ones obtained with standard methods both for survey data and for pointed observations. Due to the fine background model, the developed Bayesian method is expected to handle consistently the heterogeneities present in astronomical images composed by a mosaic of images.

Point–like and extended sources are detected independent to their morphology and the kind of background. The applications to simulated and real data have shown that the BSS

technique improves the detection of sources and their structural parameters, especially the ones with low surface brightness, with respect to standard techniques. New X–ray sources have been discovered.

The BSS algorithm can be applied to large data volumes, e.g. surveys from X–ray missions. The BSS technique is not restricted to the objects detected in this thesis (such as quasars, galaxy clusters and groups, galactic SNRs, cataclysmic variables), but also to the study of other faint celestial objects in galactic and extragalactic astronomy. In galactic astronomy, the BSS algorithm can be employed, e.g., for the study of compact stars (such as neutron stars and pulsars); stars (e.g. brown dwarfs); binary stars containing a white dwarf, neutron star or black hole; objects embedded in diffuse emissions (like pulsars) and their emissions; open clusters proper motion even when the celestial objects are embedded in nebulosity. In extragalactic astronomy, the BSS technique can be utilized for the investigation of AGNs, SNRs and for the identification of sources presenting extended surface brightness (like clusters or groups of galaxies) in sky surveys. Furthermore, the multiband analysis developed within the BSS technique allows one to investigate several celestial objects (such as AGNs) whose nature becomes obvious when studied at different wavelengths.

The BSS technique is particularly appropriate for the analysis of images of a new generation instruments. This is of major importance today, because "*The development of new observation options goes hand in hand with attempts to answer fundamental astrophysical questions*" (Burkert *et al.*, 2008), such as the formation of the universe and the distribution of the matter in the universe.

8.2 Outlook

Survey data analysis Previous works for survey data analysis in the X–ray part of the electromagnetic spectrum show to not properly account for measurement errors of source fluxes and for selection bias. The $\log N$–$\log S$ distribution for the surveyed population (e.g., clusters or groups of galaxies, AGNs) is often derived empirically, as shown in Chapter 7. The points drawn in the $\log N$–$\log S$ distribution are estimates that are characterized by uncertainties, but the uncertainties of source fluxes are not accounted into the analysis (Fig. 7.13). Usually, the $\log N$–$\log S$ distribution shows a cutoff at low and large fluxes. The cutoff at low fluxes arises because surveys are flux limited and a cut is set as a detection limit. A threshold is set at the bright end in order to avoid contaminations by stars. Particular attention is given to the faint end, where sometimes the curve bends before the cut, providing ambiguous results. Furthermore, the distance of the detected objects (from spectral observations) can be used with the source count distribution as a function of the flux to study the luminosity function of the surveyed population with respect to their distance and to analyse the spatial distribution of the surveyed population. Nonetheless, the XLF is often derived only for sources characterized by more then 30 net counts. An accurate analysis of survey data is crucial to maximize the scientific return from the extensive resources devoted to surveys: See, e.g., the work of Loredo (2004).

Source number counts for different populations of X–ray sources can be studied employing BPT. Following the work of Loredo (2007), a Bayesian technique for the estimation of the log$N$–log$S$ distribution can be developed in order to take into account, in one unique algorithm, measurement uncertainties of source fluxes, sky coverage, and selection effects when making inference about the entire population or different sub–populations of X–ray sources.

Physics governing the evolutionary processes of clusters and groups of galaxies The BSS technique demonstrated to be a suitable tool to detect galaxy clusters and groups also in cases of strongly varying background and for a wide range of source surface brightnesses, revealing complex or compact morphologies. In Chapter 7, future researches applicable surveying a large sample of clusters and groups of galaxies are described.

- Study of the gas distribution within clusters, that is related to the dynamical state of the system. Morphological studies of these rare objects contribute to our understanding in the nature of the hot gas;

- Analysis of filaments connecting clusters allows one to improve our knowledge on the amount of baryonic matter in the local universe;

- The space density of galaxy clusters and groups at different redshifts can be determined. In fact, a quantitative analysis of the abundance of clusters and groups of galaxies as a function of z allows one to constrain cosmological parameters and to test the models of structure formation. In addition, the red–sequence technique (Rosati *et al.*, 2009) can be used to identify galaxy clusters and groups in order to confirm the X–ray detection.

The reader is addressed to Chapter 7 for more details.

Background modelling The BSS algorithm improves the background model with respect to standard techniques employed for X–ray surveys (see Chapters 5, 6 and 7). So far, the background is modelled with a two–dimensional spline function with the number of spline's supporting points chosen equally spaced or selected in specific regions of the analysed image. The flexibility of the Bayesian technique allows for further developments. The background model can be extended employing adaptive supporting points: The number of spline's supporting points and positions are free parameters and are automatically adapted by the data to the astronomical image. This study would improve automatism for the background model, especially, for survey missions, e.g. the forthcoming all–sky survey with the *eROSITA* (extended Röntgen Survey with an Imaging Telescope Array) satellite (Predehl *et al.*, 2006).

Crowded fields The application to real data demonstrated that the BSS technique is capable to separate close by objects, faint sources close to bright sources, and sources superposed to a diffuse emission. Source confusion in crowded fields may still be a problem.

In the frame of BPT, following the work of Fischer and Dose (2002), the two–component mixture model can be extended to a variable number of components. Special problems such as the analysis of crowded fields (e.g., in rich clusters or the Galactic center) could be solved.

Source fitting routine The BSS algorithm is capable to detect point–like and extended sources equally well. Estimates in source parameters are improved with respect to standard techniques (see Chapters 5, 6 and 7). The technique for source characterization (Section 2.3) can be extended employing Bayesian model selection. With the Bayesian model selection analysis, the most suitable model describing the photon count profile of the detected sources can be found. The models to be employed are, for instance, instrumental point spread function (PSF) model, Gaussian profile, King profile, de Vaucouleurs model and Hubble model. The proposed extension to the existing method would allow an improvement in the estimation of the shape parameters and their uncertainties for faint or extended sources.

Probability of a source to be extended As shown in Chapter 7, standard techniques employed so far for providing evidence for an object to be extended are not accounting for the source full dimensionality. With BPT, a probability of a source to be extended can be provided comparing volumes of the detected source with the one of the instrumental PSF. This challenging task is linked to the previous proposal since uncertainties of source parameters are crucial for estimating a probability of a source to be extended.

Extension to other statistics The BSS technique can be applied to other wavelengths (Section 2.2.1). The statistic suited for the description of a new data set has to be incorporated in the models.

The BSS technique can be extended,e.g., to Gaussian statistics. If Gaussian statistics is included, the BSS technique can be applied for a large variety of science projects also in extreme cases when faint objects are difficult to discriminate against the background. For instance, the proper motion of open clusters can be studied also when the stars are embedded in molecular clouds. The investigation of open cluster systems gives important insight in the Galaxy dynamics. Another application is the search of the central star in galactic planetary nebulae. Some central stars are not located properly at the centre of the nebulosity, sometime the nebulosity is too bright and the central star is identified with large errors in parameter estimates (Kerber *et al.*, 2003). The BSS technique, extended to Gaussian statistic, would allow a proper census of galactic planetary nebulae and their 'central' star.

Appendix A

Inverse–Gamma distribution

In the following appendix, supplementary material concerning the inverse–Gamma function prior pdf, introduced in Chapter 2, is given. In Section A.1, the inverse–Gamma function is compared to the power–law distribution. In Section A.2, the calculations for the marginal Poisson distribution for source detection are shown when employing the inverse–Gamma function prior pdf.

A.1 Relation between inverse–Gamma and power–law distributions

The inverse–Gamma distribution is a continuous probability distribution described by a positive variable and two parameters. It derives from the Gamma distribution with the variable described by its reciprocal.

The Gamma distribution is defined as:

$$p(x|\alpha,\theta) = \frac{x^{\alpha-1}\exp(-x/\theta)}{\theta^{\alpha}\Gamma(\alpha)},\ \text{for } x>0,\ \alpha>0,\ \theta>0. \tag{A.1}$$

α and θ are the shape and the scale parameters, respectively. Note that the gamma function is defined as $\Gamma(n) = \int_0^{\infty} u^{n-1}\exp(-u)du$ for $n > 0$. The gamma function is used to derive the gamma distribution. The denominator in eq. (A.1) is the normalization factor obtained integrating over the numerator.

The inverse–Gamma function is derived from eq. (A.1), replacing $x = 1/y$ and $\beta = 1/\theta$:

$$p(y|\alpha,\beta) = y^{-\alpha-1}\exp(-\beta/y)\frac{\beta^{\alpha}}{\Gamma(\alpha)},\ \text{for } y>0,\ \alpha>0,\ \beta>0. \tag{A.2}$$

β, the scale parameter, is also known as rate parameter.

The inverse–Gamma distribution is of interest since it allows the prior of the source signal to be described by a power–law. However, the inverse–Gamma function has two components: a power–law distribution and an exponential function. Figure A.1 shows that only small values of β allows the inverse–Gamma function to behave as a power–law

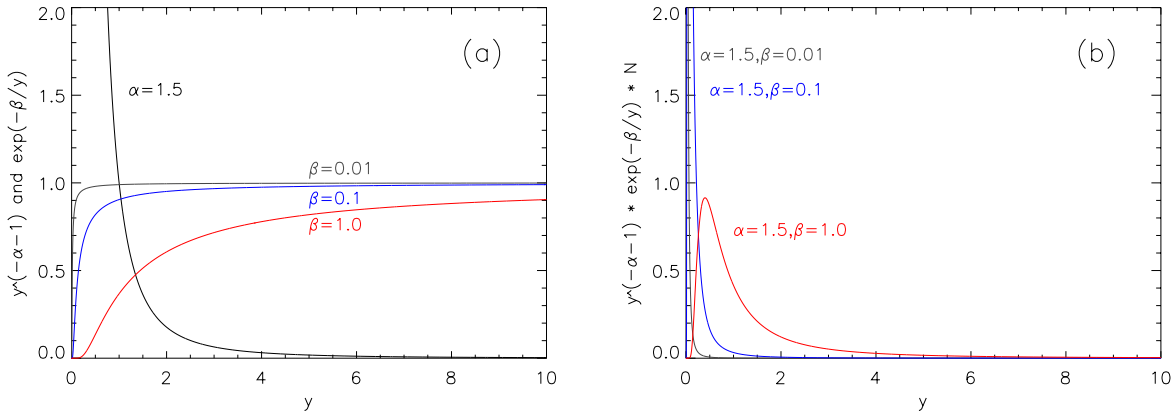

Figure A.1: Panel (a): power–law and exponential components of the inverse–Gamma function, eq. (A.2). Panel (b): inverse–Gamma function distribution with N indicating the normalization factor. Panels (a) and (b) contain the same parameter values.

distribution. In panel (a), the power–law and the exponential components of the inverse–Gamma function are drawn separately. The power–law and exponential components are plotted with values of $\alpha = 1.5$ and $\beta = 0.01, 0.1, 1$. In panel (b), the inverse–Gamma function behaves as the power–law only for values of $\beta < 1$.

Note that the inverse–Gamma function distribution, as defined in eq. (2.23), derives from eq. (A.2): α is replaced by $\alpha - 1$ and y indicates the number of counts per pixel. In addition, the inverse–Gamma distribution is not defined for values of $y = 0$. Hence, the prior pdf of the source signal attributes to the background all pixels presenting no counts.

A.2 Derivation of the marginal Poisson likelihood

The marginal Poisson likelihood, as given by eq. (2.23), is the mathematical solution of eq. (2.19):

$$p(d_{ij}|\overline{B}_{ij}, b_{ij}, \alpha, a) = \int_0^\infty \frac{(b_{ij}+s_{ij})^{d_{ij}}}{d_{ij}!}\exp(-b_{ij}-s_{ij})s_{ij}^{-\alpha}\exp\Big(-\frac{a}{s_{ij}}\Big)\frac{a^{\alpha-1}}{\Gamma(\alpha-1)}ds. \qquad (A.3)$$

The mathematical solution to the integral is obtained employing the binomial expansion of $(b_{ij}+s_{ij})^{d_{ij}} = \sum_{k=0}^{d_{ij}} \frac{d_{ij}!}{k!(d_{ij}-k)!} b_{ij}^{d_{ij}-k} s_{ij}^{k}$. Equation (A.3) is written as follow:

$$\begin{aligned} p(d_{ij}|\overline{B}_{ij}, b_{ij}, \alpha, a) &= \frac{a^{\alpha-1}}{\Gamma(\alpha-1)}\int_0^\infty \sum_{k=0}^{d_{ij}} \frac{b_{ij}^{d_{ij}-k}s_{ij}^{k}}{k!(d_{ij}-k)!}\exp(-b_{ij}-s_{ij})s_{ij}^{-\alpha}\exp\Big(-\frac{a}{s_{ij}}\Big)ds \\ &= \frac{a^{\alpha-1}}{\Gamma(\alpha-1)}\sum_{k=0}^{d_{ij}} \frac{b_{ij}^{d_{ij}-k}\exp(-b_{ij})}{k!(d_{ij}-k)!}\int_0^\infty s_{ij}^{k-\alpha}\exp\Big(-s_{ij}-\frac{a}{s_{ij}}\Big)ds. \qquad (A.4) \end{aligned}$$

The Bessel function of imaginary argument, $K_\nu(z)$, defines $\int_0^\infty x^{\nu-1}\exp\Big(-\frac{\beta}{x}-\gamma x\Big)dx = 2(\frac{\beta}{\gamma})^{\nu/2}K_\nu(2\sqrt{\beta\gamma})$, with $R\,\beta > 0$ and $R\,\gamma > 0$. Hence, eq. (A.4) can be written as follow:

$$\begin{aligned} p(d_{\rm ij}|\overline{B}_{\rm ij}, b_{\rm ij}, \alpha, a) &= \frac{a^{\alpha-1}}{\Gamma(\alpha-1)}\sum_{k=0}^{d_{\rm ij}}\frac{b_{\rm ij}^{d_{\rm ij}-k}\exp(-b_{\rm ij})}{\Gamma(k+1)\Gamma(d_{\rm ij}-k+1)}2a^{\frac{k-\alpha+1}{2}}K_{k-\alpha+1}(2\sqrt{a}) \\ &= \frac{2}{\Gamma(\alpha-1)}\exp(-b_{\rm ij})\sum_{k=0}^{d_{\rm ij}}a^{\frac{k+\alpha-1}{2}}\frac{b_{\rm ij}^{d_{\rm ij}-k}}{\Gamma(k+1)\Gamma(d_{\rm ij}-k+1)}K_{k-\alpha+1}(2\sqrt{a}). \end{aligned} \quad (A.5)$$

Equation (A.5) provides the marginal Poisson likelihood as reported in eq. (2.23).

Appendix B

The spline model

In this appendix, spline functions are explained and details about the TPS are given.

B.1 Introduction

Splines are a broad class of functions used in diverse domains of numerical analysis, such as interpolation, data smoothing, numerical solution of differential and integral equations. In this thesis, splines are used as an interpolant of the background over scattered data in image analysis. Between the available spline functions, the RBF is chosen.

Historically, in the works of Schoenberg (1964*b*,*a*) (Wahba, 1990) is shown that a smooth function of degree $k > 0$, $f^{(k)}(x)$, can be found with $k-1$ continuous derivatives and k-th derivative square integrable, to minimize

$$\int_a^b [f^{(k)}(x)]^2 dx, \tag{B.1}$$

subject to $f(x_\mathrm{i}) = f_\mathrm{i}$ with $i = 1, 2, \ldots, j$ indicating the pivots. Provided $j \geq k$, this minimizer is the unique natural polynomial spline satisfying the conditions of continuity and differentiability, given that the function goes through the supporting points. Schoenberg called this object a spline, due to its resemblance (when $k = 2$) to the mechanical spline used by draftsmen. The mechanical spline is a thin strip used to draw curves. Weights were placed on the strip to force it to go through given points. The free portion of the strip would assume a position in space that minimizes the (two–dimensional) bending energy. With $k = 2$, the quantity (B.1) is the (one–dimensional) curvature.

Commonly, the term spline is related to the restricted setting of one–dimensional polynomial splines (piece–wise polynomial functions). The piece–wise polynomials are often cubic functions (e.g., B–splines) defined on a finite interval $[a, b]$ and satisfing $f^{(j)}(a) = f^{(j)}(b) = 0$, with $j = k, \ldots, 2k-1$: See,e.g., Dierckx (1995) for more details.

A natural generalization of univariate polynomial splines to the multivariate settings are given by RBFs. The RBF is particularly suited to model data in more than one dimension. The main advantages of the RBF are: The high accuracy to the approximated

target function; The support points are not necessarily restricted on a mesh. Last, RBFs are popular for interpolating scattered data as the associated system of linear equations is guaranteed to be invertible under very mild conditions on the locations of the data points (Carr, 2003). An RBF is, in general, a function of the form:

$$s(\mathbf{x}) = \sum_{j=1}^{N} \lambda_{\mathrm{j}} \Phi(|\mathbf{x} - \mathbf{x}_{\mathrm{j}}|),$$

where $\mathbf{x}$ is a point in d space dimensions and the *basis function* Φ is a real valued function on $[0, \infty)$, usually unbounded and of non–compact support, defined on a vector space of functions $f(\mathbf{x})$. The λ_{j} are called *weights* and the $\mathbf{x}_{\mathrm{j}}$ are the *centres* of the RBF. The centres are scattered data points (pivots). The values of the RBF depends on the distance from the pivots.

Among the possible choices on $\Phi(r)$ for fitting smooth functions of two variables, $\Phi(r)$ is represented by a TPS: $\Phi(r) = r^2 \ln r$ or $\tilde{\Phi}(r) = r^2 \ln r^2$. The theoretical foundations for the TPS were laid by the works of Duchon (1975, 1976, 1977) and Meinguet (1979).

A low order polynomial is added to $s(\mathbf{x})$ and some mild extra conditions ($\sum_{j=1}^{N} \lambda_{\mathrm{j}} = 0$, $\sum_{j=1}^{N} \lambda_{\mathrm{j}} x = 0$, $\sum_{j=1}^{N} \lambda_{\mathrm{j}} y = 0$) are applied in order to guarantee the unique existence of the interpolants.

In Section B.2, it is demonstrated that if $f(x)$ is the smoothest of all possible interpolating curves (i.e., it minimizes the integral of the square of the second derivatives), than also $s(x)$ is the smoothest of all possible interpolating curves. This demonstration is carried out in the simplest case of employing a 3^{rd} order polynomial.

In Section B.3, the Laplace equation is used to demonstrate that the conditions for the minimum are satisfied for a two–dimensional function if the 2^{nd} order derivatives exist and are continuous. In this Section it is also demonstrated that the TPS is a solution of the Euler–Lagrange equation, also when adding a plane to the TPS.

In Section B.4, the interpolation problem using a TPS is shown to be valid only taking into account three extra conditions.

The demonstrations are following private communications with Prof.Dr. Dr.h.c. Volker Dose.

B.2 Interpolation in one dimension space

Be $f(x)$ a real–valued function defined on a finite interval $[a, b]$. The global curvature of $f(x)$ is defined as:

$$c_1 = \int_{\mathrm{a}}^{\mathrm{b}} |f''|^2 dx. \tag{B.2}$$

The minimum of the global curvature is searched to identify the smoothest of all possible interpolating curves (Lagrange problem). The functional $\Phi = (f'')^2$ has to be minimized

over a set of admissible functions f (i.e., $c_1 = \int_{\mathrm{a}}^{\mathrm{b}} \Phi(f(x), f'(x))dx$), and with fixed boundary conditions ($f(a) = f_{\mathrm{a}}, f(b) = f_{\mathrm{b}}$). In order to minimize $f(x)$ a small deviation $\delta f(x)$ is considered in standard calculus. The condition for the minimum to be satisfied is:

$$\delta c_1 = \int_{\mathrm{a}}^{\mathrm{b}} [\Phi(f + \delta f, f' + \delta f') - \Phi(f, f')]dx = 0. \tag{B.3}$$

The integrand in eq. (B.3) can be expanded, resulting:

$$\int_{\mathrm{a}}^{\mathrm{b}} [\frac{\partial \Phi}{\partial f}\delta f + \frac{\partial \Phi}{\partial f'}\delta f']dx = 0. \tag{B.4}$$

Integrating by parts, eq. (B.4) becomes:

$$\delta c_1 = \int_{\mathrm{a}}^{\mathrm{b}} [\frac{\partial \Phi}{\partial f} - \frac{\partial}{\partial x}(\frac{\partial \Phi}{\partial f'})]\delta f(x)dx = 0, \tag{B.5}$$

that is satisfied only if:

$$\frac{\partial \Phi}{\partial f} - \frac{\partial}{\partial x}(\frac{\partial \Phi}{\partial f'}) = 0. \tag{B.6}$$

Expression (B.6) is the Euler–Lagrange equation, well–known in classical mechanics.

The function $f(x)$ can be represented with a 3^{rd} order polynomial. Employing $f(x)$, it is possible to demonstrate that the minimum property is conserved if the spline function $s(x)$: 1) is a piece–wise 3^{rd} order polynomial; 2) is two times continuosly differentiable; 3) takes a particular value y_{i} at the point x_{i} if are satisfied the auxiliary conditions: $\int_{\mathrm{a}}^{\mathrm{b}} |f'' - s''|^2 dx \geq 0$ and $\int_{\mathrm{a}}^{\mathrm{b}} |f''|^2 dx \geq \int_{\mathrm{a}}^{\mathrm{b}} |s''|^2 dx$.

Considering the following:

$$\int_{\mathrm{a}}^{\mathrm{b}} |f'' - s''|^2 dx = \int_{\mathrm{a}}^{\mathrm{b}} (|f''|^2 - |s''|^2)dx - 2\int_{\mathrm{a}}^{\mathrm{b}} (f'' - s'')s''dx, \tag{B.7}$$

the proof is given when demonstrating that the last term in eq. (B.7) assumes a null value:

$$\int_{\mathrm{a}}^{\mathrm{b}} (f'' - s'')s''dx = \sum_{i=0}^{N-1} \int_{\mathrm{x_i}}^{\mathrm{x_{i+1}}} (f'' - s'')s''dx, \tag{B.8}$$

integrating by parts:

$$\int_{\mathrm{a}}^{\mathrm{b}} (f'' - s'')s''dx = [f'(b) - s'(b)]s''(b) - [f'(a) - s'(a)]s''(a) = 0. \tag{B.9}$$

Equation (B.9) is null only if the following conditions are satisfied: $s''(b) = s''(a) = 0$ or $f'(a) = s'(a)$ or $f'(b) = s'(b)$ Q.E.D. Hence, $s(x)$ satisfies also the condition for the minimum.

B.3 Interpolation in two dimensions

The global curvature of a real–valued function $f(x, y)$ is defined as:

$$c_2 = \int\int (f_{\mathrm{xx}}^2 + 2f_{\mathrm{xy}}^2 + f_{\mathrm{yy}}^2) dxdy.$$

The aim is to determine the minimum of c_2, i.e. the minimum of all possible global curvatures. Therefore, the smoothest of all possible interpolating curves is searched:

$$c_2 = \int_{-\infty}^{+\infty}\int_{-\infty}^{+\infty} (f_{\mathrm{xx}}^2 + 2f_{\mathrm{xy}}^2 + f_{\mathrm{yy}}^2) dxdy \geq 0 \equiv \min_f. \tag{B.10}$$

No analytic solutions are known on a finite support for this integral.
$\Phi = f_{\mathrm{xx}}^2 + 2f_{\mathrm{xy}}^2 + f_{\mathrm{yy}}^2$ is defined as the penalty functional, function of which one wants to measure the minimum. The Euler–Lagrange equation is used as derived for higher–order derivatives:

$$\frac{\delta\Phi}{\delta f} = \frac{\partial\Phi}{\partial f} - \sum_i \frac{\partial}{\partial x_{\mathrm{i}}}\frac{\partial\Phi}{\partial f_{\mathrm{x_i}}} + \sum_{i,k} \frac{\partial^2}{\partial x_{\mathrm{i}}\partial x_{\mathrm{k}}}\frac{\partial^2\Phi}{\partial f_{\mathrm{x_i}}\partial f_{\mathrm{x_k}}}. \tag{B.11}$$

In particular $\frac{\delta\Phi}{\delta f} = 0$ has to be satisfied in order to have the minimum of Φ. From eq. (B.11), where $\frac{\partial\Phi}{\partial f} = 0$ and $\frac{\partial\Phi}{\partial f_{\mathrm{x_i}}} = 0$, it follows:

$$\frac{\delta\Phi}{\delta f} = \sum_{\mathrm{i,k}} \frac{\partial^2}{\partial x_{\mathrm{i}}\partial x_{\mathrm{k}}}(2f_{\mathrm{xx}} + 4f_{\mathrm{xy}} + 2f_{\mathrm{yy}}) = 2\frac{\partial^2}{\partial x^2}f_{\mathrm{xx}} + 4\frac{\partial^2}{\partial x\partial y}f_{\mathrm{xy}} + 2\frac{\partial^2}{\partial y^2}f_{\mathrm{yy}}. \tag{B.12}$$

In order to demonstrate that $\frac{\delta\Phi}{\delta f} = 0$ in equation (B.12), the Laplace's equation is considered:

$$\triangle f = \nabla^2 f = \triangle\{\frac{\partial^2 f}{\partial x^2} + \frac{\partial^2 f}{\partial y^2}\} = 0,$$

this is the differential equation from which the required function can be obtained: $\triangle f = \frac{\partial^2}{\partial x^2}f_{\mathrm{xx}} + 2\frac{\partial^2}{\partial x\partial y}f_{\mathrm{xy}} + \frac{\partial^2}{\partial y^2}f_{\mathrm{yy}} = 0$ Q.E.D.
Therefore $f(x, y)$ is an analytic function and solution of Laplace's equation with the conditions that the second derivatives exist and are continuous.
From eq. (B.10), a minimum can be obtained if all terms under the integral vanish:

$$\frac{\partial^2}{\partial x^2}f_{\mathrm{xx}} + 2\frac{\partial^2}{\partial x\partial y}f_{\mathrm{xy}} + \frac{\partial^2}{\partial y^2}f_{\mathrm{yy}} = 0 \quad \rightarrow \text{absolute minimum.}$$

If a plane $E(x, y) = \alpha x + \beta y + \gamma$ is added to the functional Φ, the Euler–Lagrange equation is still satisfied: $f(x, y) \rightarrow f(x, y) + E(x, y)$.

Now it is possible to show that $f(x, y) = r^2\ln(r^2)$, where r is the distance of radially symmetric basis, is a solution of the Euler–Lagrange equation.

The Laplace's equation can be rewritten in polar coordinates ($\triangle = \frac{1}{r}\frac{\partial}{\partial r} r \frac{\partial}{\partial r}$):

$$\triangle f = \frac{1}{r}\frac{\partial}{\partial r} r \frac{\partial}{\partial r}[r^2 \ln(r)] = 4\ln(r) + 4,$$

$$\triangle^2 f = 4\frac{1}{r}\frac{\partial}{\partial r} r \frac{\partial}{\partial r}[\ln(r) + 1] = 0 \quad \forall \ r \neq 0.$$

If $r \to 0$, instead, a value $\epsilon \to 0$ is considered:

$$\int \triangle^2 f(r) dA = \int_0^{\epsilon} \triangle^2 f \ \ r dr \int_0^{2\pi} d\varphi = 8\pi,$$

without dependency on ϵ. Q.E.D.

B.4 Interpolation using TPSs

The interpolating function over scattered data has been chosen to be:

$$s(\mathbf{x}) = E(\mathbf{x}) + \sum_{l=1}^{N} a_{\mathrm{l}} f(\mathbf{x} - \mathbf{x}_{\mathrm{l}}),$$

where $\mathbf{x} = (x, y)$. $E(\mathbf{x})$ is the added plane. $\sum_{\mathrm{l}=1}^{N} a_{\mathrm{l}} f(\mathbf{x} - \mathbf{x}_{\mathrm{l}})$ is the sum of basis functions centred on the pivots positions ($\mathbf{x}_{\mathrm{i}}$).
The requirements necessary for succeeding in the interpolation are:

- the function $s(\mathbf{x})$ goes through the support points: $s(\mathbf{x}_{\mathrm{i}}) = z_{\mathrm{i}}$,
- $c_2 = \int\int (f_{\mathrm{xx}}^2 + 2f_{\mathrm{xy}}^2 + f_{\mathrm{yy}}^2) dx dy \equiv \min_f$.

The function $f(x, y)$ is defined as:

$$f(x, y) = \{(x - x_{\mathrm{i}})^2 + (y - y_{\mathrm{i}})^2\} \cdot \ln\{(x - x_{\mathrm{i}})^2 + (y - y_{\mathrm{i}})^2\} = R_{\mathrm{i}}^2 \cdot \ln R_{\mathrm{i}}^2$$

and $f = r^2 \ln r$, or $\tilde{f} = r^2 \ln r^2$, is identified. The conditions to impose to $f(x, y)$ are now investigated in order to satisfy the condition of a finite integral. Therefore the partial derivatives are solved:

- $\frac{1}{2} f_{\mathrm{xy}} = 2\frac{(x - x_{\mathrm{i}})(y - y_{\mathrm{i}})}{R_{\mathrm{i}}^2}$,
- $\frac{1}{2} f_{\mathrm{xx}} = \ln R_{\mathrm{i}}^2 + 2\frac{(x - x_{\mathrm{i}})^2}{R_{\mathrm{i}}^2} + 1$,
- $\frac{1}{2} f_{\mathrm{yy}} = \ln R_{\mathrm{i}}^2 + 2\frac{(y - y_{\mathrm{i}})^2}{R_{\mathrm{i}}^2} + 1$.

The partial derivatives for $s(\mathbf{x})$ are following:

$$\frac{1}{2}s_{\mathrm{xx}} = \sum_{i=1}^{N} a_{\mathrm{i}} f_{\mathrm{xx}} = \sum_{i=1}^{N} a_{\mathrm{i}}[\ln R_{\mathrm{i}}^2 + 2\frac{(x-x_{\mathrm{i}})^2}{R_{\mathrm{i}}^2} + 1], \tag{B.13}$$

$$\frac{1}{2}s_{\mathrm{yy}} = \sum_{i=1}^{N} a_{\mathrm{i}} f_{\mathrm{yy}} = \sum_{i=1}^{N} a_{\mathrm{i}}[\ln R_{\mathrm{i}}^2 + 2\frac{(y-y_{\mathrm{i}})^2}{R_{\mathrm{i}}^2} + 1], \tag{B.14}$$

$$\frac{1}{2}s_{\mathrm{xy}} = \sum_{i=1}^{N} a_{\mathrm{i}} f_{\mathrm{xy}} = \sum_{i=1}^{N} a_{\mathrm{i}} \frac{2(x-x_{\mathrm{i}})(y-y_{\mathrm{i}})}{R_{\mathrm{i}}^2}. \tag{B.15}$$

In order to have a converging integral, some necessary (but not sufficient) conditions are introduced. First, in order to have $s(\mathbf{x})$ finite, the "1" in eqs (B.13), (B.14) has to vanish. Therefore the following condition has to be satisfied:

$$\sum_{i=1}^{N} a_{\mathrm{i}} = 0 \tag{B.16}$$

which reduce the number of pivots. Eq. (B.13) can be written as follow:

$$\frac{1}{2}s_{\mathrm{xx}} = \sum_{i=1}^{N} a_{\mathrm{i}}[\ln R_{\mathrm{i}}^2 + \frac{2}{R_{\mathrm{i}}^2}\frac{r^2}{r^2}(x-x_{\mathrm{i}})^2 - \ln r^2]$$

where $r^2 = x^2 + y^2$ and $\sum_{i=1}^{N} a_{\mathrm{i}} \ln r^2 = 0$. The fractional term can be written as:

$$\frac{R_{\mathrm{i}}^2}{r^2} = 1 + \frac{x_{\mathrm{i}}^2 + y_{\mathrm{i}}^2}{r^2} - \frac{2}{r^2}(xx_{\mathrm{i}} + yy_{\mathrm{i}})$$

where r is finite. The case when r goes to ∞ is investigated too. One can define:

$$\frac{R_{\mathrm{i}}^2}{r^2} = 1 + \Delta_{\mathrm{i}},$$

where $\Delta_{\mathrm{i}} = \frac{x_{\mathrm{i}}^2+y_{\mathrm{i}}^2}{r^2} - \frac{2}{r^2}(xx_{\mathrm{i}} + yy_{\mathrm{i}})$ is a small term. These definitions are used to calculate:

$$\frac{1}{2}s_{\mathrm{xx}} = \sum_{i=1}^{N} a_{\mathrm{i}}[\ln R_{\mathrm{i}}^2 + \frac{2}{r^2}\frac{r^2}{R_{\mathrm{i}}^2}(x-x_{\mathrm{i}})^2 - \ln r^2] = \sum_{i=1}^{N} a_{\mathrm{i}}[\ln(1+\Delta_{\mathrm{i}}) + \frac{2}{r^2}(1-\Delta_{\mathrm{i}})(x-x_{\mathrm{i}})^2].$$

Developing the calculations and using the first necessary but not sufficient condition, eq. (B.16), one obtains:

$$\frac{1}{2}s_{\mathrm{xx}} = \frac{1}{r^2}\sum_{i=1}^{N} a_{\mathrm{i}}[3x_{\mathrm{i}}^2 - 6xx_{\mathrm{i}} - 2yy_{\mathrm{i}} + y_{\mathrm{i}}^2].$$

In order to have the integral converging, two more conditions have to be introduced:

$$\sum_{i=1}^{N} a_{\mathrm{i}} x_{\mathrm{i}} = 0,$$

$$\sum_{i=1}^{N} a_{\mathrm{i}} y_{\mathrm{i}} = 0.$$

So that $s_{\mathrm{xx}} = 0$, where $s_{\mathrm{xx}} = 2\sum_{i=1}^{N} a_{\mathrm{i}} f_{\mathrm{xx}}$. Therefore the conditions of existence for the interpolation function on the pivots are:

$$\begin{cases} \sum_{i=1}^{N} a_{\mathrm{i}} & = & 0, \\ \sum_{i=1}^{N} a_{\mathrm{i}} x_{\mathrm{i}} & = & 0, \\ \sum_{i=1}^{N} a_{\mathrm{i}} y_{\mathrm{i}} & = & 0. \end{cases}$$

Note the asymptotic behavior of the TPS when pixels positions coincide with the pivots positions.

Appendix C

Minimization procedure for the background model

In this appendix, details about the minimization procedure employed for the background model are given.

C.1 Introduction

In order to determine the optimal form and characteristics of the background model that corresponds most closely to the one arising from the data, a procedure designed for minimizing a smooth nonlinear function is employed. Therefore, the negative value of the logarithm of the posterior pdf of the background (see Section 2.2.3 for more details) is sought, which is the objective function of the optimization routine. Constraint functions are used. The objective function and the constraint functions are smooth, i.e. at least twice-continuously differentiable. The objective function is a single measure of goodness, which depends on the parameters entering the model. The constraint functions are evaluated at the support points positions. For a pixel position (i, j), the constraint function is given by the TPS amplitude:

$$b_{\mathrm{ij}} = \{\sum_{k=1}^{N_{\mathrm{p}}} \lambda_{\mathrm{k}} r^2 \log(r^2) + c_0 + c_1 x_{\mathrm{ij}} + c_2 y_{\mathrm{ij}}\} \times E_{\mathrm{ij}}. \tag{C.1}$$

r represents the distance between the pixel position $\{ij\}$ and the k–th pivot. E_{ij} is the telescope's exposure time at the pixel position $\{ij\}$. The role of the constraint function is to ensure a positive background.

For maximum reliability of the employed procedure, all partial derivatives of the objective function and of the nonlinear constraints function are provided. In the following paragraphs, the partial derivatives for the objective function are given for each prior pdf of the source signal employed.

Partial derivatives for objective function: inverse–Gamma function prior case. Considering the case of selecting the inverse–Gamma function prior pdf, the likelihood for the mixture model can be written as follow:

$$p(D|b,\beta,\alpha) = \prod_{ij} \Big\{ \beta \frac{b_{\mathrm{ij}}^{d_{\mathrm{ij}}}}{d_{\mathrm{ij}}!} e^{-b_{\mathrm{ij}}} + 2(1-\beta) \frac{e^{-b_{\mathrm{ij}}}}{\Gamma(\alpha-1)} \sum_{k=0}^{d_{\mathrm{ij}}} \frac{a^{\frac{\alpha+k-1}{2}} b_{\mathrm{ij}}^{d_{\mathrm{ij}}-k}}{\Gamma(d_{\mathrm{ij}}-k+1)} \frac{K_{k-\alpha+1}(2\sqrt{a})}{\Gamma(k+1)} \Big\}. \quad \text{(C.2)}$$

The objective function F is a function of the transformed variables: $F = F(s_1, \ldots, s_{\mathrm{N_P}})$. The scaled pivots amplitudes are a function of the original variables: $s_{\mathrm{p}} = s_{\mathrm{p}}(z_{\mathrm{p}})$, with $p = 1, \ldots, N_{\mathrm{p}}$.
Therefore the individual objective gradients are given by:

$$\frac{\partial F}{\partial s_{\mathrm{p}}} = \frac{1}{S_{\mathrm{F}}} \frac{\partial F}{\partial z_{\mathrm{p}}}, \quad \text{(C.3)}$$

where S_{F} is the scaling factor used to obtain the transformed variables from the original ones.
Because the background amplitudes are a function of the support points, the gradient on the right hand side of eq. (C.3) can be written as follows:

$$\frac{\partial F}{\partial z_{\mathrm{p}}} = \sum_{\mu\nu} \frac{\partial F}{\partial b_{\mu\nu}} \frac{\partial b_{\mu\nu}}{\partial z_{\mathrm{p}}}. \quad \text{(C.4)}$$

After computing the two partial derivatives in eq. (C.4), the solution to equation (C.3) is:

$$\begin{aligned} \frac{\partial F}{\partial s_{\mathrm{p}}} \;=\; & \frac{1}{S_{\mathrm{F}}} \sum_{\mu\nu} \Big(-\frac{1}{f_{\mu\nu}} \Big) \Big\{ \frac{\beta e^{-b_{\mu\nu}}}{\Gamma(d_{\mu\nu}+1)} b_{\mu\nu}^{d_{\mu\nu}} \Big(\frac{d_{\mu\nu}}{b_{\mu\nu}} - 1 \Big) \\ & + \frac{2(1-\beta)}{\Gamma(\alpha-1)} e^{-b_{\mu\nu}} \sum_{k=0}^{d_{\mu\nu}} \frac{a^{\frac{\alpha+k-1}{2}}}{\Gamma(d_{\mu\nu}-k+1)} \frac{k_{k-\alpha+1}(2\sqrt{a})}{\Gamma(k+1)} b_{\mu\nu}^{(d_{\mu\nu}-k)} \Big(\frac{d_{\mu\nu}-k}{b_{\mu\nu}} - 1 \Big) \Big\} \\ & \times E_{\mu\nu} \Big\{ \sum_{j=1}^{N_{\mathrm{P}}} [(x_{\mu\nu}-x_{\mathrm{j}})^2 + (y_{\mu\nu}-y_{\mathrm{j}})^2] \cdot \log[(x_{\mu\nu}-x_{\mathrm{j}})^2 + (y_{\mu\nu}-y_{\mathrm{j}})^2] \\ & \times \overline{m}_{j,p} + \overline{m}_{N_{\mathrm{P}+1},p} + x_{\mu\nu} \overline{m}_{N_{\mathrm{P}+2},p} + y_{\mu\nu} \overline{m}_{\mathrm{N_{P+3}},p} \Big\}, \end{aligned} \quad \text{(C.5)}$$

exploited over the complete field. $f_{\mu\nu}$ is explained in equation (C.2). The matrix components $\overline{m}_{k,p}$, with $k, p = 1, \ldots, N_{P+3}$, are the elements of the inverse of the matrix M:

$$M = \begin{pmatrix} F & Q \\ Q^T & 0 \end{pmatrix};$$

for more explanations of the matrix M and its components see eq. (2.25) in Section 2.2.2. The Jacobian elements of the nonlinear constraint function are given by $\partial b_{\mu\nu}/\partial z_p$, whose solution is written in the last two lines of eq. (C.5).

Partial derivatives for objective function: exponential prior case. The likelihood for the mixture model employing the exponential prior pdf is given by:

$$p(D|b,\beta,\lambda) = \prod_{ij} \Big\{ \beta \frac{b_{\mathrm{ij}}^{d_{\mathrm{ij}}}}{d_{\mathrm{ij}}!} \mathrm{e}^{-b_{\mathrm{ij}}} + \frac{(1-\beta)\mathrm{e}^{b_{\mathrm{ij}}/\lambda}}{\lambda(1+\frac{1}{\lambda})^{(d_{\mathrm{ij}}+1)}} \cdot \frac{\Gamma[(d_{\mathrm{ij}}+1), b_{\mathrm{ij}}(1+\frac{1}{\lambda})]}{\Gamma(d_{\mathrm{ij}}+1)} \Big\}. \tag{C.6}$$

Employing eq. (C.6), the solution to equation (C.3) is the following:

$$\begin{aligned}
\frac{\partial F}{\partial s_{\mathrm{p}}} \;=\; & \frac{1}{S_{\mathrm{F}}} \sum_{\mu\nu} \Big(-\frac{1}{f_{\mu\nu}} \Big) \frac{1}{\Gamma(d_{\mu\nu}+1)} \Big\{ \beta \mathrm{e}^{-b_{\mu\nu}} b_{\mu\nu}^{d_{\mu\nu}} \Big(\frac{d_{\mu\nu}}{b_{\mu\nu}} - 1 \Big) \\
& + \frac{(1-\beta)}{\lambda} \Big[\frac{\mathrm{e}^{b_{\mu\nu}/\lambda} \Gamma[(d_{\mu\nu}+1), b_{\mu\nu}(1+\frac{1}{\lambda})]}{\lambda(1+\frac{1}{\lambda})^{d_{\mu\nu}+1}} - b_{\mu\nu}^{d_{\mu\nu}} \mathrm{e}^{-b_{\mu\nu}} \Big] \Big\} \\
& \times E_{\mu\nu} \Big\{ \sum_{k=1}^{N_{\mathrm{P}}} [(x_{\mu\nu} - x_{\mathrm{k}})^2 + (y_{\mu\nu} - y_{\mathrm{k}})^2] \cdot \log[(x_{\mu\nu} - x_{\mathrm{k}})^2 + (y_{\mu\nu} - y_{\mathrm{k}})^2] \\
& \times \overline{m}_{k,p} + \overline{m}_{N_{\mathrm{P}+1},p} + \overline{m}_{N_{\mathrm{P}+2},p} x_{\mu\nu} + \overline{m}_{\mathrm{N_{P+3}},\mathrm{p}} y_{\mu\nu} \Big\}.
\end{aligned} \tag{C.7}$$

The same explanations given for equation (C.5) are valid for equation (C.7).

Bibliography

Abazajian, K. e. a. (2003). 'The First Data Release of the Sloan Digital Sky Survey'. *AJ* **126**, 2081–2086.

Abazajian, K. e. a. (2004). 'The Second Data Release of the Sloan Digital Sky Survey'. *AJ* **128**, 502–512.

Abazajian, K. N. e. a. (2009). 'The Seventh Data Release of the Sloan Digital Sky Survey'. *ApJS* **182**, 543–558.

Abell, G. O., H. G. Corwin, Jr. and R. P. Olowin (1989). 'A catalog of rich clusters of galaxies'. *ApJS* **70**, 1–138.

Ajello, M., L. Costamante, R. M. Sambruna, N. Gehrels, J. Chiang, A. Rau, A. Escala, J. Greiner, J. Tueller, J. V. Wall and R. F. Mushotzky (2009). 'The Evolution of Swift/BAT Blazars and the Origin of the MeV Background'. *ApJ* **699**, 603–625.

Alexander, D. M., F. E. Bauer, W. N. Brandt, D. P. Schneider, A. E. Hornschemeier, C. Vignali, A. J. Barger, P. S. Broos, L. L. Cowie, G. P. Garmire, L. K. Townsley, M. W. Bautz, G. Chartas and W. L. W. Sargent (2003). 'The Chandra Deep Field North Survey. XIII. 2 Ms Point-Source Catalogs'. *AJ* **126**, 539–574.

Aschenbach, B. (1998). 'Discovery of a young nearby supernova remnant'. *Nature* **396**, 141–142.

Aschenbach, B., A. F. Iyudin and V. Schönfelder (1999). 'Constraints of age, distance and progenitor of the supernova remnant RX J0852.0-4622/GRO J0852-4642'. *A&A* **350**, 997–1006.

Aschenbach, B., R. Egger and J. Trumper (1995). 'Discovery of Explosion Fragments Outside the VELA Supernova Remnant Shock-Wave Boundary'. *Nature* **373**, 587–+.

Astone, P., G. D'Agostini and S. D'Antonio (2003). 'Bayesian model comparison applied to the Explorer Nautilus 2001 coincidence data'. *Classical and Quantum Gravity* **20**, 769–+.

Balestra, I., V. Mainieri, P. Popesso, M. Dickinson, M. Nonino, P. Rosati, H. Teimoorinia, E. Vanzella, S. Cristiani, C. Cesarsky, R. A. E. Fosbury, H. Kuntschner, A. Rettura and

the GOODS team (2010). 'The Great Observatories Origins Deep Survey - VLT/VIMOS Spectroscopy in the GOODS-South Field: Part II'. *ArXiv e-prints*.

Ball, N. M. and R. J. Brunner (2009). 'Data Mining and Machine Learning in Astronomy'. *ArXiv e-prints*.

Bayes, T. (1783). 'An essay towards solving a problem in the doctrine of chances'. *Phil. Trans. Roy. Soc.* **53**, 370–418.

Becker, A. C., N. M. Silvestri, R. E. Owen, Ž. Ivezić and R. H. Lupton (2007). 'In Pursuit of LSST Science Requirements: A Comparison of Photometry Algorithms'. *PASP* **119**, 1462–1482.

Benjamini, Y. and Y. Hochberg (1995). 'Controlling the False Discovery Rate: A Practical and Powerful Approach to Multiple Testing'. *Journal of the Royal Statistical Society. Series B (Methodological)* **57**(1), 289–300.

Berger, J. (1997). Some recent developments in Bayesian analysis, with astronomical illustrations (with discussion). In G. Babu and E. Feigelson (Eds.). 'Statistical Challenges in Modern Astronomy II'. Springer, New York. pp. 15–39.

Berger, J. and D. Berry (1988). 'Analyzing data: Is objectivity possible?'. *American Scientist* **76**, 159–165.

Berger, J. and M. Delampady (1987). 'Testing precise hypothesis (with discussion)'. *Statist. Science* **2**, 317–352.

Berger, J. and T. Sellke (1987). 'Testing of a point null hypothesis: The irreconcilability of significance levels and evidence (with discussion)'. *J. Amer. Statist. Assoc.* **82**, 112–139.

Berger, J. O. (1985). *Statistical Decision Theory and Bayesian Analysis*. Springer-Verlag, New York.

Berger, J. O. (2003). 'Could fisher, jeffreys and neyman have agreed on testing?'. *Statistical Science* **18**(1), 1–12.

Bernardo, J. M. and A. F. Smith (1994). *Bayesian Theory*. John Wiley & Sons, New York.

Bernardo, J. M. and F. J. Girón (1988). A Bayesian Analysis of Simple Mixture Problems. In J. M. Bernardo, M. H. DeGroot, C. V. Lindley and A. F. M. Smith (Eds.). 'Bayesian Statistics 3'. Oxford University Press. pp. 67–78.

Berry, R. and J. Burnell (2005). *The handbook of astronomical image processing*. Richmond, VA: Willmann-Bell.

Bertin, E. and S. Arnouts (1996). 'SExtractor: Software for source extraction.'. *A&AS* **117**, 393–404.

Boese, F. G. (2000). 'The ROSAT point spread functions and associates'. *A&AS* **141**, 507–521.

Boese, F. G. (2004). 'On the precision of X-ray source parameters estimated from ROSAT data'. *A&A* **426**, 1119–1134.

Boese, F. G. and S. Doebereiner (2001). 'Maximum likelihood estimation of single X-ray point-source parameters in ROSAT data'. *A&A* **370**, 649–671.

Böhringer, H., G. W. Pratt, M. Arnaud, S. Borgani, J. H. Croston, T. J. Ponman, S. Ameglio, R. F. Temple and K. Dolag (2010). 'Substructure of the galaxy clusters in the REXCESS sample: observed statistics and comparison to numerical simulations'. *A&A* **514**, A32+.

Böhringer, H., P. Schuecker, L. Guzzo, C. A. Collins, W. Voges, R. G. Cruddace, A. Ortiz-Gil, G. Chincarini, S. De Grandi, A. C. Edge, H. T. MacGillivray, D. M. Neumann, S. Schindler and P. Shaver (2004). 'The ROSAT-ESO Flux Limited X-ray (REFLEX) Galaxy cluster survey. V. The cluster catalogue'. *A&A* **425**, 367–383.

Böhringer, H., P. Schuecker, L. Guzzo, C. A. Collins, W. Voges, S. Schindler, D. M. Neumann, R. G. Cruddace, S. De Grandi, G. Chincarini, A. C. Edge, H. T. MacGillivray and P. Shaver (2001). 'The ROSAT-ESO flux limited X-ray (REFLEX) galaxy cluster survey. I. The construction of the cluster sample'. *A&A* **369**, 826–850.

Böhringer, H., W. Voges, J. P. Huchra, B. McLean, R. Giacconi, P. Rosati, R. Burg, J. Mader, P. Schuecker, D. Simiç, S. Komossa, T. H. Reiprich, J. Retzlaff and J. Trümper (2000). 'The Northern ROSAT All-Sky (NORAS) Galaxy Cluster Survey. I. X-Ray Properties of Clusters Detected as Extended X-Ray Sources'. *ApJS* **129**, 435–474.

Boschin, W. (2002). 'A deep cluster survey in Chandra archival data. First results'. *A&A* **396**, 397–409.

Boschin, W. (2003). 'A deep cluster survey in Chandra archival data. First results'. *Memorie della Societa Astronomica Italiana* **74**, 440–+.

Brandt, W. N. and G. Hasinger (2005). 'Deep Extragalactic X-Ray Surveys'. *ARA&A* **43**, 827–859.

Bretthorst, G. L. (1988). *Bayesian Spectrum Analysis and Parameter Estimation (Lecture Notes in Statistics)*. Springer-Verlag.

Bunker, A. J., E. R. Stanway, R. S. Ellis, R. G. McMahon and P. J. McCarthy (2003). 'A star-forming galaxy at z= 5.78 in the Chandra Deep Field South'. *MNRAS* **342**, L47–L51.

Burkert, A., R. Genzel, G. Hasinger, G. Morfil, P. Schneider and D. Koester (2008). *Status and Prospects of Astronomy in Germany 2003-2016*. Wiley-VCH Verl., Weinheim.

Carr, J. C. (2003). Smooth surface reconstruction from noisy range data. In 'ACM Graphite 2003, Melbourne, Australia'. pp. 119–126.

Carvalho, P., G. Rocha and M. P. Hobson (2009). 'A fast Bayesian approach to discrete object detection in astronomical data sets - PowellSnakes I'. *MNRAS* **393**, 681–702.

Cash, W. (1979). 'Parameter estimation in astronomy through application of the likelihood ratio'. *ApJ* **228**, 939–947.

Cavaliere, A. and R. Fusco-Femiano (1978). 'The Distribution of Hot Gas in Clusters of Galaxies'. *A&A* **70**, 677–+.

Cimatti, A., M. Mignoli, E. Daddi, L. Pozzetti, A. Fontana, P. Saracco, F. Poli, A. Renzini, G. Zamorani, T. Broadhurst, S. Cristiani, S. D'Odorico, E. Giallongo, R. Gilmozzi and N. Menci (2002). 'The K20 survey. III. Photometric and spectroscopic properties of the sample'. *A&A* **392**, 395–406.

Colless, M., G. Dalton, S. Maddox, W. Sutherland, P. Norberg, S. Cole, J. Bland-Hawthorn, T. Bridges, R. Cannon, C. Collins, W. Couch, N. Cross, K. Deeley, R. De Propris, S. P. Driver, G. Efstathiou, R. S. Ellis, C. S. Frenk, K. Glazebrook, C. Jackson, O. Lahav, I. Lewis, S. Lumsden, D. Madgwick, J. A. Peacock, B. A. Peterson, I. Price, M. Seaborne and K. Taylor (2001). 'The 2dF Galaxy Redshift Survey: spectra and redshifts'. *MNRAS* **328**, 1039–1063.

Collet, C. and F. Murtagh (2004). 'Multiband segmentation based on a hierarchical Markov model'. *Pattern Recognition* **37**(12), 2337–2347.

Connors, A. (1997). Periodic Analysis of Time Series Data as an Exemplar of Bayesian Methods. In V. Di Gesu, M. J. B. Duff, A. Heck, M. C. Maccarone, L. Scarsi and H. U. Zimmerman (Eds.). 'Data Analysis in Astronomy IV'. pp. 251–+.

Cox, R. T. (1946). 'Probability, frequency and reasonable expectation'. *Am. J. Phys.* **14**, 1–13.

Cristiani, S., I. Appenzeller, S. Arnouts, M. Nonino, A. Aragón-Salamanca, C. Benoist, L. da Costa, M. Dennefeld, R. Rengelink, A. Renzini, T. Szeifert and S. White (2000). 'The first VLT FORS1 spectra of Lyman-break candidates in the HDF-S and AXAF Deep Field'. *A&A* **359**, 489–492.

Croom, S. M., B. J. Boyle, T. Shanks, R. J. Smith, L. Miller and N. S. Loaring (2000). Large-scale structure in the 2dF QSO Redshift Survey. In 'Bulletin of the American Astronomical Society'. Vol. 32 of *Bulletin of the American Astronomical Society*. pp. 1561–+.

Croom, S. M., S. J. Warren and K. Glazebrook (2001). 'A small-area faint KX redshift survey for QSOs in the ESO Imaging Survey Chandra Deep Field South'. *MNRAS* **328**, 150–158.

Cruddace, R. G., G. R. Hasinger and J. H. Schmitt (1988). The application of a maximum likelihood analysis to detection of sources in the ROSAT data base. In F. Murtagh and A. Heck (Eds.). 'Astronomy from large databases: Scientific objectives and methodological approaches; Proceedings of the Conference, Garching, Federal Republic of Germany, Oct. 12-14, 1987 (A89-27176 10-82). Garching, Federal Republic of Germany, European Southern Observatory, 1988, p. 177-182.'. pp. 177–182.

Cutri, R. M., M. F. Skrutskie, S. van Dyk, C. A. Beichman, J. M. Carpenter, T. Chester, L. Cambresy, T. Evans, J. Fowler, J. Gizis, E. Howard, J. Huchra, T. Jarrett, E. L. Kopan, J. D. Kirkpatrick, R. M. Light, K. A. Marsh, H. McCallon, S. Schneider, R. Stiening, M. Sykes, M. Weinberg, W. A. Wheaton, S. Wheelock and N. Zacarias (2003). *2MASS All Sky Catalog of point sources.*. The IRSA 2MASS All-Sky Point Source Catalog, NASA/IPAC Infrared Science Archive. http://irsa.ipac.caltech.edu/applications/Gator/.

Damiani, F., A. Maggio, G. Micela and S. Sciortino (1997). 'A Method Based on Wavelet Transforms for Source Detection in Photon-counting Detector Images. I. Theory and General Properties'. *ApJ* **483**, 350–+.

Dar, A. (2007). Cosmic ray origin of the diffuse gamma-ray background radiation. In N. P. B. P. Supplements (Ed.). 'Cosmic Ray International Seminars'. Vol. 165. pp. 103–109.

De Propris, R., W. J. Couch, M. Colless, G. B. Dalton, C. Collins, C. M. Baugh, J. Bland-Hawthorn, T. Bridges, R. Cannon, S. Cole, N. Cross, K. Deeley, S. P. Driver, G. Efstathiou, R. S. Ellis, C. S. Frenk, K. Glazebrook, C. Jackson, O. Lahav, I. Lewis, S. Lumsden, S. Maddox, D. Madgwick, S. Moody, P. Norberg, J. A. Peacock, W. Percival, B. A. Peterson, W. Sutherland and K. Taylor (2002). 'The 2dF Galaxy Redshift Survey: a targeted study of catalogued clusters of galaxies'. *MNRAS* **329**, 87–101.

Delampady, M. and J.O. Berger (1990). 'Lower bounds on posterior probabilities for multinomial and chi-squared tests'. *Ann. Statist.* **18**, 1295–1316.

D'Elia, V., F. Fiore, S. Mathur and F. Cocchia (2008). 'The candidate filament close to the 3C 295 galaxy cluster: optical and X-ray spectroscopy'. *A&A* **484**, 303–309.

Diaferio, A., S. Schindler and K. Dolag (2008). 'Clusters of Galaxies: Setting the Stage'. *Space Science Reviews* **134**, 7–24.

Dickey, J. M. and F. J. Lockman (1990). 'H I in the Galaxy'. *ARA&A* **28**, 215–261.

Dickinson, M., D. Stern, M. Giavalisco, H. C. Ferguson, Z. Tsvetanov, R. Chornock, S. Cristiani, S. Dawson, A. Dey, A. V. Filippenko, L. A. Moustakas, M. Nonino, C. Papovich, S. Ravindranath, A. Riess, P. Rosati, H. Spinrad and E. Vanzella (2004). 'Color-selected Galaxies at z ˜ 6 in the Great Observatories Origins Deep Survey'. *ApJL* **600**, L99–L102.

Dickinson, M., M. Giavalisco and The Goods Team (2003). The Great Observatories Origins Deep Survey. In R. Bender and A. Renzini (Eds.). 'The Mass of Galaxies at Low and High Redshift'. pp. 324–+.

Dierckx, P. (1995). *Curve and surface fitting with splines*. Monographs on Numerical Analysis, Oxford: Clarendon.

Doherty, M., A. J. Bunker, R. S. Ellis and P. J. McCarthy (2005). 'The Las Campanas Infrared Survey - V. Keck spectroscopy of a large sample of extremely red objects'. *MNRAS* **361**, 525–549.

Dose, V. (2003). 'Bayesian inference in physics: case studies'. *Reports of Progress in Physics* **66**, 1421–1461.

Dose, V., R. Preuss and W. Von Der Linden (1998). 'Dimensionally constrained energy confinement analysis of W7-AS data'. *Nuclear Fusion* **38**, 571–583.

Downes, R., R. F. Webbink and M. M. Shara (1997). 'A Catalog and Atlas of Cataclysmic Variables-Second Edition'. *PASP* **109**, 345–440.

Draper, A. R. and D. R. Ballantyne (2009). 'Balancing the Cosmic Energy Budget: The Cosmic X-ray Background, Blazars and the Compton Thick AGN Fraction'. *ArXiv e-prints*.

Duchon, J. (1975). 'Fonctions splines et vecteurs aleatoires'. *Tech. Report 213, Seminaire d'Analyse Numerique, Universite Scientifiquew et Medical, Grenoble*.

Duchon, J. (1976). 'Fonctions-Spline et Esperances Conditionnelles de Champs Gaussiens'. *Ann. Sci. Univ. Clermont Ferrand II Math.* **14**, 19–27.

Duchon, J. (1977). Splines Minimizing Rotation-Invariant Semi-Norms in Sovolev Spaces. In W. Schempp and K. Zeller (Eds.). 'Constructive Theory of Functions of Several Variables'. pp. 85–100.

Eadie, W. T., D. Drijard, F. E. James, M. Roos and B. Sadoulet (1982). *Statistical Methods in experimental Physics*. Norh-Holland Publishing Company.

Ebeling, H., A. C. Edge, H. Bohringer, S. W. Allen, C. S. Crawford, A. C. Fabian, W. Voges and J. P. Huchra (1998). 'The ROSAT Brightest Cluster Sample - I. The compilation of the sample and the cluster log N-log S distribution'. *MNRAS* **301**, 881–914.

Ebeling, H., A. C. Edge, S. W. Allen, C. S. Crawford, A. C. Fabian and J. P. Huchra (2000). 'The ROSAT Brightest Cluster Sample - IV. The extended sample'. *MNRAS* **318**, 333–340.

Ebeling, H. and G. Wiedenmann (1993). 'Detecting structure in two dimensions combining Voronoi tessellation and percolation'. *Phys. Rev. E* **47**, 704–710.

Ebeling, H., W. Voges and H. Boehringer (1994). 'X-ray emission from Hickson's compact groups of galaxies: Results from the ROSAT All-Sky Survey'. *ApJ* **436**, 44–55.

Ebisawa, K., G. Bourban, A. Bodaghee, N. Mowlavi and T. J.-L. Courvoisier (2003). 'High-energy sources before INTEGRAL. INTEGRAL reference catalog'. *A&A* **411**, L59–L62.

Everitt, B. S. and D. J. Hand (1981). *Finite Mixture Distributions*. Chapman and Hall, London.

Fan, X., M. A. Strauss, D. P. Schneider and J. E. Gunn (2001). Quasars in the Sloan Digital Sky Survey. In S. Cristiani, A. Renzini and R. E. Williams (Eds.). 'Deep Fields'. pp. 277–+.

Finoguenov, A., L. Guzzo, G. Hasinger, N. Z. Scoville, H. Aussel, H. Böhringer, M. Brusa, P. Capak, N. Cappelluti, A. Comastri, S. Giodini, R. E. Griffiths, C. Impey, A. M. Koekemoer, J.-P. Kneib, A. Leauthaud, O. Le Fèvre, S. Lilly, V. Mainieri, R. Massey, H. J. McCracken, B. Mobasher, T. Murayama, J. A. Peacock, I. Sakelliou, E. Schinnerer, J. D. Silverman, V. Smolčić, Y. Taniguchi, L. Tasca, J. E. Taylor, J. R. Trump and G. Zamorani (2007). 'The XMM-Newton Wide-Field Survey in the COSMOS Field: Statistical Properties of Clusters of Galaxies'. *ApJS* **172**, 182–195.

Fischer, R., A. Dinklage and E. Pasch (2003). 'Bayesian modelling of fusion diagnostics'. *Plasma Physics and Controlled Fusion* **45**, 1095–1111.

Fischer, R. and A. Dinklage (2004). 'Integrated data analysis of fusion diagnostics by means of the Bayesian probability theory'. *Review of Scientific Instruments* **75**, 4237–4239.

Fischer, R. and A. Dinklage (2007). The concept of Integrated Data Analysis of complementary experiments. In K. H. Knuth, A. Caticha, A. Giffin and C. C. Rodríguez (Eds.). 'Bayesian Inference and Maximum Entropy Methods in Science and Engineering'. Vol. 954 of *American Institute of Physics Conference Series*. pp. 195–202.

Fischer, R. and V. Dose (2002). Physical mixture modeling with unknown number of components. In R.-L. Fry (Ed.). 'AIP Conf. Proc. 617: Bayesian Inference and Maximum Entropy Methods in Science and Engineering'. pp. 143–154.

Fischer, R., K. M. Hanson, V. Dose and W. von der Linden (2000). 'Background estimation in experimental spectra'. *Phys. Rev. E* **61**, 1152–1160.

Fischer, R., K. M. Hanson, V. Dose and W. von der Linden (2001). Bayesian background estimation. In J. T. Rychert, G. J. Erickson and C. R. Smith (Eds.). 'Bayesian Inference and Maximum Entropy Methods in Science and Engineering'. Vol. 567 of *AIP Conf. Proc.*. Amer. Inst. Phys.. Melville, NY. pp. 193–212.

Fischer, R., M. Mayer, W. von der Linden and V. Dose (1997). 'Enhancement of the energy resolution in ion-beam experimentswith the maximum-entropy method'. *Phys. Rev. E* **55**, 6667–6673.

Freeman, P. E., V. Kashyap, R. Rosner and D. Q. Lamb (2002). 'A Wavelet-Based Algorithm for the Spatial Analysis of Poisson Data'. *ApJS* **138**, 185–218.

Fukugita, M. and P. J. E. Peebles (2004). 'The Cosmic Energy Inventory'. *ApJ* **616**, 643–668.

Gehrels, N. (1986). 'Confidence limits for small numbers of events in astrophysical data'. *ApJ* **303**, 336–346.

Gelman, A., J. B. Carlin, H. S. Stern and D. B. Rubin (1995). *Bayesian Data Analysis*. Chapman & Hall, London.

Gelman, A., J. B. Carlin, H. S. Stern and D. B. Rubin (2004). *Bayesian Data Analysis*. Chapman & Hall, London.

Giacconi, R., A. Zirm, J. Wang, P. Rosati, M. Nonino, P. Tozzi, R. Gilli, V. Mainieri, G. Hasinger, L. Kewley, J. Bergeron, S. Borgani, R. Gilmozzi, N. Grogin, A. Koekemoer, E. Schreier, W. Zheng and C. Norman (2002*a*). 'Chandra Deep Field South. 1 Ms catalog (Giacconi+, 2002)'. *VizieR Online Data Catalog* **213**, 90369–+.

Giacconi, R., A. Zirm, J. Wang, P. Rosati, M. Nonino, P. Tozzi, R. Gilli, V. Mainieri, G. Hasinger, L. Kewley, J. Bergeron, S. Borgani, R. Gilmozzi, N. Grogin, A. Koekemoer, E. Schreier, W. Zheng and C. Norman (2002*b*). 'Chandra Deep Field South: The 1 Ms Catalog'. *ApJS* **139**, 369–410.

Giacconi, R., H. Gursky, F. R. Paolini and B. B. Rossi (1962). 'Evidence for x Rays From Sources Outside the Solar System'. *Physical Review Letters* **9**, 439–443.

Giacconi, R., P. Rosati, P. Tozzi, M. Nonino, G. Hasinger, C. Norman, J. Bergeron, S. Borgani, R. Gilli, R. Gilmozzi and W. Zheng (2001). 'First Results from the X-Ray and Optical Survey of the Chandra Deep Field South'. *ApJ* **551**, 624–634.

Gilli, R., A. Cimatti, E. Daddi, G. Hasinger, P. Rosati, G. Szokoly, P. Tozzi, J. Bergeron, S. Borgani, R. Giacconi, L. Kewley, V. Mainieri, M. Mignoli, M. Nonino, C. Norman, J. Wang, G. Zamorani, W. Zheng and A. Zirm (2003). 'Tracing the Large-Scale Structure in the Chandra Deep Field South'. *ApJ* **592**, 721–727.

Gilliland, R. L. (1992). Details of Noise Sources and Reduction Processes. In S. B. Howell (Ed.). 'Astronomical CCD Observing and Reduction Techniques'. Vol. 23 of *Astronomical Society of the Pacific Conference Series*. pp. 68–+.

Gioia, I. M., T. Maccacaro, R. E. Schild, A. Wolter, J. T. Stocke, S. L. Morris and J. P. Henry (1990). 'The Einstein Observatory Extended Medium-Sensitivity Survey. I - X-ray data and analysis'. *ApJS* **72**, 567–619.

Giommi, P., G. Tagliaferri, K. Beuermann, G. Branduardi-Raymont, R. Brissenden, U. Graser, K. O. Mason, J. D. P. Mittaz, P. Murdin, G. Pooley, H.-C. Thomas and I. Tuohy (1991). 'The EXOSAT high Galactic latitude survey'. *ApJ* **378**, 77–92.

Grazian, A., A. Fontana, C. de Santis, M. Nonino, S. Salimbeni, E. Giallongo, S. Cristiani, S. Gallozzi and E. Vanzella (2006). 'The GOODS-MUSIC sample: a multicolour catalog of near-IR selected galaxies in the GOODS-South field'. *A&A* **449**, 951–968.

Gregory, P. C. (2005). *Bayesian Logical Data Analysis for the Physical Sciences: A Comparative Approach with 'Mathematica' Support*. Cambridge University Press, Cambridge, UK.

Gregory, P. C. and T. J. Loredo (1992). 'A new method for the detection of a periodic signal of unknown shape and period'. *ApJ* **398**, 146–168.

Groenewegen, M. A. T., L. Girardi, E. Hatziminaoglou, C. Benoist, L. F. Olsen, L. da Costa, S. Arnouts, R. Madejsky, R. P. Mignani, C. Rité, G. Sikkema, R. Slijkhuis and B. Vandame (2002). 'ESO Imaging Survey. The stellar catalogue in the Chandra deep field south'. *A&A* **392**, 741–755.

Grogin, N. A., A. M. Koekemoer, E. J. Schreier, J. Bergeron, R. Giacconi, G. Hasinger, L. Kewley, C. Norman, P. Rosati, P. Tozzi and A. Zirm (2003). 'Hubble Space Telescope Imaging in the Chandra Deep Field-South. III. Quantitative Morphology of the 1 Million Second Chandra Counterparts and Comparison with the Field Population'. *ApJ* **595**, 685–697.

Gruber, R., T. Boller, J. Englhauser, F. Haberl, W. Pietsch, W. Voges and H.-U. Zimmermann (1997). Producing the ROSAT Bright Source Catalogue: The Screening Process. In V. Di Gesu, M. J. B. Duff, A. Heck, M. C. Maccarone, L. Scarsi, & H. U. Zimmerman (Ed.). 'Data Analysis in Astronomy IV'. pp. 197–+.

Guglielmetti, F., R. Fischer and V. Dose (2004*a*). Mixture Modeling for Background and Sources Separation in x-ray Astronomical Images. In R. Fischer, R. Preuss and U. von Toussaint (Eds.). 'American Institute of Physics Conference Series'. pp. 111–118.

Guglielmetti, F., R. Fischer and V. Dose (2009). 'Background-source separation in astronomical images with Bayesian probability theory - I. The method'. *MNRAS* **396**, 165–190.

Guglielmetti, F., R. Fischer, P. Rosati, V. Mainieri and V. Dose (2005). Searching Faint and Extended Sources in the X-ray Universe. In K. H. Knuth, A. E. Abbas, R. D. Morris and J. P. Castle (Eds.). 'AIP Conf. Proc. 803: Bayesian Inference and Maximum Entropy Methods in Science and Engineering'. pp. 162–169.

Guglielmetti, F., R. Fischer, W. Voges, G. Boese and V. Dose (2004*b*). Source Detection and Background Estimation with Bayesian Inference. In V. Schoenfelder, G. Lichti

and C. Winkler (Eds.). 'ESA SP-552: 5th INTEGRAL Workshop on the INTEGRAL Universe'. pp. 847–+.

Guglielmetti, F., W. Voges, R. Fischer, G. Boese and V. Dose (2004*c*). Source Detection with Bayesian Inference on ROSAT All-Sky Survey Data Sample. In F. Ochsenbein, M. G. Allen and D. Egret (Eds.). 'ASP Conf. Ser. 314: Astronomical Data Analysis Software and Systems (ADASS) XIII'. pp. 253–+.

Gupta, A. and M. Galeazzi (2009). 'Contribution of Unresolved Point Sources to the Diffuse X-ray Background Below 1 keV'. *ApJ* **702**, 270–276.

Guzzo, L., P. Schuecker, H. Boehringer, C. A. Collins, A. Ortiz-Gil, S. de Grandi, A. C. Edge, D. M. Neumann, S. Schindler, C. Altucci and P. A. Shaver (2009). 'REFLEX galaxies redshifts (Guzzo+, 2009)'. *VizieR Online Data Catalog* **349**, 90357–+.

Hao, L., M. A. Strauss, C. A. Tremonti, D. J. Schlegel, T. M. Heckman, G. Kauffmann, M. R. Blanton, X. Fan, J. E. Gunn, P. B. Hall, Ž. Ivezić, G. R. Knapp, J. H. Krolik, R. H. Lupton, G. T. Richards, D. P. Schneider, I. V. Strateva, N. L. Zakamska, J. Brinkmann, R. J. Brunner and G. P. Szokoly (2005). 'Active Galactic Nuclei in the Sloan Digital Sky Survey. I. Sample Selection'. *AJ* **129**, 1783–1794.

Harnden, Jr., F. R., D. G. Fabricant, D. E. Harris and J. Schwarz (1984). 'Scientific Specification of the Data Analysis System for the EINSTEIN Observatory (HEAO-2) Imaging Proportional Counter'. *SAO Special Report*.

Hasinger, G. (1985). 'Detection of X-ray sources with ROSAT'. *Bulletin d'Information du Centre de Donnees Stellaires* **28**, 87–+.

Hasinger, G. (2002). Evolution of X-Ray Sources at High Redshift. In M. Gilfanov, R. Sunyeav and E. Churazov (Eds.). 'Lighthouses of the Universe: The Most Luminous Celestial Objects and Their Use for Cosmology'. pp. 555–+.

Hasinger, G., H. M. Johnston and F. Verbunt (1994). 'Discovery of multiple X-ray sources in 47 Tucanae'. *A&A* **288**, 466–471.

Hasinger, G., J. Bergeron, V. Mainieri, P. Rosati, G. Szokoly and Cdfs Team (2002). 'Understanding the sources of the X-ray background: VLT identifications in the Chandra/XMM-Newton Deep Field South'. *The Messenger* **108**, 11–16.

Hasinger, G., N. Cappelluti, H. Brunner, M. Brusa, A. Comastri, M. Elvis, A. Finoguenov, F. Fiore, A. Franceschini, R. Gilli, R. E. Griffiths, I. Lehmann, V. Mainieri, G. Matt, I. Matute, T. Miyaji, S. Molendi, S. Paltani, D. B. Sanders, N. Scoville, L. Tresse, C. M. Urry, P. Vettolani and G. Zamorani (2007). 'The XMM-Newton Wide-Field Survey in the COSMOS Field. I. Survey Description'. *ApJS* **172**, 29–37.

Henry, J. P., C. R. Mullis, W. Voges, H. Böhringer, U. G. Briel, I. M. Gioia and J. P. Huchra (2006). 'The ROSAT North Ecliptic Pole Survey: The X-Ray Catalog'. *ApJS* **162**, 304–328.

Hobson, M. P. and C. McLachlan (2003). 'A Bayesian approach to discrete object detection in astronomical data sets'. *MNRAS* **338**, 765–784.

Hogg, D. W., I. K. Baldry, M. R. Blanton and D. J. Eisenstein (2002). 'The K correction'. *ArXiv Astrophysics e-prints*.

Hopkins, A. M., C. J. Miller, A. J. Connolly, C. Genovese, R. C. Nichol and L. Wasserman (2002). 'A New Source Detection Algorithm Using the False-Discovery Rate'. *AJ* **123**, 1086–1094.

Hubbard, R. and M. J. Bayarri (2003). 'Confusion Over Measures of Evidence (p's) Versus Errors (α's) in Classical Statistical Testing'. *The American Statistician* **57**, 171–182.

Inoue, Y., T. Totani and Y. Ueda (2008). 'The Cosmic MeV Gamma-Ray Background and Hard X-Ray Spectra of Active Galactic Nuclei: Implications for the Origin of Hot AGN Coronae'. *ApJL* **672**, L5–L8.

Jansen, F., D. Lumb, B. Altieri, J. Clavel, M. Ehle, C. Erd, C. Gabriel, M. Guainazzi, P. Gondoin, R. Much, R. Munoz, M. Santos, N. Schartel, D. Texier and G. Vacanti (2001). 'XMM-Newton observatory. I. The spacecraft and operations'. *A&A* **365**, L1–L6.

Jarrett, T. H., T. Chester, R. Cutri, S. Schneider, M. Skrutskie and J. P. Huchra (2000). '2MASS Extended Source Catalog: Overview and Algorithms'. *AJ* **119**, 2498–2531.

Jaynes, E. T. (1968). 'Prior Probabilities'. *IEEE Transactions on Systems Science and Cybernetics* **4**, 227–241.

Jaynes, E. T. (1984). Prior Information and Ambiguity in Inverse Problems. In D. W. McLaughlin (Ed.). 'Inverse Problems'. Vol. 14 of *SIAM-AMS Proceedings*. Am. Math. Soc., Providence, RI. p. 151.

Jaynes, E. T. (2003). *Probability Theory the Logic of Science*. Cambridge University Press.

Jeffreys, H. (1938). 'The correction of frequencies for a known standard error of observation'. *MNRAS* **98**, 190–+.

Jeffreys, H. (1961). *Theory of Probability*. Clarendon Press, Oxford.

Jeffreys, W. and J.O. Berger (1992). 'Ockham's razor and bayesian analysis'. *American Scientist* **80**, 64–72.

Jones, C. and W. Forman (1984). 'The structure of clusters of galaxies observed with Einstein'. *ApJ* **276**, 38–55.

Jones, C. and W. Forman (1999). 'Einstein Observatory Images of Clusters of Galaxies'. *ApJ* **511**, 65–83.

Kalberla, P. M. W., W. B. Burton, D. Hartmann, E. M. Arnal, E. Bajaja, R. Morras and W. G. L. Pöppel (2005). 'The Leiden/Argentine/Bonn (LAB) Survey of Galactic HI. Final data release of the combined LDS and IAR surveys with improved stray-radiation corrections'. *A&A* **440**, 775–782.

Kass, R. and L.A. Wasserman (1996). 'The selection of prior distributions by formal rules'. *Journal of the American Statistical Association* **91**, 1343–1370.

Kass, R. E. and Adrian E. Raftery (1995). 'Bayes Factors'. *Journal of the American Statistical Association* **90**(430), 773–795.

Kass, R. E., L. Tierney and J.B. Kadane (1990). The validity of posterior expansions based on Laplace's method. In S. Geisser, J. S. Hodges, S. J. Press and A. Zellner (Eds.). 'Essays in Honor of George Bernard'. Amsterdam: North Holland. pp. 473–488.

Kendall, M. and A. Stuart (1979). *The Advanced Theory of Statistics. Vol. 2.*. Griffin, London.

Kerber, F., R. P. Mignani, F. Guglielmetti and A. Wicenec (2003). 'Galactic Planetary Nebulae and their central stars. I. An accurate and homogeneous set of coordinates'. *A&A* **408**, 1029–1035.

King, I. (1962). 'The structure of star clusters. I. an empirical density law'. *AJ* **67**, 471–+.

Kocevski, D. D. and H. Ebeling (2006). 'On the Origin of the Local Group's Peculiar Velocity'. *ApJ* **645**, 1043–1053.

Kolaczyk, E. D. and D. D. Dixon (2000). 'Nonparametric Estimation of Intensity Maps Using Haar Wavelets and Poisson Noise Characteristics'. *ApJ* **534**, 490–505.

Laidler, V. G., C. Papovich, N. A. Grogin, R. Idzi, M. Dickinson, H. C. Ferguson, B. Hilbert, K. Clubb and S. Ravindranath (2007). 'TFIT: A Photometry Package Using Prior Information for Mixed-Resolution Data Sets'. *PASP* **119**, 1325–1344.

Laplace, P. S. (1812). *Theorie Analytique des Probabilities*. Courcier, Paris.

Lasker, B. M., M. G. Lattanzi, B. J. McLean, B. Bucciarelli, R. Drimmel, J. Garcia, G. Greene, F. Guglielmetti, C. Hanley, G. Hawkins, V. G. Laidler, C. Loomis, M. Meakes, R. Mignani, R. Morbidelli, J. Morrison, R. Pannunzio, A. Rosenberg, M. Sarasso, R. L. Smart, A. Spagna, C. R. Sturch, A. Volpicelli, R. L. White, D. Wolfe and A. Zacchei (2008). 'The Second-Generation Guide Star Catalog: Description and Properties'. *AJ* **136**, 735–766.

Lazzati, D., S. Campana, P. Rosati, M. R. Panzera and G. Tagliaferri (1999). 'The Brera Multiscale Wavelet ROSAT HRI Source Catalog. I. The Algorithm'. *ApJ* **524**, 414–422.

Le Fèvre, O., G. Vettolani, B. Garilli, L. Tresse, D. Bottini, V. Le Brun, D. Maccagni, J. P. Picat, R. Scaramella, M. Scodeggio, A. Zanichelli, C. Adami, M. Arnaboldi, S. Arnouts, S. Bardelli, M. Bolzonella, A. Cappi, S. Charlot, P. Ciliegi, T. Contini, S. Foucaud, P. Franzetti, I. Gavignaud, L. Guzzo, O. Ilbert, A. Iovino, H. J. McCracken, B. Marano, C. Marinoni, G. Mathez, A. Mazure, B. Meneux, R. Merighi, S. Paltani, R. Pellò, A. Pollo, L. Pozzetti, M. Radovich, G. Zamorani, E. Zucca, M. Bondi, A. Bongiorno, G. Busarello, F. Lamareille, Y. Mellier, P. Merluzzi, V. Ripepi and D. Rizzo (2005). 'The VIMOS VLT deep survey. First epoch VVDS-deep survey: 11 564 spectra with $17.5 \leq IAB \leq 24$, and the redshift distribution over $0 \leq z \leq 5$'. *A&A* **439**, 845–862.

Lehmer, B. D., W. N. Brandt, D. M. Alexander, F. E. Bauer, D. P. Schneider, P. Tozzi, J. Bergeron, G. P. Garmire, R. Giacconi, R. Gilli, G. Hasinger, A. E. Hornschemeier, A. M. Koekemoer, V. Mainieri, T. Miyaji, M. Nonino, P. Rosati, J. D. Silverman, G. Szokoly and C. Vignali (2005). 'The Extended Chandra Deep Field-South Survey: Chandra Point-Source Catalogs'. *ApJS* **161**, 21–40.

Lieu, R. and M. Bonamente (2009). 'Soft X-Ray Excess of Clusters: A Thermal Filament Model and the Strong Lensing of Background Galaxy Groups'. *ApJ* **698**, 1301–1306.

Linnemann, J. (2003). Measures of Significance in HEP and Astrophysics. In L. Lyons, R. Mount and R. Reitmeyer (Eds.). 'Statistical Problems in Particle Physics, Astrophysics, and Cosmology'. pp. 35–+.

Loredo, T. J. (1990). From Laplace to Supernova SN 1987A: Bayesian Inference in Astrophysics. In P. F. Fougere (Ed.). 'Maximum Entropy and Bayesian Methods'. Kluwer Academic Publishers, Dordrecht, The Netherlands. pp. 81–142.

Loredo, T. J. (1992). The Promise of Bayesian Inference for Astrophysics. In E. D. Feigelson and G. J. Babu (Eds.). 'Statistical Challenges in Modern Astronomy'. Springer-Verlag, New York. pp. 275–297.

Loredo, T. J. (1995). 'From Laplace to Supernova SN 1987A: Bayesian Inference in Astrophysics'. *Ph.D. Thesis*.

Loredo, T. J. (1999). Computational Technology for Bayesian Inference. In 'Astronomical Society of the Pacific Conference Series'. pp. 297–+.

Loredo, T. J. (2004). Accounting for Source Uncertainties in Analyses of Astronomical Survey Data. In R. Fischer, R. Preuss, & U. von Toussaint (Ed.). 'Bayesian Inference and Maximum Entropy Methods in Science and Engineering'. Vol. 735 of *American Institute of Physics Conference Series*. pp. 195–206.

Loredo, T. J. (2007). Analyzing Data from Astronomical Surveys: Issues and Directions. In G. J. Babu and E. D. Feigelson (Eds.). 'Statistical Challenges in Modern Astronomy IV'. Vol. 371 of *Astronomical Society of the Pacific Conference Series*. pp. 121–+.

Loredo, T. J. (2009). No Free Lunch: Challenging Problems for Frequentist & Bayesian Approaches. In CosmoStats09, 26-31 July 2009, Ascona, Switzerland. pp. http://www.itp.uzh.ch/cosmostats/talks/Loredo–Cosmostats09.pdf.

Loredo, T. J. and Donald Q. Lamb (2002). 'Bayesian analysis of neutrinos observed from supernova sn 1987a'. *Phys. Rev. D* **65**(6), 063002.

Loredo, T. J., E. E. Flanagan and I. M. Wasserman (1997). 'Bayesian analysis of the polarization of distant radio sources: Limits on cosmological birefringence'. *Phys. Rev. D* **56**, 7507–7512.

Luo, B., F. E. Bauer, W. N. Brandt, D. M. Alexander, B. D. Lehmer, D. P. Schneider, M. Brusa, A. Comastri, A. C. Fabian, A. Finoguenov, R. Gilli, G. Hasinger, A. E. Hornschemeier, A. Koekemoer, V. Mainieri, M. Paolillo, P. Rosati, O. Shemmer, J. D. Silverman, I. Smail, A. T. Steffen and C. Vignali (2008). 'The Chandra Deep Field-South Survey: 2 Ms Source Catalogs'. *ApJS* **179**, 19–36.

Luo, B., F. E. Bauer, W. N. Brandt, D. M. Alexander, B. D. Lehmer, D. P. Schneider, M. Brusa, A. Comastri, A. C. Fabian, A. Finoguenov, R. Gilli, G. Hasinger, A. E. Hornschemeier, A. Koekemoer, V. Mainieri, M. Paolillo, P. Rosati, O. Shemmer, J. D. Silverman, I. Smail, A. T. Steffen and C. Vignali (2009). 'CDFS survey: 2 Ms source catalogs (Luo+, 2008)'. *VizieR Online Data Catalog* **217**, 90019–+.

Massey, P. and G. H. Jacoby (1992). CCD Data: The Good, The Bad, and The Ugly. In S. B. Howell (Ed.). 'Astronomical CCD Observing and Reduction Techniques'. Vol. 23 of *Astronomical Society of the Pacific Conference Series*. pp. 240–+.

Maughan, B. J., L. R. Jones, H. Ebeling, E. Perlman, P. Rosati, C. Frye and C. R. Mullis (2003). 'Chandra X-Ray Analysis of the Massive High-Redshift Galaxy Clusters Cl J1113.1-2615 and Cl J0152.7-1357'. *ApJ* **587**, 589–604.

Meinguet, J. (1979). 'Multivariate Interpolation at Arbitrary Points Made Simple'. *J. Appl. Math. Phys. (ZAMP)* **30**, 292–304.

Mignoli, M., A. Cimatti, G. Zamorani, L. Pozzetti, E. Daddi, A. Renzini, T. Broadhurst, S. Cristiani, S. D'Odorico, A. Fontana, E. Giallongo, R. Gilmozzi, N. Menci and P. Saracco (2005). 'The K20 survey. VII. The spectroscopic catalogue: Spectral properties and evolution of the galaxy population'. *A&A* **437**, 883–897.

Miller, C. J., C. Genovese, R. C. Nichol, L. Wasserman, A. Connolly, D. Reichart, A. Hopkins, J. Schneider and A. Moore (2001). 'Controlling the False-Discovery Rate in Astrophysical Data Analysis'. *AJ* **122**, 3492–3505.

Miyata, E., H. Tsunemi, B. Aschenbach and K. Mori (2001). 'Chandra X-Ray Observatory Study of Vela Shrapnel A'. *ApJL* **559**, L45–L48.

Monet, D. G., S. E. Levine, B. Canzian, H. D. Ables, A. R. Bird, C. C. Dahn, H. H. Guetter, H. C. Harris, A. A. Henden, S. K. Leggett, H. F. Levison, C. B. Luginbuhl, J. Martini, A. K. B. Monet, J. A. Munn, J. R. Pier, A. R. Rhodes, B. Riepe, S. Sell, R. C. Stone, F. J. Vrba, R. L. Walker, G. Westerhout, R. J. Brucato, I. N. Reid, W. Schoening, M. Hartley, M. A. Read and S. B. Tritton (2003). 'The USNO-B Catalog'. *AJ* **125**, 984–993.

Moy, E., P. Barmby, D. Rigopoulou, J.-S. Huang, S. P. Willner and G. G. Fazio (2003). 'H-band observations of the Chandra Deep Field South'. *A&A* **403**, 493–499.

Mukai, K. (1993). 'PIMMS and Viewing: proposal preparation tools'. *Legacy, vol. 3, p.21-31* **3**, 21–31.

Mulchaey, J. S. and A. I. Zabludoff (1998). 'The Properties of Poor Groups of Galaxies. II. X-Ray and Optical Comparisons'. *ApJ* **496**, 73–+.

Mulchaey, J. S., D. S. Davis, R. F. Mushotzky and D. Burstein (1996). 'The Intragroup Medium in Poor Groups of Galaxies'. *ApJ* **456**, 80–+.

Murtagh, F., A. Raftery and J.-L. Starck (2005). 'Bayesian inference for multiband image segmentation via model-based cluster trees'. *Image and Vision Computing* **23**(6), 587 – 596.

Mushotzky, R. (1996). X-ray spectra of clusters and groups.. In H. U. Zimmermann, J. Trümper and H. Yorke (Eds.). 'Roentgenstrahlung from the Universe'. pp. 545–551.

Nandra, K., E. S. Laird, K. Adelberger, J. P. Gardner, R. F. Mushotzky, J. Rhodes, C. C. Steidel, H. I. Teplitz and K. A. Arnaud (2005). 'A deep Chandra survey of the Groth Strip - I. The X-ray data'. *MNRAS* **356**, 568–586.

Neal, R. M. (1992). Bayesian mixture modeling. In C. R. Smith, G. J. Erickson and P. O. Neudorfer (Eds.). 'Maximum Entropy and Bayesian Methods: Proceedings of the 11th nternational Workshop on Maximum Entropy and Bayesian Methods of Statistical Analysis'. Kluwer Academic Publishers, Dordrecht. pp. 197–211.

Ochsenbein, F., P. Bauer and J. Marcout (2000). 'The VizieR database of astronomical catalogues'. *A&AS* **143**, 23–32.

O'Hagan, A. (2000). *Kendall's Advanced Theory of Statistics, Vol. 2B: Bayesian Inference*. Arnold, a member of the Hodder Headline Group.

O'Hagan, A. and J. Forster (2004). *Kendall's advanced theory of statistics. Vol.2B: Bayesian inference*. London: Hodder Arnold.

Pacaud, F., M. Pierre, A. Refregier, A. Gueguen, J.-L. Starck, I. Valtchanov, A. M. Read, B. Altieri, L. Chiappetti, P. Gandhi, O. Garcet, E. Gosset, T. J. Ponman and J. Surdej (2006). 'The XMM Large-Scale Structure survey: the X-ray pipeline and survey selection function'. *MNRAS* **372**, 578–590.

Paolillo, M., E. J. Schreier, R. Giacconi, A. M. Koekemoer and N. A. Grogin (2004). 'Prevalence of X-Ray Variability in the Chandra Deep Field-South'. *ApJ* **611**, 93–106.

Peacock, J. A. (1999). *Cosmological Physics*. Cambridge, UK: Cambridge University Press.

Pierre, M., I. Valtchanov, B. Altieri and et al. (2004). 'The XMM-LSS survey. Survey design and first results.'. *Journal of Cosmology and Astro-Particle Physics* **9**, 11–+.

Popesso, P., M. Dickinson, M. Nonino, E. Vanzella, E. Daddi, R. A. E. Fosbury, H. Kuntschner, V. Mainieri, S. Cristiani, C. Cesarsky, M. Giavalisco, A. Renzini and GOODS Team (2009). 'The great observatories origins deep survey. VLT/VIMOS spectroscopy in the GOODS-south field'. *A&A* **494**, 443–460.

Predehl, P., G. Hasinger, H. Böhringer, U. Briel, H. Brunner, E. Churazov, M. Freyberg, P. Friedrich, E. Kendziorra, D. Lutz, N. Meidinger, M. Pavlinsky, E. Pfeffermann, A. Santangelo, J. Schmitt, P. Schuecker, A. Schwope, M. Steinmetz, L. Strüder, R. Sunyaev and J. Wilms (2006). eROSITA. In 'Society of Photo-Optical Instrumentation Engineers (SPIE) Conference Series'. Vol. 6266 of *Society of Photo-Optical Instrumentation Engineers (SPIE) Conference Series*.

Rasera, Y., R. Teyssier, P. Sizun, M. Cassé, P. Fayet, B. Cordier and J. Paul (2006). 'Soft gamma-ray background and light dark matter annihilation'. *Phys. Rev. E* **73**(10), 103518–+.

Ravikumar, C. D., M. Puech, H. Flores, D. Proust, F. Hammer, M. Lehnert, A. Rawat, P. Amram, C. Balkowski, D. Burgarella, P. Cassata, C. Cesarsky, A. Cimatti, F. Combes, E. Daddi, H. Dannerbauer, S. di Serego Alighieri, D. Elbaz, B. Guiderdoni, A. Kembhavi, Y. C. Liang, L. Pozzetti, D. Vergani, J. Vernet, H. Wozniak and X. Z. Zheng (2007). 'New spectroscopic redshifts from the CDFS and a test of the cosmological relevance of the GOODS-South field'. *A&A* **465**, 1099–1108.

Raymond, J. C. and B. W. Smith (1977). 'Soft X-ray spectrum of a hot plasma'. *ApJS* **35**, 419–439.

Reiprich, T. H. and H. Böhringer (2002). 'The Mass Function of an X-Ray Flux-limited Sample of Galaxy Clusters'. *ApJ* **567**, 716–740.

Rengelink, R. B., Y. Tang, A. G. de Bruyn, G. K. Miley, M. N. Bremer, H. J. A. Roettgering and M. A. R. Bremer (1997). 'The Westerbork Northern Sky Survey (WENSS), I. A 570 square degree Mini-Survey around the North Ecliptic Pole'. *A&AS* **124**, 259–280.

ROSAT Scientific Team (2000). 'ROSAT HRI Pointed Observations (1RXH) (ROSAT Team, 2000)'. *VizieR Online Data Catalog* **9028**, 0–+.

Rosati, P. (1995). Campioni di ammassi di galassie selezionati in banda X. PhD thesis. Università "La Sapienza" di Roma.

Rosati, P., P. Tozzi, R. Giacconi, R. Gilli, G. Hasinger, L. Kewley, V. Mainieri, M. Nonino, C. Norman, G. Szokoly, J. X. Wang, A. Zirm, J. Bergeron, S. Borgani, R. Gilmozzi, N. Grogin, A. Koekemoer, E. Schreier and W. Zheng (2002*a*). 'The Chandra Deep Field-South: The 1 Million Second Exposure'. *ApJ* **566**, 667–674.

Rosati, P., P. Tozzi, R. Gobat, J. S. Santos, M. Nonino, R. Demarco, C. Lidman, C. R. Mullis, V. Strazzullo, H. Böhringer, R. Fassbender, K. Dawson, M. Tanaka, J. Jee, H. Ford, G. Lamer and A. Schwope (2009). 'Multi-wavelength study of XMMU J2235.3-2557: the most massive galaxy cluster at z ¿ 1'. *A&A* **508**, 583–591.

Rosati, P., R. della Ceca, C. Norman and R. Giacconi (1998). 'The ROSAT Deep Cluster Survey: The X-Ray Luminosity Function Out to z=0.8'. *ApJL* **492**, L21+.

Rosati, P., R. della Ceca, R. Burg, C. Norman and R. Giacconi (1995). 'A first determination of the surface density of galaxy clusters at very low x-ray fluxes'. *ApJL* **445**, L11–L14.

Rosati, P., S. Borgani and C. Norman (2002*b*). 'The Evolution of X-ray Clusters of Galaxies'. *ARA&A* **40**, 539–577.

Rosati, P., S. Borgani, R. della Ceca, A. Stanford, P. Eisenhardt and C. Lidman (2000). The Most Distant X-ray Clusters & the Evolution of their Space Density. In M. Plionis and I. Georgantopoulos (Eds.). 'Large Scale Structure in the X-ray Universe, Proceedings of the 20-22 September 1999 Workshop, Santorini, Greece'. pp. 13–+.

Saracco, P., E. Giallongo, S. Cristiani, S. D'Odorico, A. Fontana, A. Iovino, F. Poli and E. Vanzella (2001). 'Deep near-IR observations of the Chandra Deep Field and of the HDF South. Color and number counts'. *A&A* **375**, 1–13.

Savage, R. S. and S. Oliver (2007). 'Bayesian Methods of Astronomical Source Extraction'. *ApJ* **661**, 1339–1346.

Scargle, J. D. (1998). 'Studies in Astronomical Time Series Analysis. V. Bayesian Blocks, a New Method to Analyze Structure in Photon Counting Data'. *ApJ* **504**, 405–+.

Scharf, C. A., L. R. Jones, H. Ebeling, E. Perlman, M. Malkan and G. Wegner (1997). 'The Wide-Angle ROSAT Pointed X-Ray Survey of Galaxies, Groups, and Clusters. I. Method and First Results'. *ApJ* **477**, 79–+.

Schmitt, J. H. M. M. (1991). 'First results from the ROSAT XRT'. *Advances in Space Research* **11**, 115–123.

Schoenberg, I. J. (1964*a*). 'On interpolation by spline functions and its minimum properties'. *Internat. Ser. Numer. Anal.* **5**, 109–129.

Schoenberg, I. J. (1964*b*). 'Spline functions and the problem of graduation'. *Proc. Nat. Acad. Sci. U. S. A.* **52**, 947–950.

Schuecker, P., H. Böhringer and W. Voges (2004). 'Detection of X-ray clusters of galaxies by matching RASS photons and SDSS galaxies within GAVO'. *A&A* **420**, 61–74.

Schwope, A., G. Hasinger, I. Lehmann, R. Schwarz, H. Brunner, S. Neizvestny, A. Ugryumov, Y. Balega, J. Trümper and W. Voges (2000). 'The ROSAT Bright Survey: II. Catalogue of all high-galactic latitude RASS sources with PSPC countrate CR > 0.2 s^{-1}'. *Astronomische Nachrichten* **321**, 1–52.

Sellke, T., M. J. Bayarri and James O. Berger (2001). 'Calibration of p values for testing precise null hypotheses'. *The American Statistician* **55**(1), 62–71.

Shannon, C. E. (1948). 'A mathematical theory of Communication'. *Bell System Technical Journal* **27**, 379–423, 623–656.

Sivia, D. S. (1990). Bayesian Inductive Inference, Maximum Entropy & Neutron Scattering. Lecture notes at Los Alamos Science Summer 1990.

Sivia, D. S. (1996). *Data Analysis: A Bayesian Tutorial*. Clarendon Press, Oxford.

Sivia, D. S. (1997). Dealing with duff data. In Sears, M. and Nedeljkovic, V. and Pendock, N. E. and Sibisi,S. (Ed.). 'MAXENT96: Proc. Maximum Entropy Conf.'. NMB Printers, Port Elizabeth, South Africa. pp. 131–137.

Skellam, J. G. (1946). 'The Frequency Distribution of the Difference Between Two Poisson Variates Belonging to Different Populations'. *Journal of the Royal Statistical Society* **109**, 296.

Slezak, E., A. Bijaoui and G. Mars (1990). 'Identification of structures from galaxy counts - Use of the wavelet transform'. *A&A* **227**, 301–316.

Śliwa, W., A. M. Soltan and M. J. Freyberg (2001). 'The harmonic power spectrum of the soft X-ray background. I. The data analysis'. *A&A* **380**, 397–408.

Snowden, S. L. and M. J. Freyberg (1993). 'The scattered solar X-ray background of the ROSAT PSPC'. *ApJ* **404**, 403–411.

Snowden, S. L., D. McCammon, D. N. Burrows and J. A. Mendenhall (1994). 'Analysis procedures for ROSAT XRT/PSPC observations of extended objects and the diffuse background'. *ApJ* **424**, 714–728.

Spergel, D. N., L. Verde, H. V. Peiris, E. Komatsu, M. R. Nolta, C. L. Bennett, M. Halpern, G. Hinshaw, N. Jarosik, A. Kogut, M. Limon, S. S. Meyer, L. Page, G. S. Tucker, J. L. Weiland, E. Wollack and E. L. Wright (2003). 'First-Year Wilkinson Microwave Anisotropy Probe (WMAP) Observations: Determination of Cosmological Parameters'. *ApJS* **148**, 175–194.

Stanway, E. R., A. J. Bunker, R. G. McMahon, R. S. Ellis, T. Treu and P. J. McCarthy (2004*a*). 'Hubble Space Telescope Imaging and Keck Spectroscopy of z ˜ 6 i-Band Dropout Galaxies in the Advanced Camera for Surveys GOODS Fields'. *ApJ* **607**, 704–720.

Stanway, E. R., K. Glazebrook, A. J. Bunker, R. G. Abraham, I. Hook, J. Rhoads, P. J. McCarthy, B. Boyle, M. Colless, D. Crampton, W. Couch, I. Jørgensen, S. Malhotra, R. Murowinski, K. Roth, S. Savaglio and Z. Tsvetanov (2004*b*). 'Three Lyα Emitters at z ˜ 6: Early GMOS/Gemini Data from the GLARE Project'. *ApJL* **604**, L13–L16.

Starck, J.-L., A. Bijaoui, I. Valtchanov and F. Murtagh (2000). 'A combined approach for object detection and deconvolution'. *A&AS* **147**, 139–149.

Starck, J.-L., A. Llebaria and T. Loredo (2008). 'Guest editorial'. *Statistical Methodology* **5**, D5+.

Starck, J.-L. and F. Murtagh (2006). *Astronomical Image and Data Analysis*. Berlin: Springer.

Starck, J.-L. and M. Pierre (1998). 'Structure detection in low intensity X-ray images'. *A&AS* **128**, 397–407.

Stark, A. A., C. F. Gammie, R. W. Wilson, J. Bally, R. A. Linke, C. Heiles and M. Hurwitz (1992). 'The Bell Laboratories H I survey'. *ApJS* **79**, 77–104.

Stewart, I. M. (2006). 'Matched filters for source detection in the Poissonian noise regime'. *A&A* **454**, 997–1009.

Stewart, I. M. (2009). 'Maximum-likelihood detection of sources among Poissonian noise'. *A&A* **495**, 989–1003.

Strolger, L.-G. e. a. (2004). 'The Hubble Higher z Supernova Search: Supernovae to z ˜ 1.6 and Constraints on Type Ia Progenitor Models'. *ApJ* **613**, 200–223.

Strong, A. W. (2003). 'Maximum Entropy imaging with INTEGRAL/SPI data'. *A&A* **411**, L127–L129.

Suchkov, A. A., R. J. Hanisch, W. Voges and T. M. Heckman (2006). 'Sloan Digital Sky Survey Active Galactic Nuclei with X-Ray Emission from ROSAT PSPC Pointed Observations'. *AJ* **132**, 1475–1484.

Szalay, A. S., A. J. Connolly and G. P. Szokoly (1999). 'Simultaneous Multicolor Detection of Faint Galaxies in the Hubble Deep Field'. *AJ* **117**, 68–74.

Szokoly, G. P., J. Bergeron, G. Hasinger, I. Lehmann, L. Kewley, V. Mainieri, M. Nonino, P. Rosati, R. Giacconi, R. Gilli, R. Gilmozzi, C. Norman, M. Romaniello, E. Schreier, P. Tozzi, J. X. Wang, W. Zheng and A. Zirm (2004). 'The Chandra Deep Field-South: Optical Spectroscopy. I.'. *ApJS* **155**, 271–349.

Tanaka, M., A. Finoguenov and Y. Ueda (2010). 'A Spectroscopically Confirmed X-ray Cluster at z = 1.62 with a Possible Companion in the Subaru/XMM-Newton Deep Field'. *ApJL* **716**, L152–L156.

Tarantola, A. (1987). *Inverse problem theory. Methods for data fitting and model parameter estimation*. Elsevier.

The, C. D. (2005). 'The DENIS database (DENIS Consortium, 2005)'. *VizieR Online Data Catalog* **2263**, 0–+.

Tikhonov, A. N. (1992). *Ill-Posed Problems in Natural Sciences*. Moscow: TVP Science.

Tozzi, P., P. Rosati, M. Nonino, J. Bergeron, S. Borgani, R. Gilli, R. Gilmozzi, G. Hasinger, N. Grogin, L. Kewley, A. Koekemoer, C. Norman, E. Schreier, G. Szokoly, J. X. Wang, W. Zheng, A. Zirm and R. Giacconi (2001). 'New Results from the X-Ray and Optical Survey of the Chandra Deep Field-South: The 300 Kilosecond Exposure. II.'. *ApJ* **562**, 42–51.

Valtchanov, I., M. Pierre and R. Gastaud (2001). 'Comparison of source detection procedures for XMM-Newton images'. *A&A* **370**, 689–706.

van der Wel, A., M. Franx, P. G. van Dokkum and H.-W. Rix (2004). 'The Fundamental Plane of Field Early-Type Galaxies at z = 1'. *ApJL* **601**, L5–L8.

van der Woerd, H. (1987). 'X-ray emission from non-magnetic cataclysmic variables'. *Ap&SS* **130**, 225–233.

Vanden Berk, D. E., J. Shen, C.-W. Yip, D. P. Schneider, A. J. Connolly, R. E. Burton, S. Jester, P. B. Hall, A. S. Szalay and J. Brinkmann (2006). 'Spectral Decomposition of Broad-Line AGNs and Host Galaxies'. *AJ* **131**, 84–99.

Vanzella, E., S. Cristiani, M. Dickinson, M. Giavalisco, H. Kuntschner, J. Haase, M. Nonino, P. Rosati, C. Cesarsky, H. C. Ferguson, R. A. E. Fosbury, A. Grazian, L. A. Moustakas, A. Rettura, P. Popesso, A. Renzini, D. Stern and The Goods Team (2008). 'The great observatories origins deep survey. VLT/FORS2 spectroscopy in the GOODS-South field: Part III'. *A&A* **478**, 83–92.

Vikhlinin, A., B. R. McNamara, W. Forman, C. Jones, H. Quintana and A. Hornstrup (1998*a*). 'A Catalog of 200 Galaxy Clusters Serendipitously Detected in the ROSAT PSPC Pointed Observations'. *ApJ* **502**, 558–+.

Vikhlinin, A., B. R. McNamara, W. Forman, C. Jones, H. Quintana and A. Hornstrup (1998*b*). 'Evolution of Cluster X-Ray Luminosities and Radii: Results from the 160 Square Degree ROSAT Survey'. *ApJL* **498**, L21+.

Vikhlinin, A., W. Forman, C. Jones and S. Murray (1995). 'Matched Filter Source Detection Applied to the ROSAT PSPC and the Determination of the Number-Flux Relation'. *ApJ* **451**, 542–+.

Virani, S. N., E. Treister, C. M. Urry and E. Gawiser (2006). 'The Extended Chandra Deep Field-South Survey: X-Ray Point-Source Catalog'. *AJ* **131**, 2373–2382.

Voges, W. and T. Boller (1998). 'X-ray variability study of ROSAT sources'. *Astronomische Nachrichten* **319**, 3–6.

Voges, W., B. Aschenbach, T. Boller, H. Bräuninger, U. Briel, W. Burkert, K. Dennerl, J. Englhauser, R. Gruber, F. Haberl, G. Hartner, G. Hasinger, M. Kürster, E. Pfeffermann, W. Pietsch, P. Predehl, C. Rosso, J. H. M. M. Schmitt, J. Trümper and H. U. Zimmermann (1999). 'The ROSAT all-sky survey bright source catalogue'. *A&A* **349**, 389–405.

Voges, W., B. Aschenbach, T. Boller, H. Brauninger, U. Briel, W. Burkert, K. Dennerl, J. Englhauser, R. Gruber, F. Haberl, G. Hartner, G. Hasinger, E. Pfeffermann, W. Pietsch, P. Predehl, J. Schmitt, J. Trumper and U. Zimmermann (2000). 'ROSAT all-sky survey faint source catalogue'. *IAUC* **7432**, 1–+.

Voges, W., T. Boller, K. Dennerl, J. Englhauser, R. Gruber, F. Haberl, J. Paul, W. Pietsch, J. Trümper and H. U. Zimmermann (1996). Identification of the ROSAT All-Sky Survey sources.. In H. U. Zimmermann, J. Trümper, & H. Yorke (Ed.). 'Roentgenstrahlung from the Universe'. pp. 637–640.

von der Linden, W., V. Dose and R. Fischer (1997). How to separate the signal from the background. In Sears, M. and Nedeljkovic, V. and Pendock, N. E. and Sibisi, S. (Ed.). 'Maximum Entropy and Bayesian Methods'. NMB Printers, Port Elizabeth, South Africa. pp. 146–153.

von der Linden, W., V. Dose, J. Padayachee and V. Prozesky (1999). 'Signal and background separation'. *Phys. Rev. E* **59**, 6527–6534.

von Toussaint, U. and S. Gori (2007). Deconvolution using thin-plate splines. In 'Bayesian Inference and Maximum Entropy Methods in Science and Engineering'. Vol. 954 of *American Institute of Physics Conference Series*. pp. 212–220.

Wahba, G. (1990). *Spline Models for Observational Data*. Society for Industrial and Applied Mathematics, Pennsylvania.

Wahba, G. (2006). *Spline Models for Observational Data*. Society for Industrial and Applied Mathematics(SIAM), Philadelphia, PA(US).

Watson, M. G., A. C. Schröder, D. Fyfe, C. G. Page, G. Lamer, S. Mateos, J. Pye, M. Sakano, S. Rosen, J. Ballet, X. Barcons, D. Barret, T. Boller, H. Brunner, M. Brusa, A. Caccianiga, F. J. Carrera, M. Ceballos, R. Della Ceca, M. Denby, G. Denkinson, S. Dupuy, S. Farrell, F. Fraschetti, M. J. Freyberg, P. Guillout, V. Hambaryan, T. Maccacaro, B. Mathiesen, R. McMahon, L. Michel, C. Motch, J. P. Osborne, M. Page, M. W. Pakull, W. Pietsch, R. Saxton, A. Schwope, P. Severgnini, M. Simpson, G. Sironi, G. Stewart, I. M. Stewart, A. Stobbart, J. Tedds, R. Warwick, N. Webb, R. West, D. Worrall and W. Yuan (2008). 'The XMM-Newton Serendipitous Survey. V. The Second XMM-Newton Serendipitous Source Catalogue'. *ArXiv e-prints*.

Watson, M. G., J. P. Pye, M. Denby, J. P. Osborne, D. Barret, T. Boller, H. Brunner, M. T. Ceballos, R. Della Ceca, D. J. Fyfe, G. Lamer, T. Maccacaro, L. Michel, C. Motch, W. Pietsch, R. D. Saxton, A. C. Schröder, I. M. Stewart, J. A. Tedds and N. Webb (2003). 'The XMM-Newton serendipitous source catalogue'. *Astronomische Nachrichten* **324**, 89–92.

Weisskopf, M. C., H. D. Tananbaum, L. P. Van Speybroeck and S. L. O'Dell (2000). Chandra X-ray Observatory (CXO): overview. In J. E. Truemper & B. Aschenbach (Ed.). 'Society of Photo-Optical Instrumentation Engineers (SPIE) Conference Series'. Vol. 4012 of *Presented at the Society of Photo-Optical Instrumentation Engineers (SPIE) Conference*. pp. 2–16.

Werner, N., A. Finoguenov, J. S. Kaastra, A. Simionescu, J. P. Dietrich, J. Vink and H. Böhringer (2008). 'Detection of hot gas in the filament connecting the clusters of galaxies Abell 222 and Abell 223'. *A&A* **482**, L29–L33.

White, N. E., P. Giommi and L. Angelini (1994). The WGA Catalog of ROSAT Point Sources. In 'Bulletin of the American Astronomical Society'. Vol. 26 of *Bulletin of the American Astronomical Society*. pp. 1372–+.

Wolf, C., H. Hildebrandt, E. N. Taylor and K. Meisenheimer (2008). 'Calibration update of the COMBO-17 CDFS catalogue'. *A&A* **492**, 933–936.

Wolf, C., K. Meisenheimer, M. Kleinheinrich, A. Borch, S. Dye, M. Gray, L. Wisotzki, E. F. Bell, H.-W. Rix, A. Cimatti, G. Hasinger and G. Szokoly (2004). 'A catalogue of the Chandra Deep Field South with multi-colour classification and photometric redshifts from COMBO-17'. *A&A* **421**, 913–936.

XMM-Newton Survey Science Centre, C. (2008). 'The XMM-Newton 2nd Incremental Source Catalogue (2XMMi) (XMM-SSC, 2008)'. *VizieR Online Data Catalog* **9040**, 0–+.

Zacharias, N., D. G. Monet, S. E. Levine, S. E. Urban, R. Gaume and G. L. Wycoff (2005). 'NOMAD Catalog (Zacharias+ 2005)'. *VizieR Online Data Catalog* **1297**, 0–+.

Zappacosta, L., F. Nicastro, R. Maiolino, G. Tagliaferri, D. A. Buote, T. Fang, P. J. Humphrey and F. Gastaldello (2010). 'Studying the WHIM Content of Large-scale Structures Along the Line of Sight to H 2356-309'. *ApJ* **717**, 74–84.

Zeldovich, I. B. (1978). The theory of the large scale structure of the universe. In M. S. Longair and J. Einasto (Eds.). 'Large Scale Structures in the Universe'. Vol. 79 of *IAU Symposium*. pp. 409–420.

Acknowledgments

My deeply–felt thanks go to all the scientific community that helped to make this thesis possible. Many names should be mentioned here. Seeking for brevity in an already long thesis, I must omit the name of those individuals not directly involved in my thesis, but they all fed me with energy, boldness and optimism.

Especially, I have a debt of gratitude to my supervisors, Prof. Dr. Dr.h.c. Volker Dose and Prof. Dr. Hans Böhringer, and my advisors, Dr. Rainer Fischer and Dr. Piero Rosati, for their thoughtful guidance, support, advices and encouragement.

I would like to emphasize my thankfulness to Dr. Rainer Fischer for being an excellent advisor, for always giving suggestions to overcome problems, for being available for questions, for understanding the kind of student he was facing and for providing the proper environment that allowed me to push forward. I also cordially thank all members of the former Center for Interdisciplinary Plasma Science (CIPS) group at the Max–Planck–Institut für Plasmaphysik (IPP) in Garching, lead by Prof. Dr. Dr.h.c. Volker Dose and with Dr. Rainer Fischer as a member: Dr. Roland Preuss, Dr. Udo von Toussaint, Silvio Gori and Ingeborg Zeising. I express my sincere gratitude to them for their advices and useful discussions, to Dr. Udo von Toussaint for revising part of my manuscript, to Silvio Gori for his fundamental prompt help in computer science and to Ingeborg Zeising for her efficient help with documents and information needed for my stay in Germany. I would like to additionally prise Prof. Dr. Dr.h.c. Volker Dose for his lessons and comments also after his retirement. The experience, that the CIPS members acquired on inverse problems and Bayesian analysis, has been fundamental for the success of this thesis. Hence, I feel indebted to them. Furthermore, I owe gratitude to the CIPS members also for giving me the possibility to participate actively at two MaxEnt conferences. I had the great pleasure to directly experience scientific discussions on different methods in data analysis from a broad range of diverse disciplines. Diverse applications of a logical and unified approach to statistics strengthened my understandings on data analysis.
Furthermore, I would like to thank Dr. Joachim Roth, department head of Material Forschung, and Dr. Wolfgang Jacob, head of Arbeitsgruppe Reaktive Plasma Prozesse, to allow me to finish my thesis at IPP.

Dr. Piero Rosati from the European Southern Observatory (ESO), Garching, deserves also my acknowledgments for being a charismatic advisor, for being available for questions, for sharing his broad knowledge in astrophysics and in image analysis, and for passing on his enthusiasm to me.

I am grateful to Dr. Vincenzo Mainieri (ESO) for providing the color composite image shown in Fig. 7.25 (panel B), to Drs Paolo Tozzi, Andrea Bignamini and Shaji Vattakunnel (Osservatorio Astronomico di Trieste) for making available the results with the WAVDETECT algorithm on the simulated and the CDF–S 500ks data sets, allowing for two blind tests with the results obtained with the BSS method, Dr. Paolo Tozzi also for providing in advance the soft image of the 4 Ms *Chandra* data of the CDF–S region.

Acknowledgments are owed to many members of the Max–Planck–Institut für extraterrestrische Physik in Garching, especially to: Prof. Dr. Günther Boese for teaching the ML technique and giving advices, Prof. Dr. Günther Hasinger (former Director of the High–Energy–Group) for giving advices and for supporting some schools and meetings; Prof. Dr. Dr.h.c. Gregor Morfill (Director of the Theory Group) for allowing me to make changes for my thesis supervision; Prof. Dr. Hans Böhringer (head of the Research Group for Clusters of Galaxies and Cosmology) for kindly accepting the request to referee this thesis and for allowing me to take part at the "Cluster group meetings" and for the many many enlightening discussions that improved this thesis.

The years before the starting of my Ph.D. were crucial for my subsequent professional development. I express, therefore, deep gratitute to the astrometric group members of the Osservatorio Astronomico of Torino (OATo), Italy, and to the former Catalogue and Survey Branch group members of the Space Telescope Science Institute (STScI) in Baltimore, MD, US. My warm and sincere thanks are due to Dr. Mario G. Lattanzi (OATo) and Dr. Brian McLean (STScI) for including me in their projects. I additionally acknowledge Dr. Richard Smart (OATo) for revising the English of part of my manuscript.

I dedicate this thesis to my parents Franca and Angelo: I wish to give you the most deep grazie! for making my educational formation possible and not less important the patience you had in the last years for sharing very little time together. *Dedico questo lavoro di tesi ai miei genitori Franca e Angelo: Desidero porgervi i miei più sentiti grazie! per aver reso possibile la mia formazione scolastica e non meno importante per la pazienza che avete avuto nel trascorrere poco tempo insieme negli ultimi anni.* My thoughts go obviously also to my sisters, Donatella and Monica. At the time of being "happy puppies", I enjoy the memories of sharing hours while solving mathematical problems with Donatella. I would like to thank Monica for being a very strong person and for being able to not suffer the real defeat that life can bring. The completion of this thesis assumes a very pleasant taste with you here.

Last, but not least, I owe my loving thanks to my husband Dr. Jörg Retzlaff and my daughter Susanna Retzlaff. During this thesis, I am greatful to you, Jörg, for your support and the infinite lessons about cosmology. And to you, my little star Susanna, I warmly thank you: Your smiles and kisses gave me the strength I needed to go through this thesis.

Publications

Journal Papers

Background-source separation in astronomical images with Bayesian probability theory - I. The method
F. Guglielmetti, R. Fischer, V. Dose; 2009
Monthly Notices of the Royal Astronomical Society, **396**, 165-190

The Second-Generation Guide Star Catalog: Description and Properties
B.M. Lasker et al.; 2008
Astronomical Journal, **136**, 735-766

Galactic orbits of Planetary Nebulae unveil thin and thick disk populations and cast light on interaction with the interstellar medium
F. Kerber, R.P. Mignani, E.-M. Pauli, A. Wicenec, F. Guglielmetti; 2004
Astronomy & Astrophysics, **420**, 207-211

Galactic Planetary Nebulae and their central stars. I. An accurate and homogeneous set of coordinates
F. Kerber, R.P. Mignani, F. Guglielmetti, A. Wicenec; 2003
Astronomy & Astrophysics, **408**, 1029-1035

The runaway black hole GRO J1655-40
I.F. Mirabel, R. Mignani, I. Rodrigues, J.A. Combi, L.F. Rodriguez, F. Guglielmetti; 2002
Astronomy & Astrophysics, **395**, 595-599

Asteroids observations with the Hubble Space Telescope. I. Observing strategy, and data analysis and modeling process
D. Hestroffer, P. Tanga, A. Cellino, F. Guglielmetti, M.-G. Lattanzi, M. Di Martino, V. Zappalà, J. Berthier; 2002
Astronomy & Astrophysics, **391**, 1123-1132

Proper motion of the central star of the Planetary Nebula Sh 2-68
F. Kerber, F. Guglielmetti, R. Mignani, M. Roth; 2002
Astronomy & Astrophysics, **381**, L9-L12

A high-velocity black hole on a Galactic-halo orbit in the solar neighbourhood
I.F. Mirabel, V. Dhawan, R.P. Mignani, I. Rodrigues, F. Guglielmetti; 2001
Nature, **413**, 139

Refereed Conference Papers

Searching Faint and Extended Sources in the X-ray Universe
F. Guglielmetti, R. Fischer, P. Rosati, V. Mainieri, V. Dose; 2005
Proc. of the Conf. *MaxEnt05*, **803**, 162-169

Mixture Modeling for Background and Source Separation in x-ray Astronomical Images
F. Guglielmetti, R. Fischer, V. Dose; 2004
Proc. of the Conf. *MaxEnt04*, **735**, 111-118

Unrefereed Conference Papers

Source Detection and Background Estimation with Bayesian Inference
F. Guglielmetti, R. Fischer, W. Voges, G. Boese, V. Dose; 2004
Proc. of the Conf. *5th INTEGRAL Workshop on the INTEGRAL Universe*, **552**, 847

Source Detection with Bayesian Inference on ROSAT All-Sky Survey Data Sample
F. Guglielmetti, W. Voges, R. Fischer, G. Boese, V. Dose; 2003
Proc. of the Conf. *ADASSXIII*
ASP Conference Proceedings, **314**, 253 (2004)

Sh2-69 - A Planetary Nebula Leaving it's Mark on the Interstellar Medium
F. Kerber, F. Guglielmetti, R. Mignani, M. Roth; 2001
Proc. of the 209th IAU Symp. *Planetary Nebulae: Their Evolution and Role in the Universe.* ASP, 2003, 525

Measurements of Angular Diameters of two Mira Variables using HST FGS#3
F. Guglielmetti, M.-G. Lattanzi, U. Munari; 2000
Proc. of the Conf. *A Decade of HST Science*

Direct Measurements of Asteroid Sizes and Duplicity Search by the HST FGS Interferometer
P. Tanga, D. Loreggia, D. Hestroffer, M.-G. Lattanzi, A. Cellino, F. Guglielmetti, M. di Martino, V. Zappalà; 1999
Bulletin of the American Astronomical Society, **31**, No. 4, 1105, #20.03